GOVT. DOC.
Y3.N21/5:6/2192

NATIONAL ADVISORY COMMITTEE FOR AERONAUTICS

TECHNICAL NOTE 2192

A SURVEY OF THE FLOW AT THE PLANE OF THE PROPELLER OF A TWIN-ENGINE AIRPLANE

By John C. Roberts and Paul F. Yaggy

Ames Aeronautical Laboratory
Moffett Field, Calif.

Washington
September 1950

BUSINESS, SCIENCE & TECHNOLOGY DEP'T.
SEP 29 1950

NATIONAL ADVISORY COMMITTEE FOR AERONAUTICS

TECHNICAL NOTE 2192

A SURVEY OF THE FLOW AT THE PLANE OF THE PROPELLER OF A TWIN-ENGINE AIRPLANE

By John C. Roberts and Paul F. Yaggy

SUMMARY

The air flow at the plane of the propeller of a full-scale twin-engine airplane was surveyed to provide data for use in the calculation of oscillating aerodynamic loadings on propellers. The investigation was conducted throughout an angle-of-attack range of 0° to 10° for two nacelle inlet mass-flow ratios. Data were obtained for wing-flap deflections of 0° and 40° for each nacelle inlet mass-flow ratio. The results are presented in the form of the following parameters: the ratio of the local velocity to the free-stream velocity, and the angles defining the direction of the local velocity relative to the survey disk. The test data are presented as the variation of these parameters with radial position for various angular positions around the thrust axis. A comparison is made between measured upwash angles and those calculated for the wing by the use of lifting-line theory. The effect of the flow field on the oscillating aerodynamic loading on a propeller is indicated. The method of using the flow-field data in calculating this loading is given in the appendix.

The most significant feature of the test results is that the measured upwash angles were much larger than the calculated wing-induced upwash angles. Thus, it appears that the nacelle and fuselage were responsible for a large portion of the upwash. Since similar results would be expected for other wing-fuselage-nacelle combinations, the importance of developing a method of predicting the contributions of nacelles and fuselages is evident.

With the partial-span wing flaps deflected, the rate of change of upwash angle with lift coefficient was about the same as with the flaps undeflected; at a given lift coefficient, however, the upwash angle was less with the flaps deflected.

Changing the nacelle inlet mass-flow ratio from about 0.14 to 0.29 had a sizable effect on only that part of the flow field immediately in front of the nacelle, and hence the change does not appear significant from the standpoint of the oscillating aerodynamic loading on a propeller.

INTRODUCTION

As a result of the trends in propeller design, the need for an accurate method of predicting the oscillating aerodynamic loadings which result in first-order vibratory stresses in propellers has become more acute. Such loadings occur on propellers, inclined or noninclined, rotating in unsymmetrical flow fields, such as those of wings, fuselages, and nacelles, or combinations thereof. However, the prediction of these loadings is complicated by the lack of theory and the meagerness of experimental data for unsymmetrical flow fields. To provide some experimental data, therefore, the flow field at the plane of one of the propellers of a twin-engine airplane has been investigated.

Presented in this report are the results of the flow measurements which were made at the plane of the port propeller, propeller removed. Also presented is a comparison of measured upwash angles with wing-induced angles calculated by lifting-line theory. In addition, the effect of the measured flow field on the oscillating aerodynamic loading on a propeller is indicated; the method used in calculating such loadings is given in the appendix.

NOTATION

A_1 nacelle inlet area, square feet

C_L lift coefficient $\left(\frac{\text{lift}}{\frac{1}{2}\rho_o V_o^2 S}\right)$

c_t section thrust coefficient $\left(\frac{t}{\rho_o n^2 D^4}\right)$

Δc_t incremental section thrust coefficient $\left(c_{t_\Omega} - c_{t_{\Omega=0}}\right)$

D propeller diameter, feet

m_1/m_o nacelle inlet mass-flow ratio $\left(\frac{\rho_1 A_1 V_1}{\rho_o A_1 V_o}\right)$

n propeller speed, revolutions per second

r distance along any radial line from the thrust axis, inches

S wing area, square feet

t propeller section thrust, pounds

V_o free-stream velocity, feet per second

V_l local velocity at any point (r,Ω) at the survey disk, feet per second
(Direction of this velocity is defined by the angles θ and ψ. See fig. 1.)

V_l/V_o velocity ratio at any point (r,Ω) at the survey disk

V_B resultant velocity acting on any blade section, neglecting propeller-induced effects, feet per second

V_1 average velocity at the nacelle inlet, feet per second

V' component of the local velocity in the plane perpendicular to a radial line, feet per second

α_G geometric angle of attack of the airplane thrust axis, degrees

β section blade angle, degrees

δ_f angle of deflection of the wing flaps, degrees

ϵ angle of upwash, measured from a line parallel to the free-stream direction in a plane parallel to the model plane of symmetry, degrees

θ angle of outflow, measured from a line parallel to the thrust axis in a plane through the thrust axis, degrees

θ' angle at which the local velocity at any point on the survey disk is inclined to the plane perpendicular to the radial line through that point, degrees

ρ_o mass density of air in the free stream, slugs per cubic foot

ρ_1 mass density of air at the nacelle inlet, slugs per cubic foot

σ sidewash angle, measured from a line parallel to the thrust axis in a plane normal to the model plane of symmetry, positive toward starboard, degrees

ψ angle of rotational flow (an apparent, not an actual, rotation), measured from a line parallel to the thrust axis in a plane perpendicular to a radial line, degrees

Ω angular position about the thrust axis, measured counterclockwise from the upper vertical position as seen from the front, degrees

The angles, θ, θ', and ψ are further defined in figure 1.

AIRPLANE AND APPARATUS

The principal dimensions of the airplane used for the investigation are shown on the three-view drawing presented in figure 2. Figure 3 shows the airplane mounted in the Ames 40- by 80-foot wind tunnel.

Coordinates of the portions of the fuselage and nacelle forward of the wing leading edge are presented in figure 4. The arrangement of the interior of the nacelle is shown in figure 5. (The reciprocating engine was replaced by an electric motor. To accommodate this change, the nacelle was lengthened as indicated in figure 2. However, the inlet shape and area remained the same.) To determine the inlet mass-flow ratio, six rakes of pressure tubes were spaced around the nacelle inlet. (See fig. 5.) Four exhaust ports, two of which are shown in figure 5, spanned approximately 40 percent of the circumference of the nacelle. The nacelle inlet mass-flow ratio was varied by sealing and unsealing these openings.

The survey rake consisted of eight directional-pitot-static tubes mounted at various intervals along a steel tube of 56-inch length. The head of each tube was essentially the same as that illustrated in figure 2 of reference 1. The rake is shown mounted on the airplane in figure 3. One end of the rake was attached to the propeller shaft and the other end was supported by means of two struts extending back to the nacelle. In order to survey a sufficiently large area, the rake was also mounted with an extension between it and the propeller shaft. Flow measurements were made at various angular positions on the survey disk by manually rotating the rake about the thrust axis to each position.

TESTS

Tests were conducted to obtain data throughout an angle-of-attack range of 0° to 10° at each angular position on the survey disk with the airplane at the following four sets of conditions:

1. $\delta_f = 0^\circ$, $m_1/m_o = 0.29$
2. $\delta_f = 40^\circ$, $m_1/m_o = 0.29$
3. $\delta_f = 0^\circ$, $m_1/m_o = 0.14$
4. $\delta_f = 40^\circ$, $m_1/m_o = 0.14$

The tunnel speeds for these tests were approximately 140 and 100 miles per hour with 0° and 40° wing-flap deflections, respectively. Tests were also conducted over a tunnel-speed range of 60 to 180 miles per hour at 0° angle of attack of the thrust axis and 0° wing-flap deflection.

RESULTS

The following table indexes the figures which present the variation of the flow parameters with radial and angular position on the survey disk for the four sets of test conditions:

Figure No.	Flow parameter	δ_f (deg)	m_1/m_o
6	Angle of rotational flow, ψ	0	0.29
7	-- do. --	40	.29
8	-- do. --	0	.14
9	-- do. --	40	.14
10	Angle of outflow, θ	0	.29
11	-- do. --	40	.29
12	-- do. --	0	.14
13	-- do. --	40	.14
14	Velocity ratio, V_l/V_o	0	.29
15	-- do. --	40	.29
16	-- do. --	0	.14
17	-- do. --	40	.14

The data obtained for varying tunnel speed are not presented because no variation in the flow parameters was found.

Tunnel-wall corrections were not applied to the data since there is considerable uncertainty as to the source of a large part of the induced flow. However, the tunnel-wall corrections for the wing-induced flow are determinable by the customary procedure and are as follows:

$$\Delta\alpha = 0.85\ C_L$$

$$\Delta\epsilon = -.50\ C_L$$

where the upwash angle correction is for a longitudinal position corresponding to the location of the survey disk. These corrections should be added algebraically to the measured angles. It should be noted further that both these corrections are applicable strictly at the tunnel center line only.

In order to illustrate the flow conditions at the survey disk, some of the data of figures 6 through 17 have been replotted in the form of contour charts (i.e., charts showing the location on the survey disk of lines of constant values of the flow parameters). Charts have been

prepared to show how the flow at the survey disk is affected by the three test variables: (1) angle of attack, (2) wing-flap deflection, and (3) nacelle inlet mass-flow ratio.

Changing the angle of attack results in changes in the distribution at the survey disk of ψ, θ, and V_l/V_o as shown in figures 18, 19, and 20, respectively. The data are also shown as upwash angle ϵ (fig. 21), and sidewash angle σ (fig. 22).[1] These plots are more suitable in studying the source of the flow angularity; whereas the plots of ψ and θ are more useful in studying the effect of the flow angularity on the oscillating aerodynamic loading on a propeller.

Figure 23 indicates the effect of wing-flap deflection, at a constant angle of attack, on the angles θ and ψ and the velocity ratio V_l/V_o. The effect of wing-flap deflection at constant lift coefficient (approximately 1.0) is indicated in figure 24.

The effect of a change in nacelle inlet mass-flow ratio on the survey-disk distribution of ψ, θ, and V_l/V_o is shown in figure 25. Since the incremental change in any parameter due to the change in this ratio was constant with angle of attack, only the contour charts showing the changes at 0° angle of attack are presented.

DISCUSSION

With respect to the oscillating loading on a propeller, the most important of the flow parameters is the rotational flow angle ψ since it contributes directly to the angle of attack of a blade section. As shown in figure 18 ($\alpha_G = 6^\circ$ and 10°), the values of ψ were greatest near the horizontal center line of the survey disk. At this line, ψ results from the angle of attack α_G and the upwash angle ϵ. The subsequent discussion, therefore, will deal primarily with the effects of the test variables on the upwash angle at the horizontal center line and with comparisons between measured and computed upwash angles at this line.

The relative importance of the effects of all the flow parameters on the oscillating aerodynamic loading on a propeller will be shown in a later section of the discussion.

Upwash Characteristics

Effect of test variables.- At any point on the horizontal center line of the survey disk, outside the maximum nacelle radius, the variation

[1]The values of ϵ and σ were calculated from the measured values of ψ and θ using the following relations:

$$\epsilon = \tan^{-1}\left(\frac{\tan\theta\cos\Omega - \tan\psi\sin\Omega}{}\right) - \alpha_G$$

$$\sigma = \tan^{-1}\left(\tan\theta\sin\Omega + \tan\psi\cos\Omega\right)$$

of upwash angle with lift coefficient was found to be nearly linear. The variations at two representative points on this line are shown in figure 26 for wing-flap deflections of 0° and 40°. The rate of change of upwash angle with lift coefficient was about the same for either wing-flap deflection. For a given lift coefficient, however, the upwash angle was less when the flaps were deflected 40°.

Change in nacelle inlet mass-flow ratio had little effect on the upwash at the horizontal center line of the survey disk.

Comparison with theory.- Since it was expected that the wing contributed a sizable amount of the induced upwash, it was considered desirable to make a theoretical determination of this contribution. Presented in figure 27 is a comparison of the experimental and theoretical variations of upwash angle along the horizontal center line of the survey disk. The theoretical values were derived by application of lifting-line theory (reference 2), using the measured span load distribution,[2] and have been adjusted to wind-tunnel conditions by use of the equation for the wall effects which was given previously. The method accounts for the effects of nacelle and fuselage only in their effect on the wing span load distribution. As may be seen in figure 27, the computed values fall far short of the experimental values. This is true even at points lying more than one nacelle diameter from the center of the survey disk. In these regions the computed upwash angles were about 65 percent of the measured upwash angles. It is reasonable to assume that the difference was due to unaccountable effects of the nacelle and fuselage since there is reason to believe that the lifting-line theory satisfactorily accounts for the inductive effects of the wing. (See reference 1.)

Figure 28 shows the changes in upwash angle that occurred along the horizontal center line of the survey disk when the wing flaps were deflected from 0° to 40° at a constant angle of attack of 6°. Also shown are the corresponding changes in upwash angle due to this flap deflection as computed by lifting-line theory. The computed values are less than the experimental values, as is the case for upwash angle due to angle of attack (fig. 27).

Effect of the Flow Field on the Oscillating Aerodynamic Loading on a Propeller

In order to demonstrate the effect of the flow field on the oscillating aerodynamic loading of an inclined propeller, calculations were made of the variation of the section thrust coefficient through one revolution of a propeller. For these calculations, a geometric angle of attack of 10° was selected and the following three flow conditions were considered: (1) free-stream velocity and no induced flow angles, (2) free-stream velocity and

[2]This distribution was obtained from unpublished data.

measured induced flow angles, and (3) measured velocities and measured induced flow angles. The calculations were limited to a blade section at the 55.3-inch radius at a blade angle of 21.7°. The assumed values of free-stream velocity and rotational speed were 242 feet per second and 1250 rpm, respectively. These particular conditions were assumed because of the availability of measured values of section thrust coefficient for a four-blade propeller rotating at these conditions in the measured flow field. The values of the measured flow parameters used in the calculations are presented in figure 29 and the method of calculation is given in the appendix.

The results of the calculations are presented in figure 30. This figure shows the variation of the incremental section thrust coefficient with angular position about the thrust axis. Also shown is the variation of incremental section thrust coefficient for the blade section of the four-blade propeller as obtained from measurements in the propeller wake. These variations are representative of and proportional to the variations of the oscillating aerodynamic loadings for the same operating conditions.

The comparisons of the load variations provided by figure 30 show the following items of interest:

1. The magnitude of the load variation, that is, the change in loading from the maximum to the minimum load peak, is increased about 75 percent by taking the induced flow angles into account (in addition to geometric angle of attack), and the variation is distorted from the near-sinusoidal variation resulting from the use of geometric angle of attack only.

2. With the measured velocities then taken into account, the major change is a further distortion of the variation; whereas the magnitude of the variation is only slightly changed - increased by about 5 percent.

3. The magnitude of the calculated load variation for the propeller rotating in the measured flow field is within 2 percent of the magnitude of the variation determined from the wake survey. In addition, the calculated loading curve has nearly the same shape as, but peaks somewhat sooner than, the measured loading curve.

It is to be noted that, as would be expected, the induced flow angles provided the major increase in the magnitude of the load variation. That the upwash angle was the main factor is indicated by the upwash-angle and sidewash-angle distributions of figures 21 and 22, respectively. It is evident, therefore, that, in the development of a method for predicting the flow-field characteristics, consideration should first be given to the upwash angle.

The local velocity variation around the survey disk is seen to have but small effect upon the magnitude of the load variation, but it cannot be assumed that this will be the case for all combinations of propellers and

operating conditions. Consequently, in the final analysis, a method of predicting the local velocity variation must be developed if more precise estimates of the oscillating aerodynamic loads on propellers are to be made. It is to be expected, however, that the effect of velocity variation will be small compared to the effect of the induced flow angles.

Although the angular positions at which the maximum and minimum loadings occur appear to be of minor importance compared to the magnitude of the load variation, it is of interest to note that better agreement between the calculated and measured positions resulted when the local velocity variation was taken into account. The calculated maximum load peak occurred about 24° sooner than the measured peak when the local velocity was used in the calculations; whereas, when it was neglected, there was about a 40° difference.

CONCLUDING REMARKS

The inductive effects of the wing–nacelle–fuselage combination on the flow at the propeller plane were quite large. Of these effects, the upwash angle was the most significant in terms of oscillating aerodynamic loading on a propeller. Values computed by the application of lifting-line theory indicated wing-induced upwash angles considerably lower than the measured upwash angles. Thus it appears that the nacelle and fuselage were responsible for a large portion of the upwash. Since similar results would be expected for other wing–fuselage–nacelle combinations, the importance of developing a method of predicting the contributions of nacelles and fuselages to the upwash is evident.

Ames Aeronautical Laboratory,
National Advisory Committee for Aeronautics,
Moffett Field, Calif., July 10, 1950.

APPENDIX

APPLICATION OF THE SURVEY DATA TO THE DETERMINATION OF OSCILLATING AERODYNAMIC LOADING ON A PROPELLER

Velocity Diagrams

The velocities upon which the blade-section loading depends are those in the plane tangent to the blade-section path of rotation. This plane is the same as that in which the angle ψ was measured. (See fig. 1.) The velocity vectors to be considered are thus V', the component of the local velocity in this plane (fig. 1), and the tangential velocity due to the propeller rotation. If propeller-induced velocities are neglected, the velocity diagram for a blade section can be drawn as shown in figure 31. Diagrams are shown for zero, negative, and positive values of ψ as denoted by the subscripts 1, 2, and 3, respectively. Values of the velocity V' are determined from the survey data as follows:

$$V' = (V_l/V_o)\, V_o \cos \theta'$$

where

$$\theta' = \tan^{-1} (\tan \theta \cos \psi)$$

Evaluation of Section Thrust Coefficient c_t

The equation for the c_t of a noninclined, isolated propeller may be derived by using steady-state propeller theory. This equation, presented in reference 3, with slightly different notation, is as follows:

$$c_t = K \pi^3 x^3 \frac{\alpha_i}{57.3} \frac{(\cot \varphi - \tan \gamma)}{\left(\cot \varphi + \frac{\alpha_i}{57.3}\right)^2}$$

where

K Goldstein correction factor for finite number of blades

x radial location of blade section $\left(\frac{r}{R}\right)$

r radius to blade section, feet

R propeller radius, feet

α_i propeller-induced angle of inflow, degrees

γ $\tan^{-1}\left(\frac{\text{blade-section drag}}{\text{blade-section lift}}\right)$, degrees

φ $\varphi_o + \alpha_i$, degrees

φ_o $\tan^{-1}\left(\frac{V_o}{\pi n D x}\right)$, degrees

For an inclined propeller rotating in a nonuniform flow field, the above equation must be modified to account for the variation, in both direction and magnitude, of the local velocity. The equation for the c_t becomes then

$$c_t = K \pi^3 x^3 \frac{\alpha_i}{57.3} \frac{(\cot \varphi - \tan \gamma)}{\left(\cot \varphi + \frac{\alpha_i}{57.3}\right)^2} \left(1 - \frac{V' \sin \psi}{\pi n D x}\right)^2$$

for which it is important to note that

$$\varphi_o = \tan^{-1}\left(\frac{V' \cos \psi}{\pi n D x - V' \sin \psi}\right)$$

as is indicated by figure 31.

REFERENCES

1. Silverstein, Abe, Katzoff, S., and Bullivant, W. Kenneth: Downwash and Wake Behind Plain and Flapped Airfoils. NACA Rep. 651, 1939.

2. Glauert, H.: The Elements of Aerofoil and Airscrew Theory. Cambridge, England, The University Press, Ch. XII, 2d ed., 1947.

3. Crigler, John L.: Comparison of Calculated and Experimental Propeller Characteristics for Four-, Six-, and Eight-Blade Single-Rotating Propellers. NACA ACR 4B04, 1944.

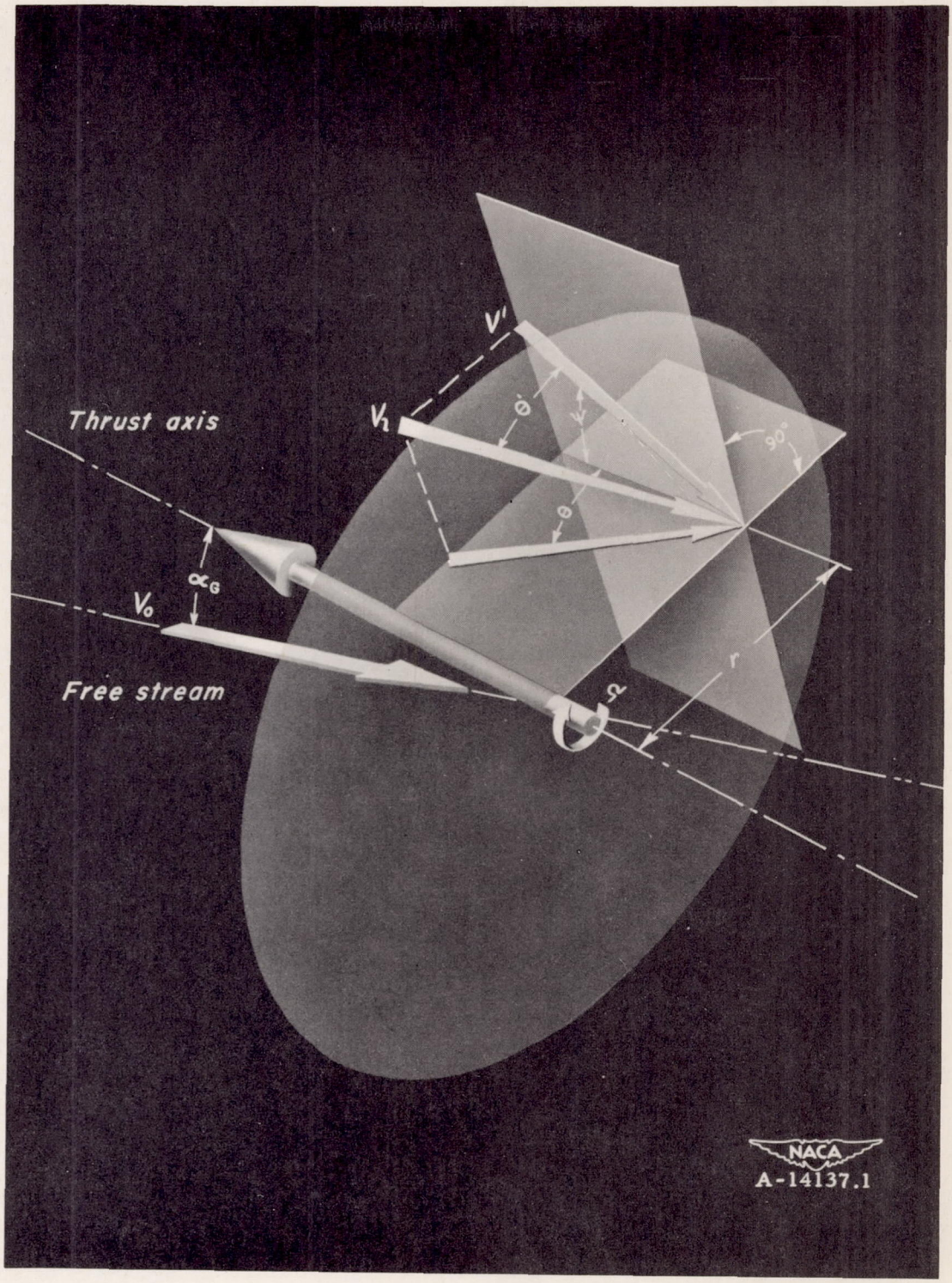


Figure 1.– Geometric characteristics of the flow parameters relative to the survey disk. All angles are shown positive.

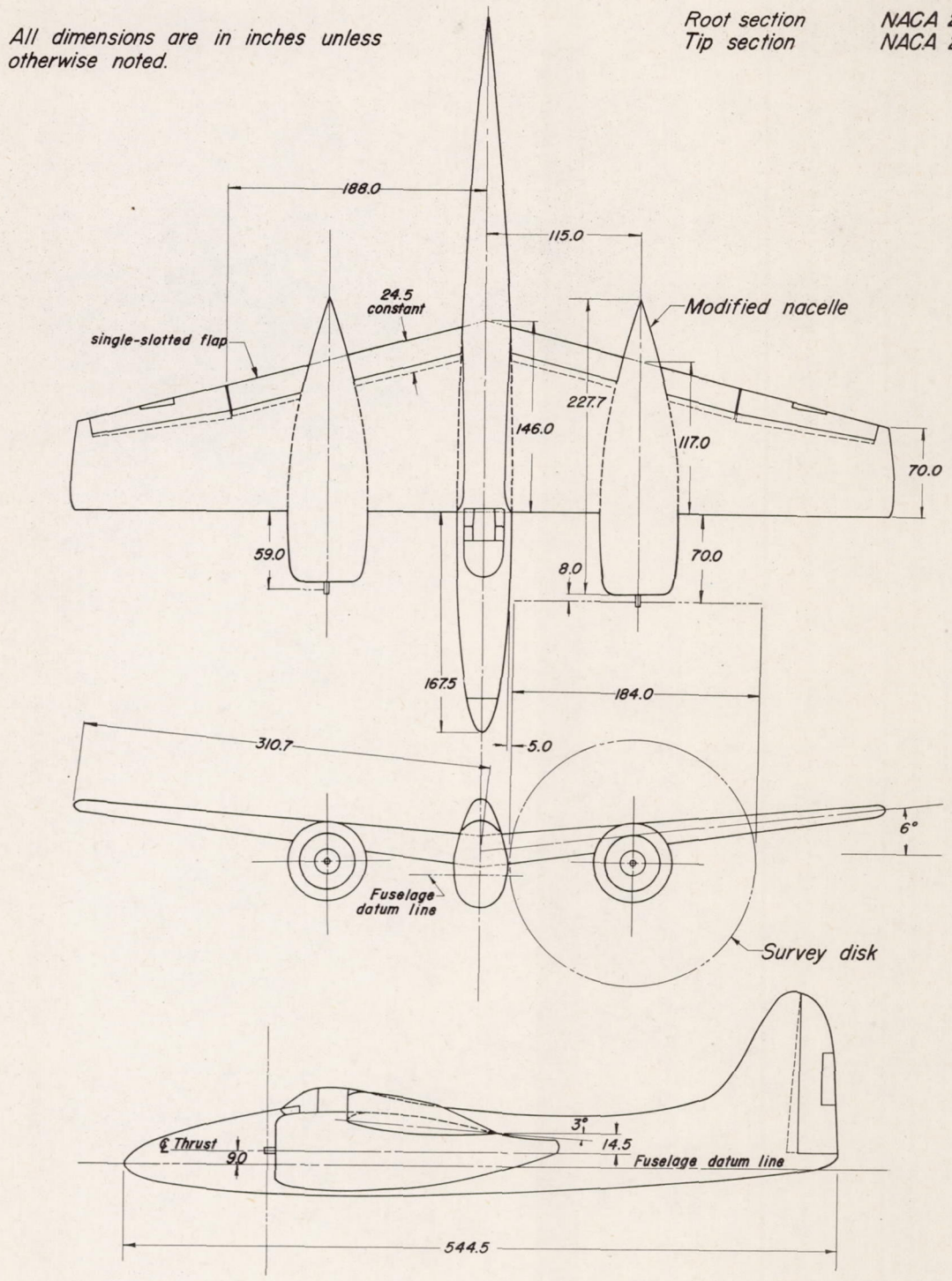


Figure 2.- Geometric characteristics of the twin-engine, fighter-type airplane.

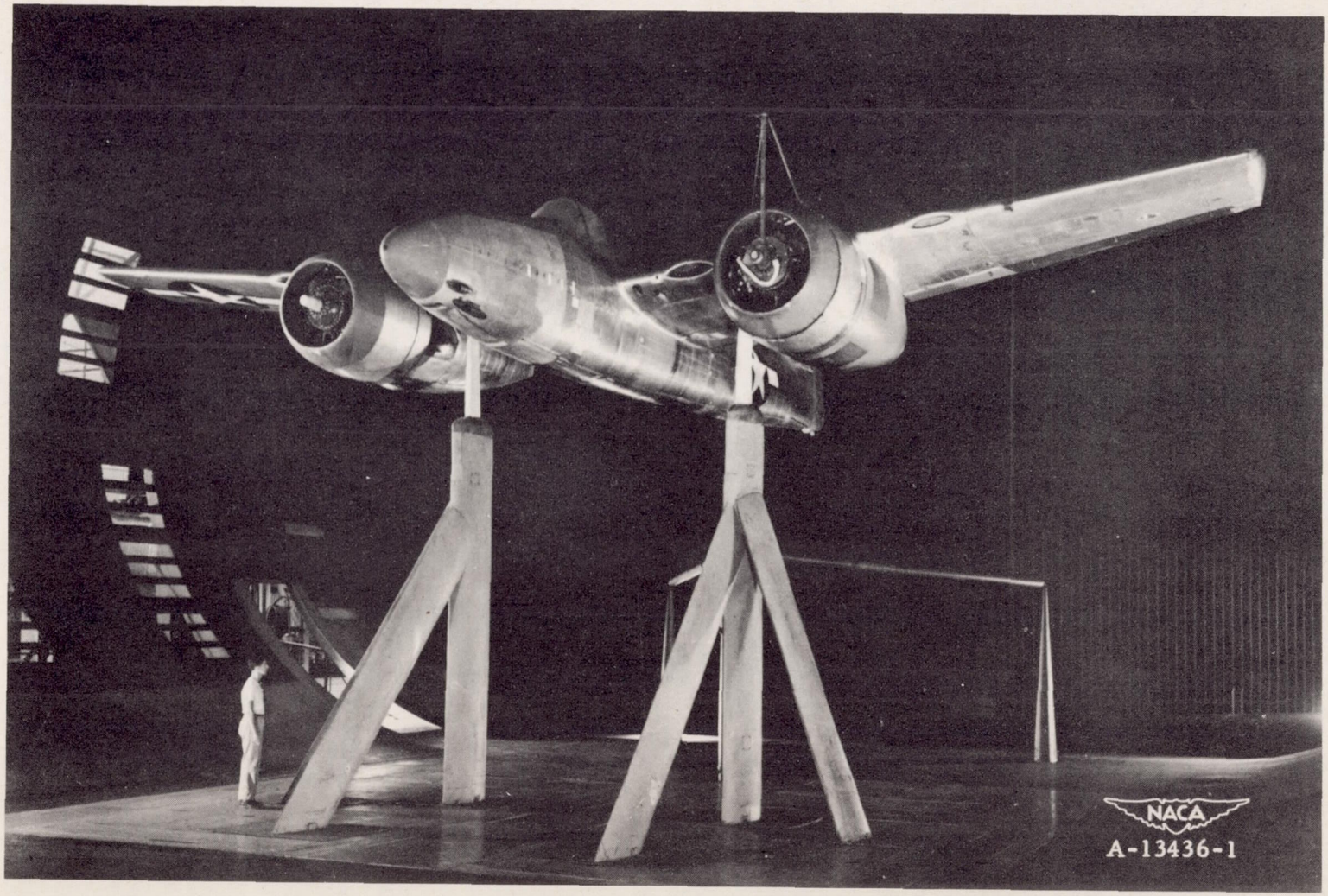
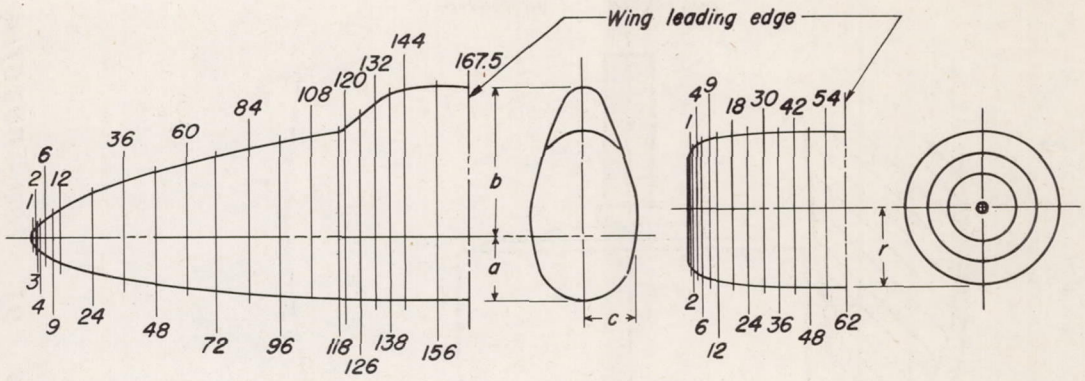


Figure 3.- The airplane mounted in the Ames 40- by 80-foot wind tunnel.



Fuselage coordinates			
Sta.	a	b	c
0	0	0	0
1	3.0	2.3	2.5
2	4.5	3.5	3.5
3	5.3	4.8	4.5
4	6.3	5.8	5.0
6	7.5	7.4	6.2
9	8.8	9.4	7.6
12	10.0	11.3	8.5
24	13.5	17.0	11.5
36	16.4	21.5	13.6
48	18.2	25.5	15.5
60	19.5	28.8	16.6
72	20.8	32.0	17.6
84	21.8	34.4	18.6
96	22.6	36.8	19.2
108	23.3	39.0	19.8
118	23.6	40.7	20.1
120	23.6	42.0	20.1
126	23.9	47.0	20.2
132	24.0	51.6	20.3
138	24.1	55.2	20.4
144	24.2	57.0	20.5
156	24.3	58.0	20.7
167.5	24.3	57.5	20.9

Nacelle coordinates	
Sta.	r
0	21.5
1	23.0
2	24.0
4	25.0
6	26.0
9	27.0
12	27.8
18	28.5
24	29.0
30	29.5
36	29.6
42	29.7
48	29.8
54	29.8
62	29.8

All dimensions are in inches.

Figure 4.— Fuselage and nacelle coordinates for the portions forward of the wing leading edge.

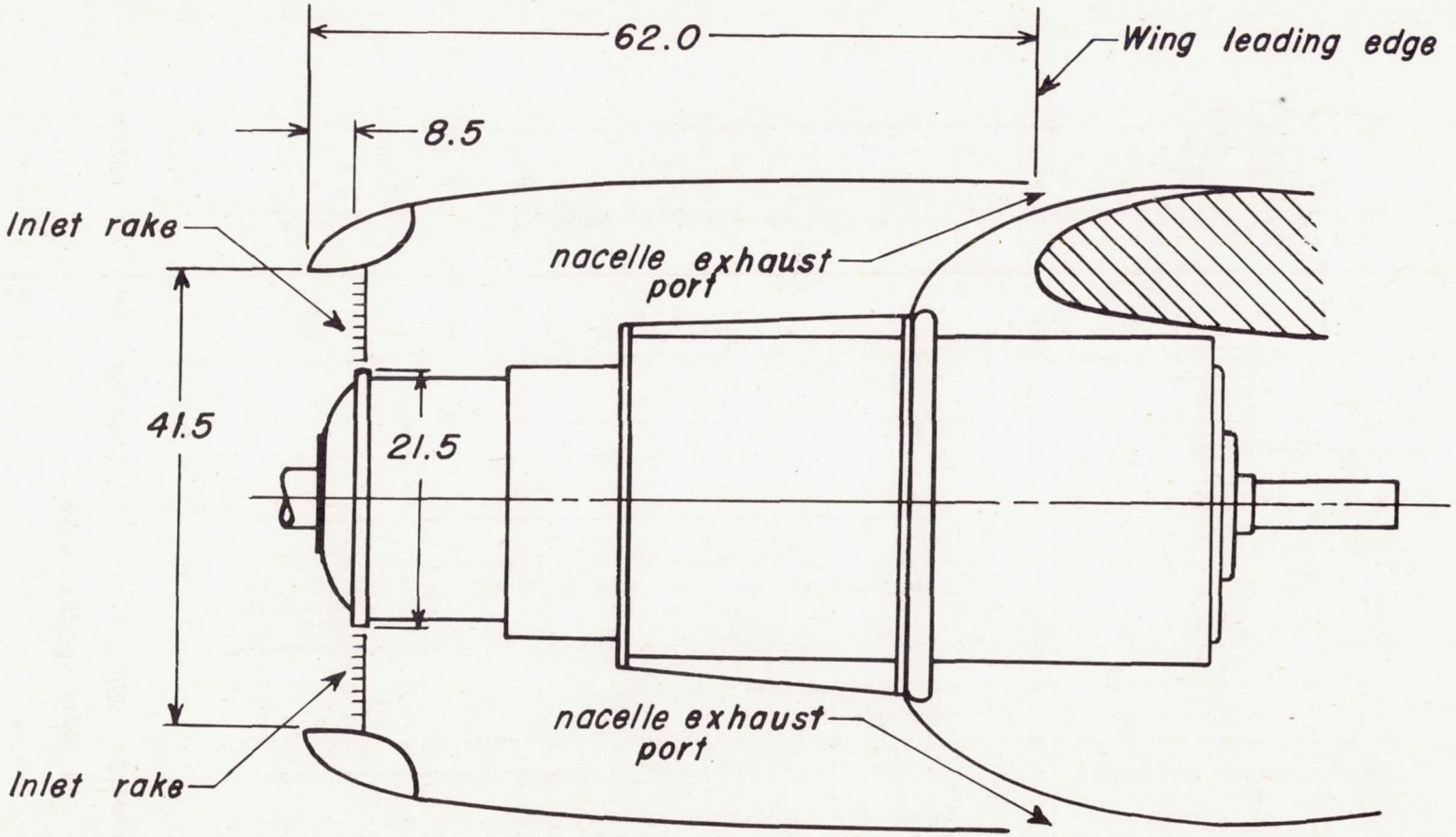
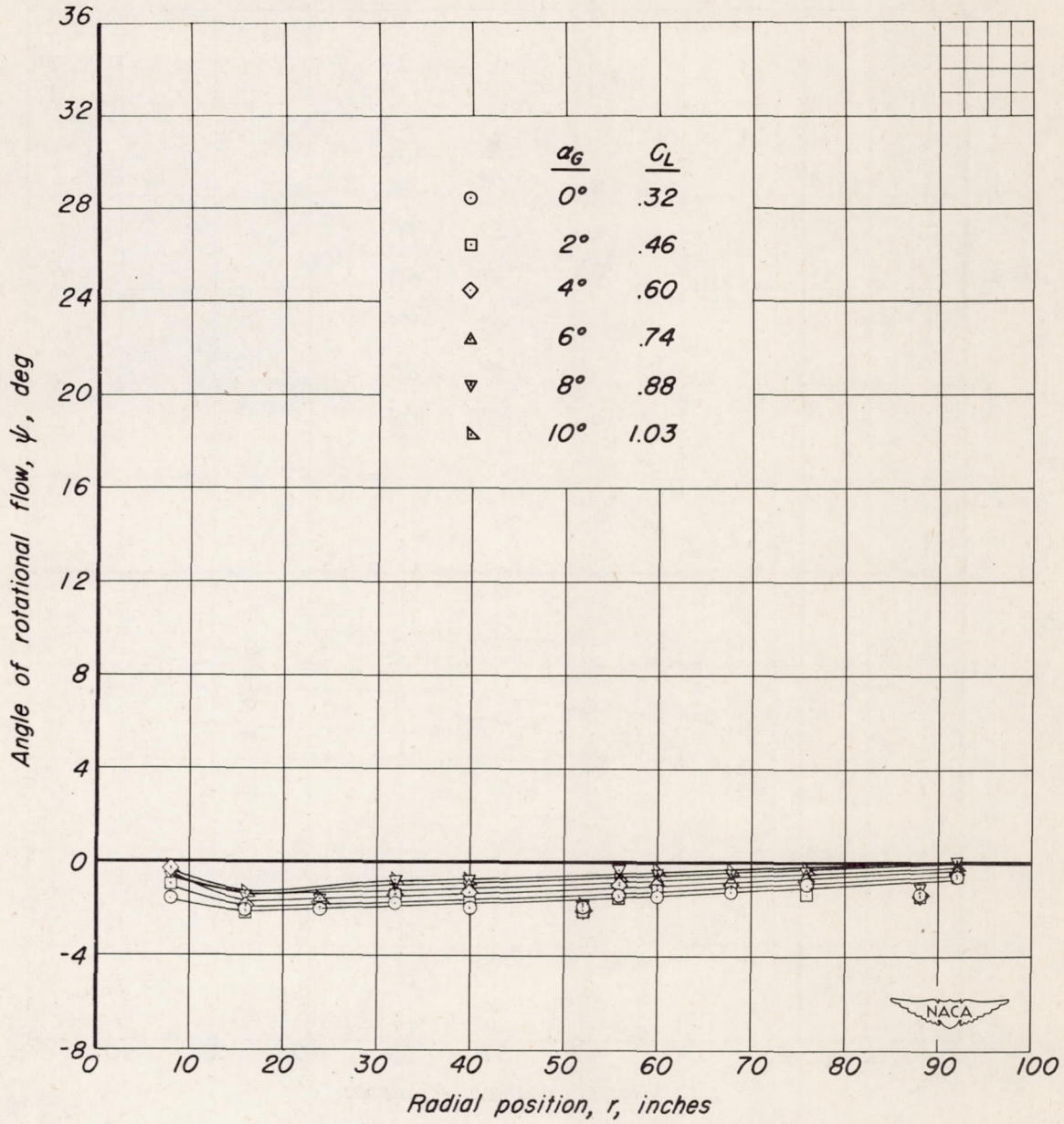
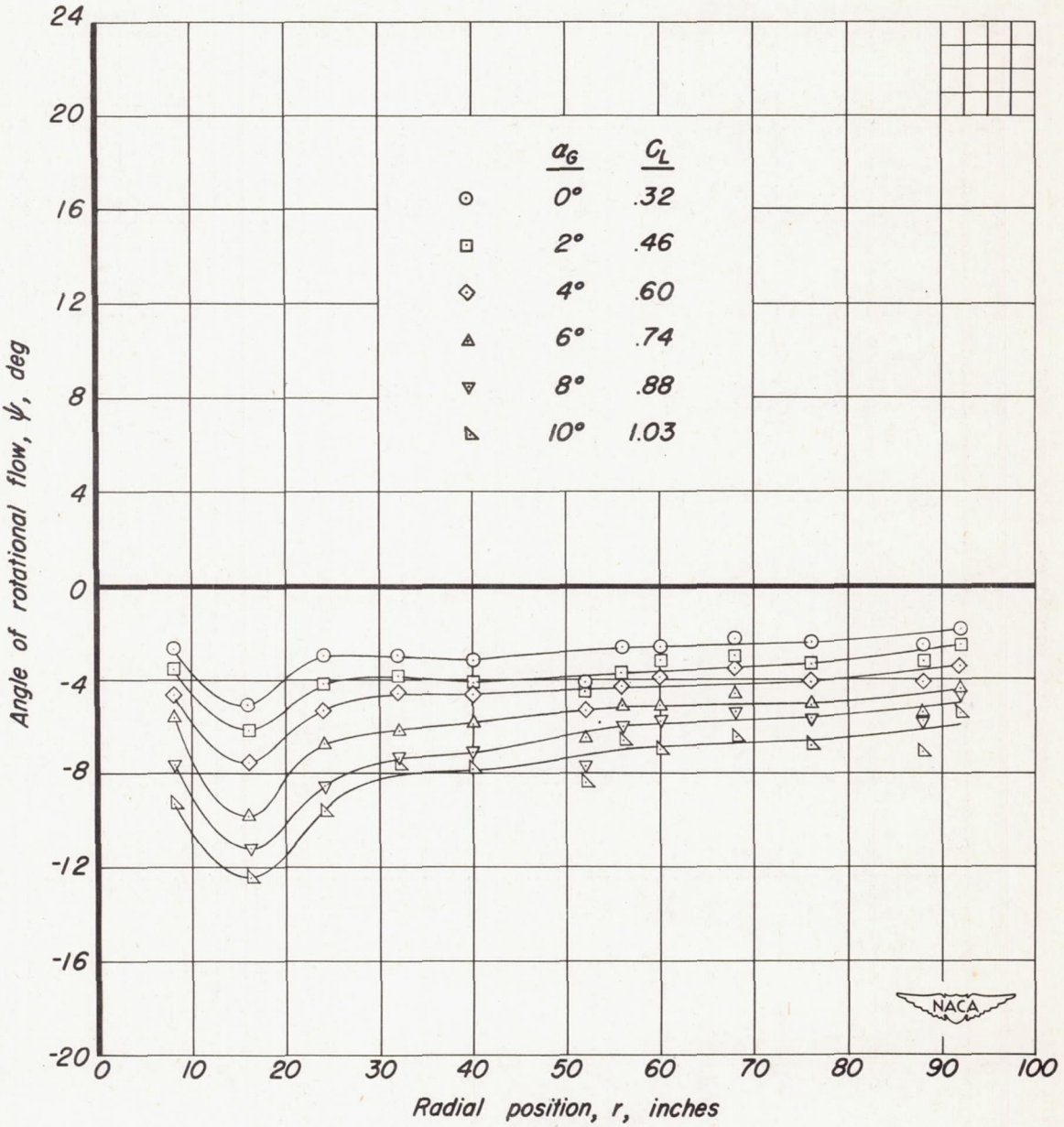


Figure 5. - General arrangement and principal dimensions of the nacelle.



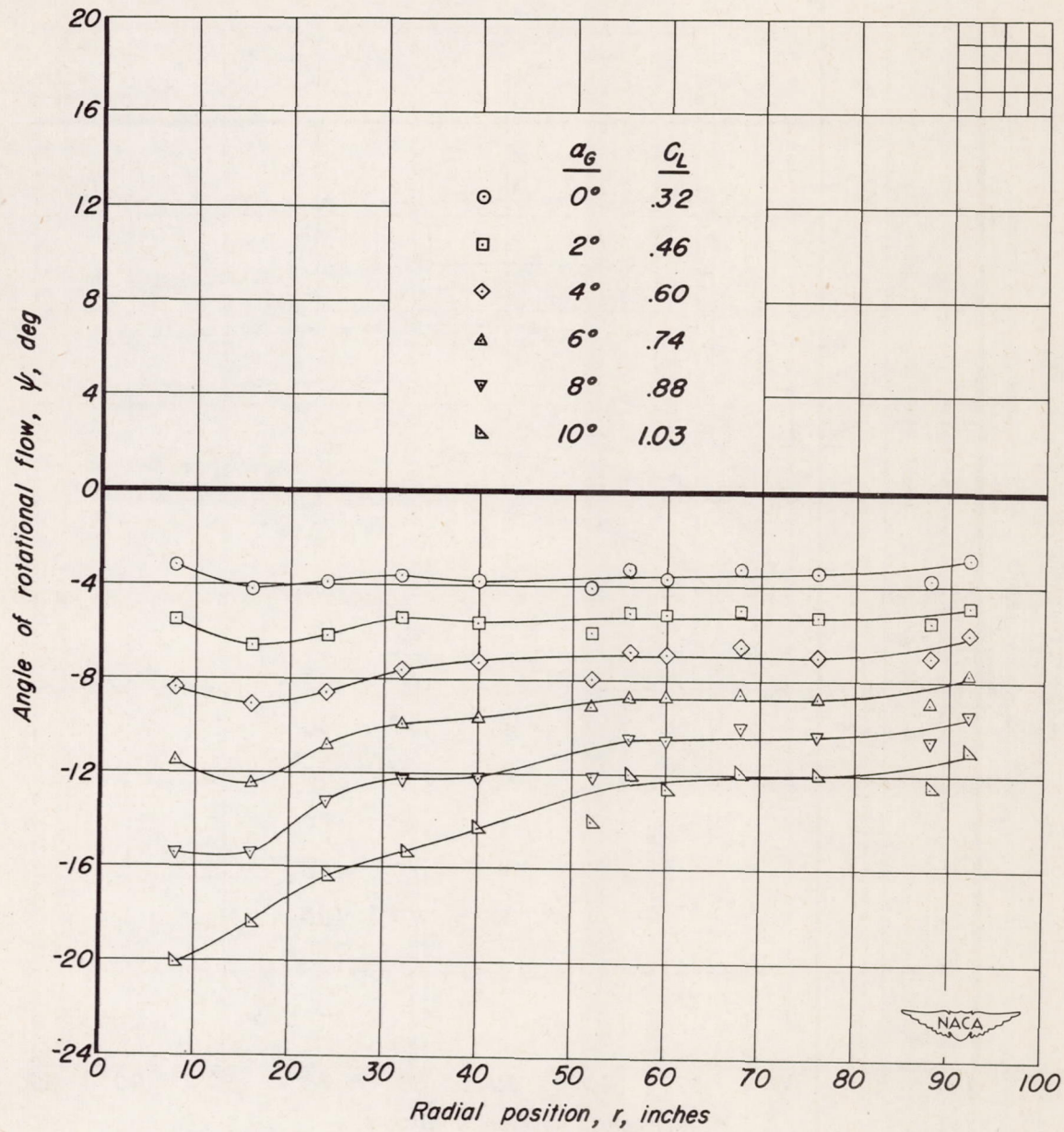
(a) $\Omega = 0.0°$.

Figure 6. - Variation of the angle of rotational flow, ψ, with radial position for several angles of attack. m_1/m_o, .29; δ_f, 0°.



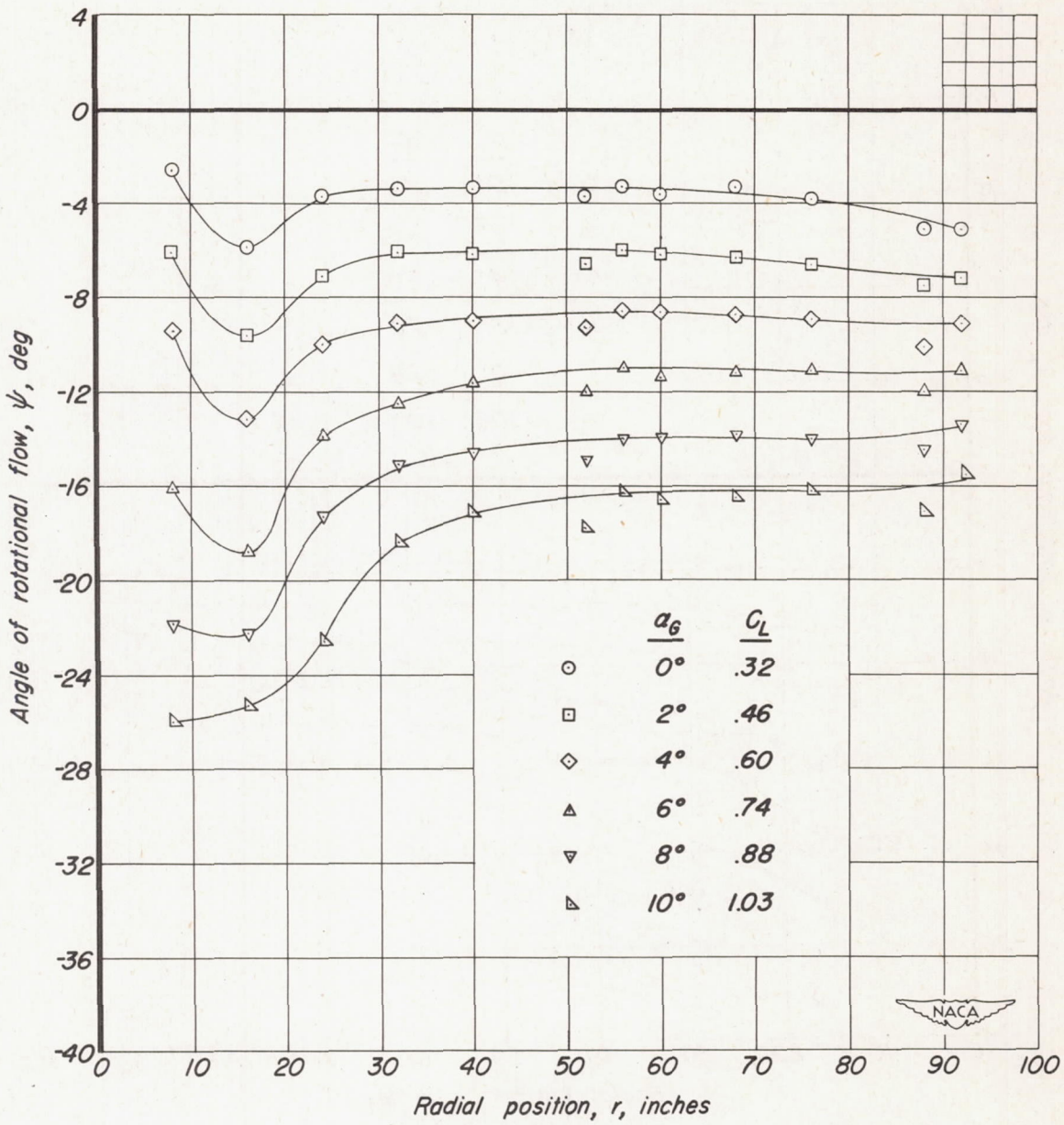
(b) $\Omega = 22.5°$.

Figure 6. - Continued.



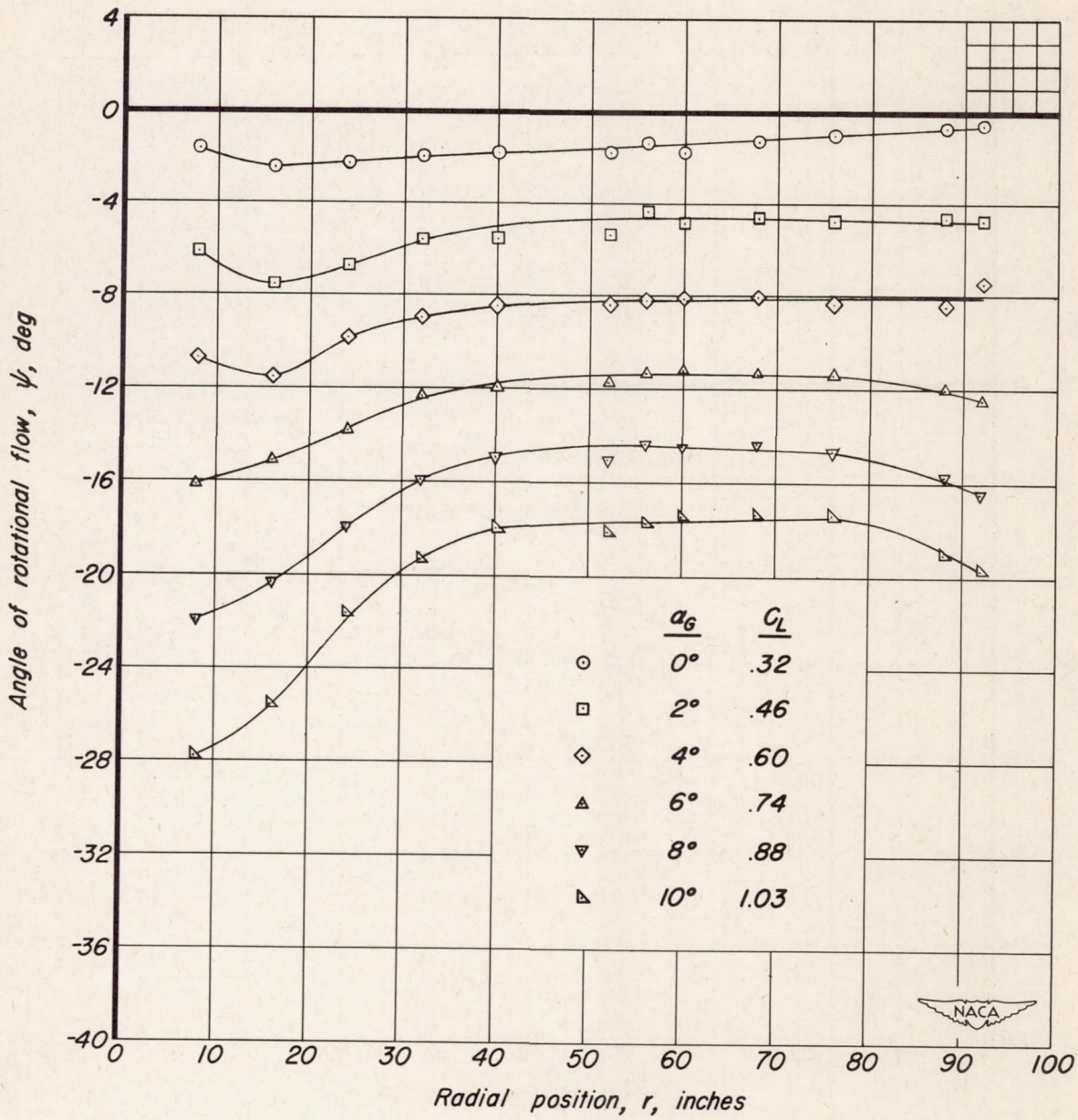
(c) $\Omega = 45.2°$.

Figure 6. - Continued.



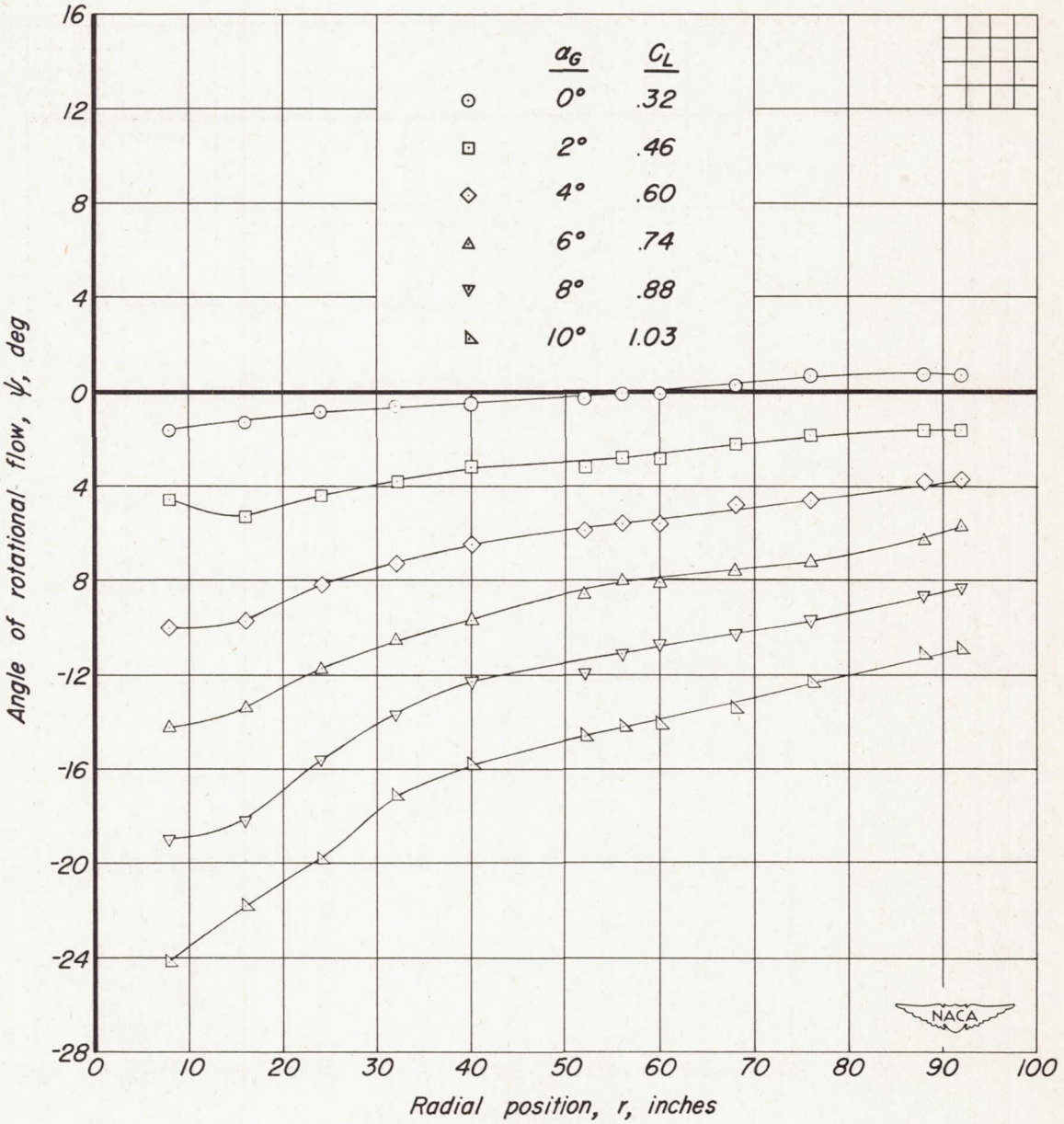
(d) Ω=68.5°.

Figure 6. - Continued.



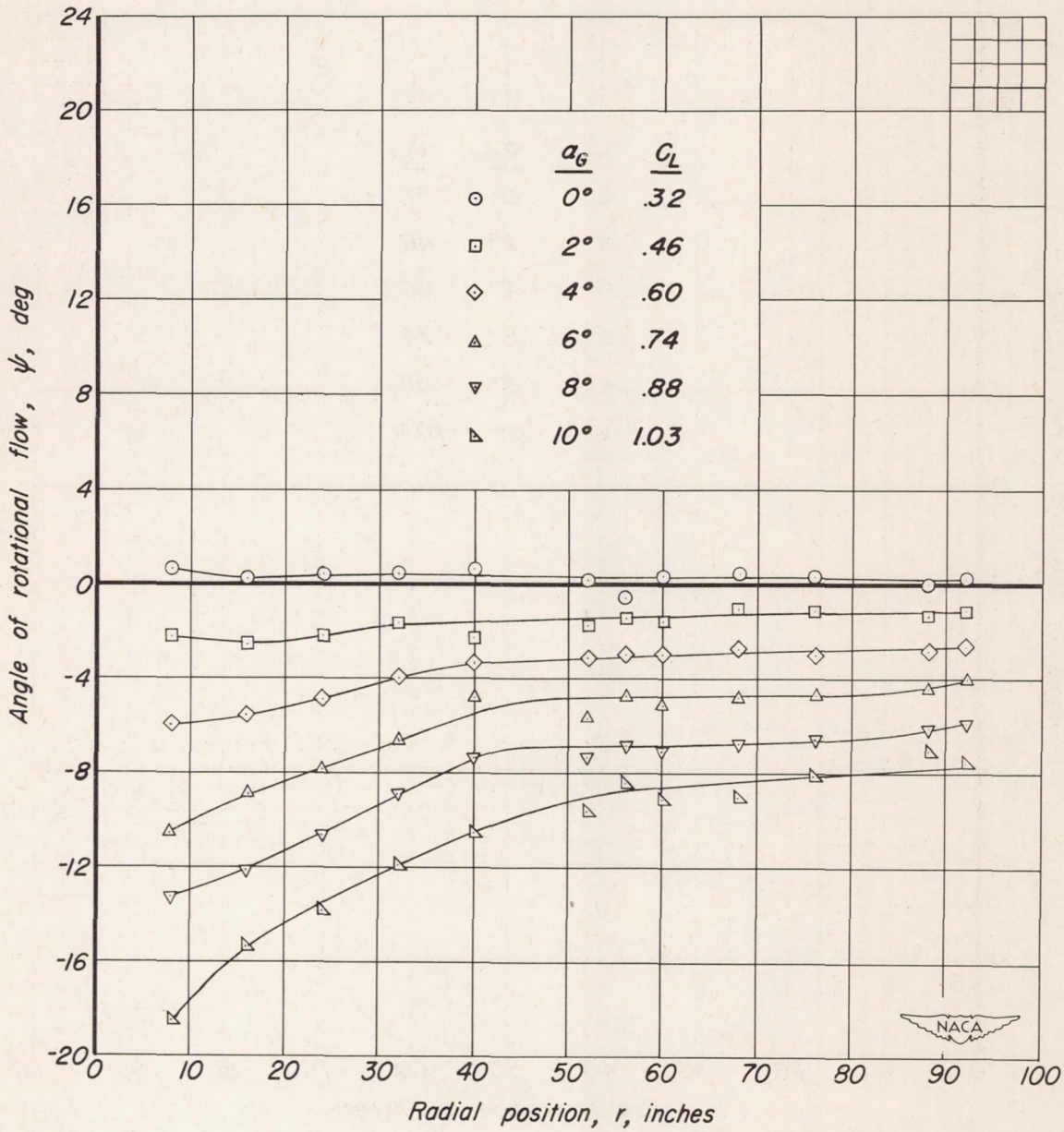
(e) $\Omega = 91.1°$.

Figure 6. - Continued.



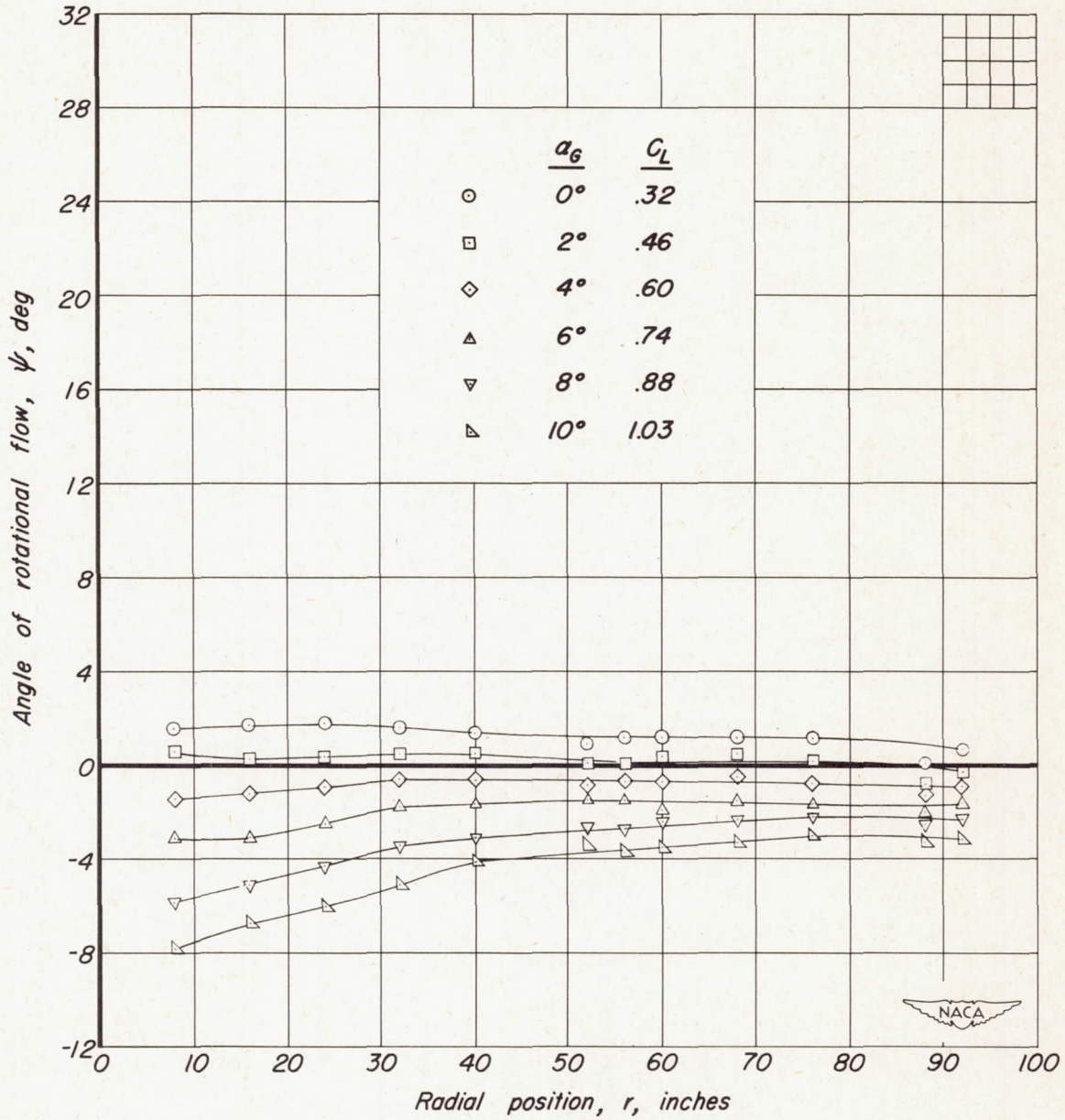
(f) Ω=113.4°

Figure 6. - Continued.



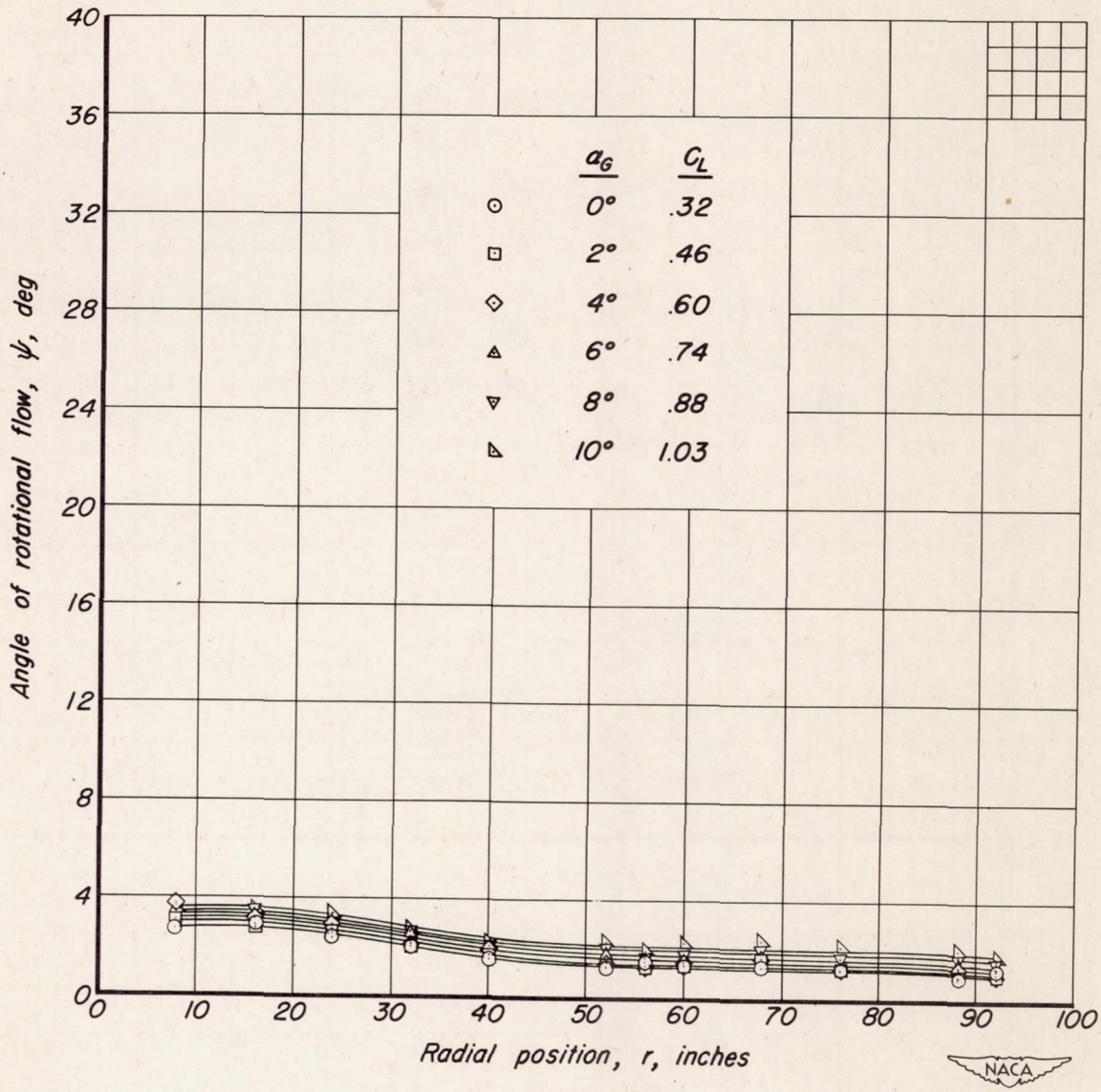
(g) Ω=135.7°.

Figure 6. - Continued.



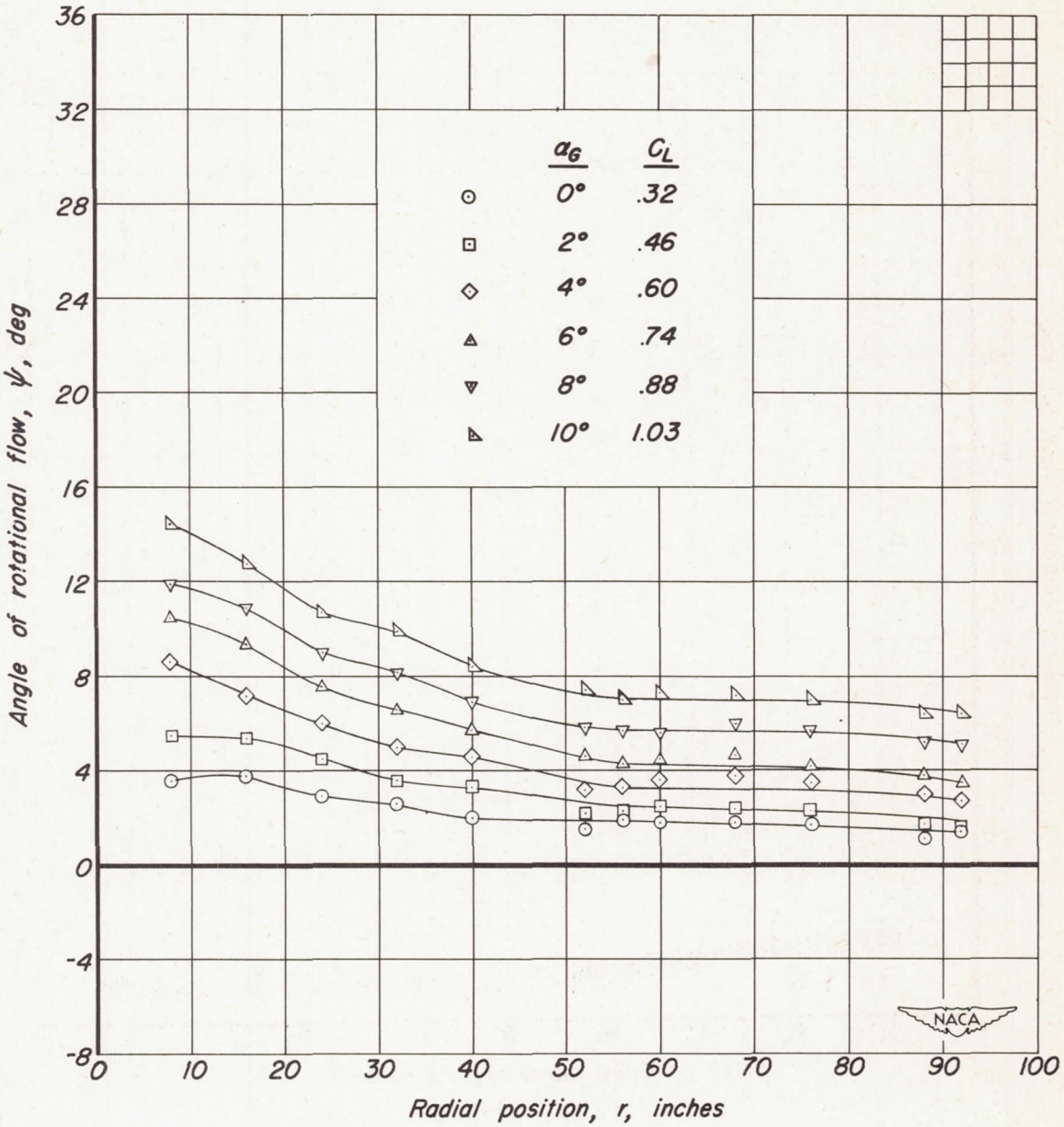
(h) Ω=158.2°.

Figure 6. - Continued.



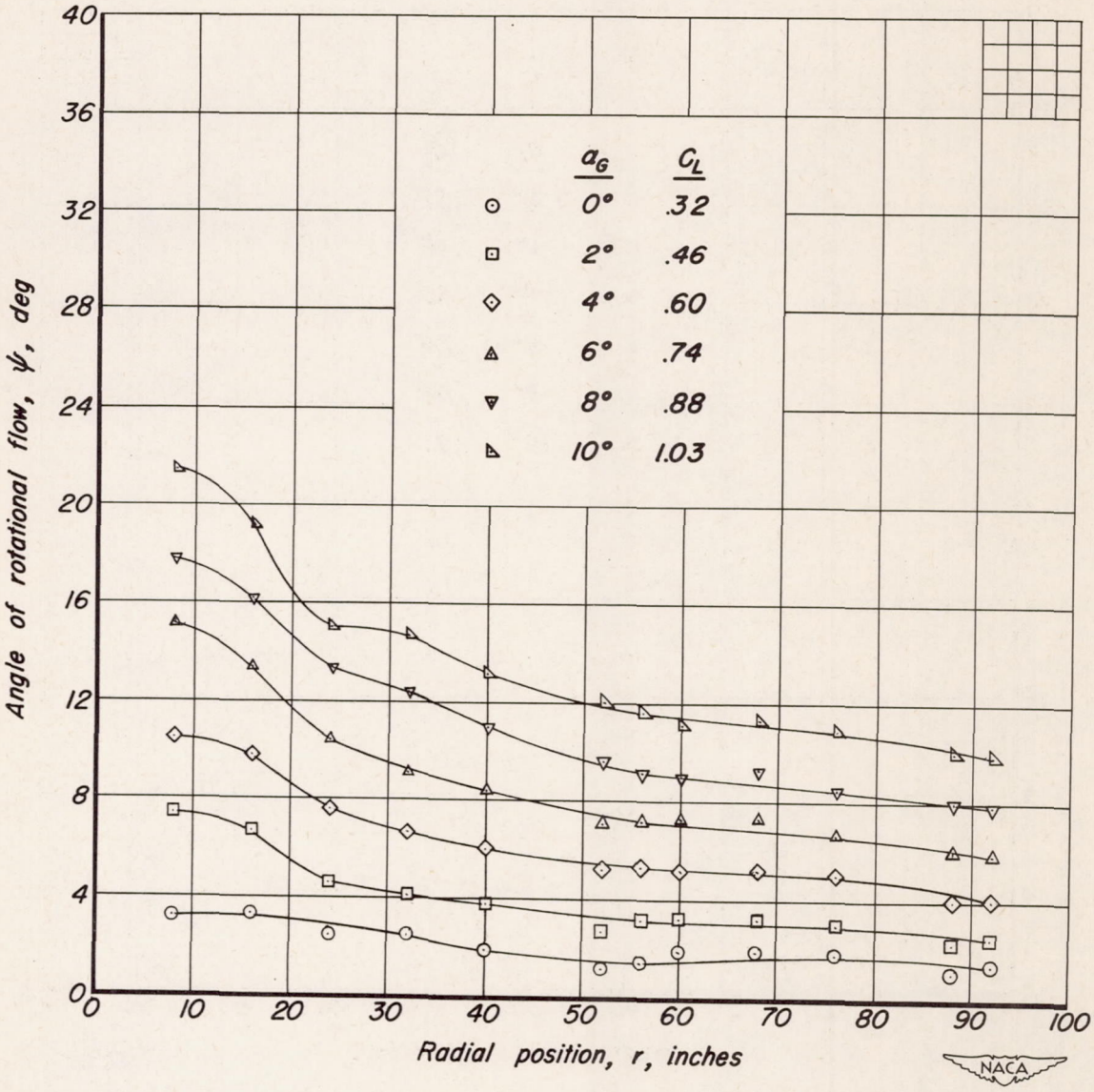
(i) Ω=180.6°.

Figure 6. - Continued.



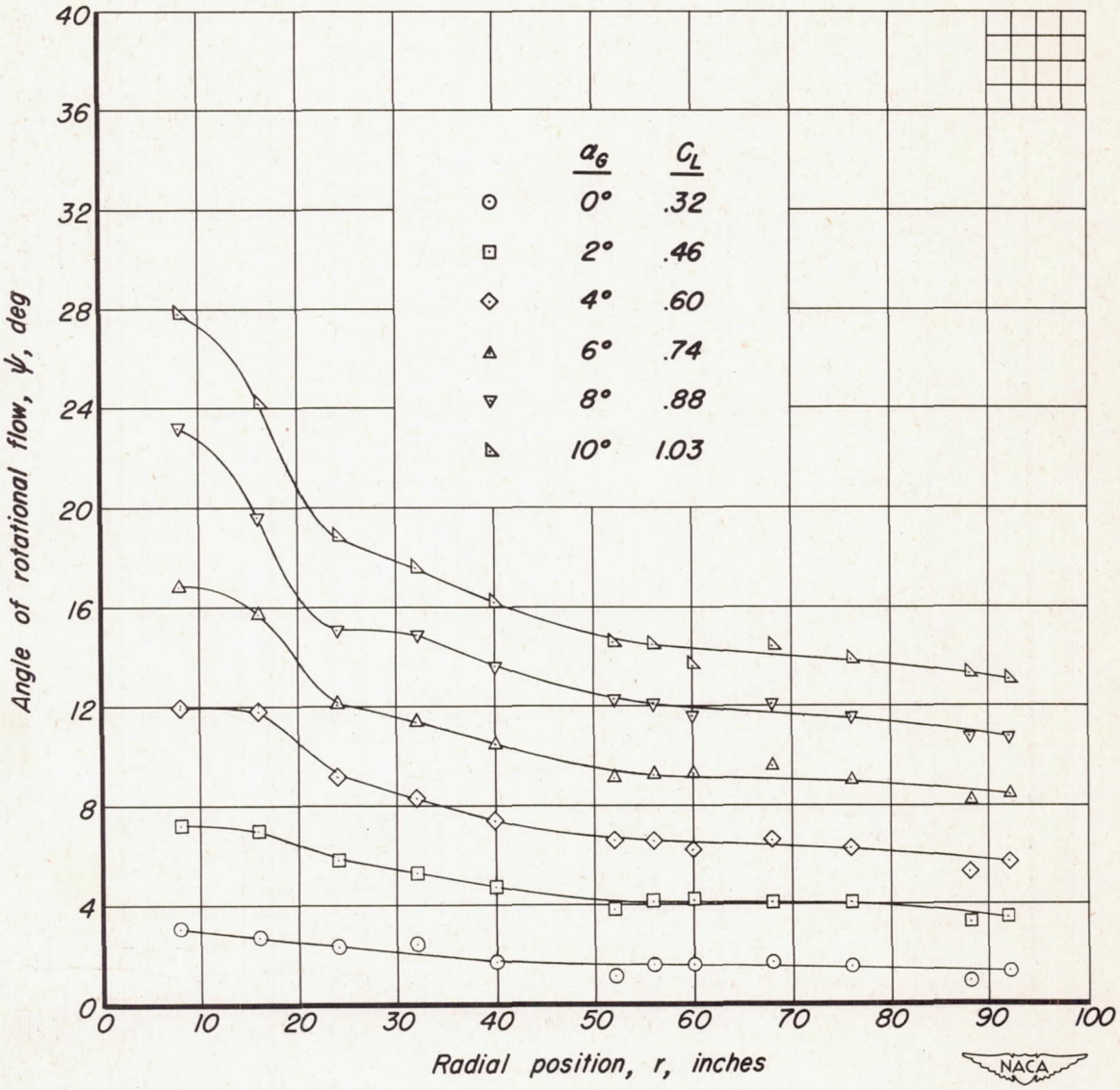
(j) $\Omega = 203.0°$.

Figure 6. - Continued.



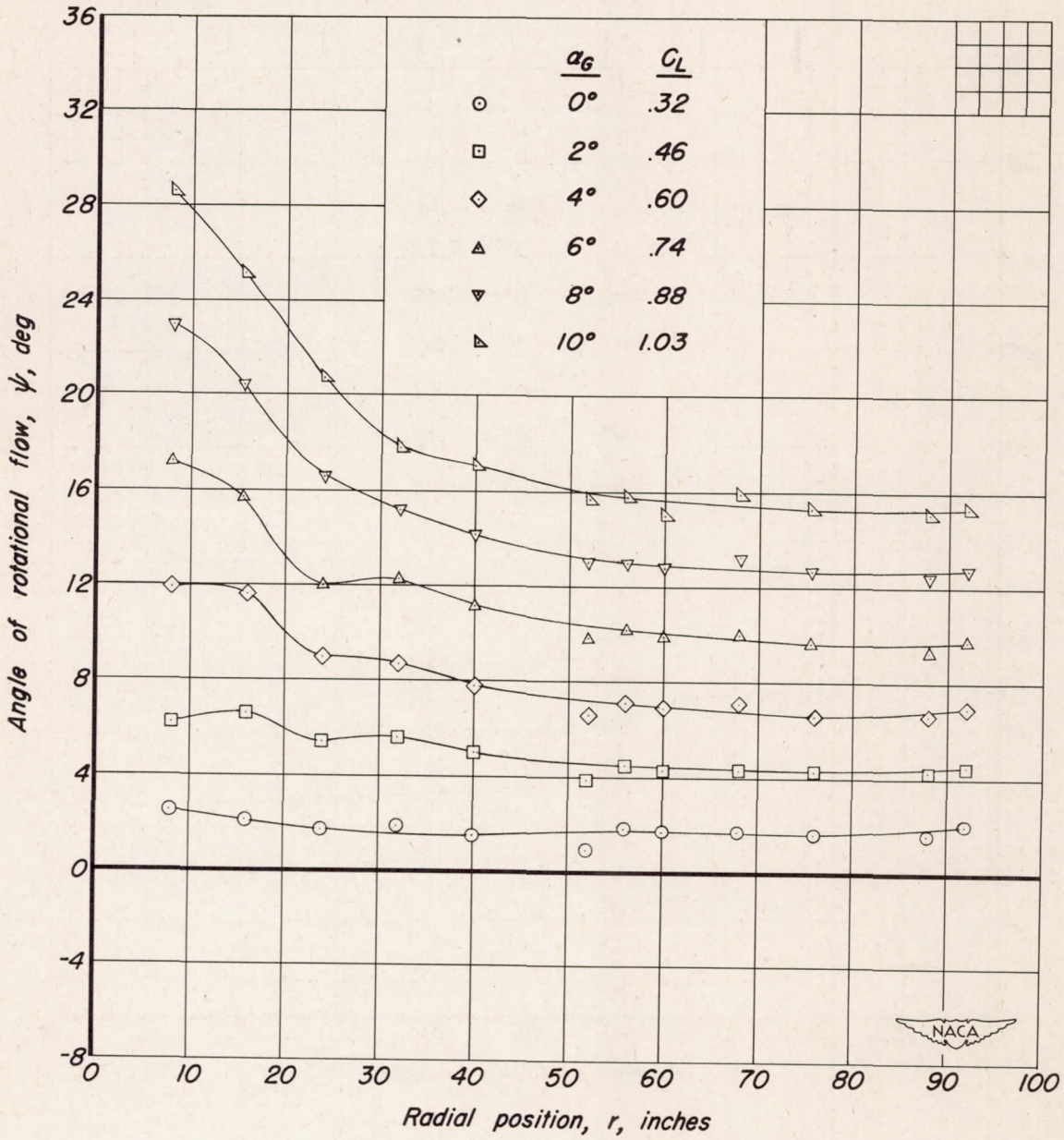
(k) $\Omega = 225.6°$.

Figure 6. - Continued.



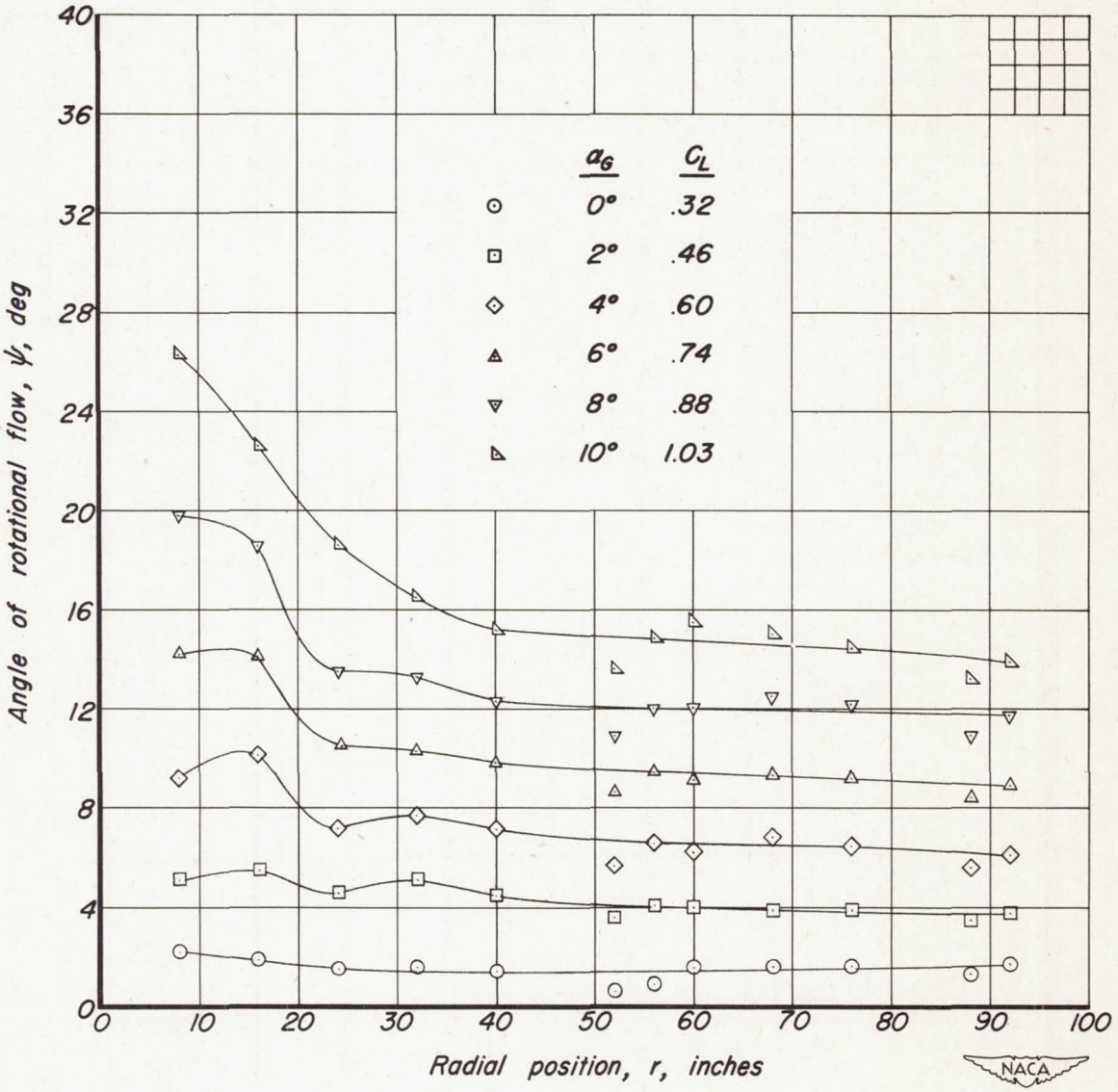
(l) $\Omega = 247.2°$.

Figure 6. - Continued.



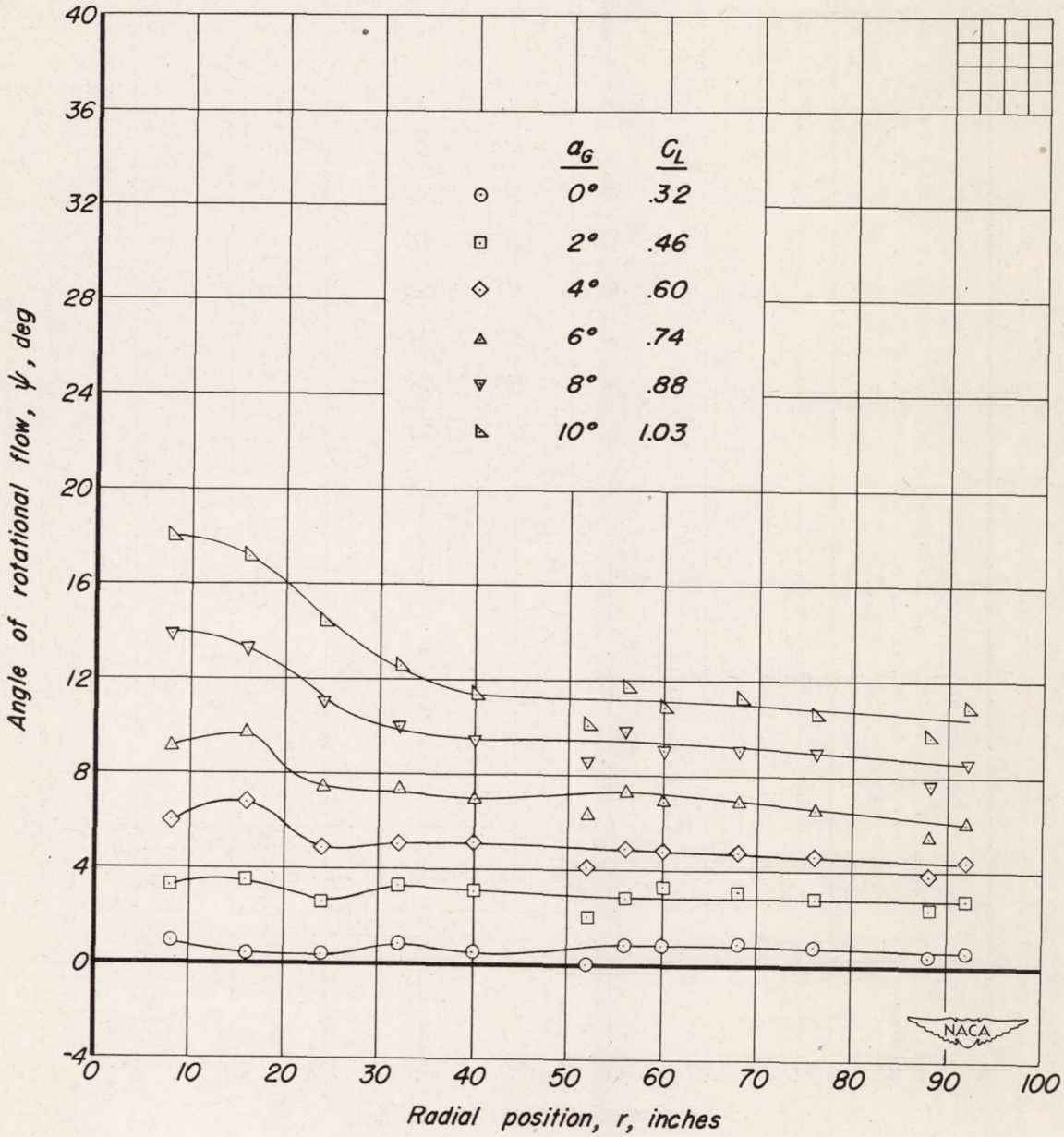
(m) $\Omega = 270.1°$.

Figure 6. - Continued.



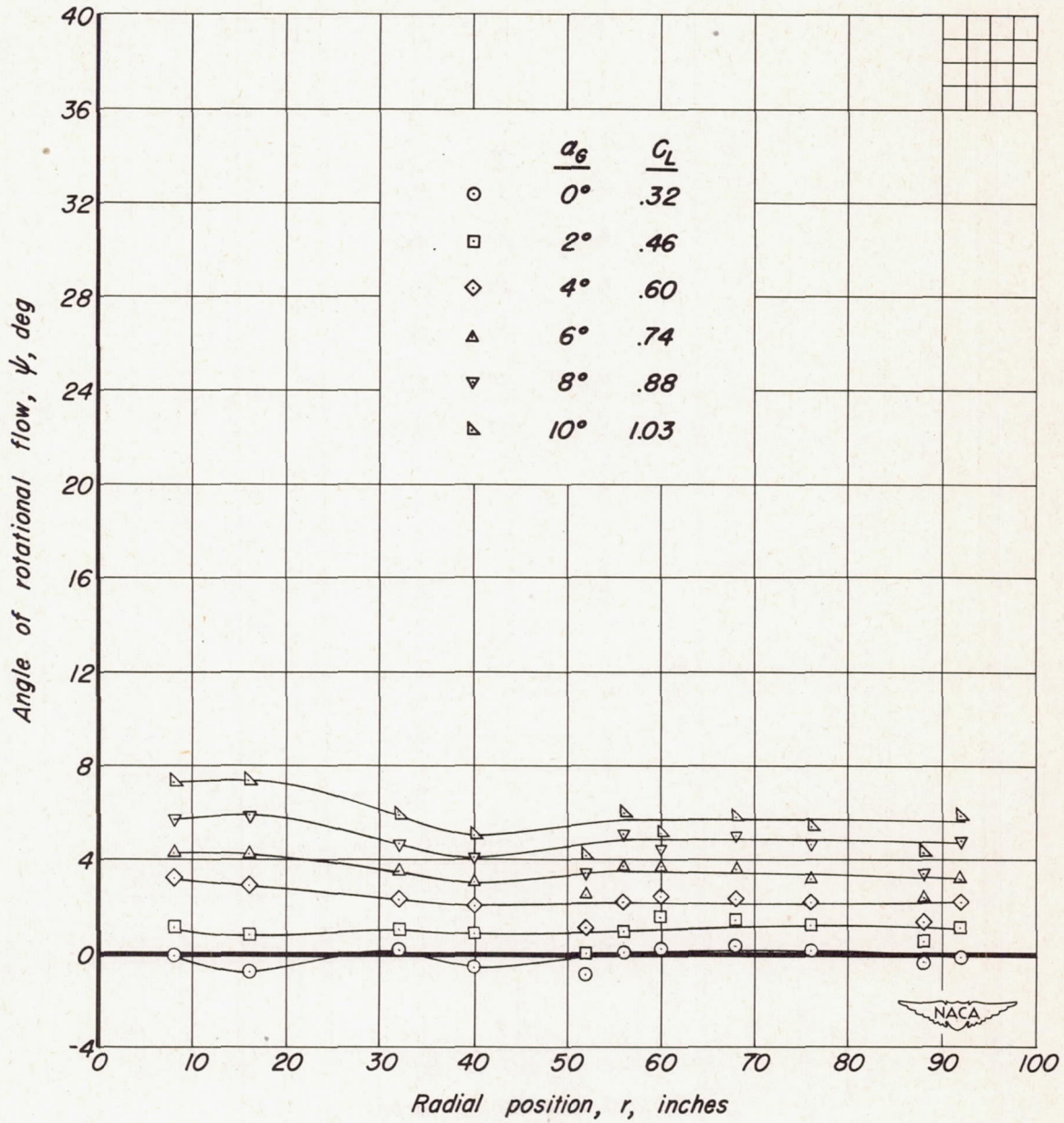
(n) $\Omega = 292.2°$.

Figure 6. - Continued.



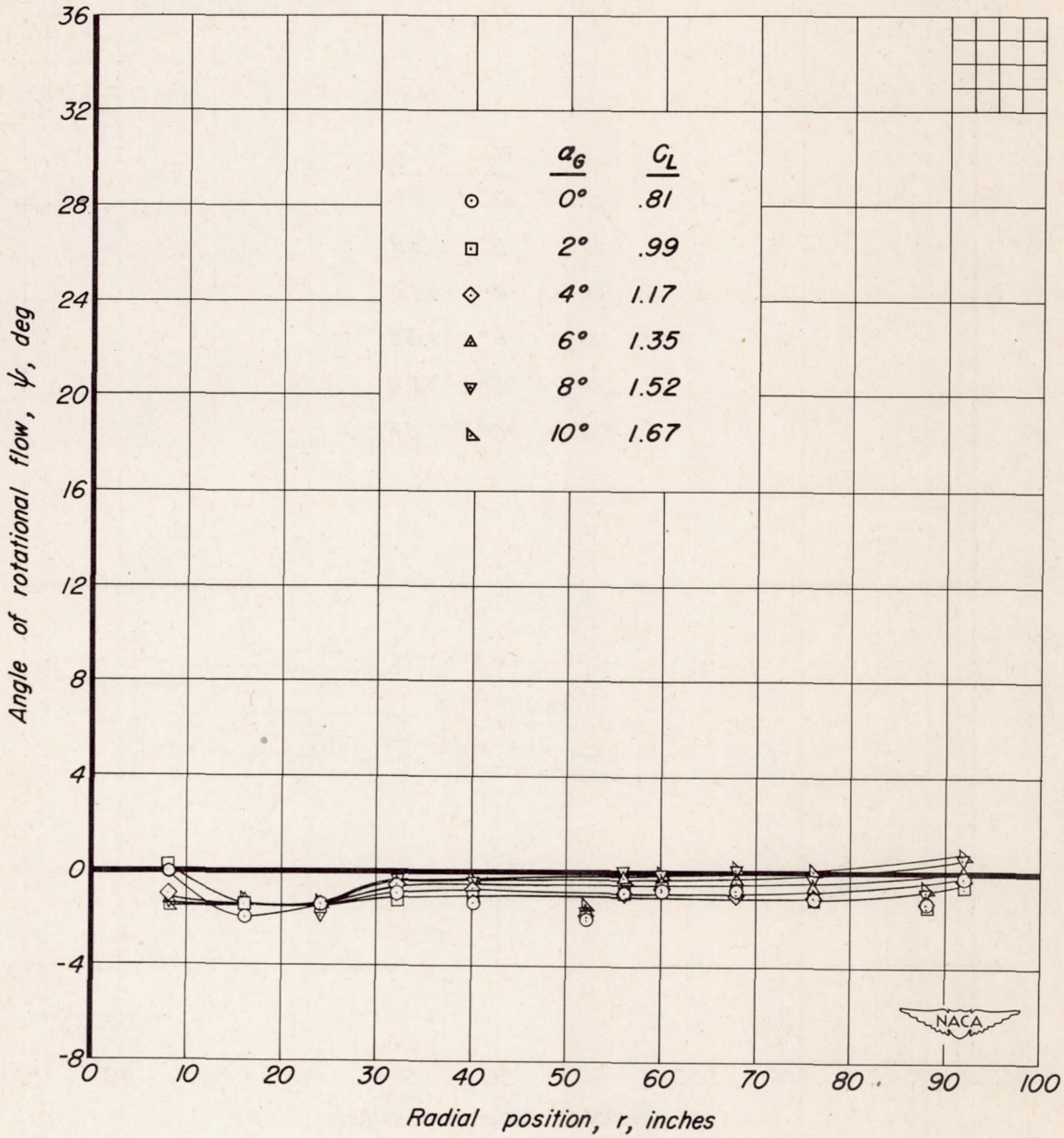
(o) $\Omega = 314.7°$.

Figure 6. - Continued.



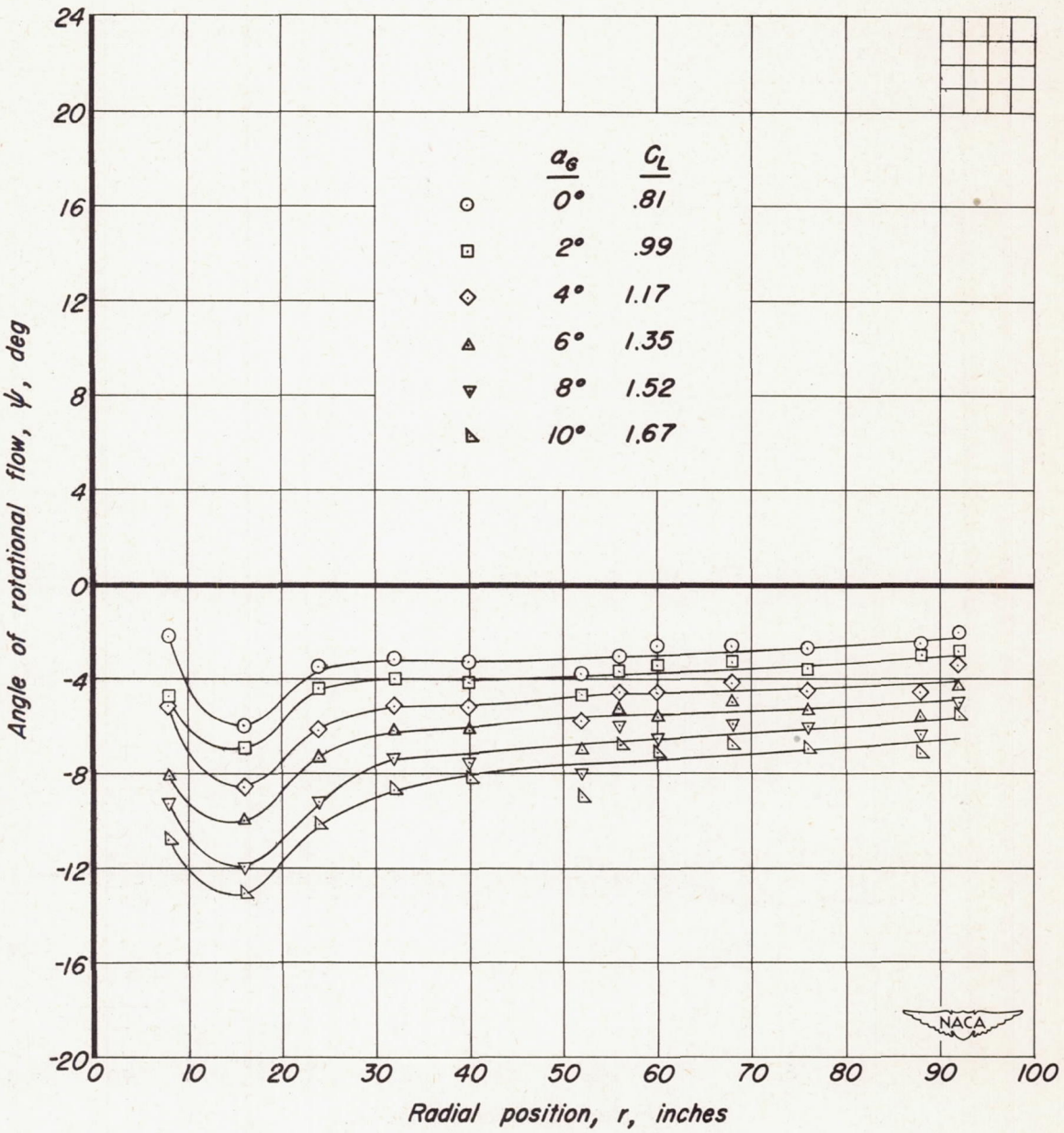
(p) $\Omega = 337.4°$.

Figure 6. - Concluded.



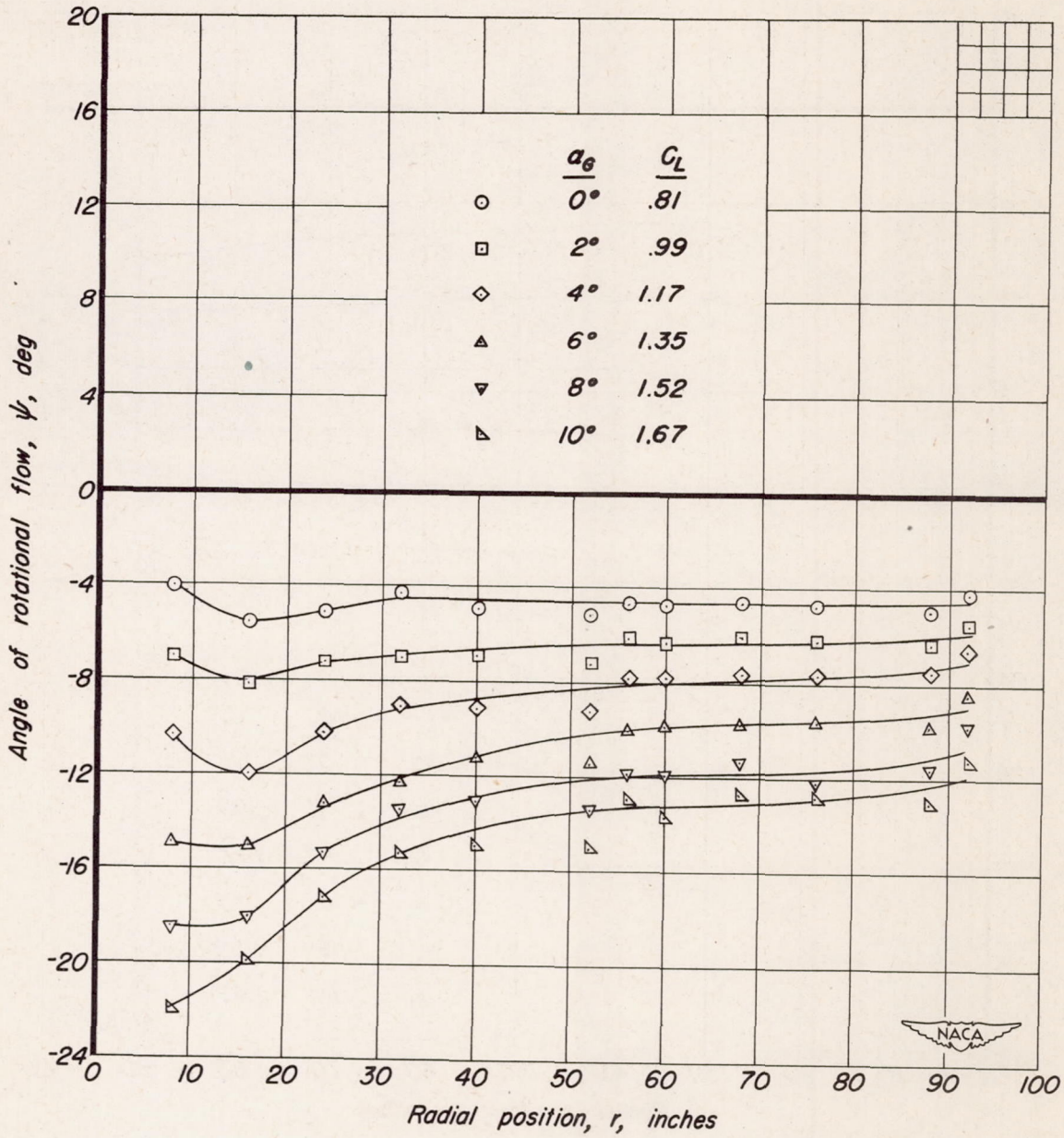
(a) $\Omega = 0.0°$.

Figure 7. - Variation of the angle of rotational flow, ψ, with radial position for several angles of attack. m_l / m_o, .29; δ_f, 40°.



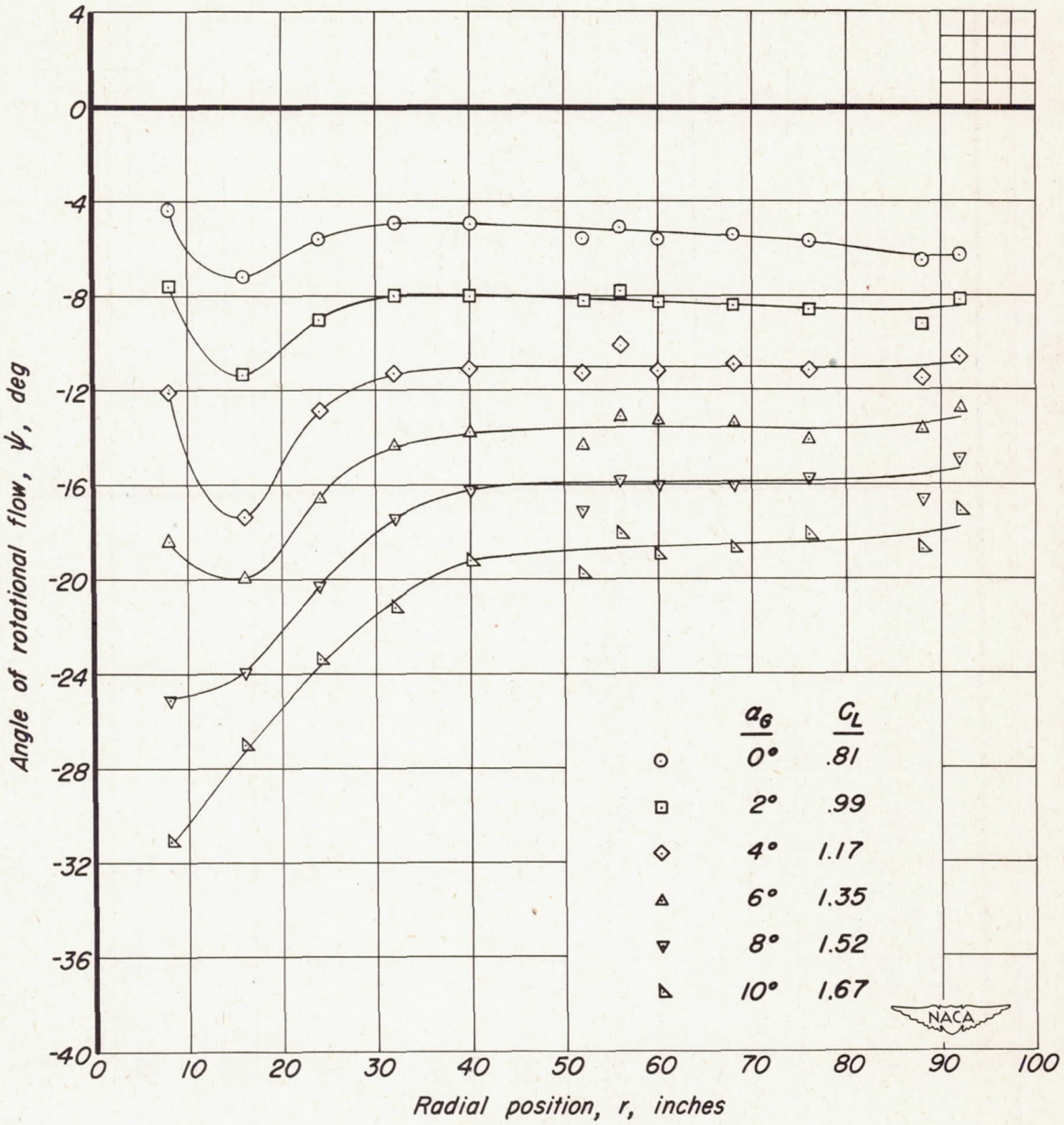
(b) $\Omega = 22.5°$.

Figure 7. - Continued.



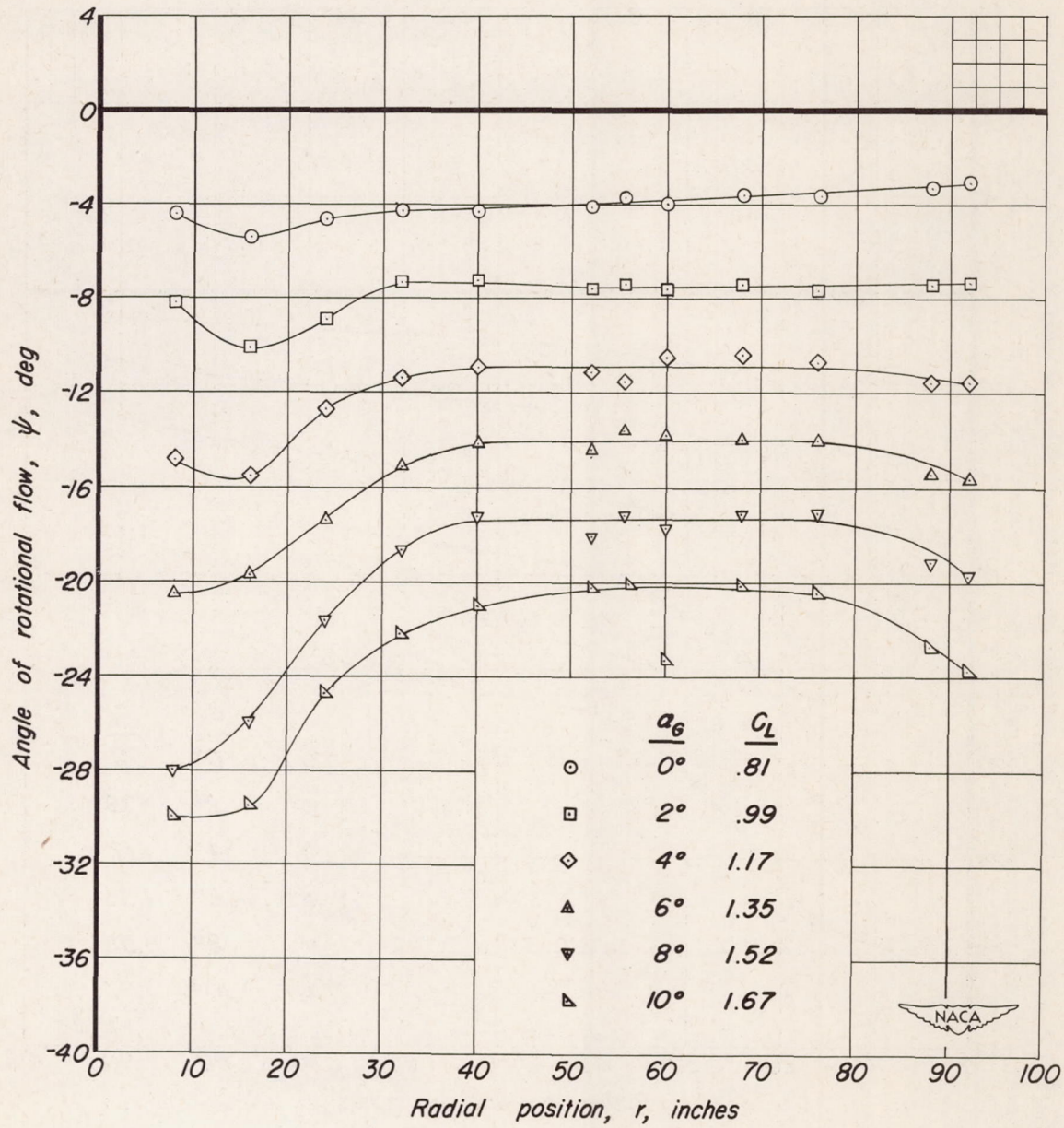
(c) $\Omega = 45.2°$.

Figure 7. - Continued.



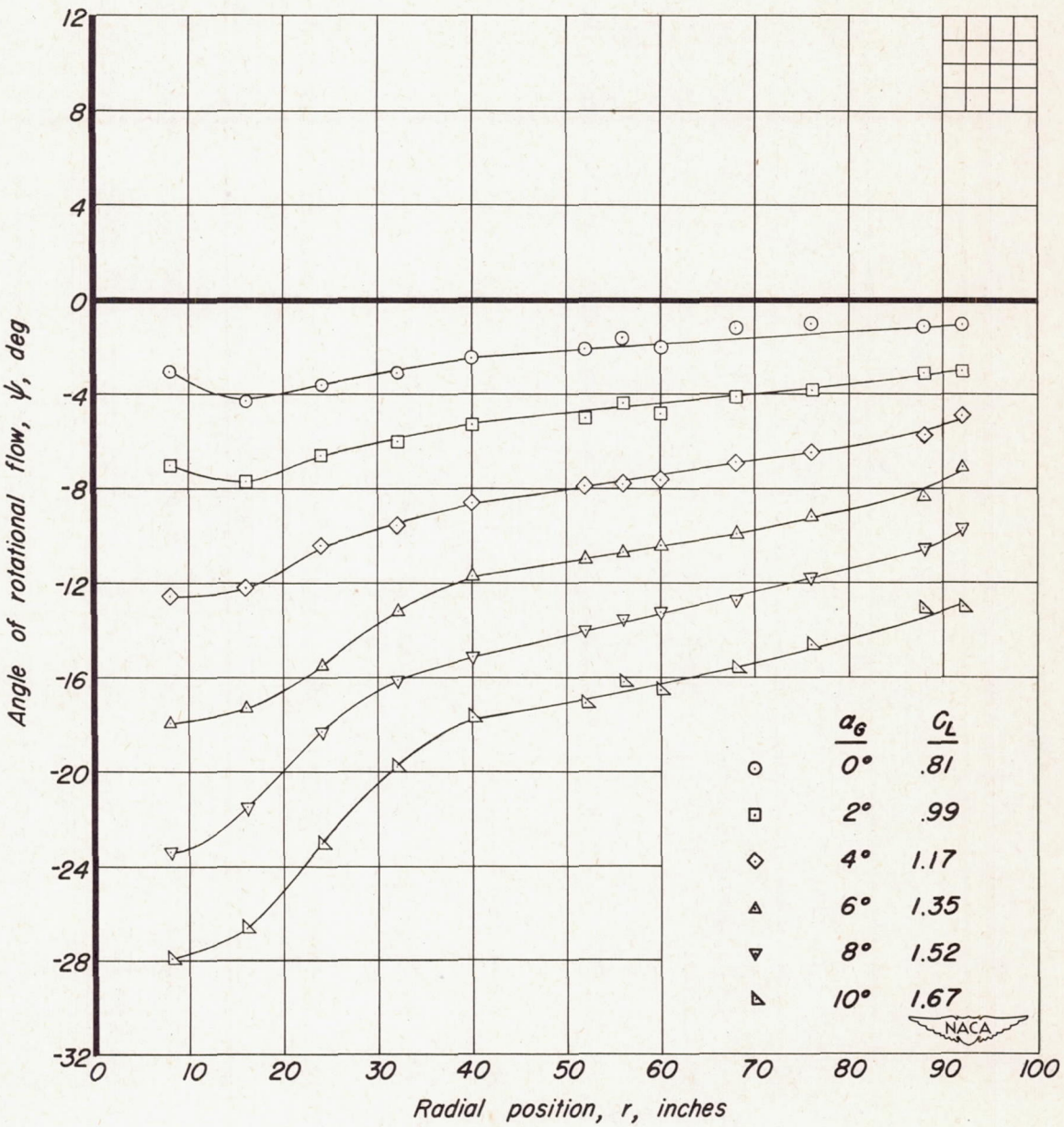
(d) Ω=68.5°.

Figure 7. - Continued.



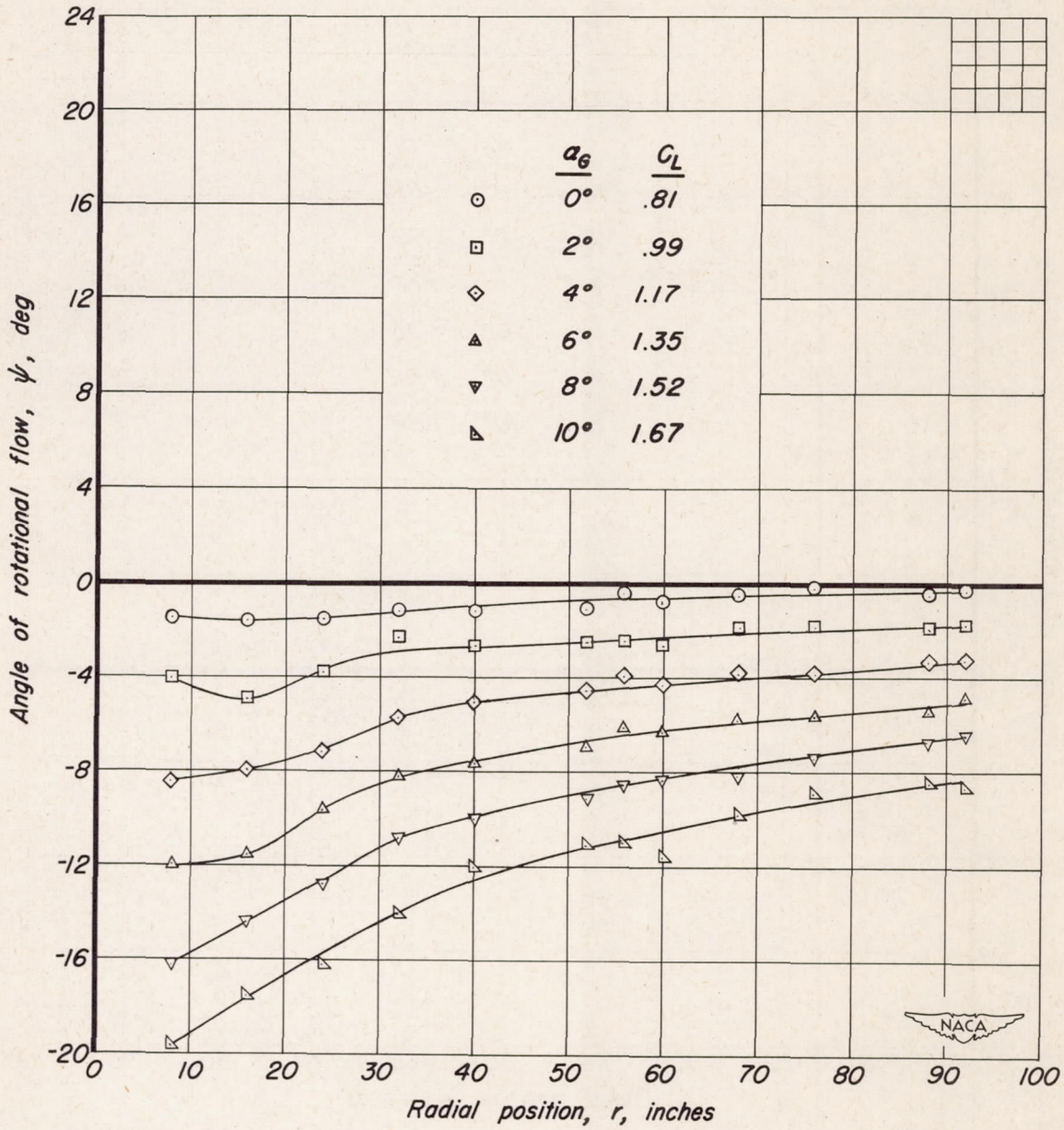
(e) $\Omega = 91.1°$.

Figure 7. - Continued.



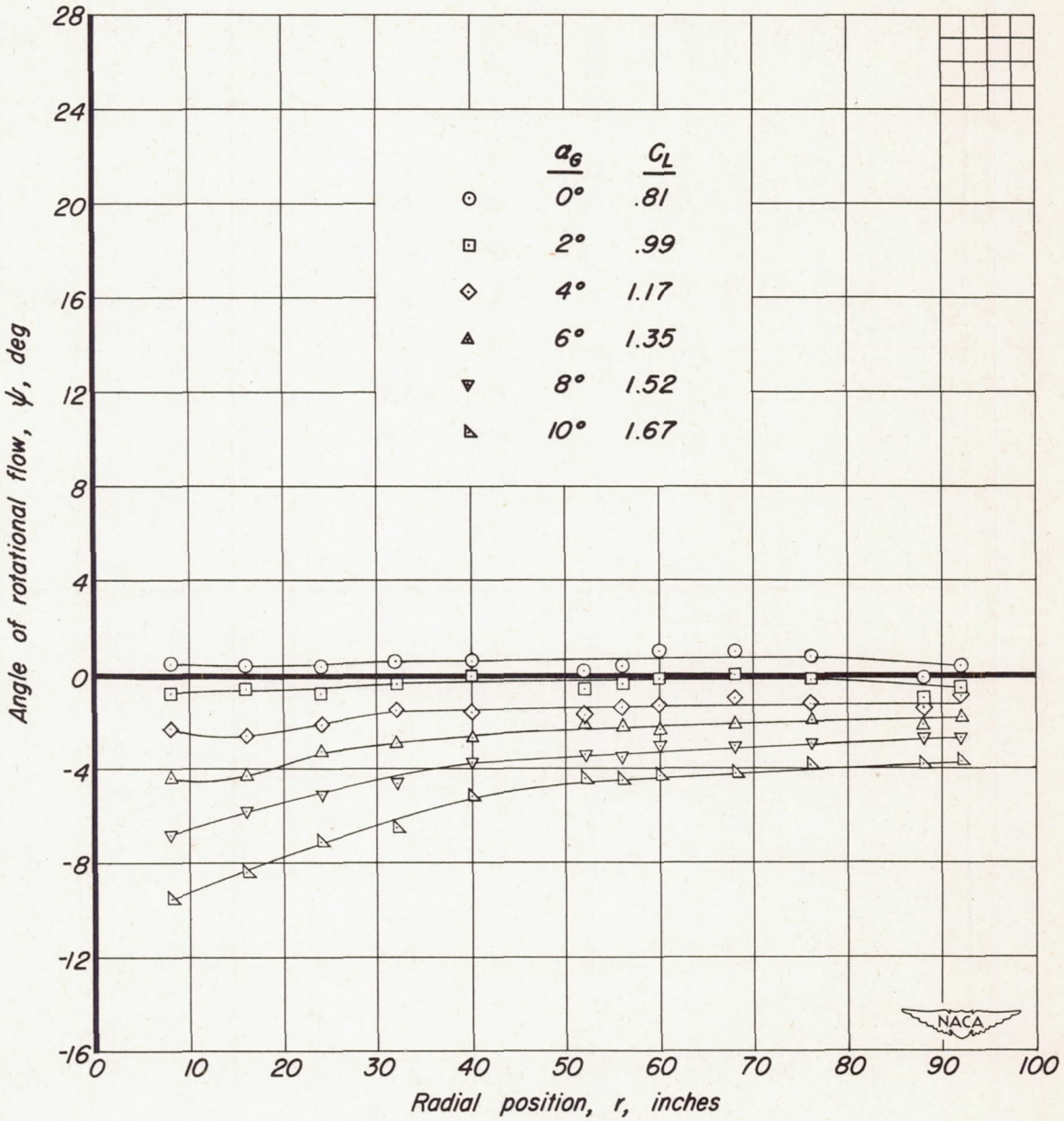
(f) Ω=113.4°.

Figure 7. - Continued.



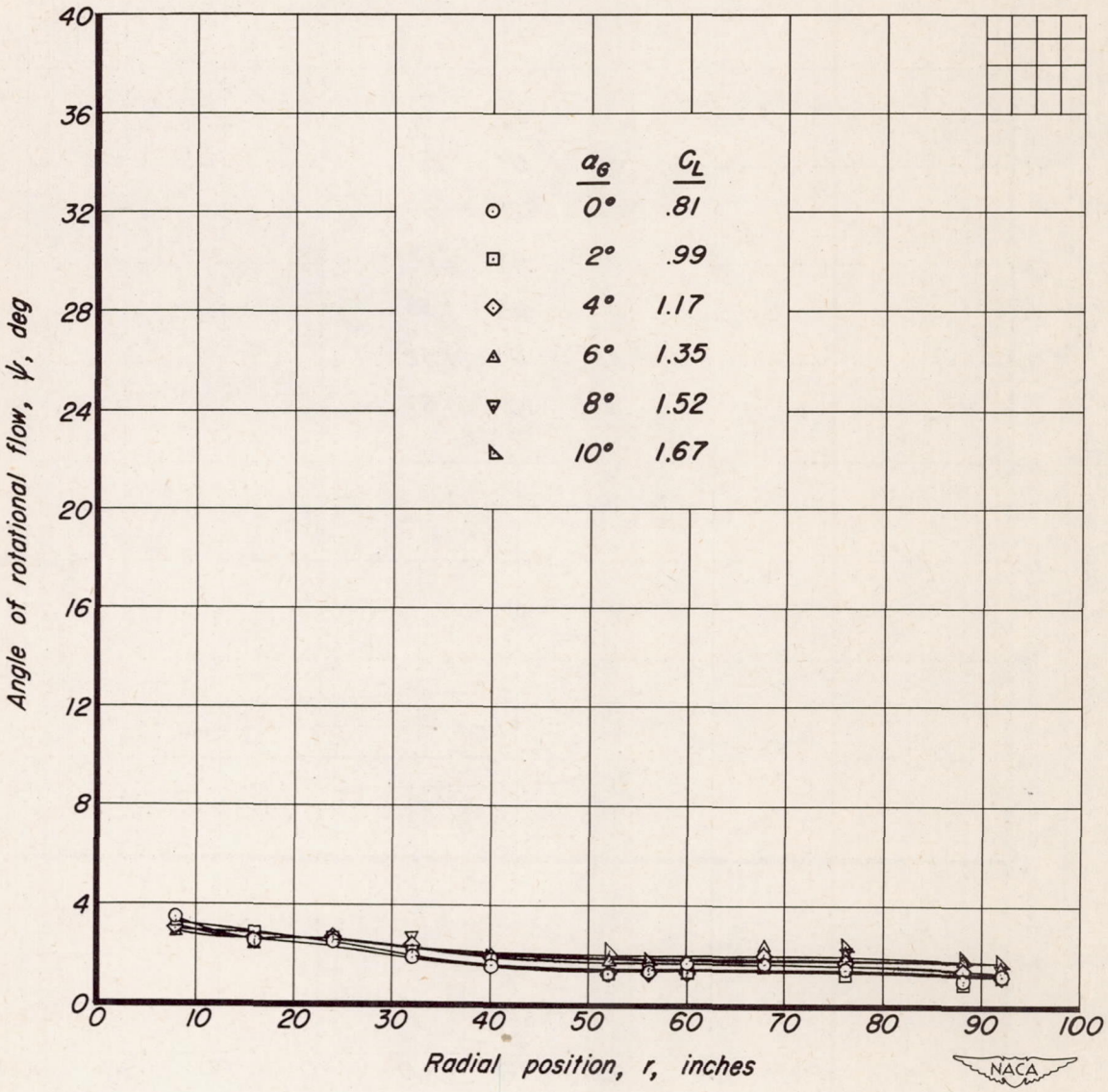
(g) Ω=135.7°.

Figure 7. - Continued.



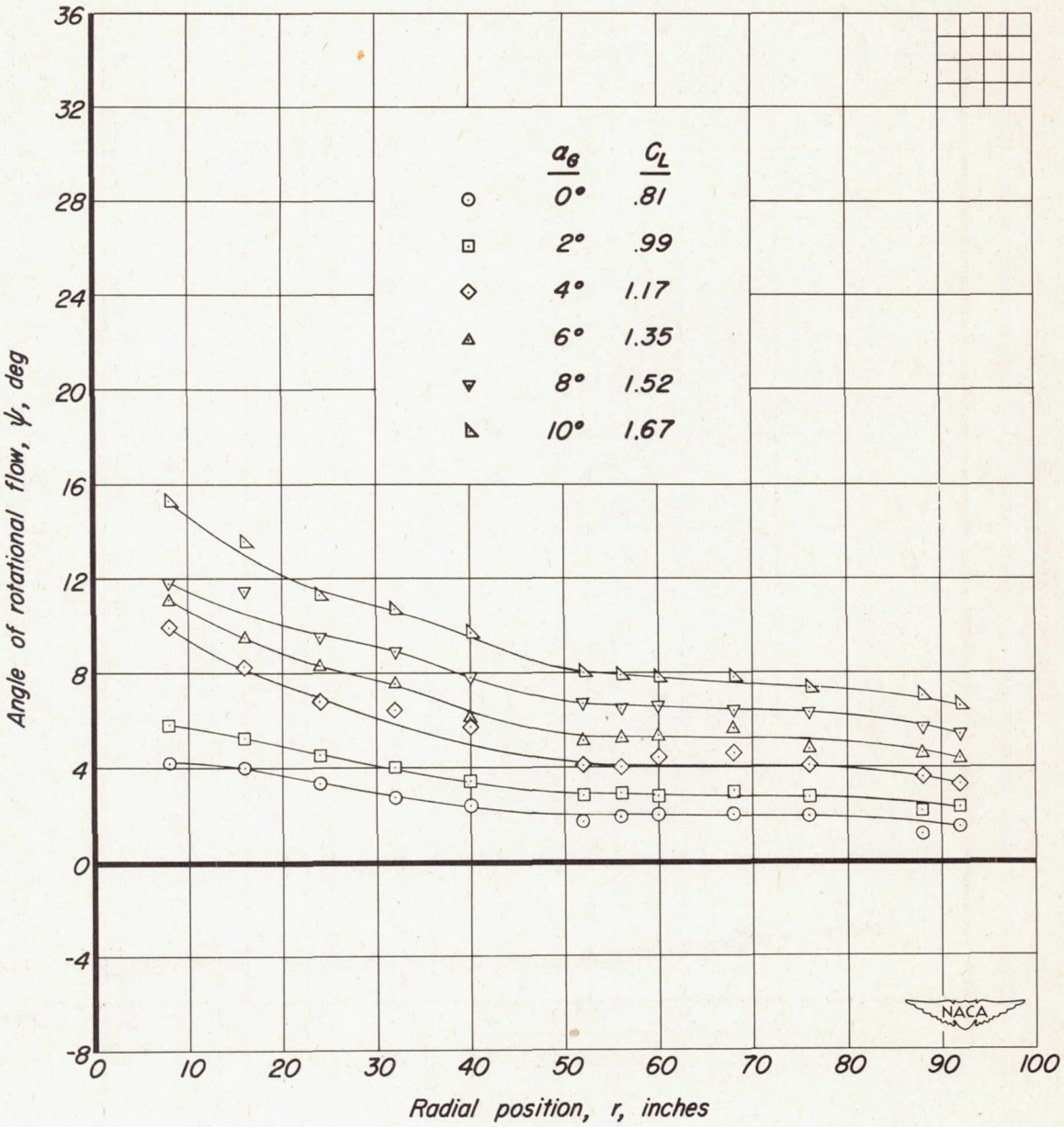
(h) Ω=158.2°.

Figure 7. - Continued.



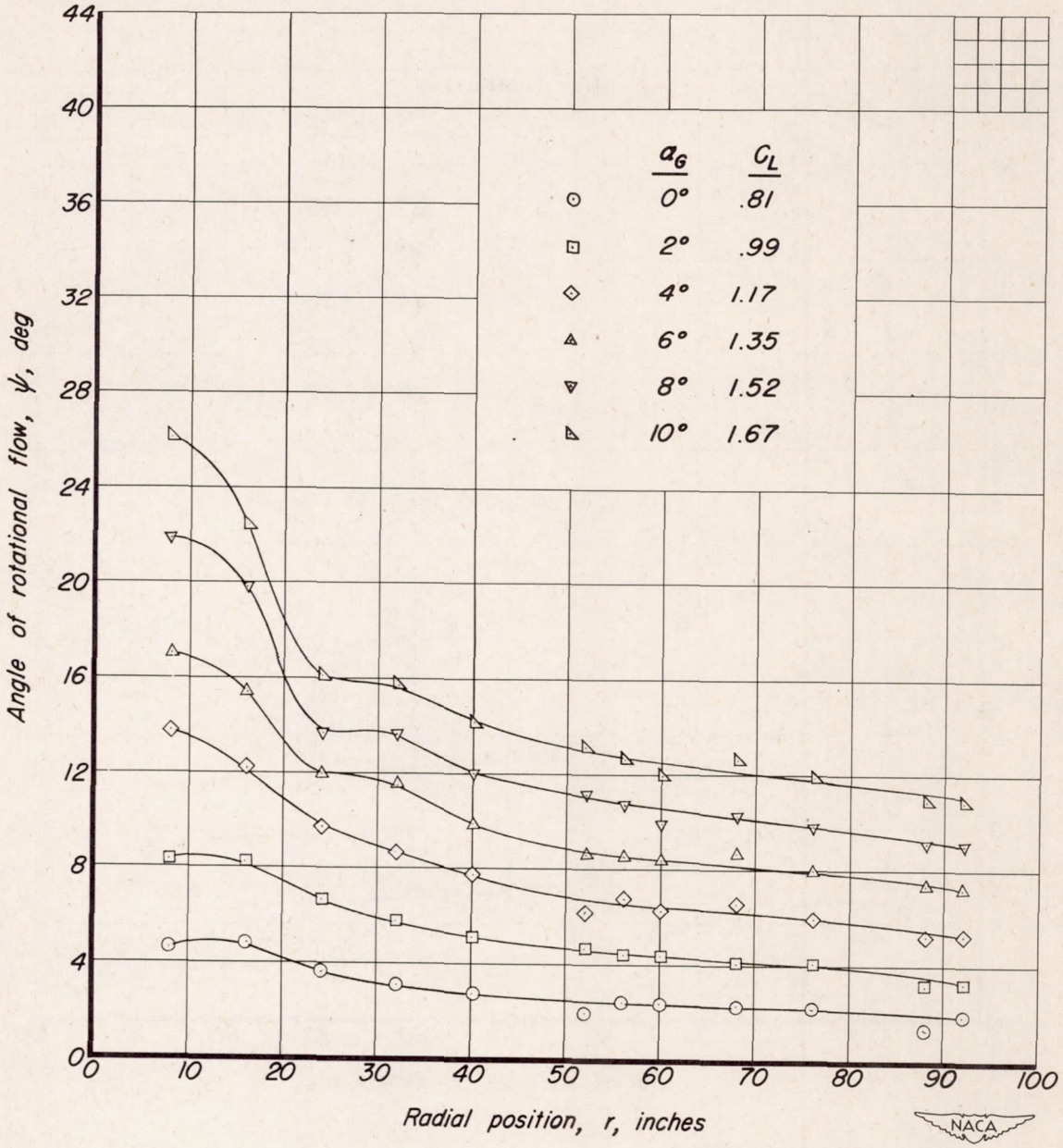
(i) Ω=180.6°

Figure 7. - Continued.



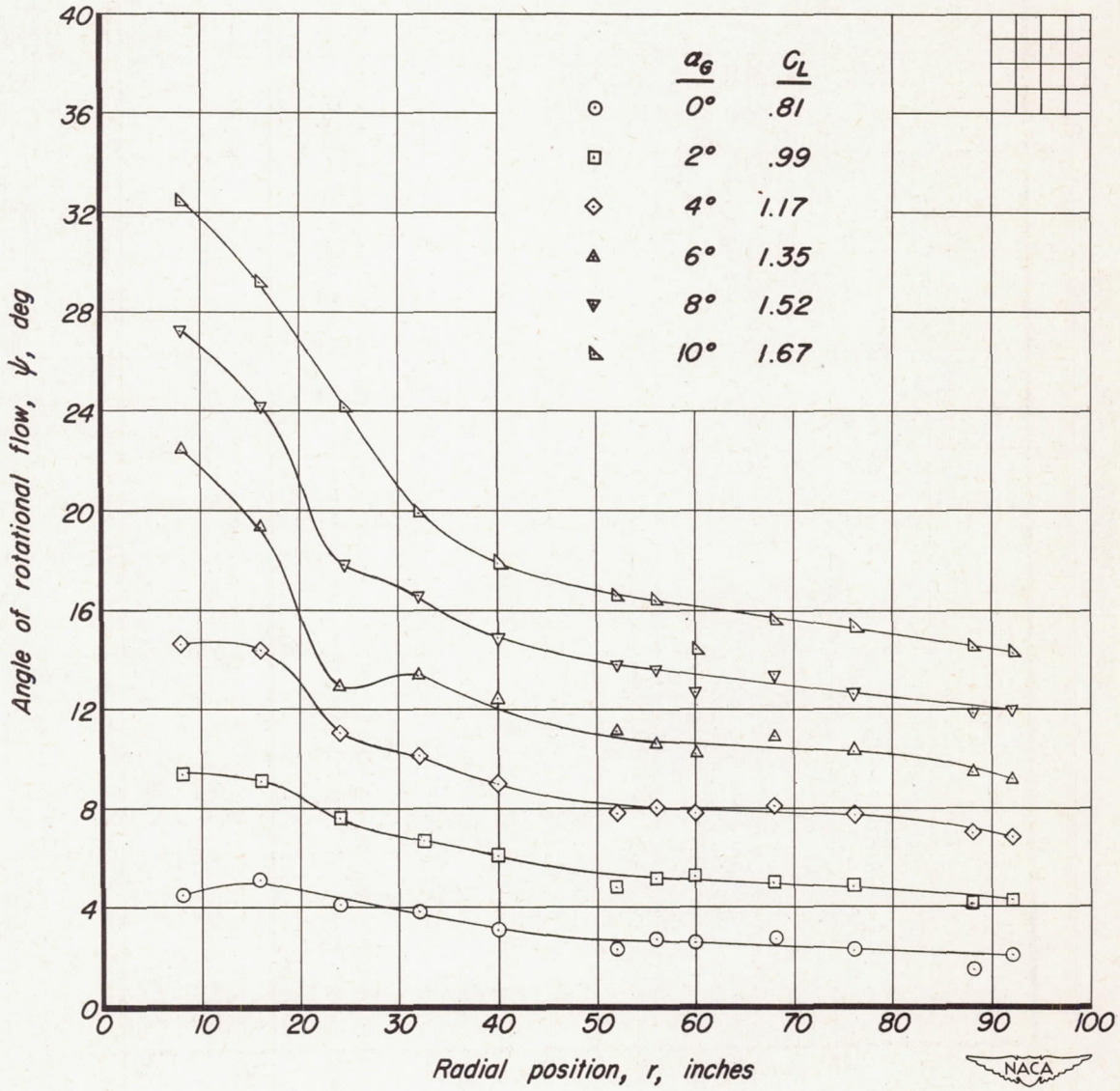
(j) Ω=203.0°.

Figure 7. - Continued.



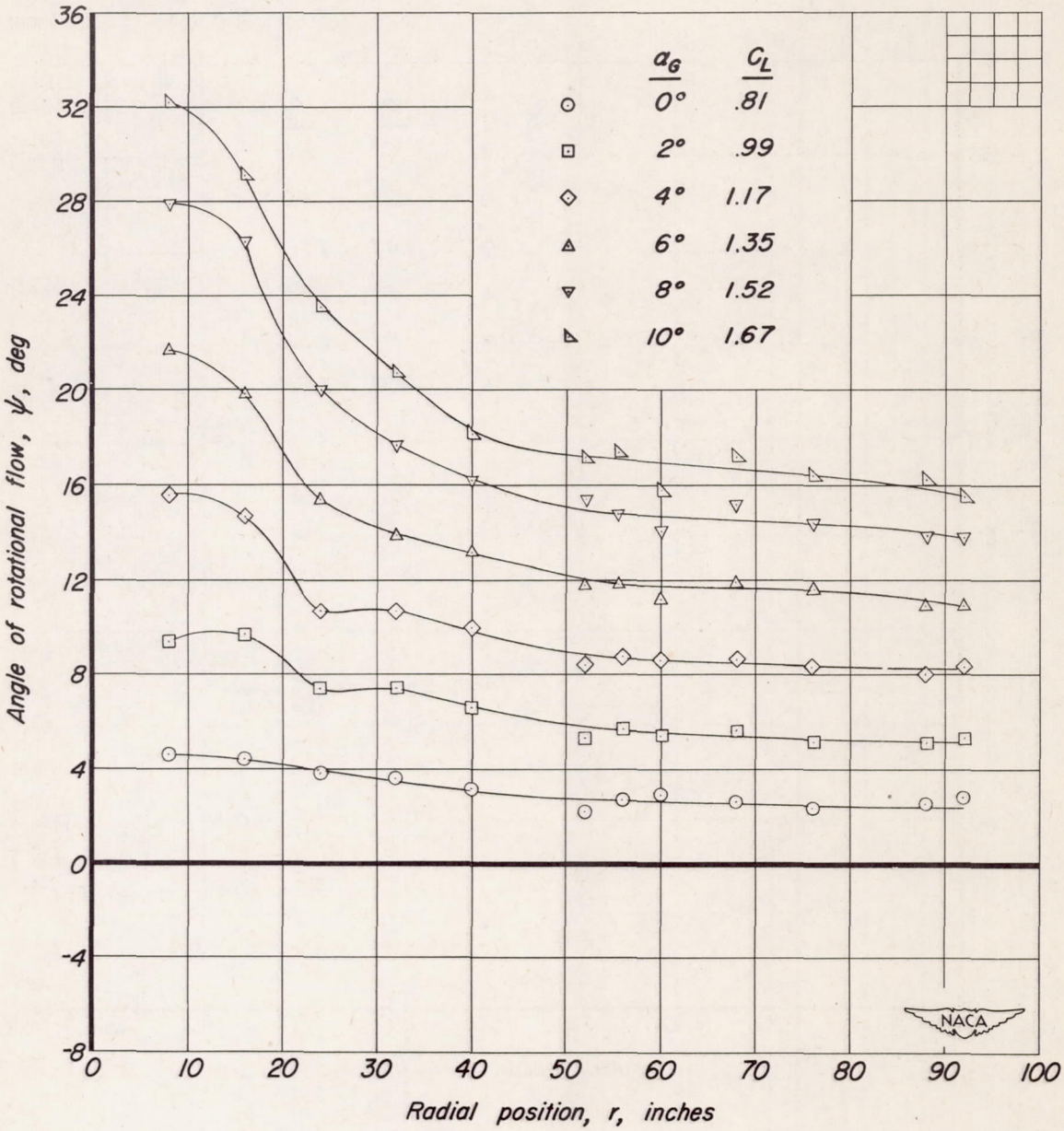
(k) $\Omega = 225.6°$.

Figure 7. - Continued.



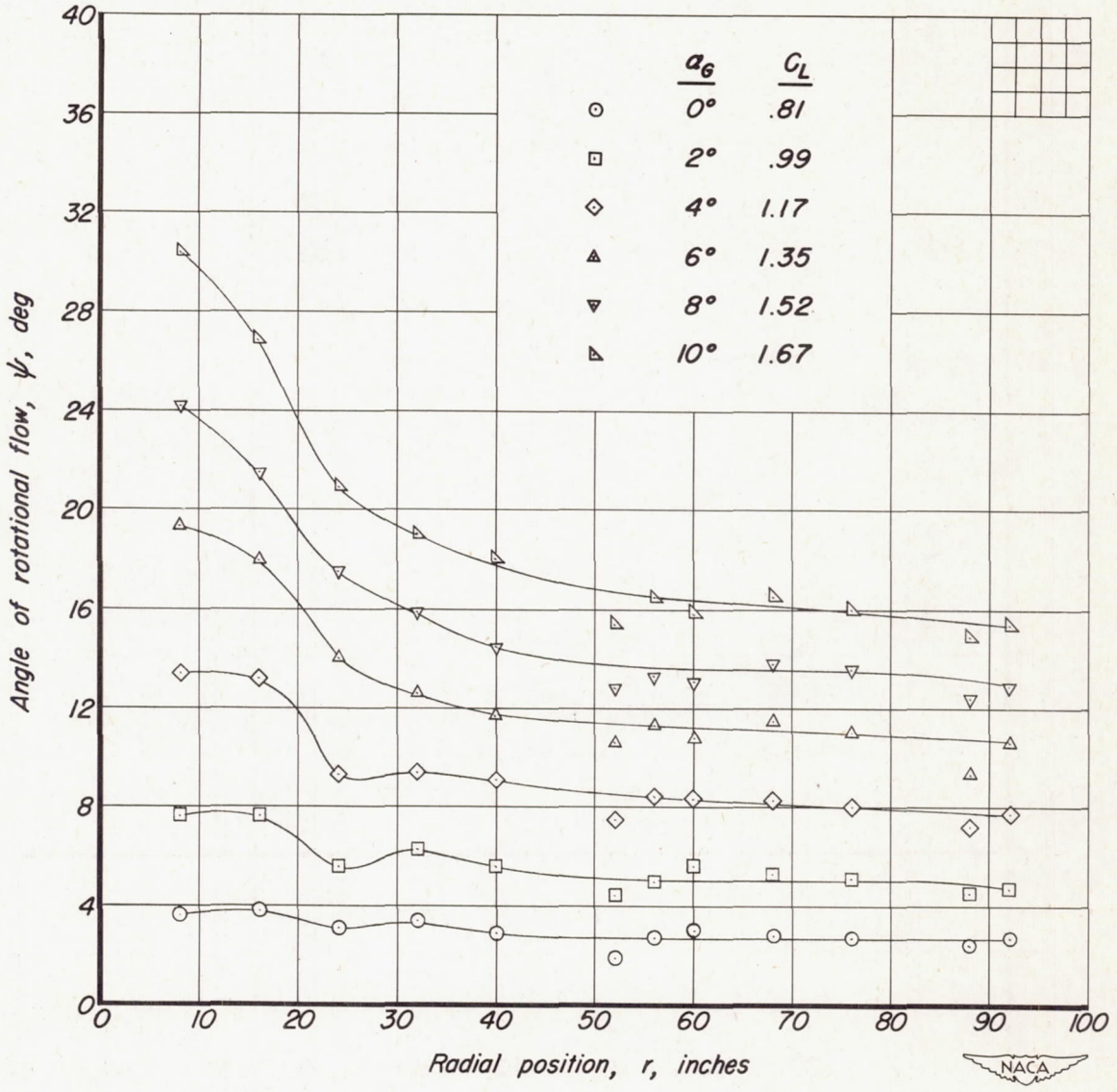
(1) $\Omega = 247.2°$.

Figure 7. - Continued.



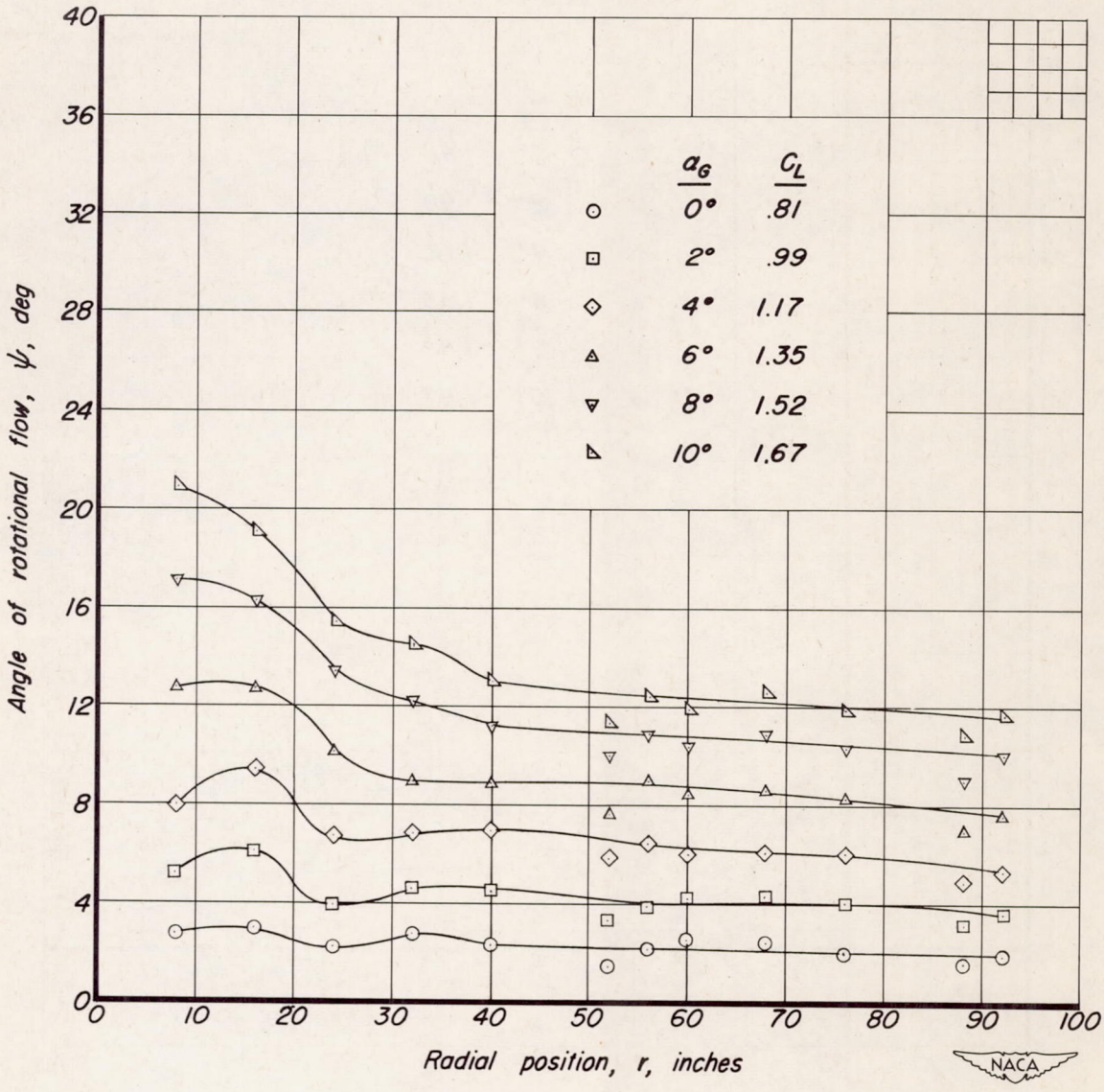
(m) $\Omega = 270.1°$.

Figure 7. - Continued.



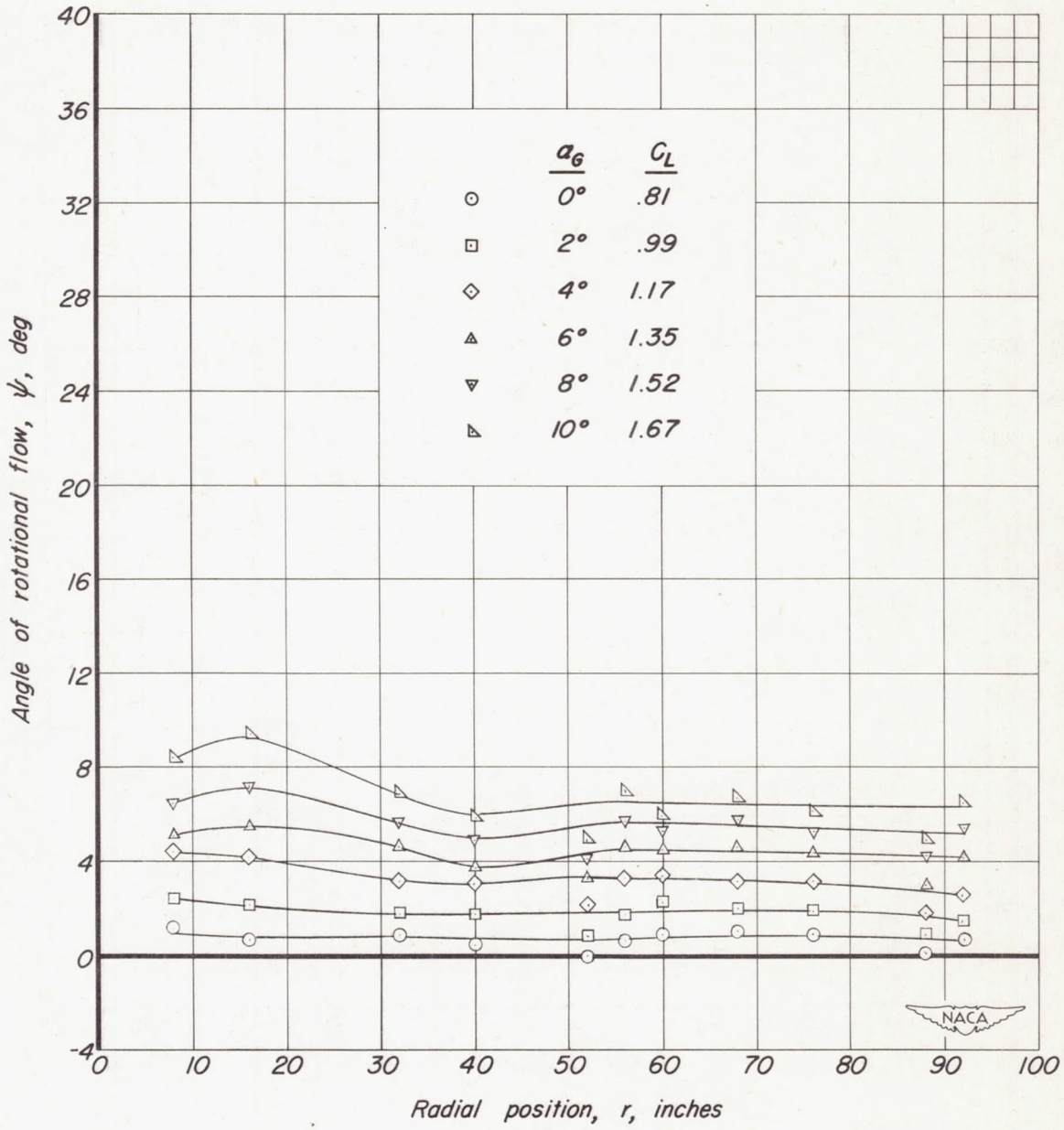
(n) $\Omega = 292.2°$.

Figure 7. - Continued.



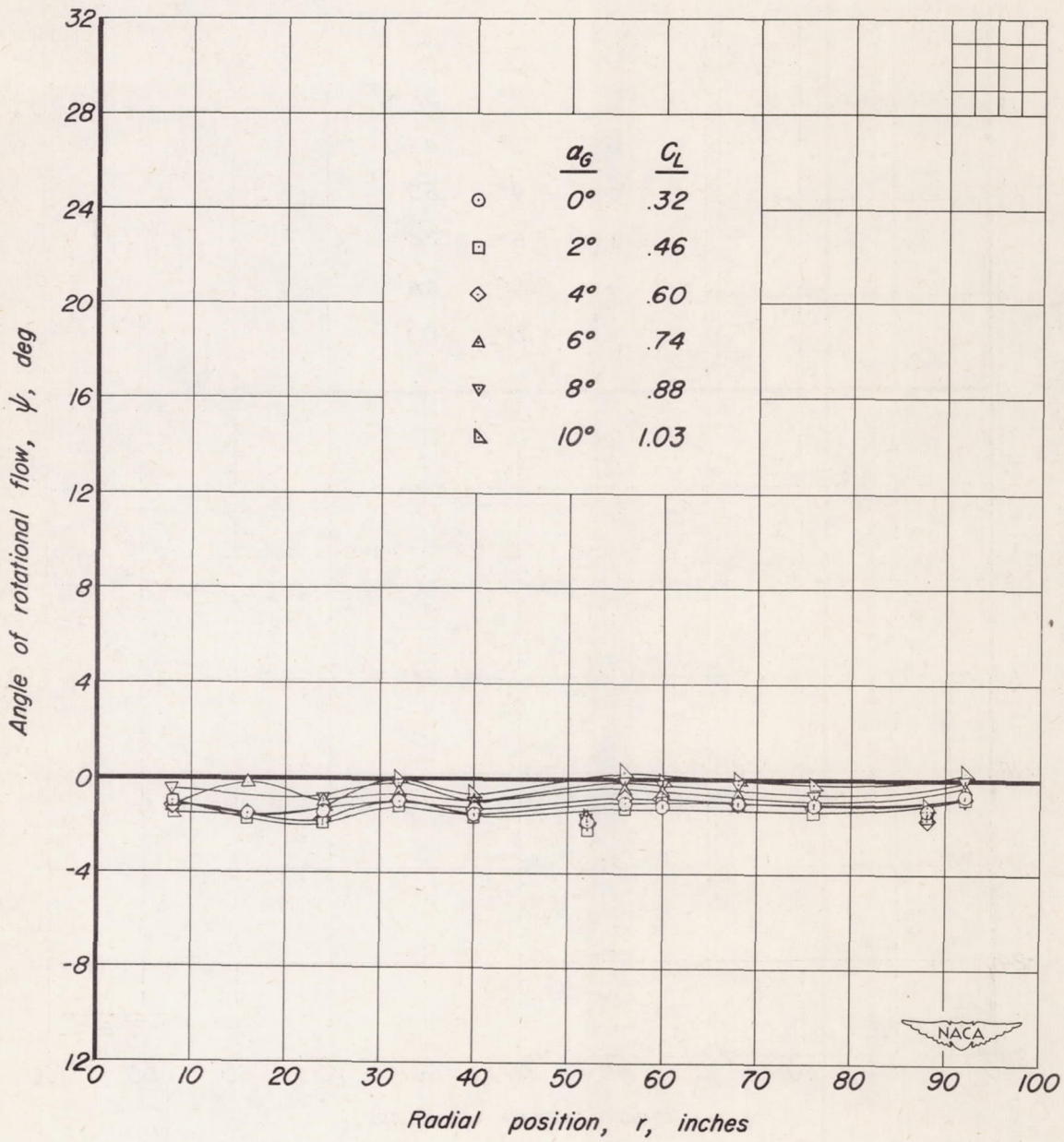
(o) $\Omega = 314.7°$.

Figure 7. - Continued.



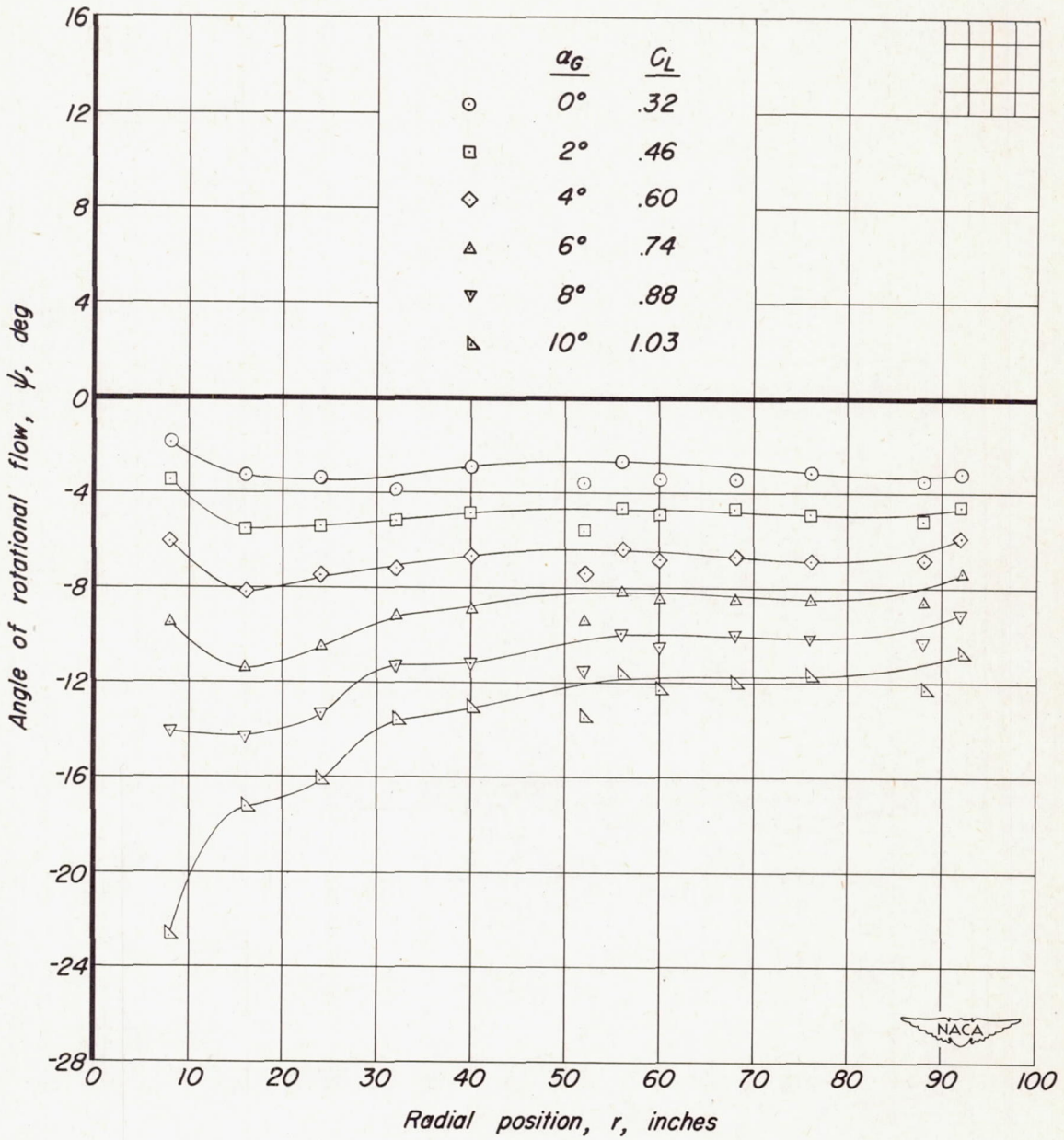
(p) $\Omega = 337.4°$.

Figure 7. - Concluded.



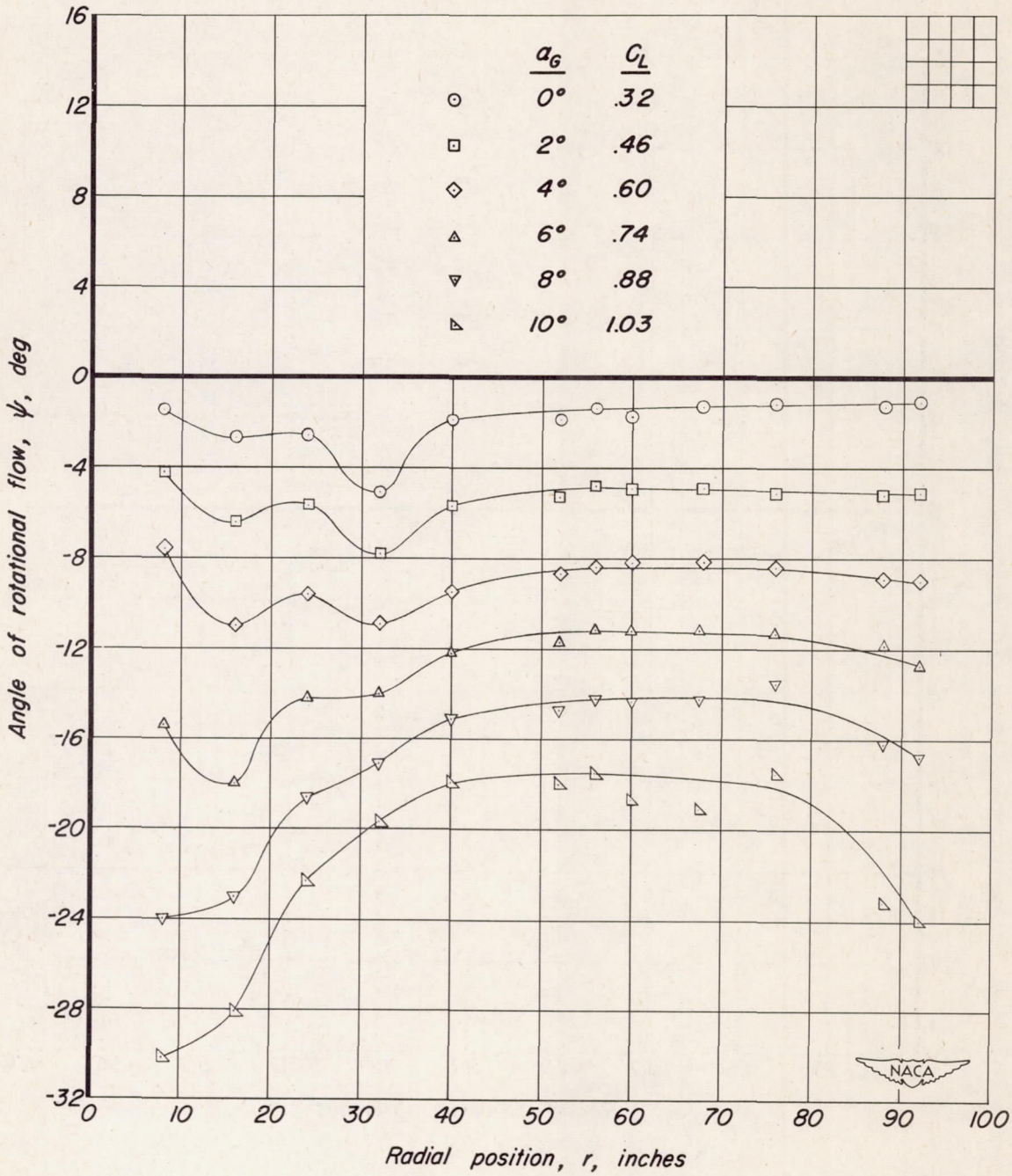
(a) $\Omega = 359.8°$.

Figure 8. - Variation of the angle of rotational flow, ψ, with radial position for several angles of attack. m_l/m_o, .14; δ_f, 0°.



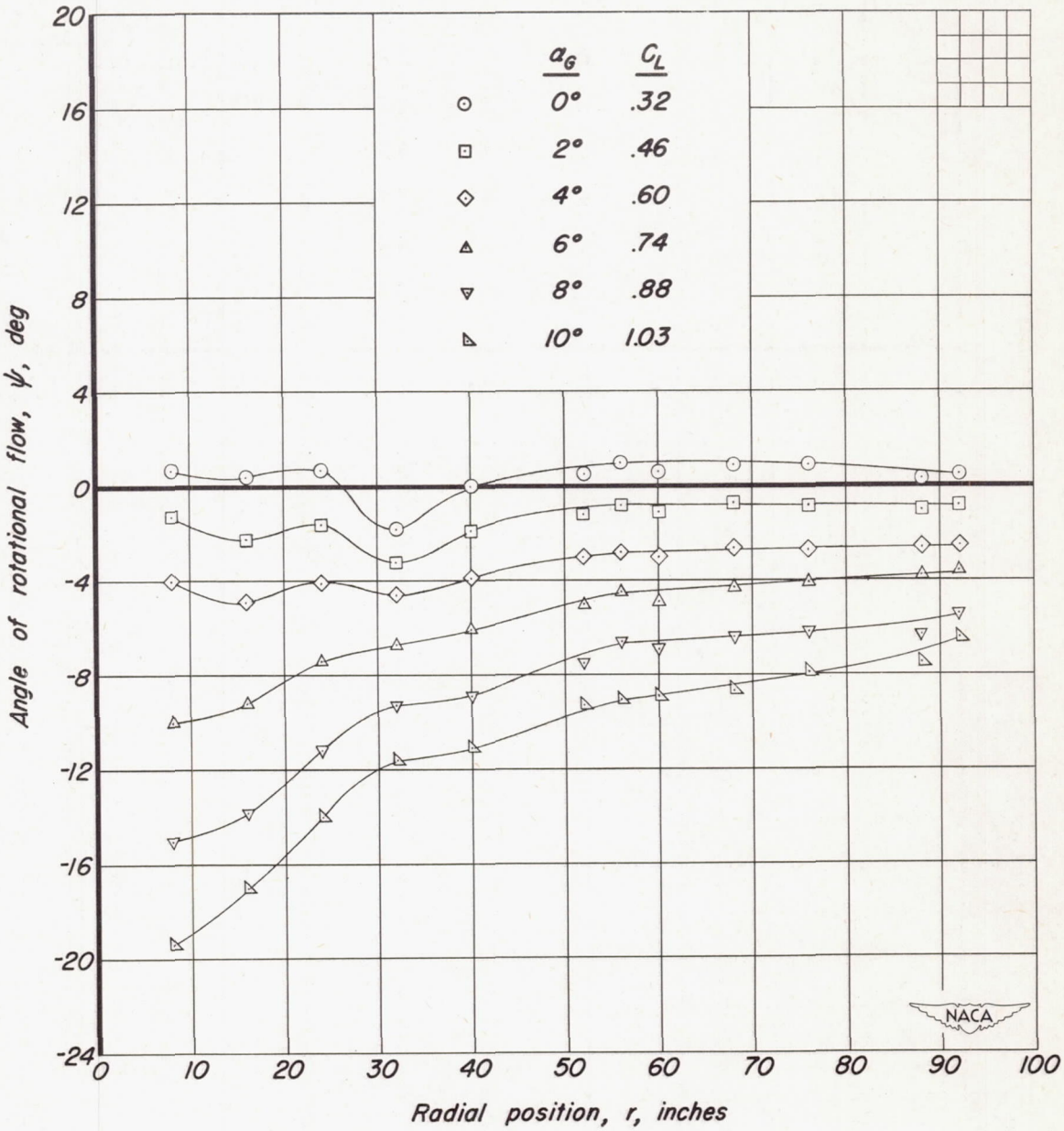
(b) $\Omega = 45.3°$.

Figure 8. - Continued.



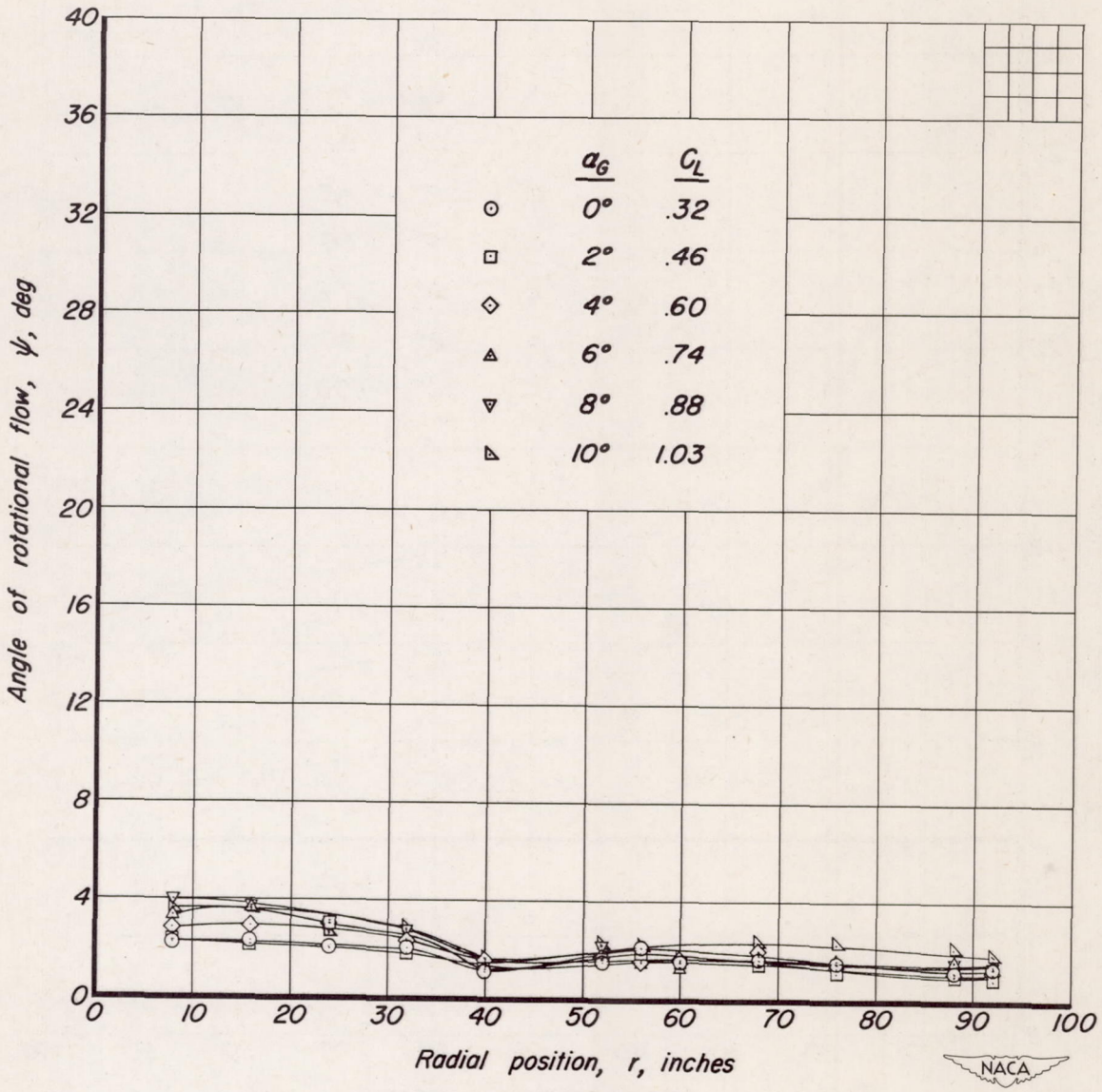
(c) $\Omega = 90.6°$.

Figure 8. - Continued.



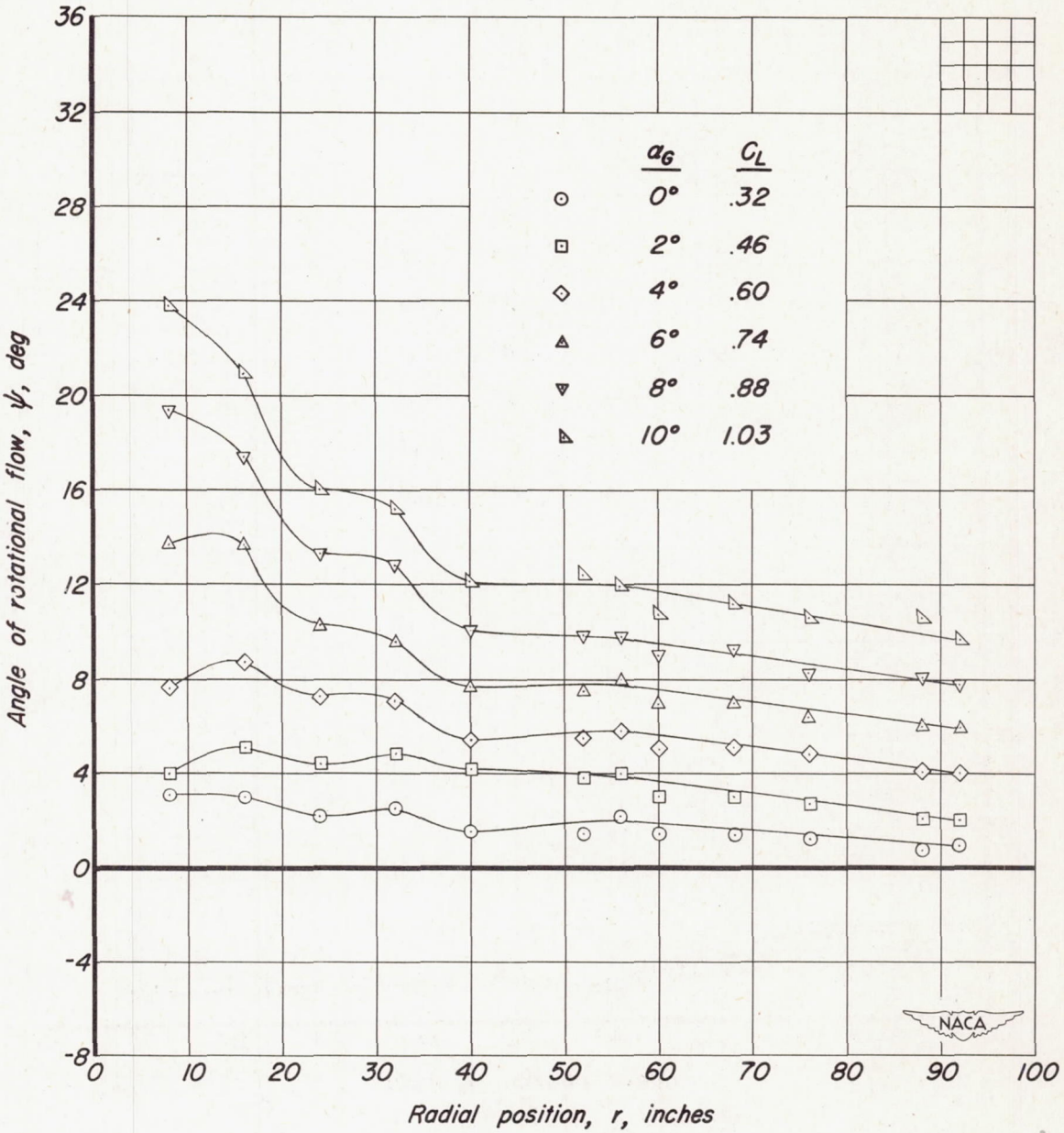
(d) Ω=135.6°.

Figure 8. - Continued.



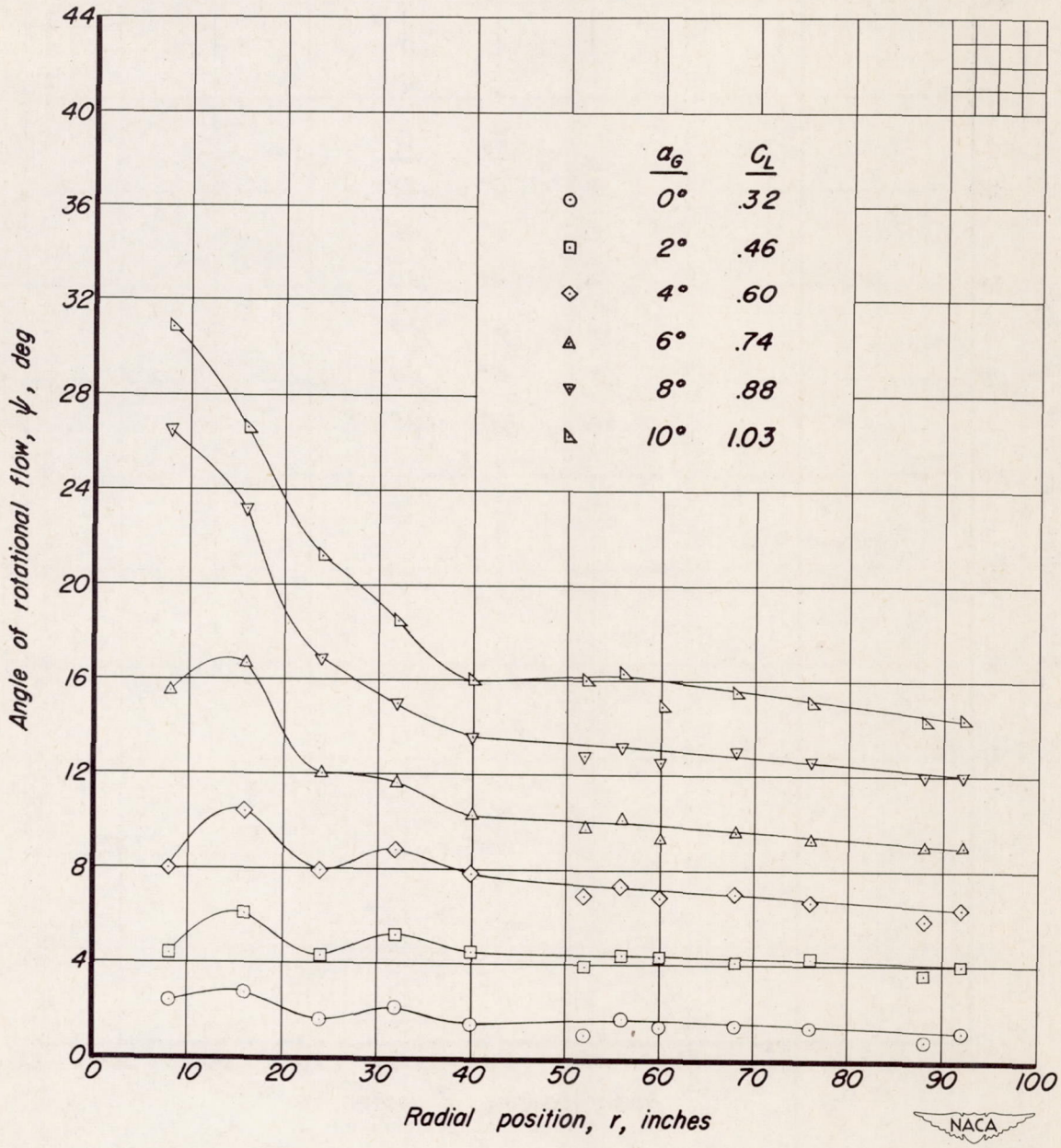
(e) Ω=180.0°.

Figure 8. - Continued.



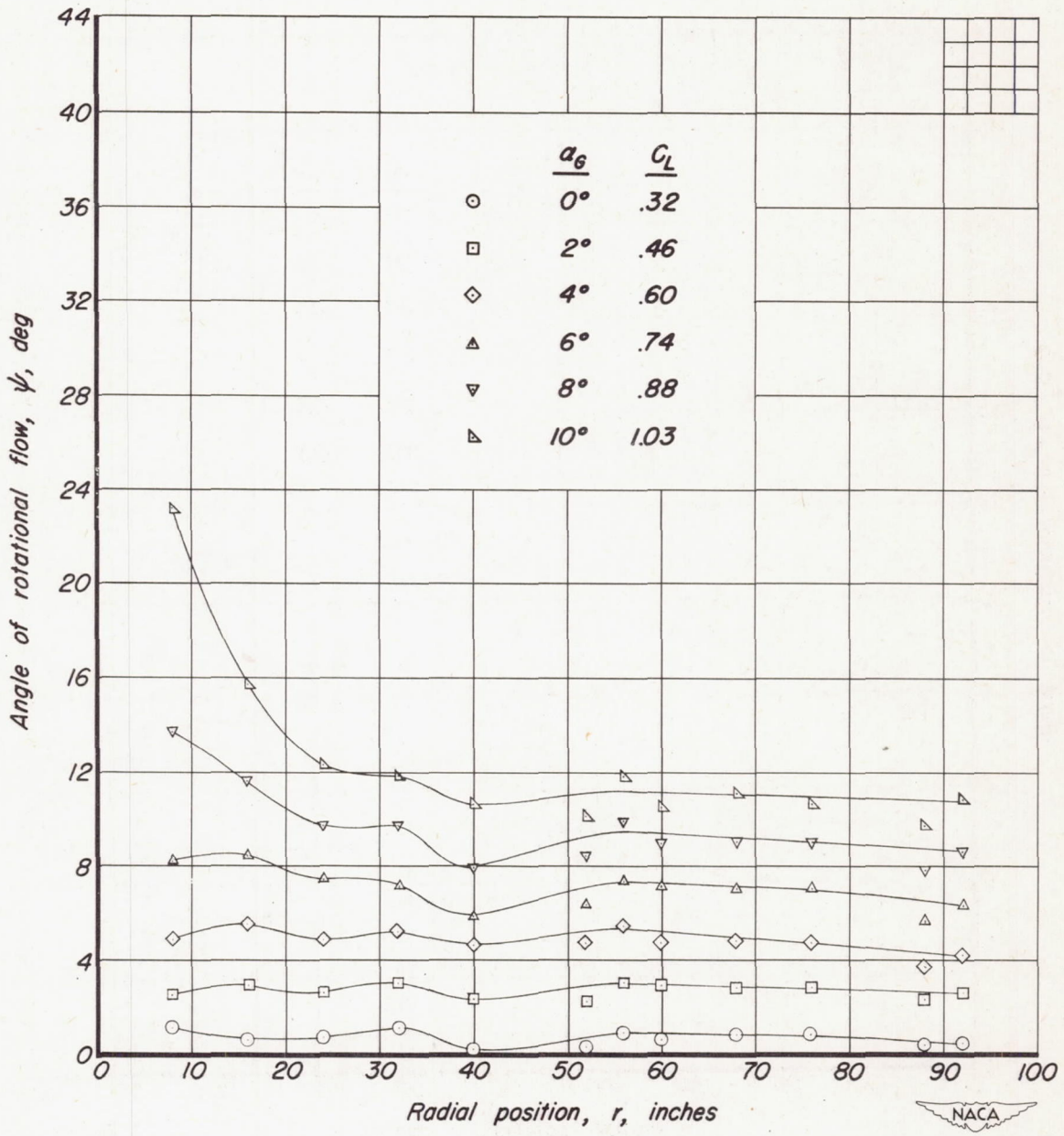
(f) $\Omega = 225.0°$.

Figure 8. - Continued.



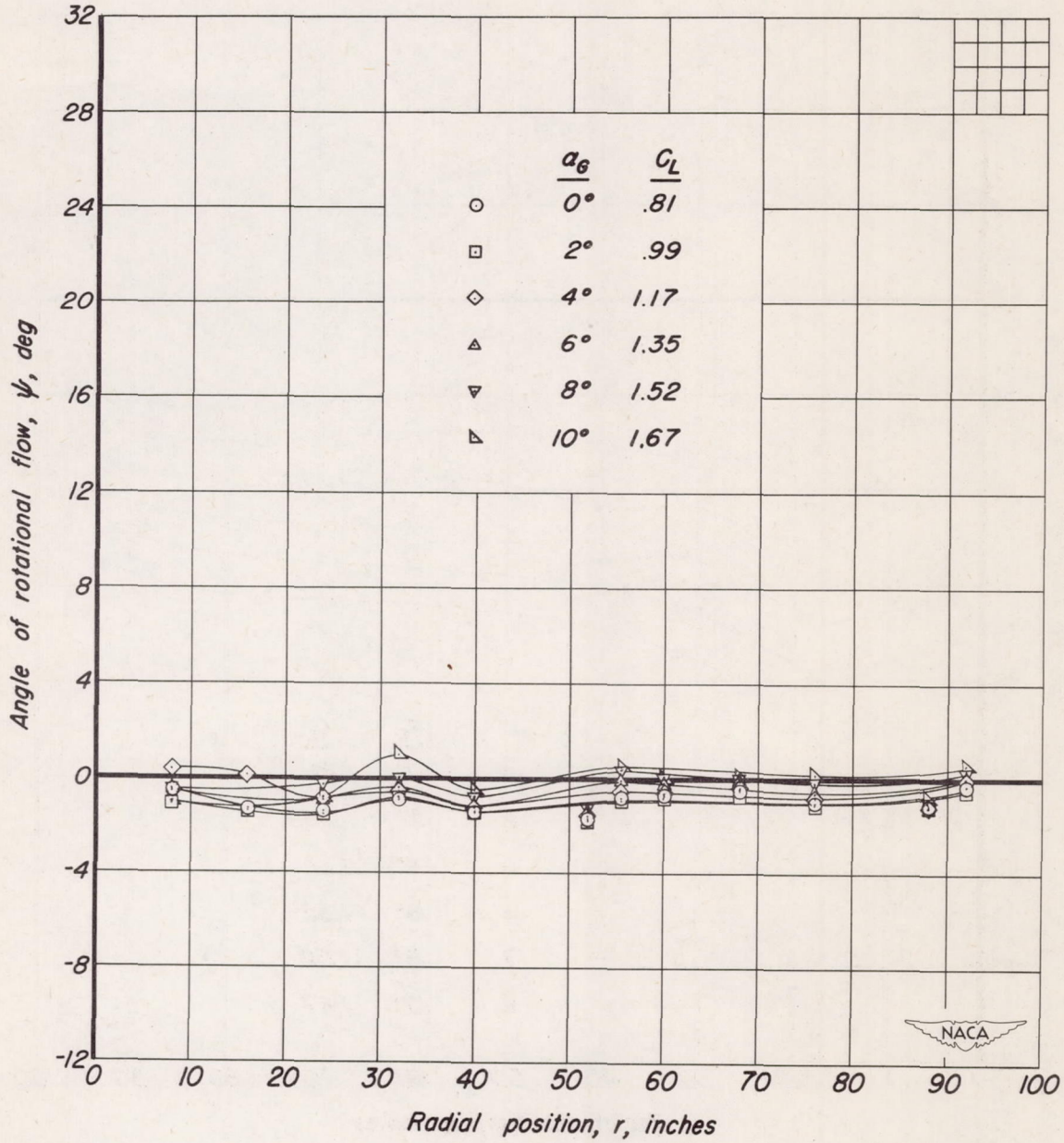
(g) $\Omega = 269.8°$.

Figure 8. - Continued.



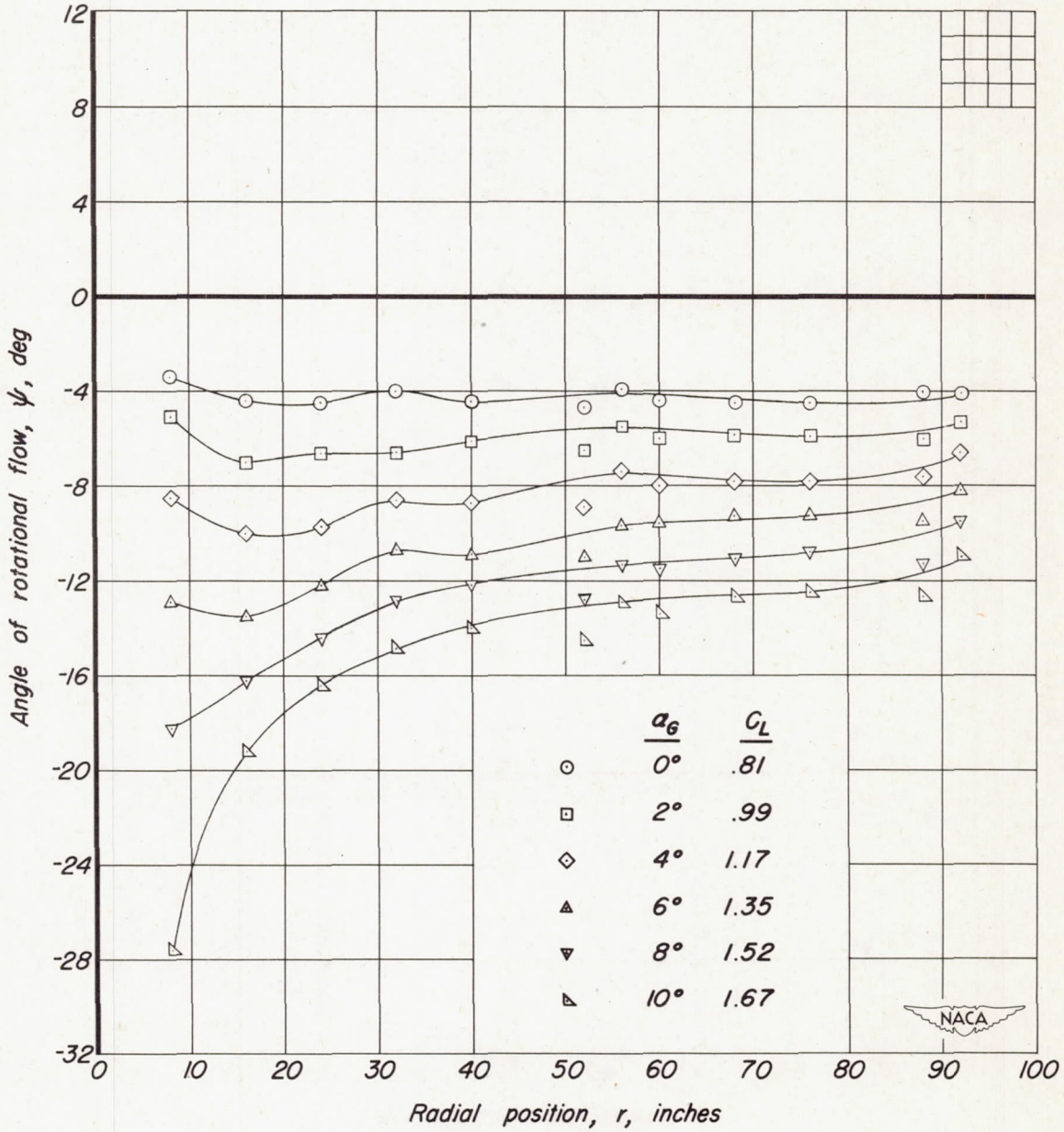
(h) $\Omega = 314.9°$.

Figure 8. - Concluded.



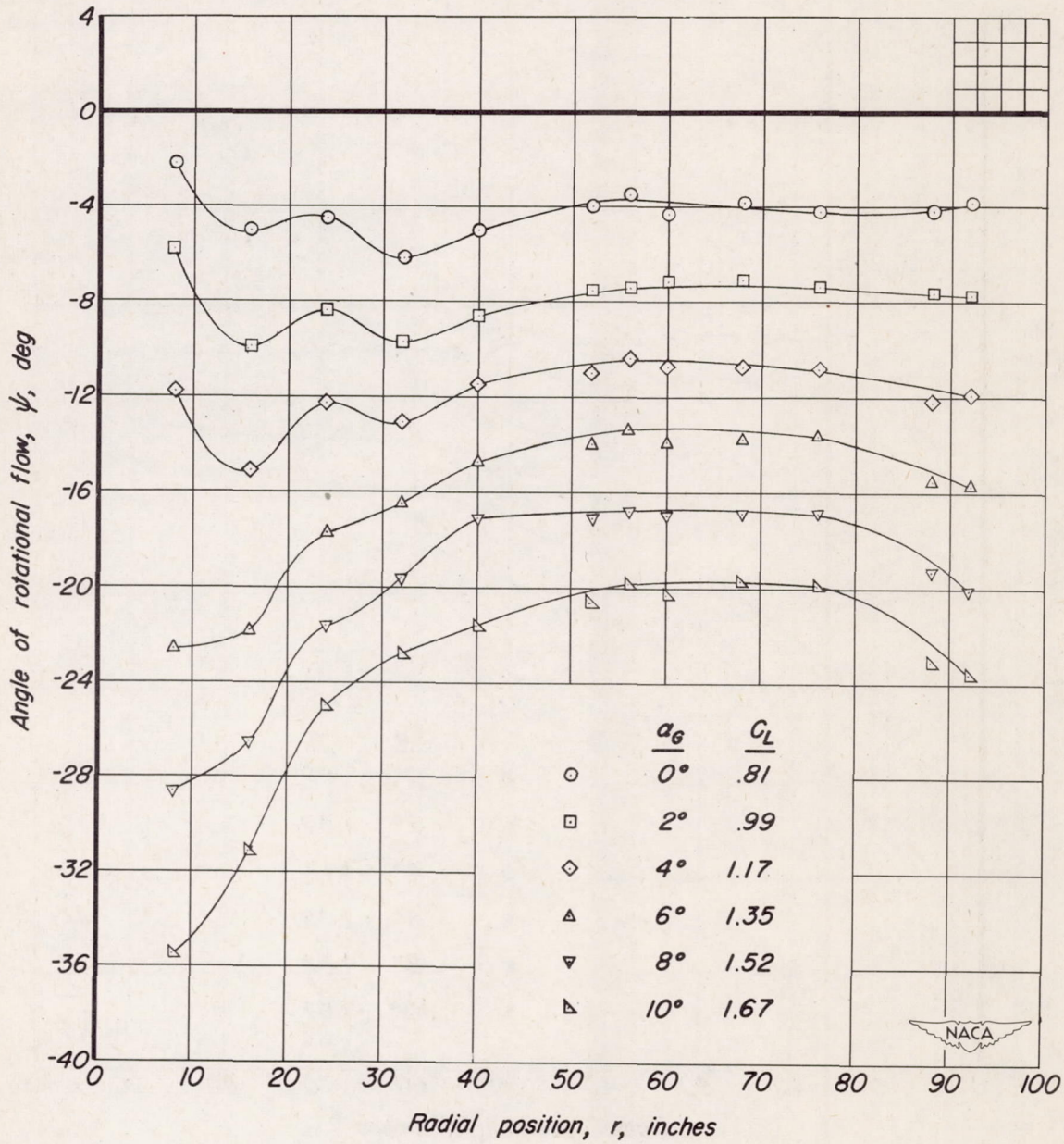
(a) $\Omega = 359.8°$.

Figure 9. – Variation of the angle of rotational flow, ψ, with radial position for several angles of attack. m_l / m_o, .14; δ_f, 40°.



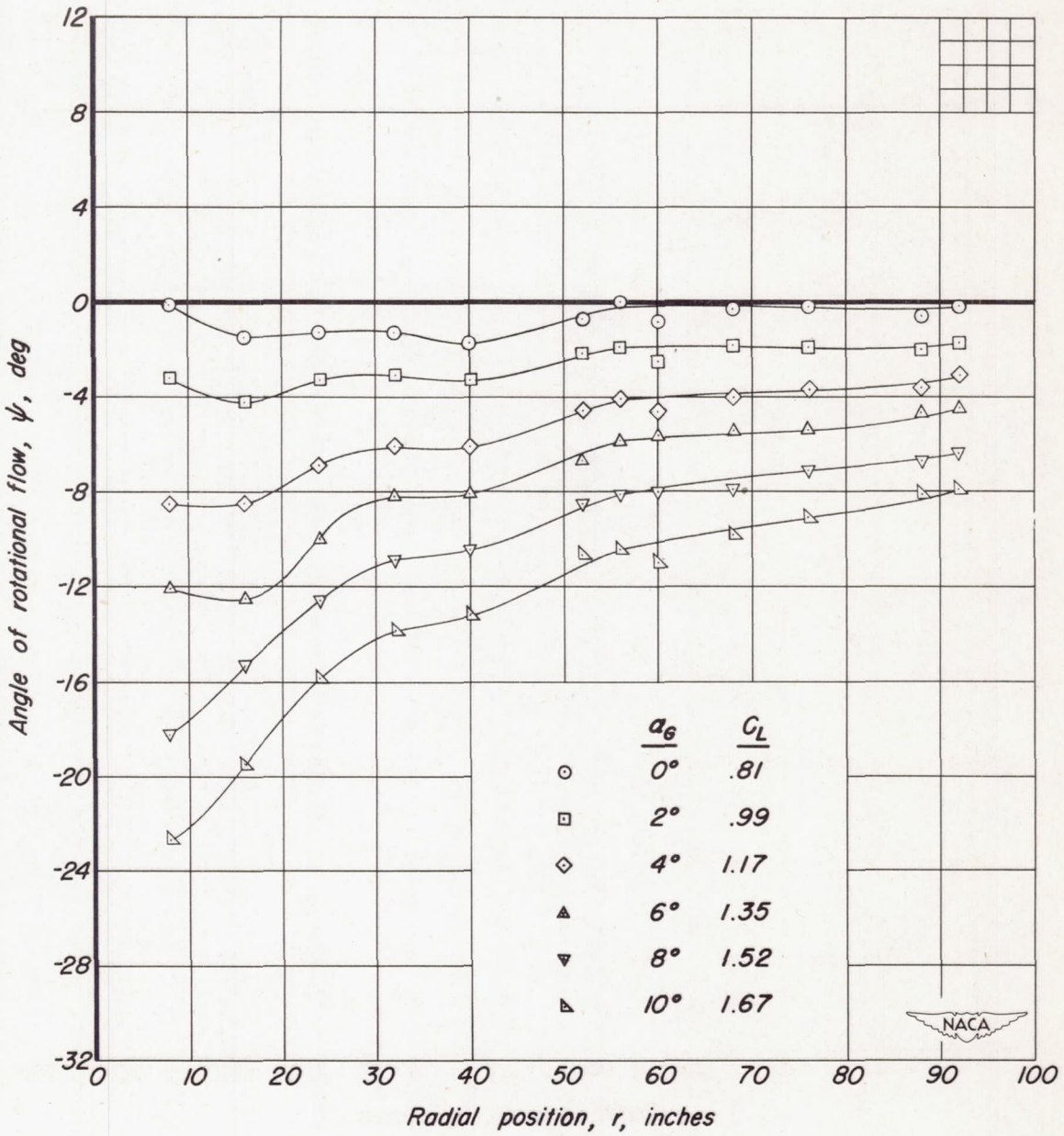
(b) $\Omega = 45.3°$.

Figure 9. - Continued.



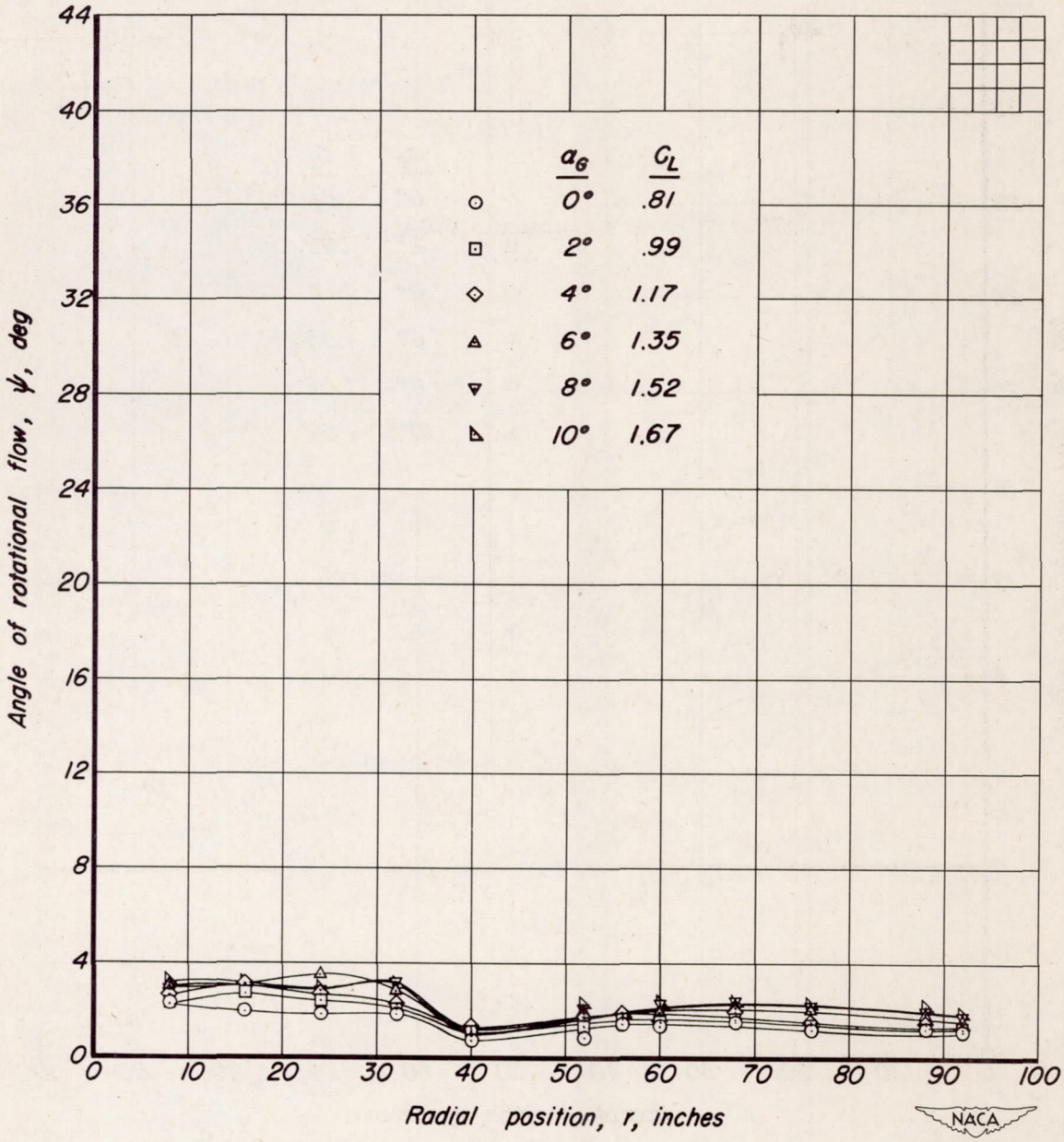
(c) $\Omega = 90.6°$.

Figure 9. - Continued.



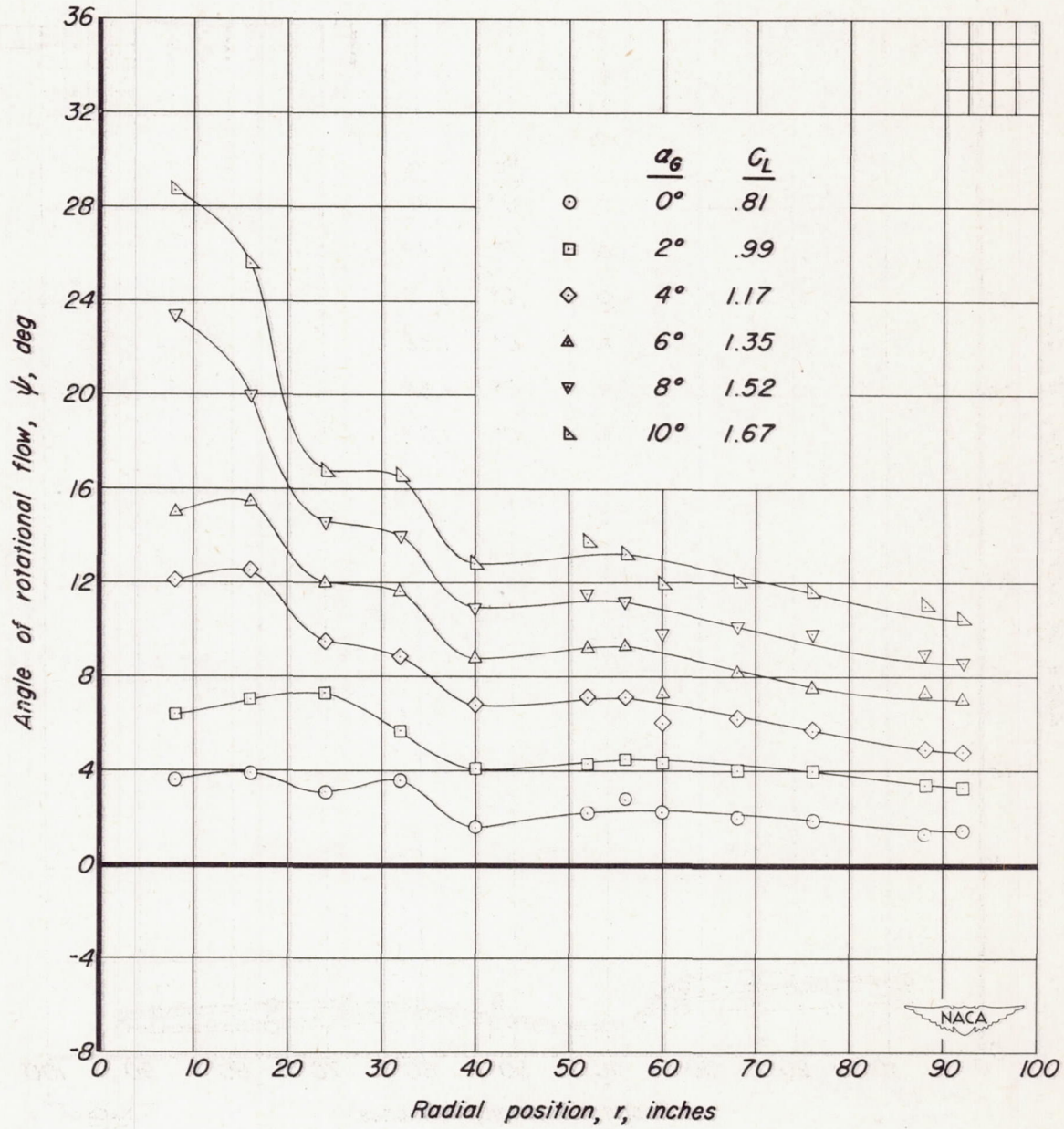
(d) $\Omega = 135.6°$.

Figure 9. - Continued.



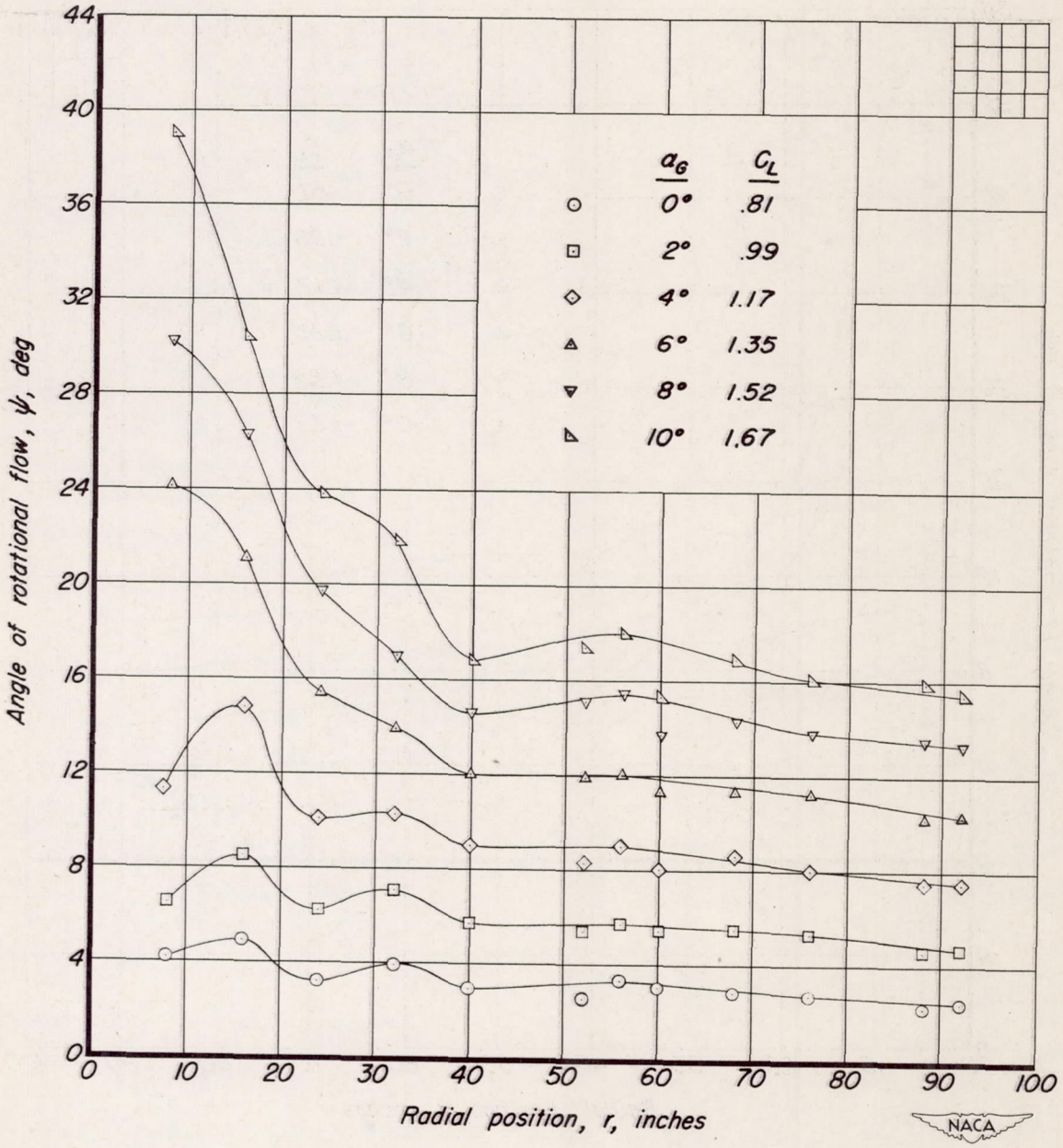
(e) $\Omega = 180.0°$.

Figure 9. - Continued.



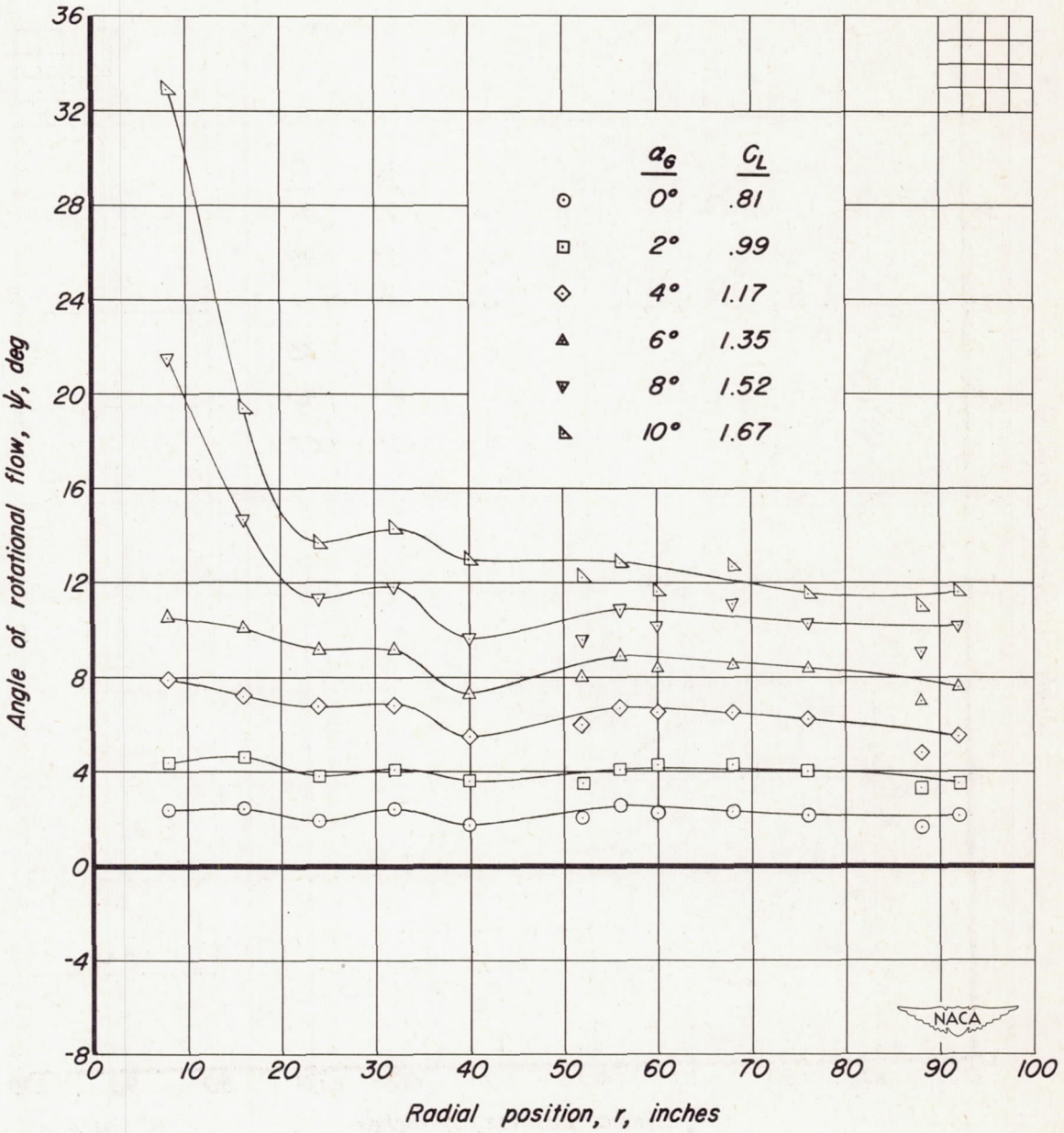
(f) $\Omega = 225.0°$.

Figure 9. - Continued.



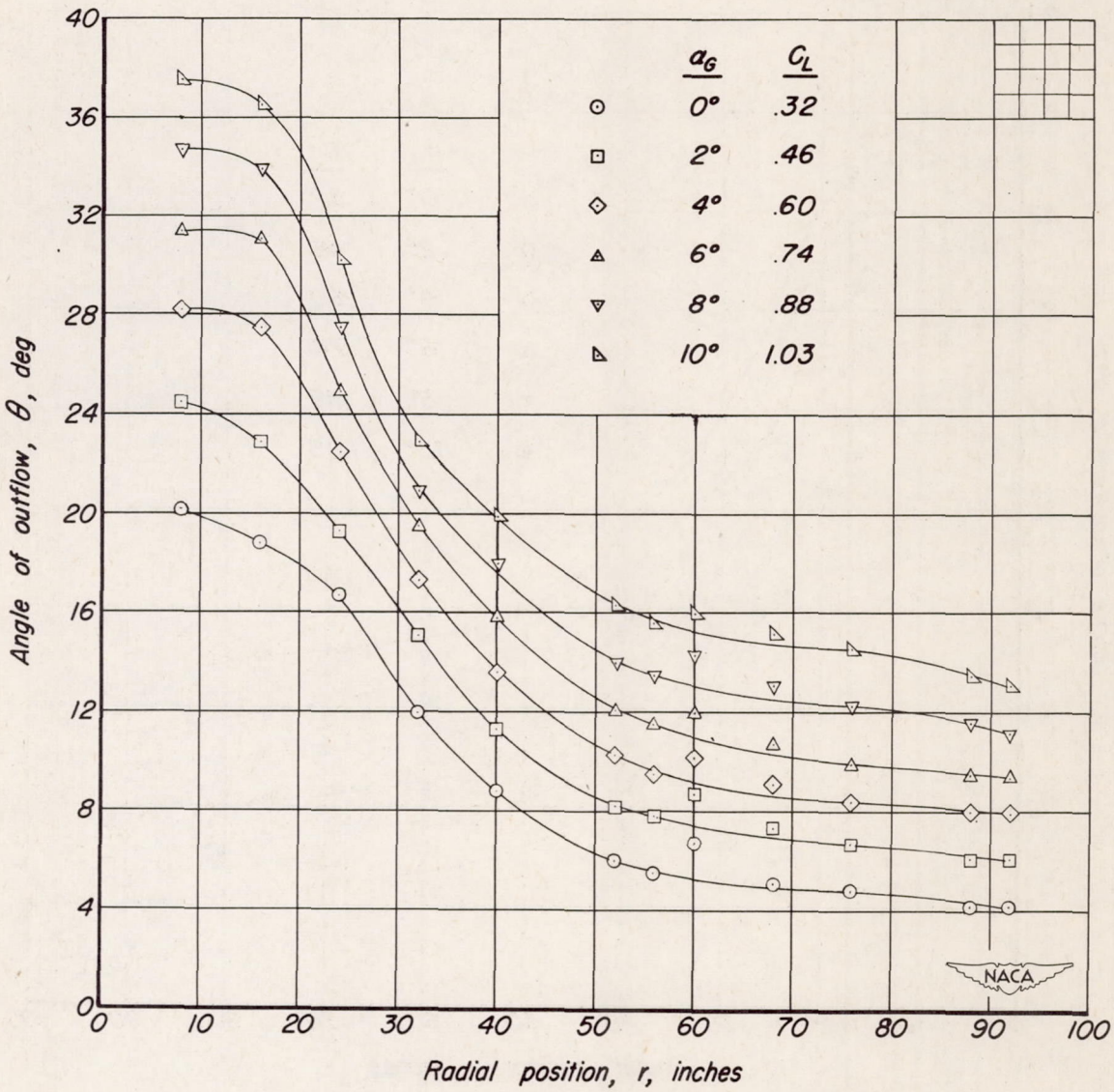
(g) $\Omega = 269.8°$.

Figure 9. – Continued.



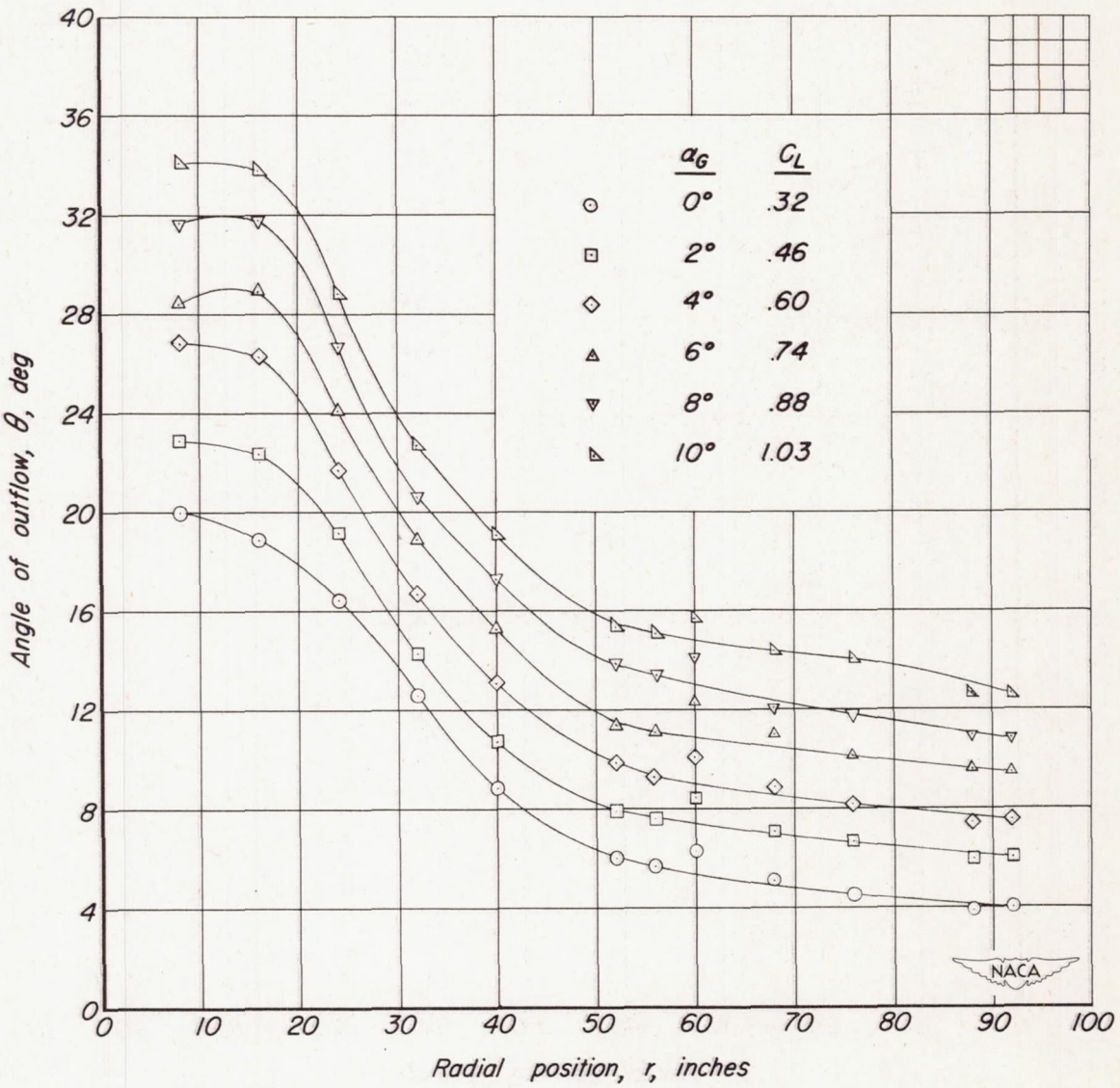
(h) $\Omega = 314.9°$.

Figure 9. - Concluded.



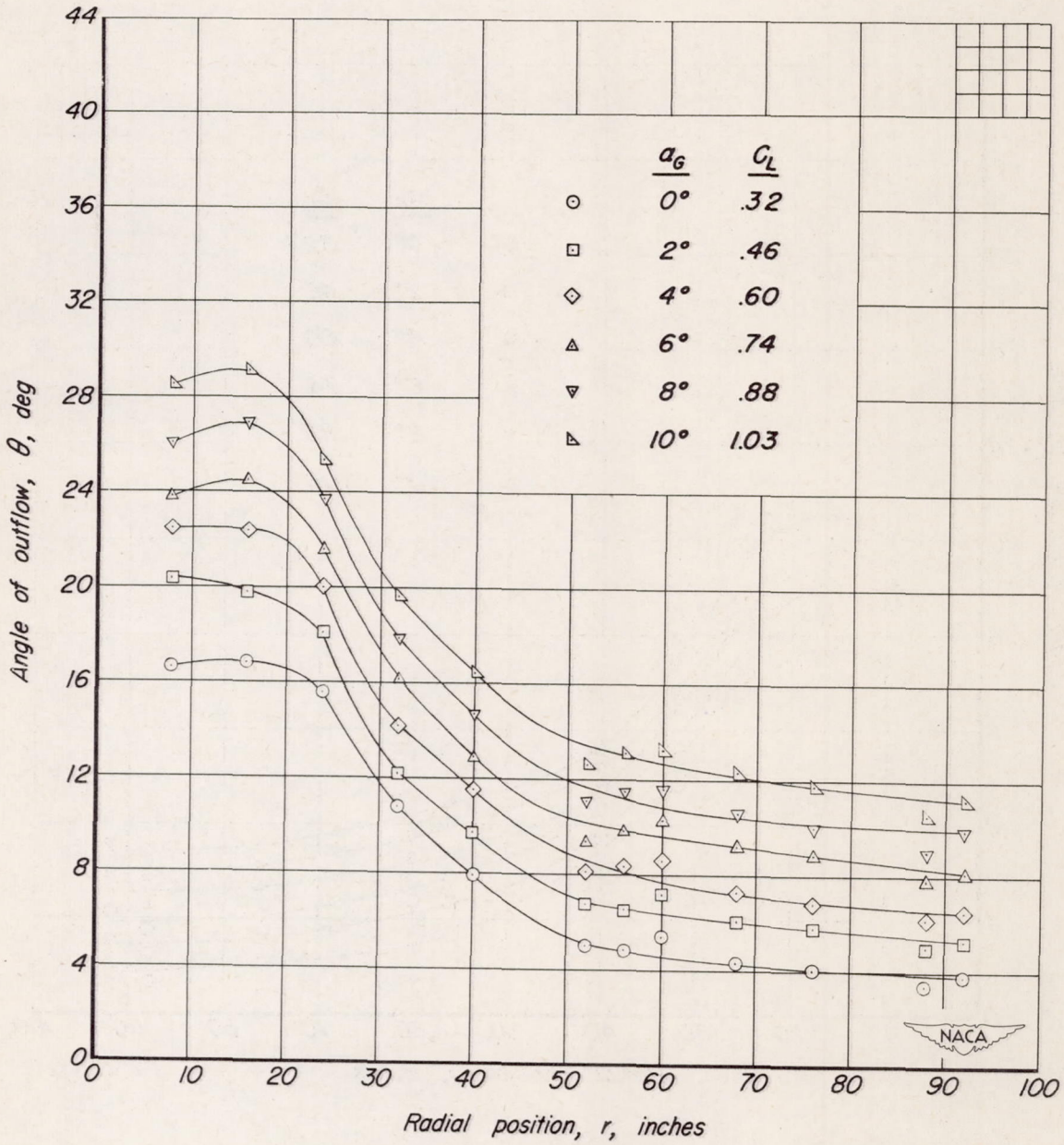
(a) $\Omega = 0.0°$.

Figure 10. – Variation of angle of outflow, θ, with radial position for several angles of attack. m_1/m_o, .29; δ_f, 0°.



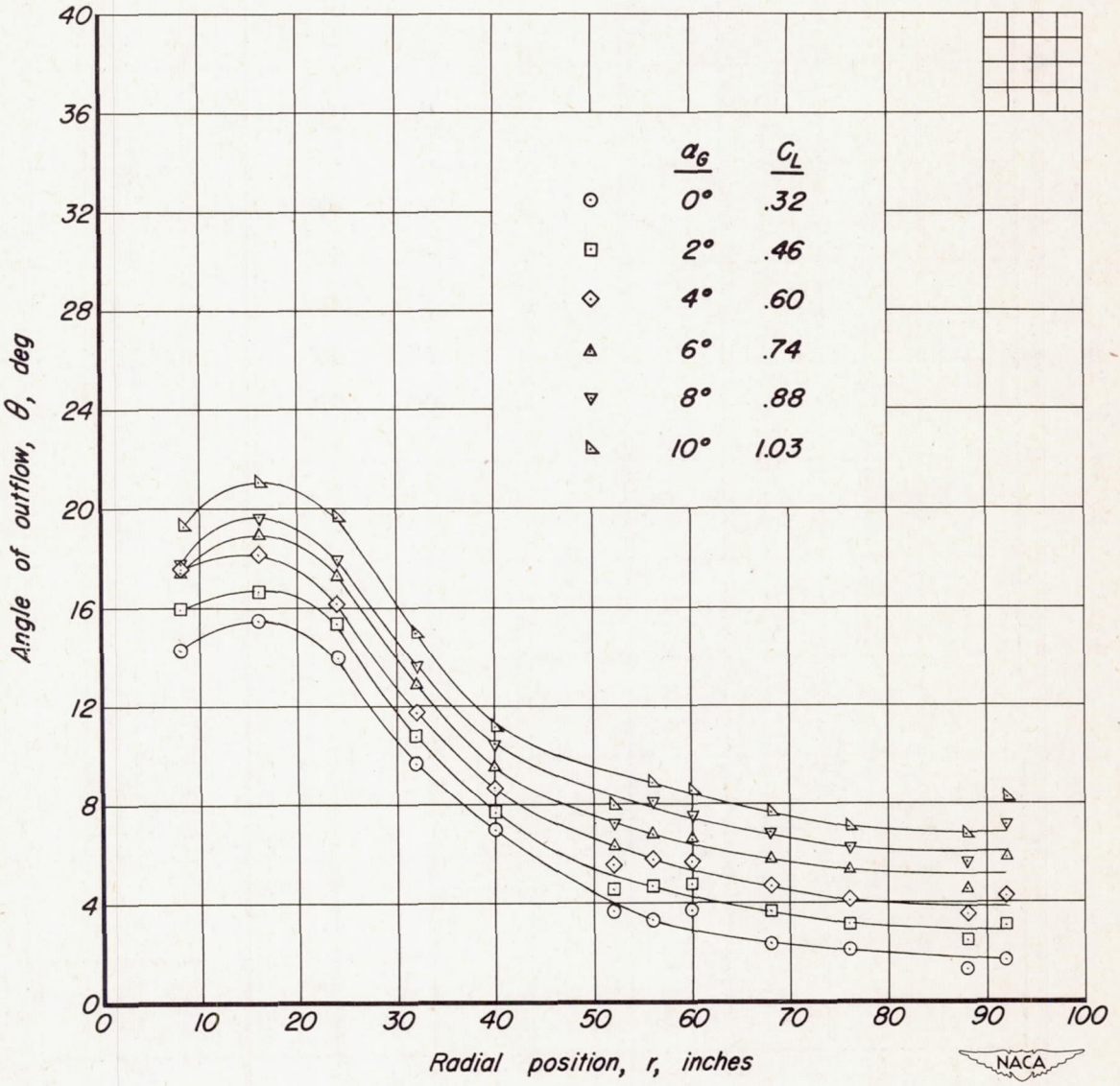
(b) $\Omega = 22.5°$.

Figure 10. - Continued.



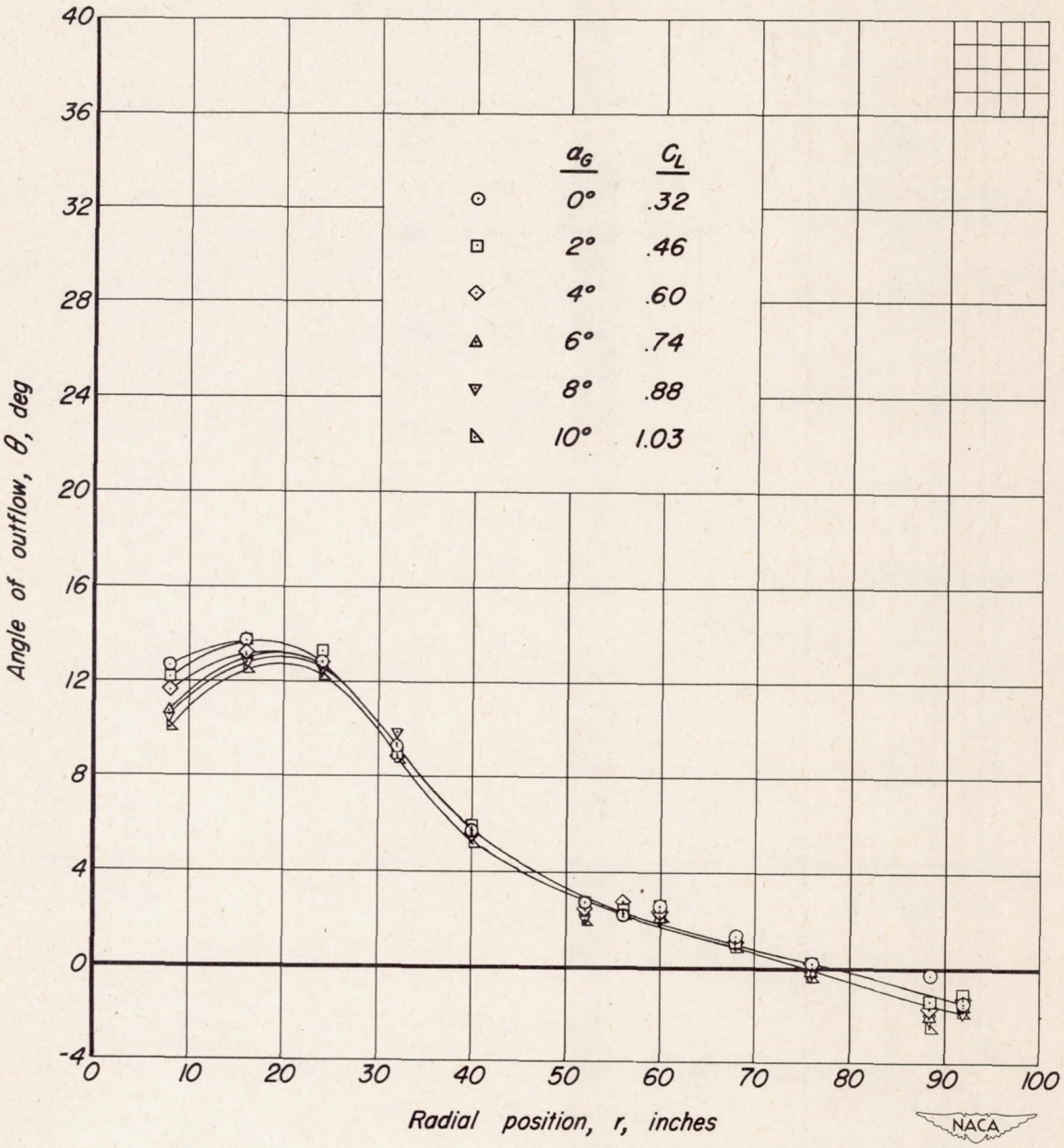
(c) $\Omega = 45.2°$.

Figure 10. - Continued.



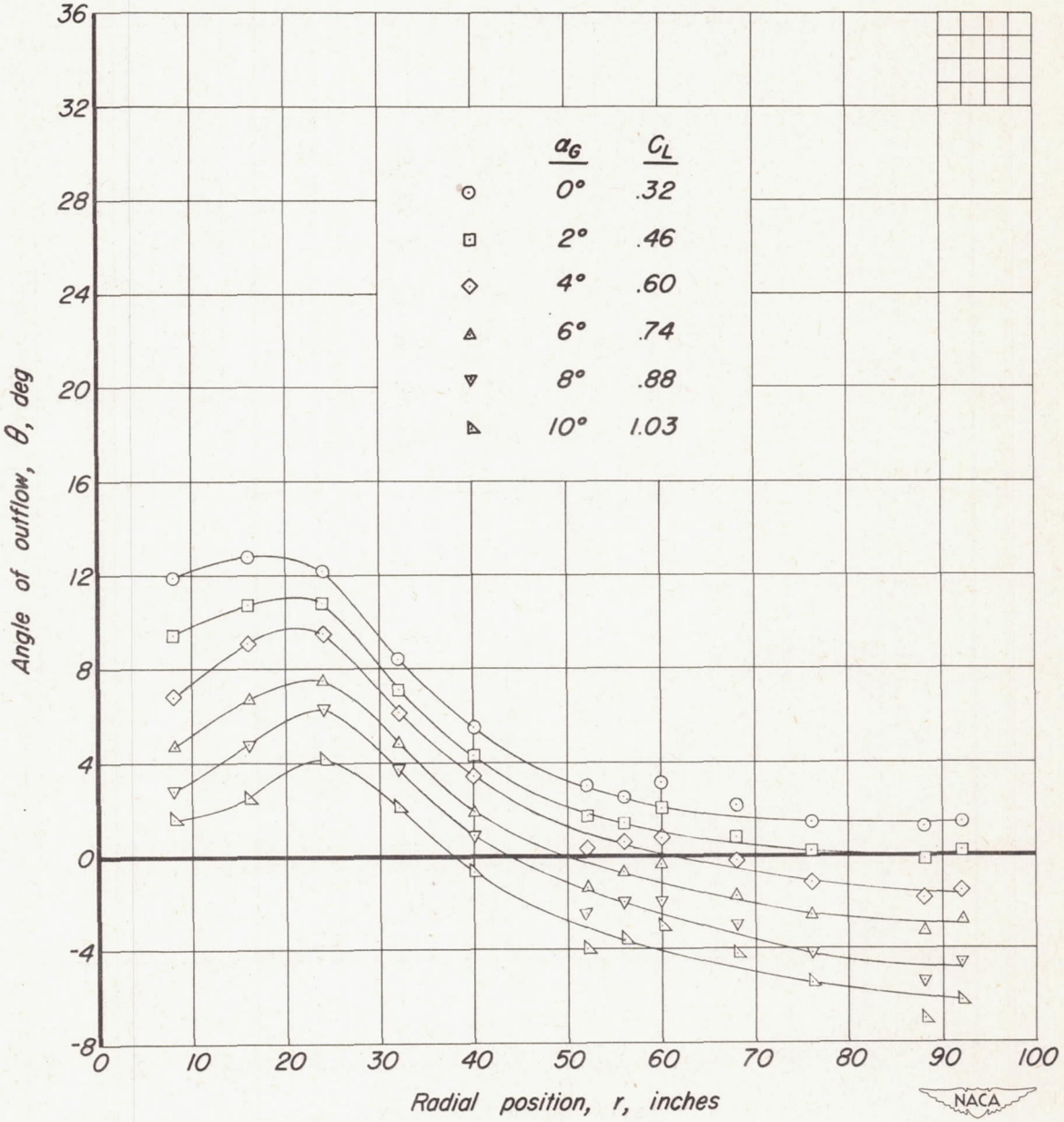
(d) Ω=68.5°.

Figure 10. - Continued.



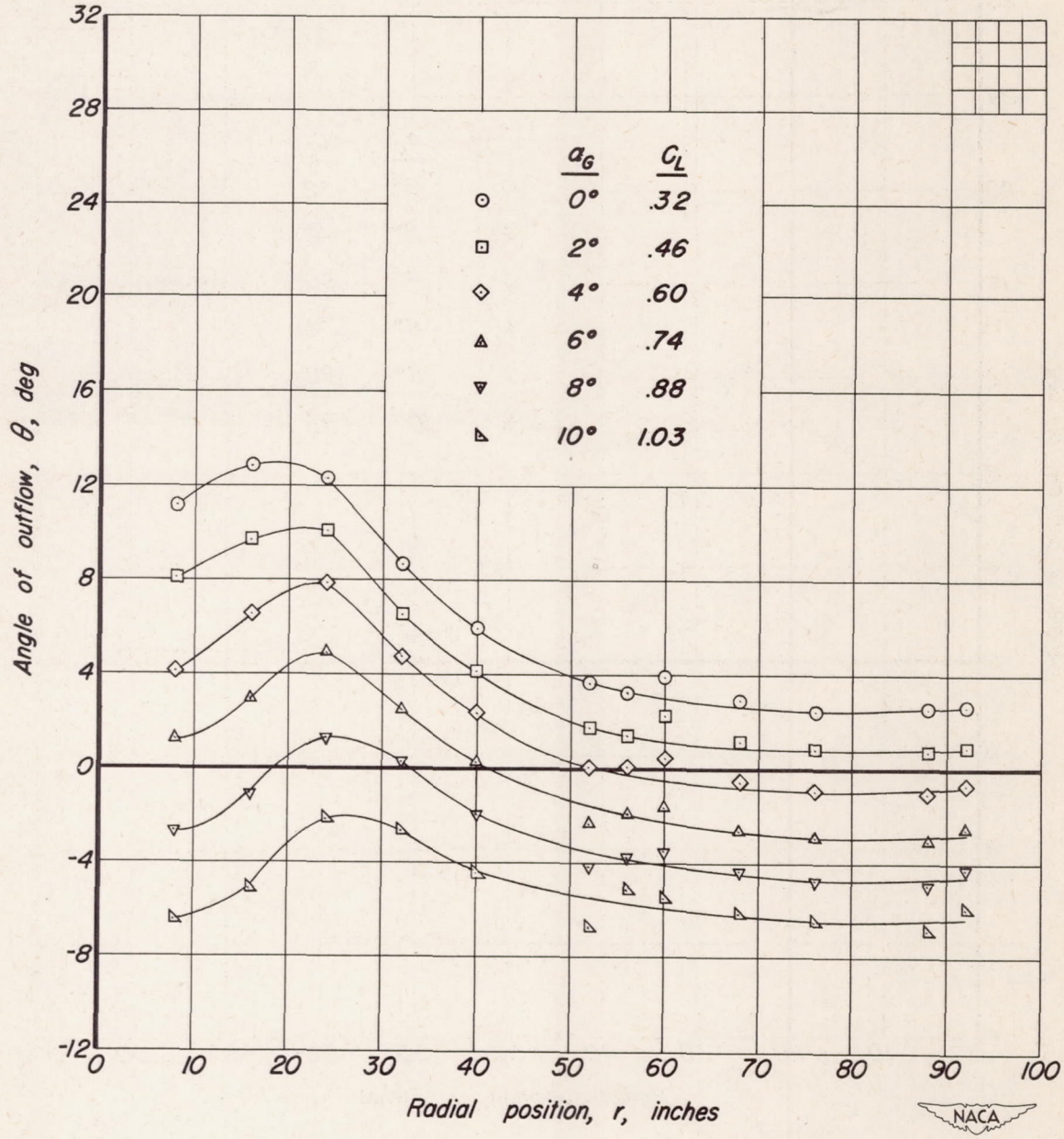
(e) $\Omega = 91.1°$.

Figure 10. - Continued.



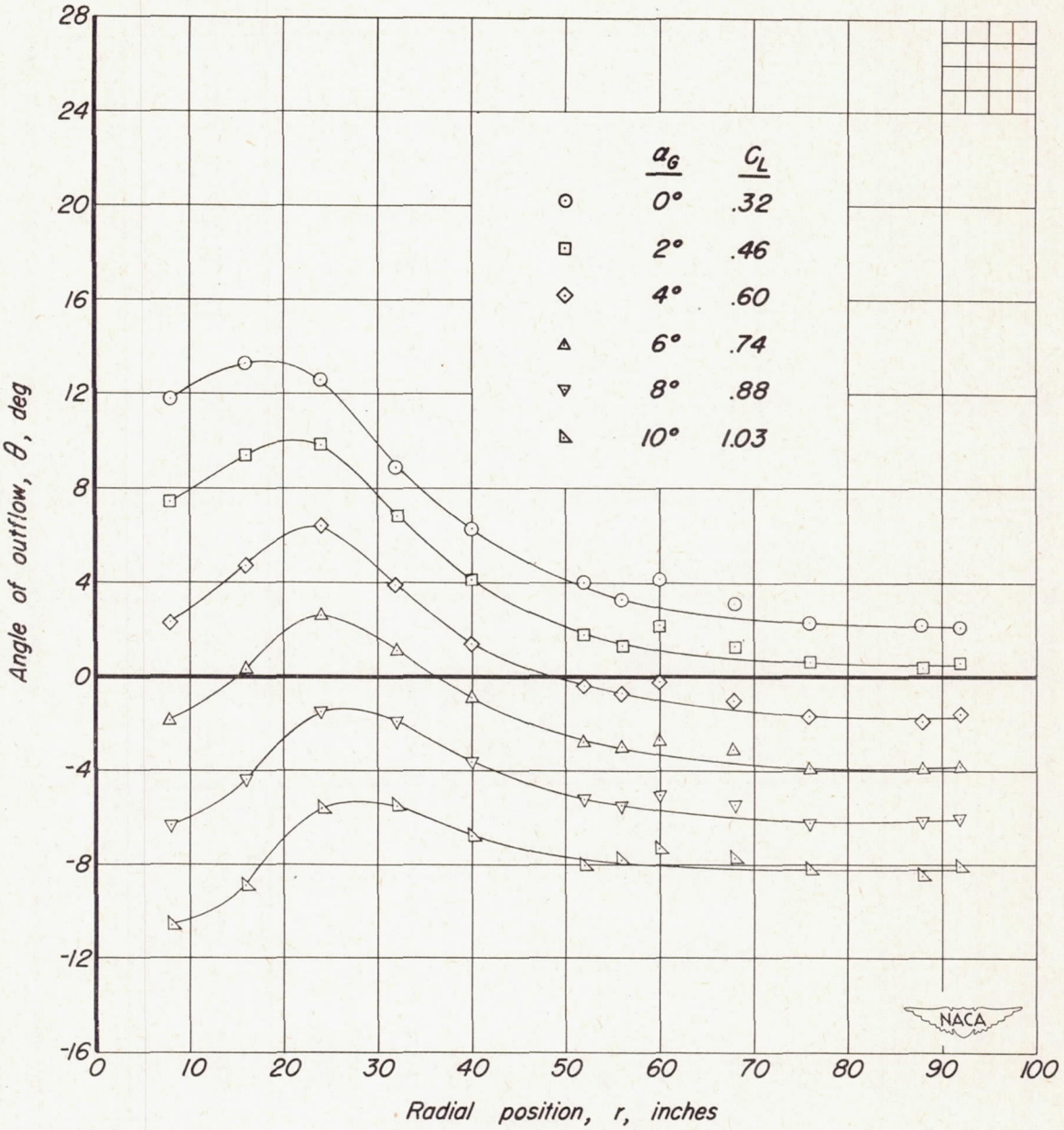
(f) Ω=113.4°.

Figure 10. - Continued.



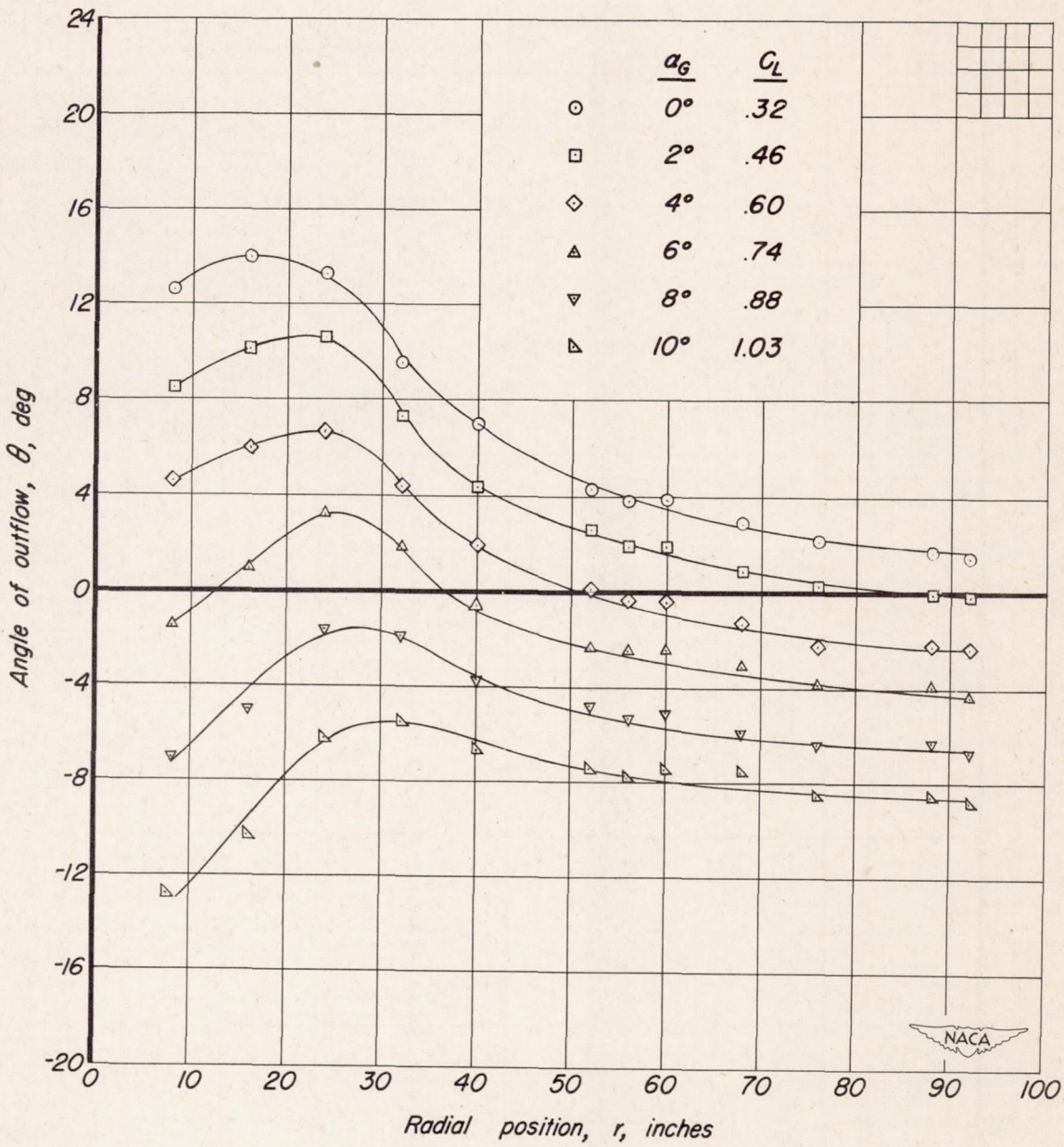
(g) Ω=135.7°.

Figure 10. - Continued.



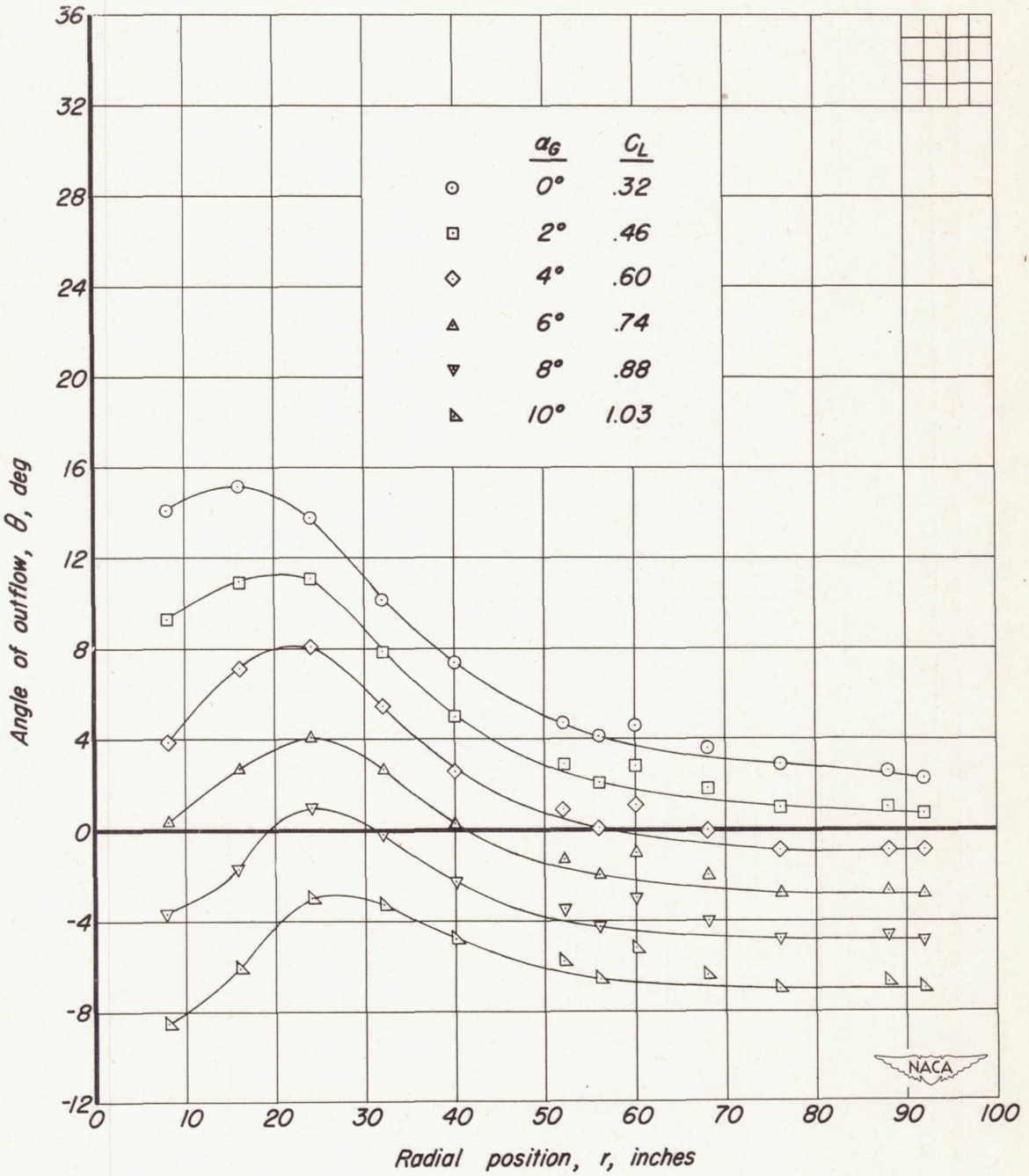
(h) Ω=158.2°.

Figure 10. - Continued.



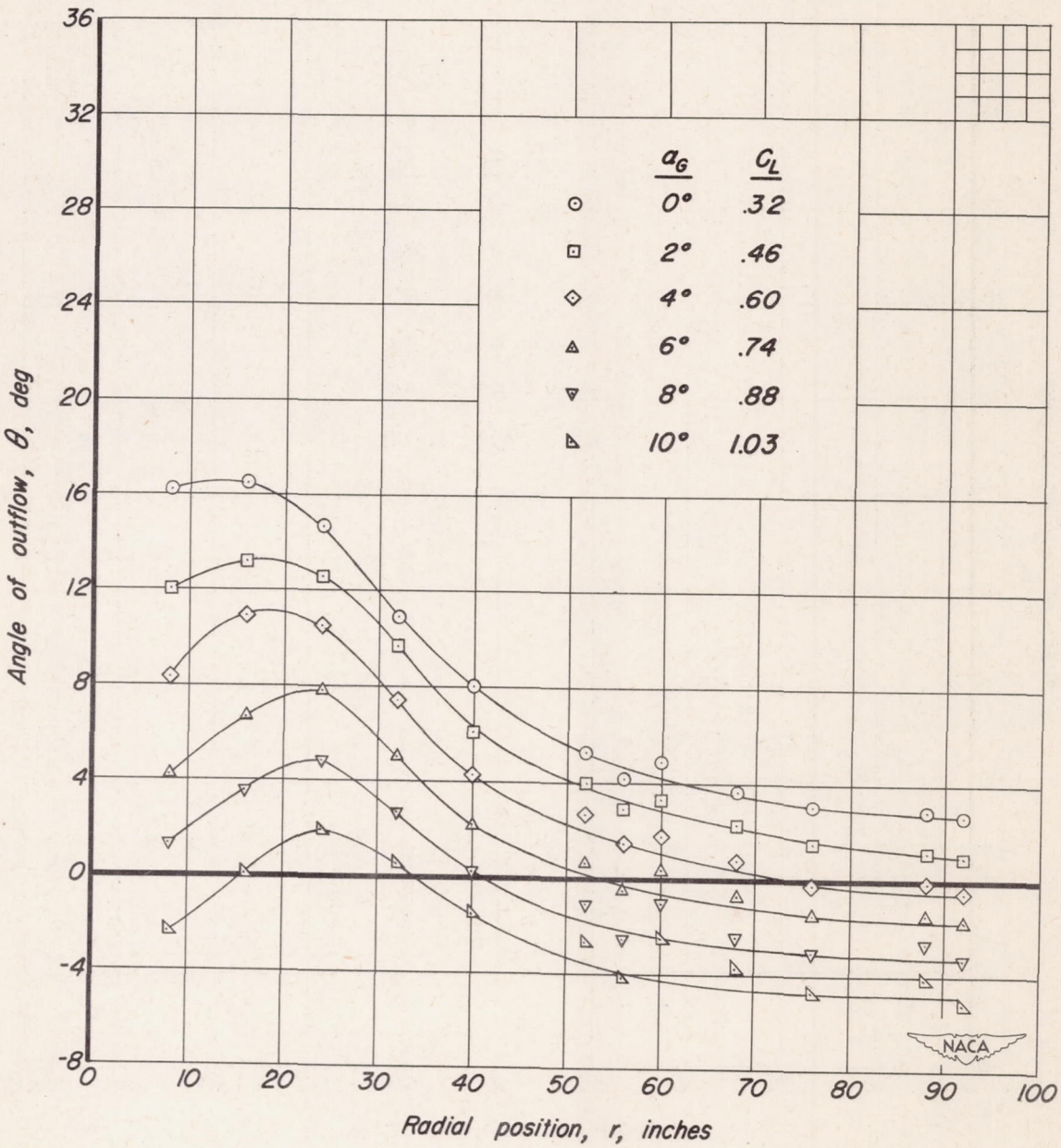
(i) Ω=180.6°.

Figure 10. - Continued.



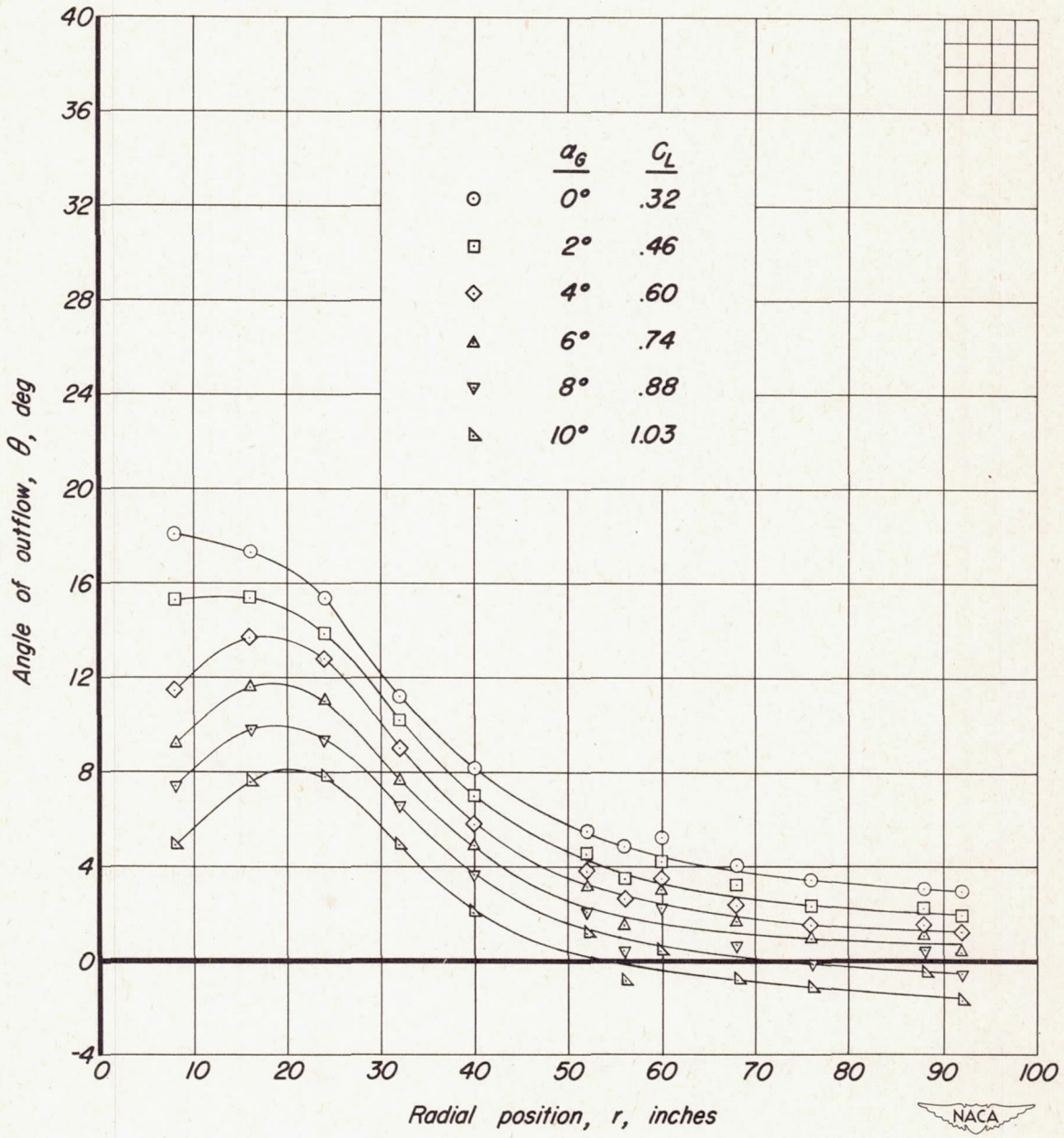
(j) Ω=203.0°.

Figure 10. - Continued.



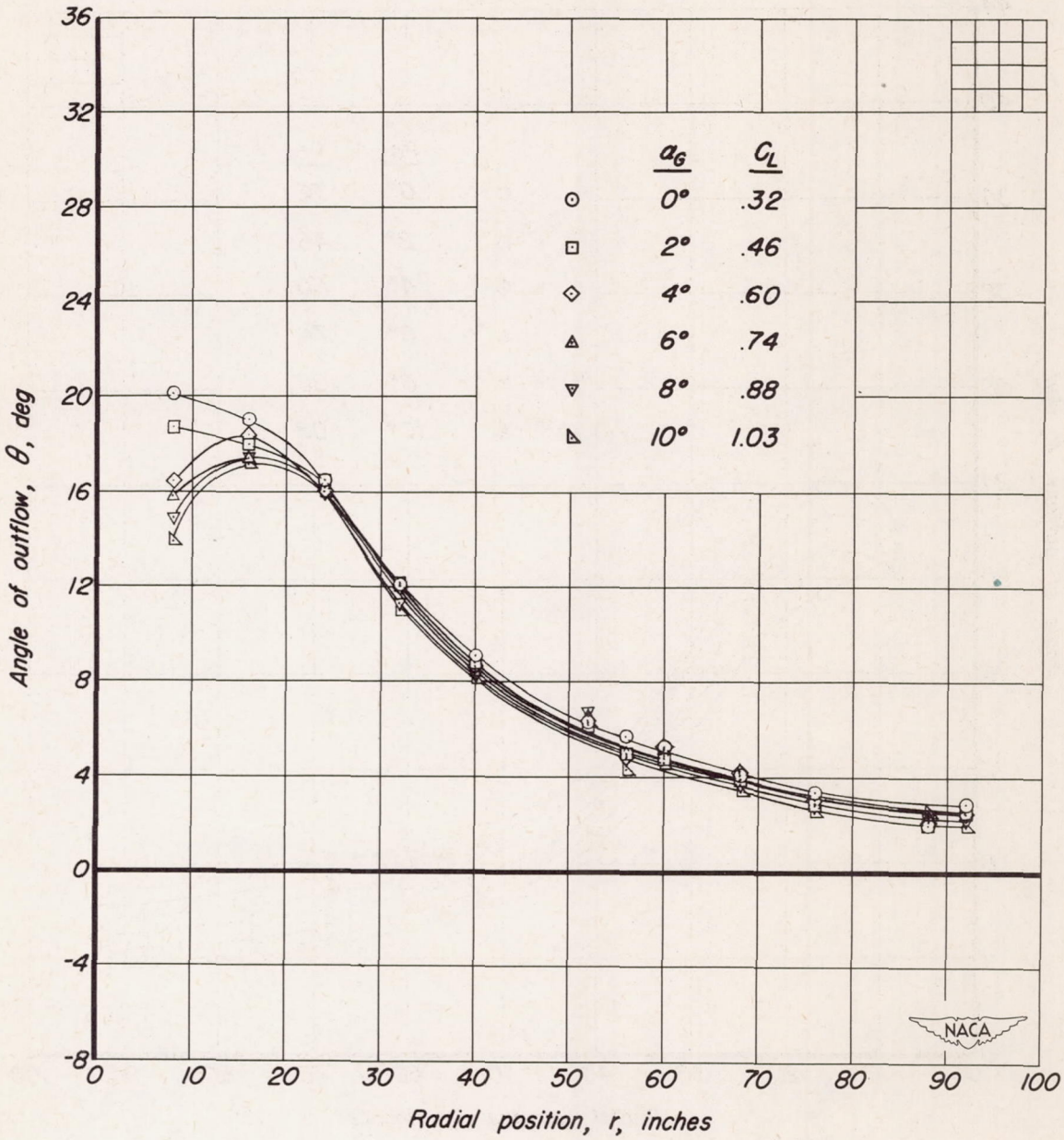
(k) $\Omega = 225.6°$.

Figure 10. - Continued.



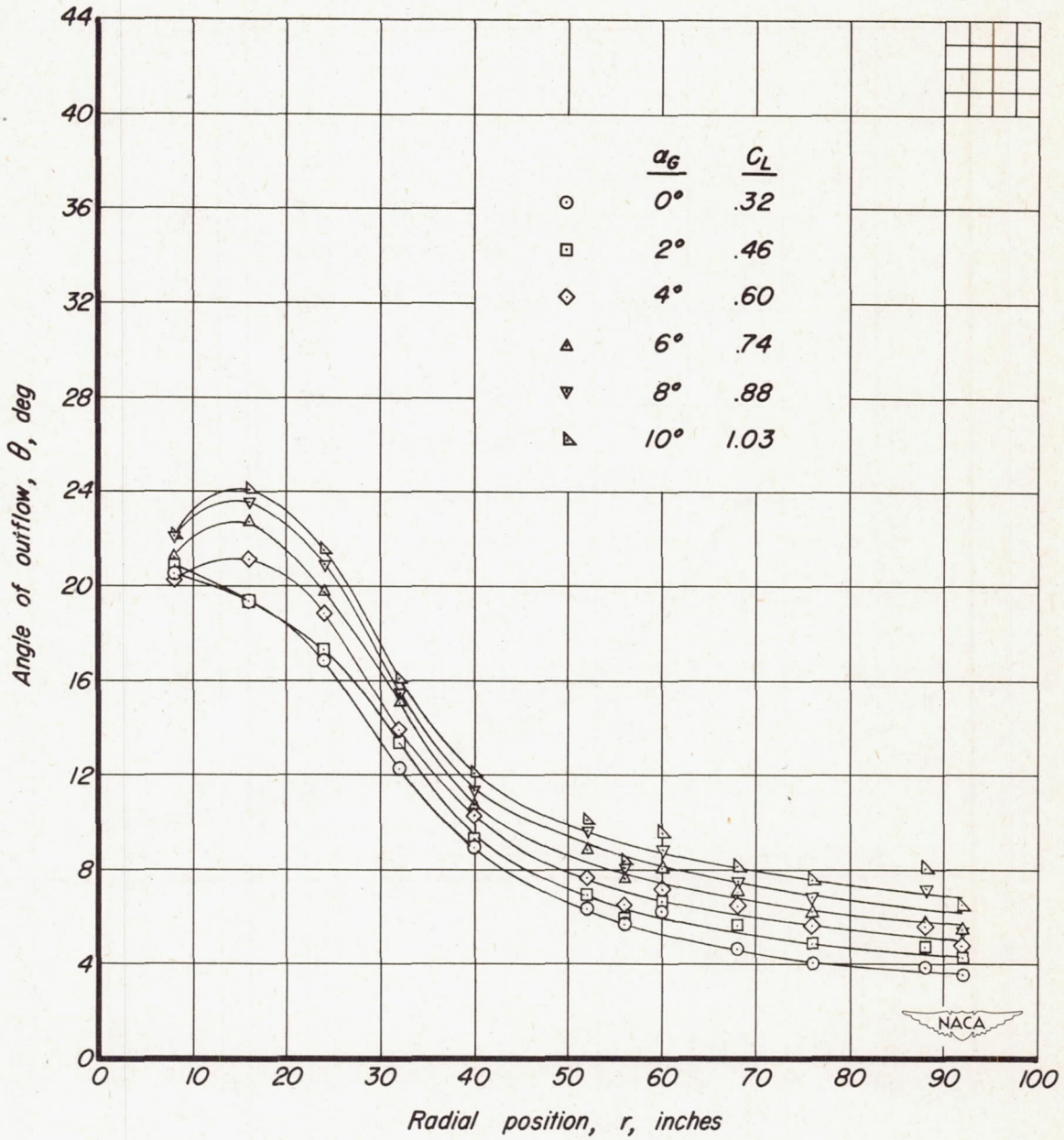
(l) $\Omega = 247.2°$.

Figure 10. - Continued.



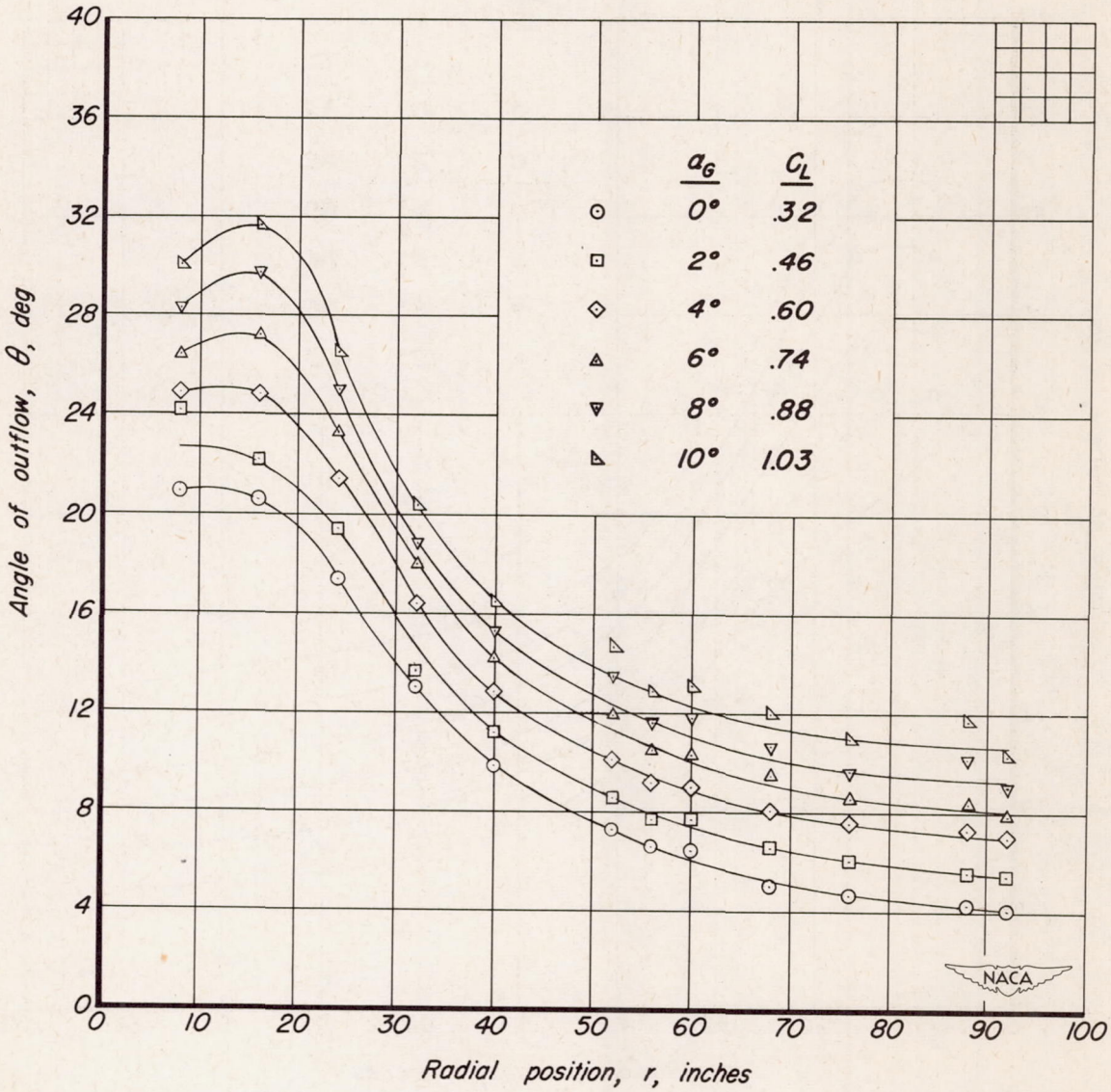
(m) Ω=270.1°.

Figure 10. - Continued.



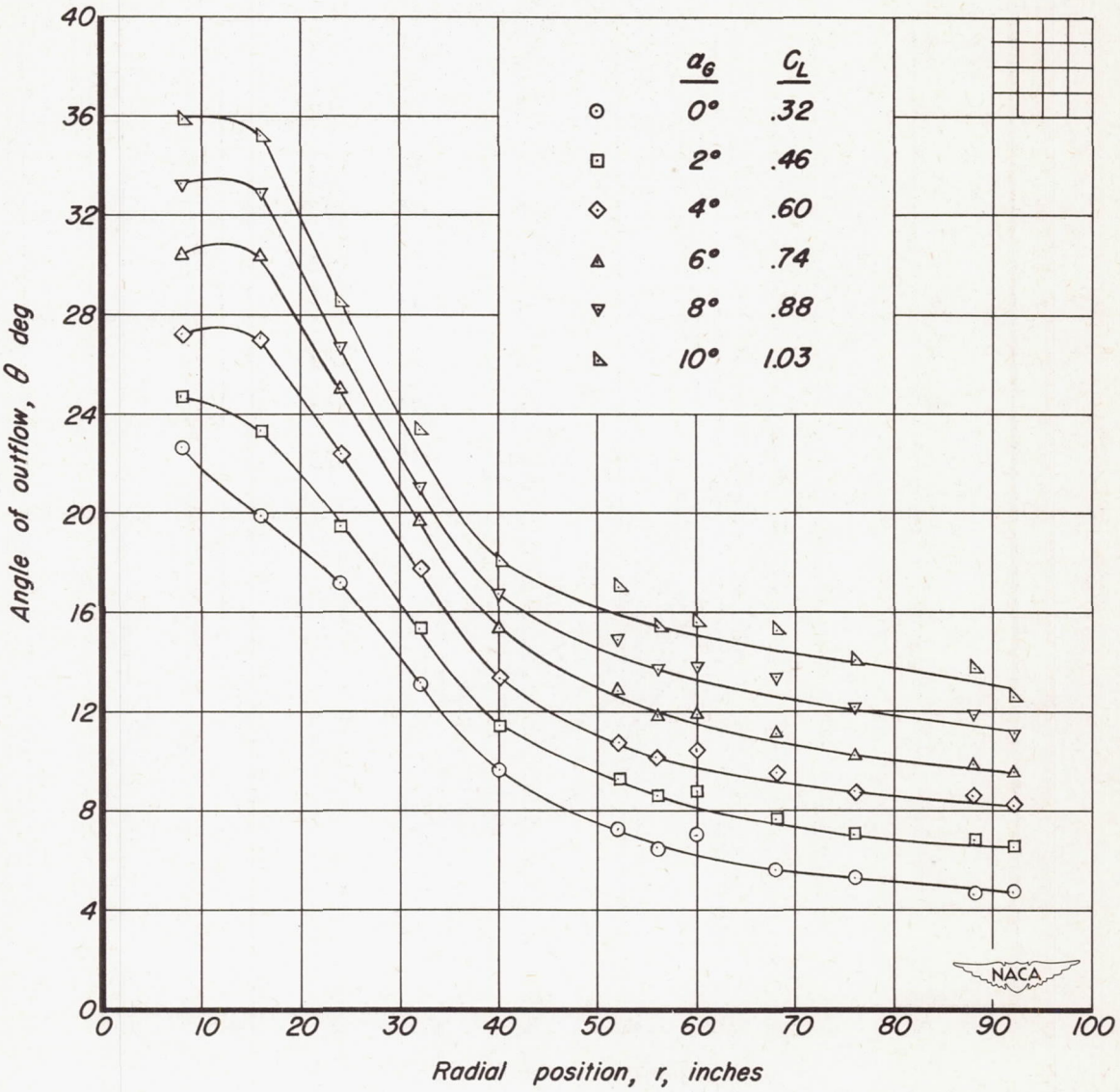
(n) $\Omega = 292.2°$.

Figure 10. - Continued.



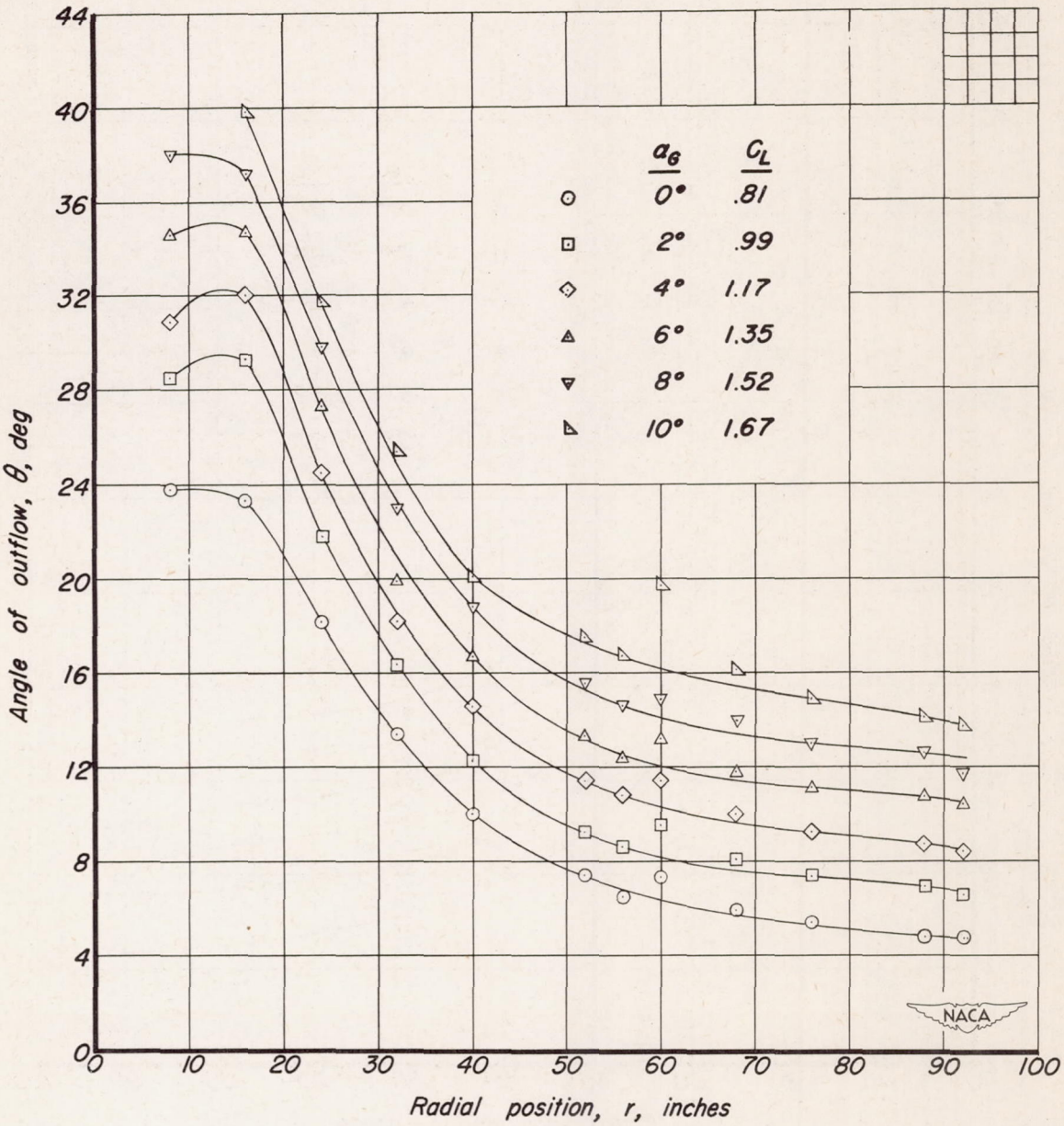
(o) $\Omega = 314.7°$.

Figure 10. - Continued.



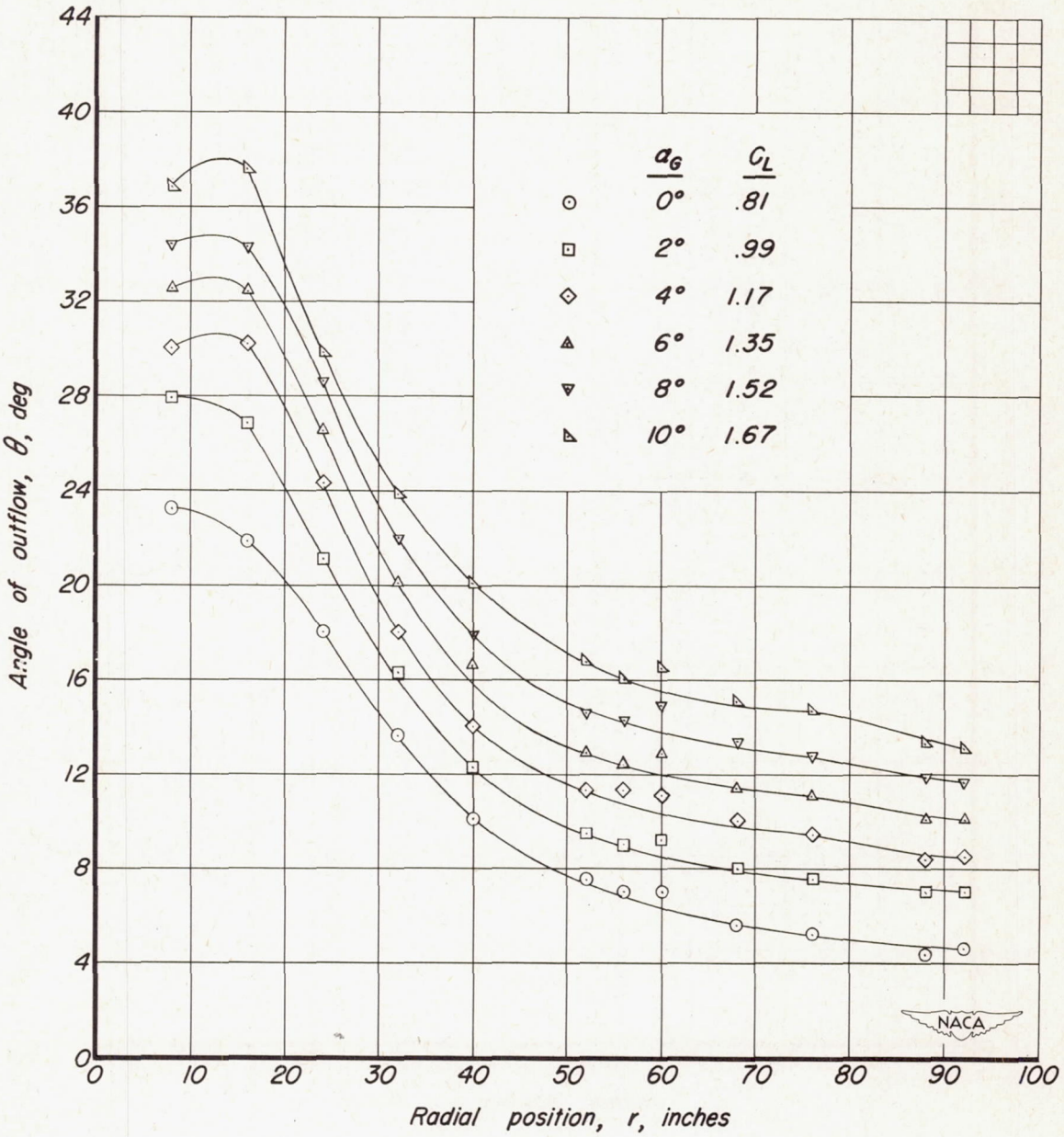
(p) $\Omega = 337.4°$.

Figure 10. - Concluded.



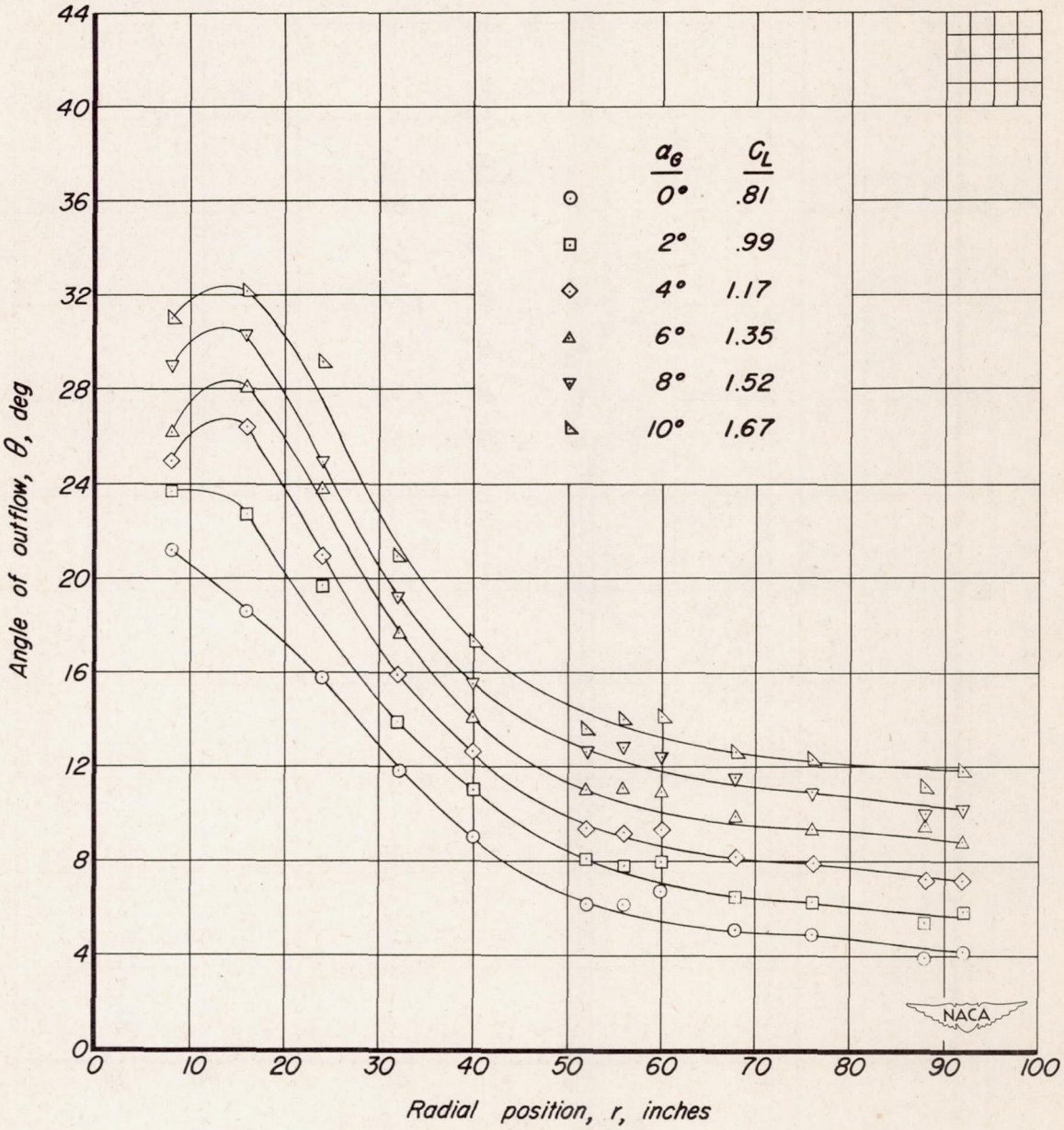
(a) $\Omega = 0.0°$.

Figure 11. - Variation of angle of outflow, θ, with radial position for several angles of attack. m_1/m_0, .29; δ_f, 40°.



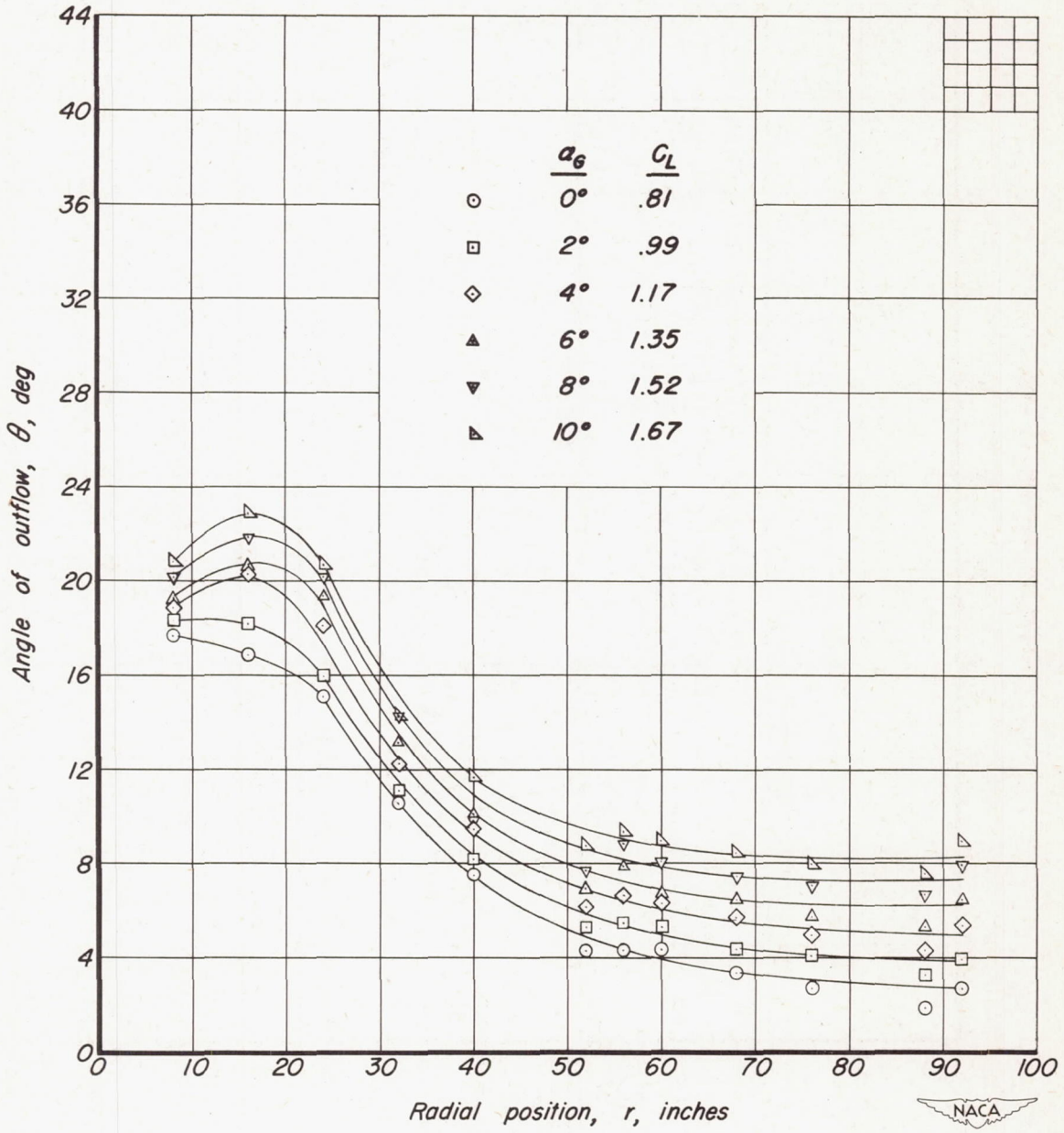
(b) $\Omega = 22.5°$.

Figure 11. - Continued.



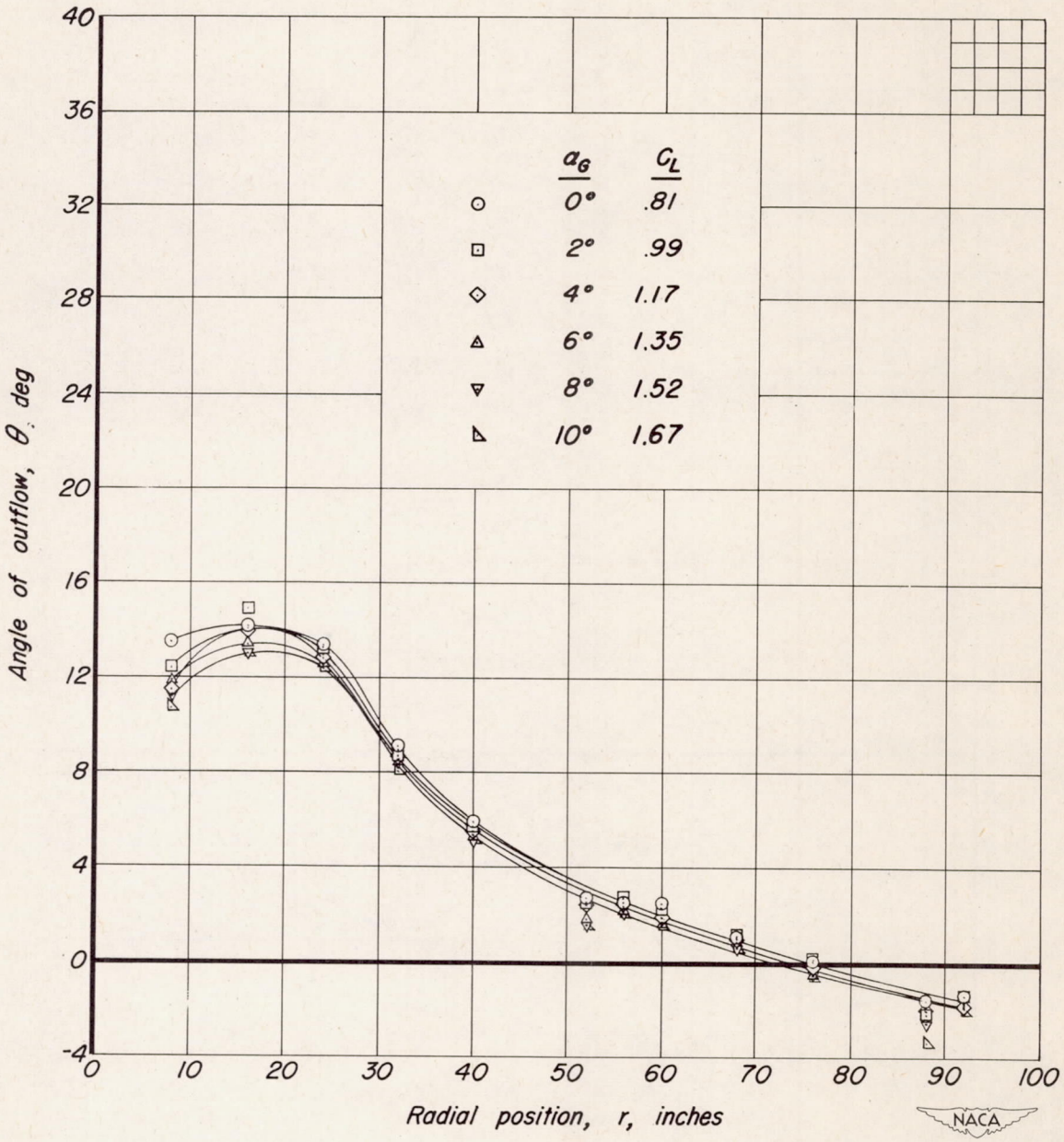
(c) $\Omega = 45.2°$.

Figure 11. - Continued.



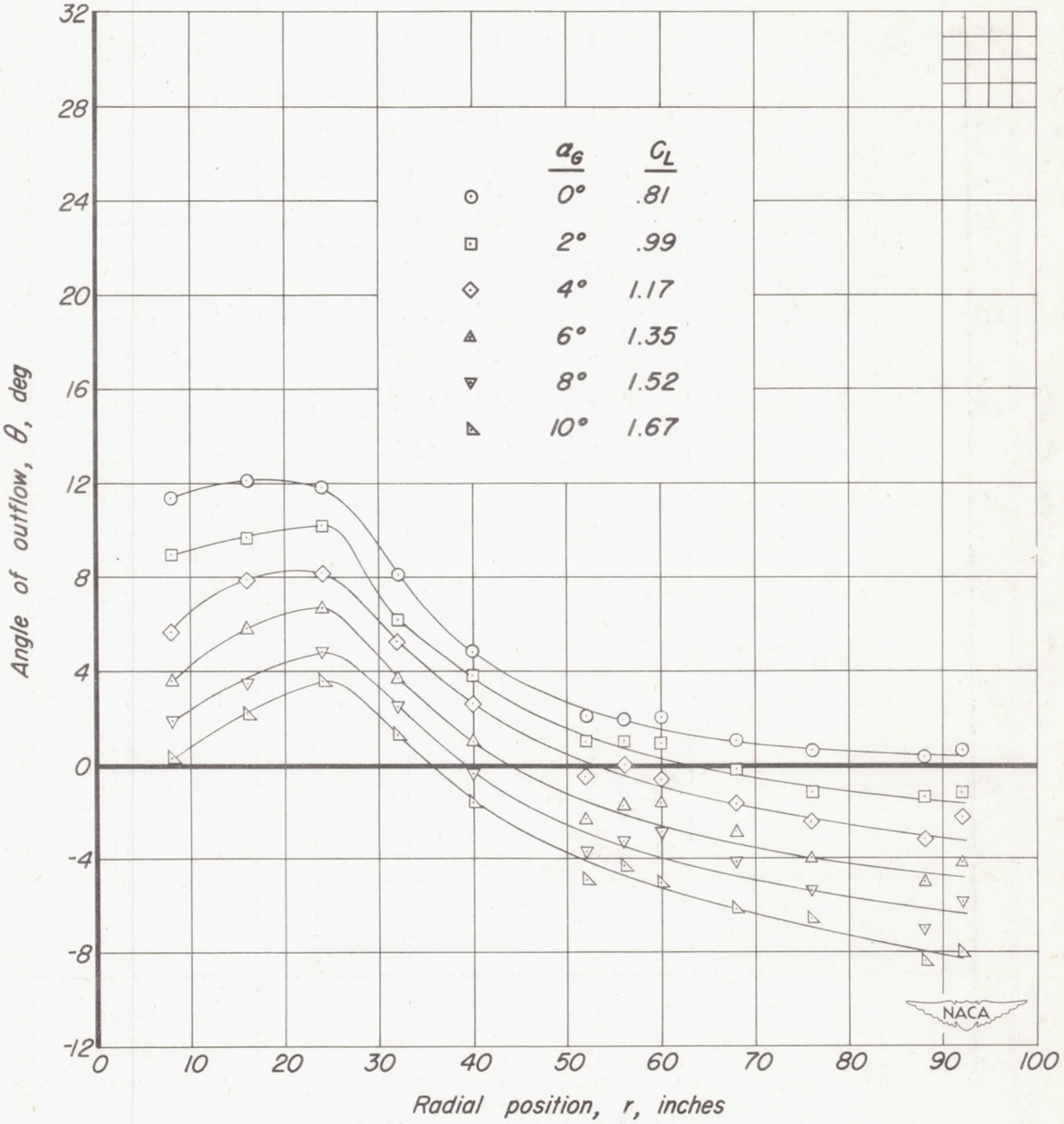
(d) Ω=68.5°.

Figure 11. - Continued.



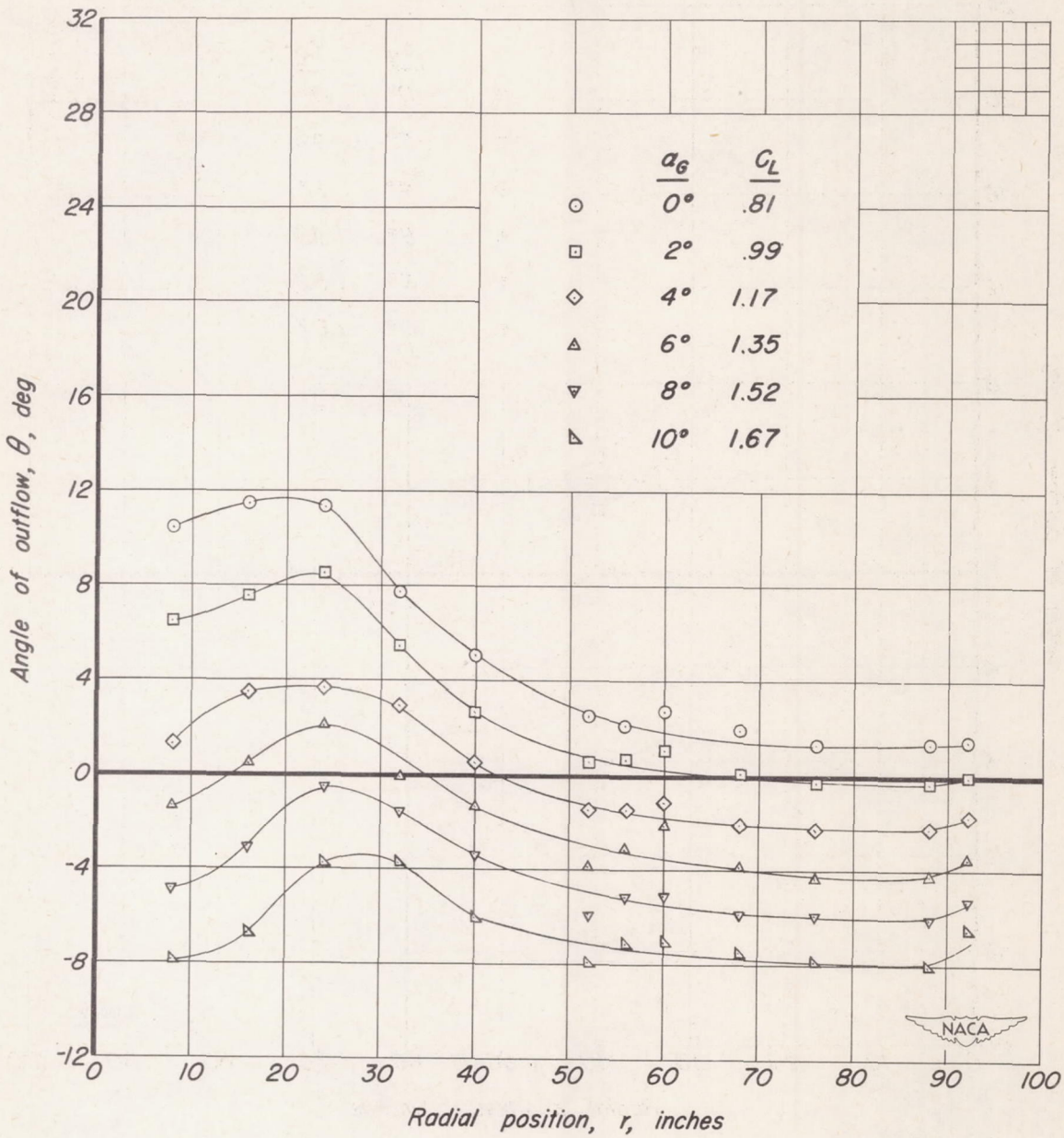
(e) $\Omega = 91.1°$.

Figure 11. - Continued.



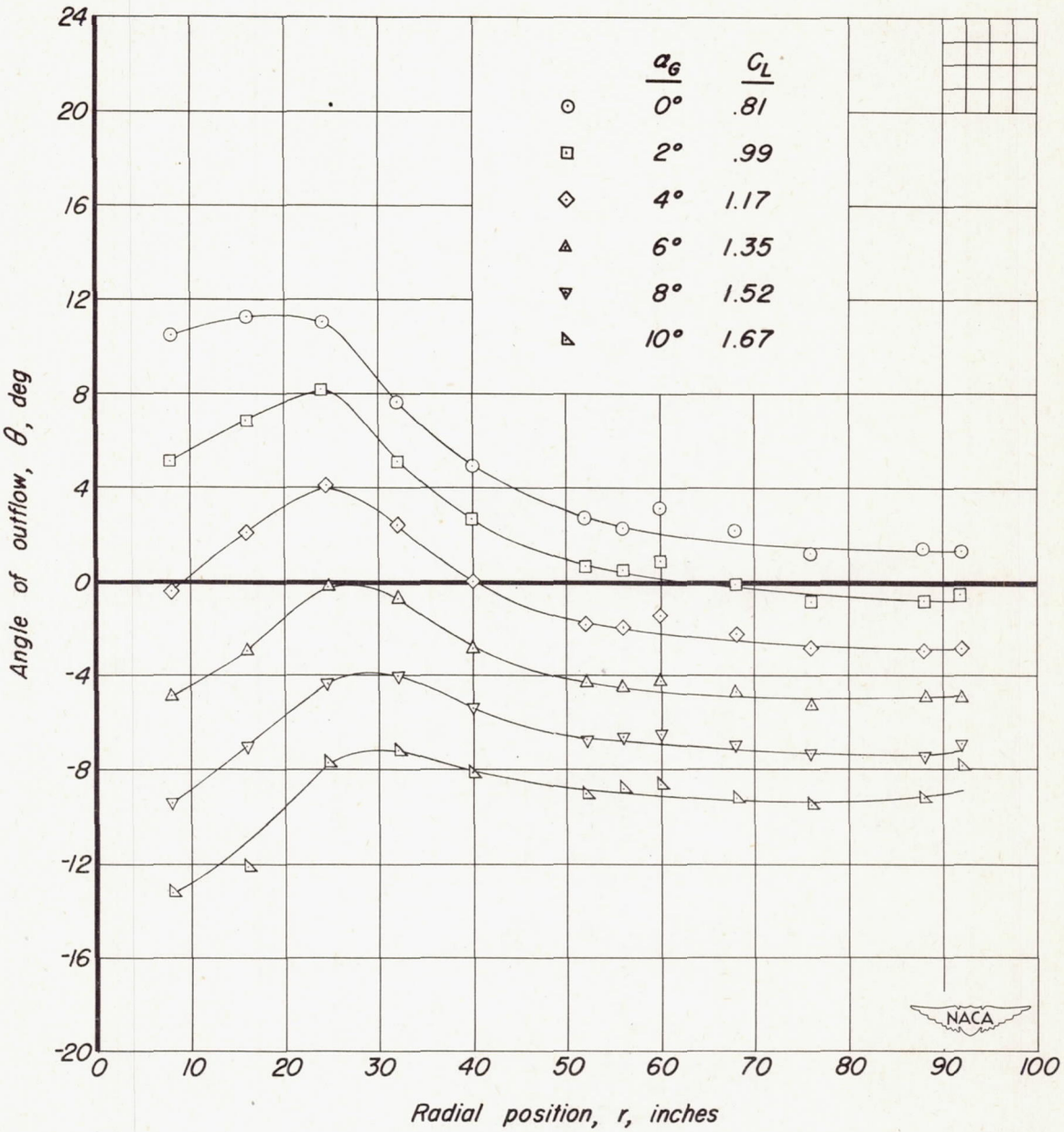
(f) Ω=113.4°.

Figure 11. - Continued.



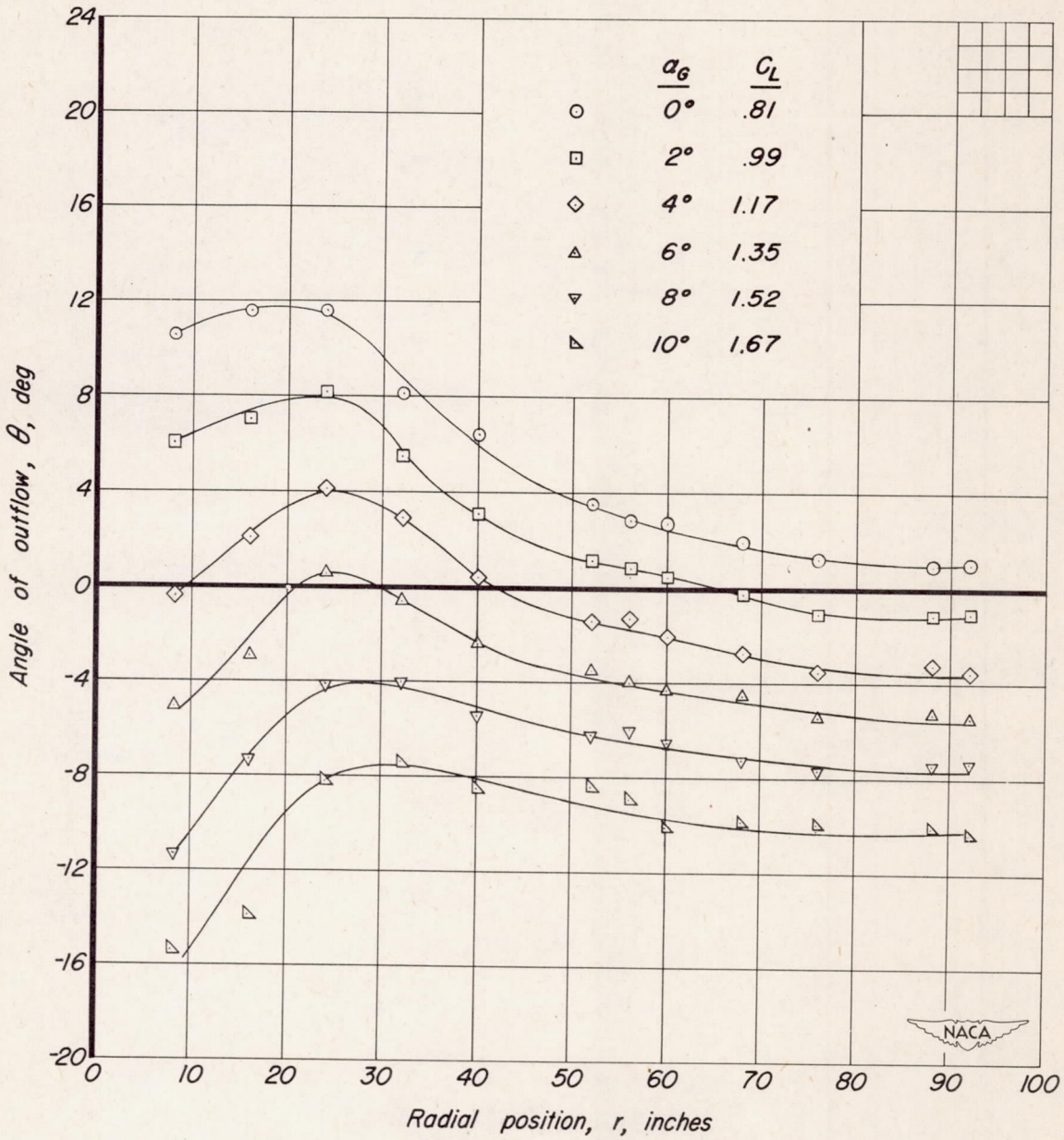
(g) Ω=135.7°.

Figure 11. - Continued.



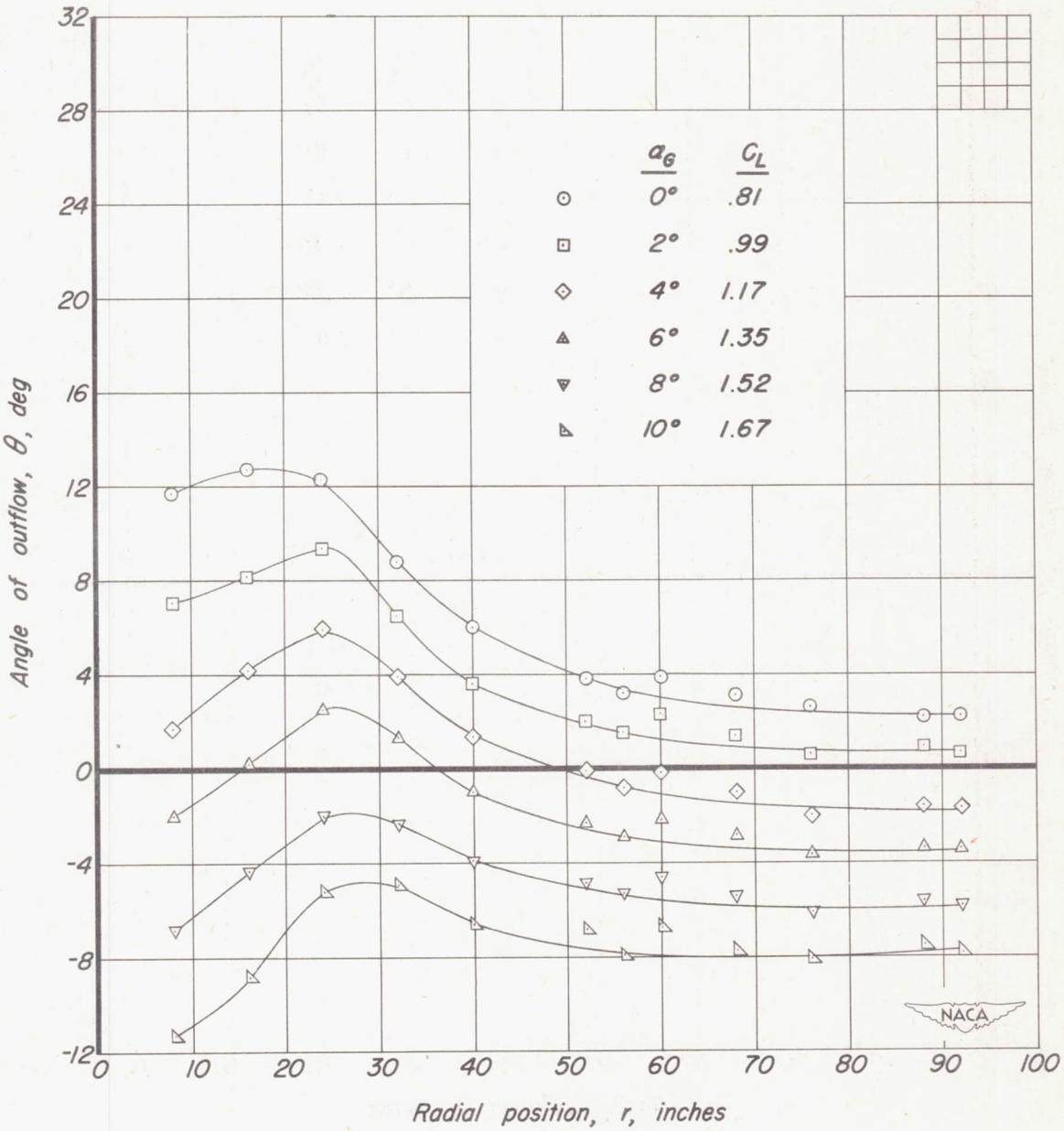
(h) $\Omega = 158.2°$.

Figure 11. - Continued.



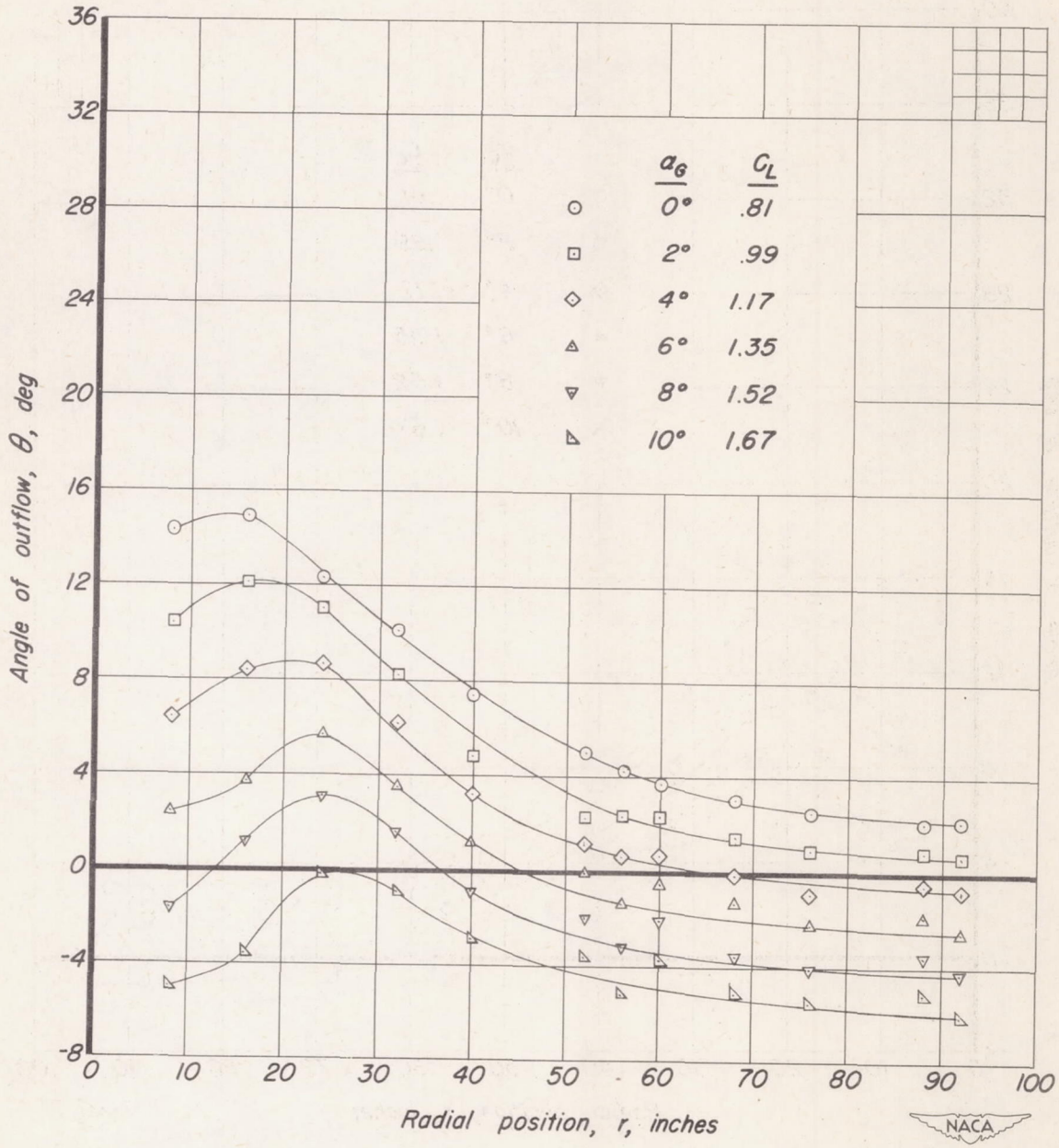
(i) $\Omega = 180.6°$.

Figure 11. - Continued.



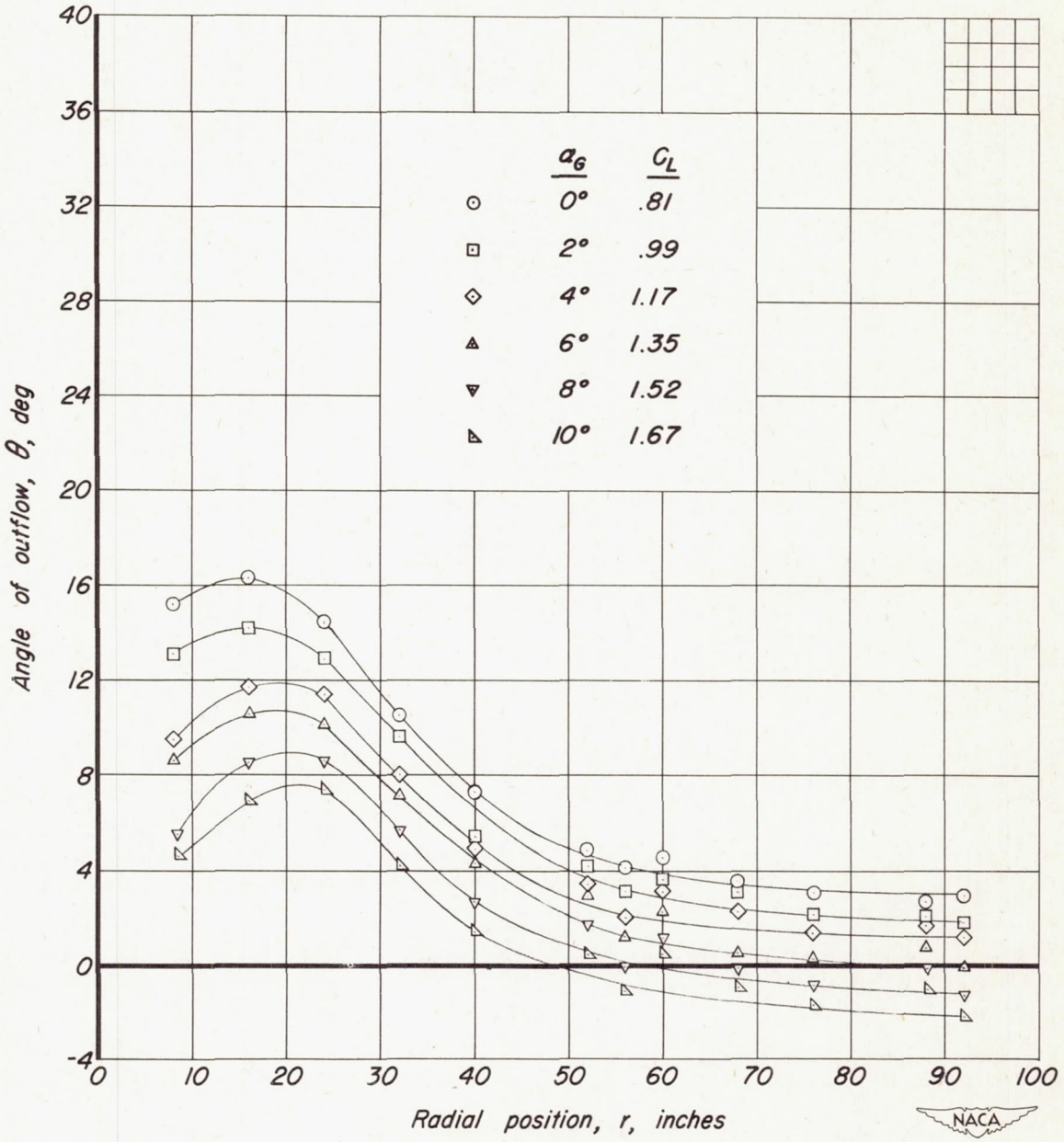
(j) Ω=203.0°.

Figure 11. - Continued.



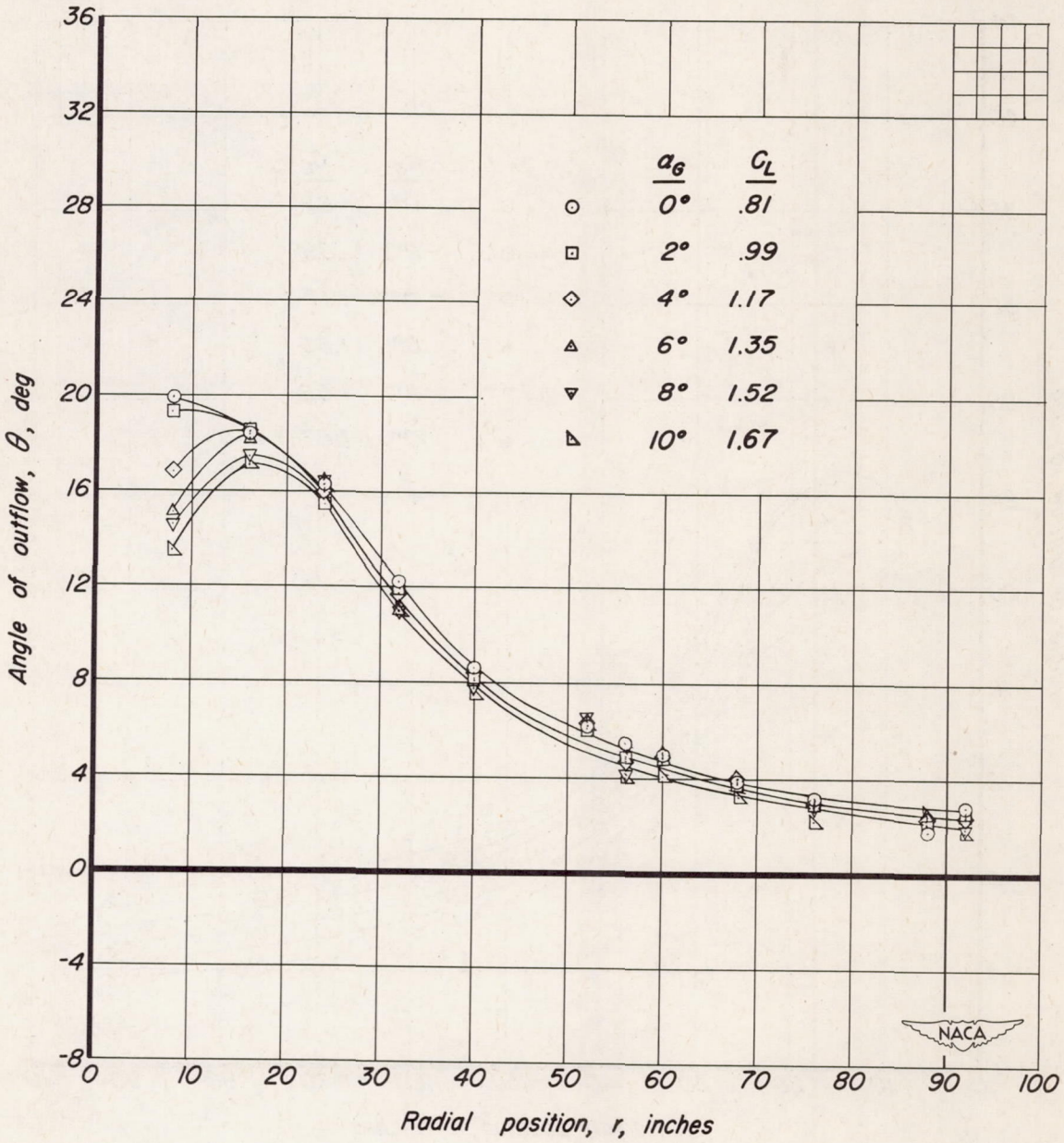
(k) $\Omega = 225.6°$.

Figure 11. - Continued.



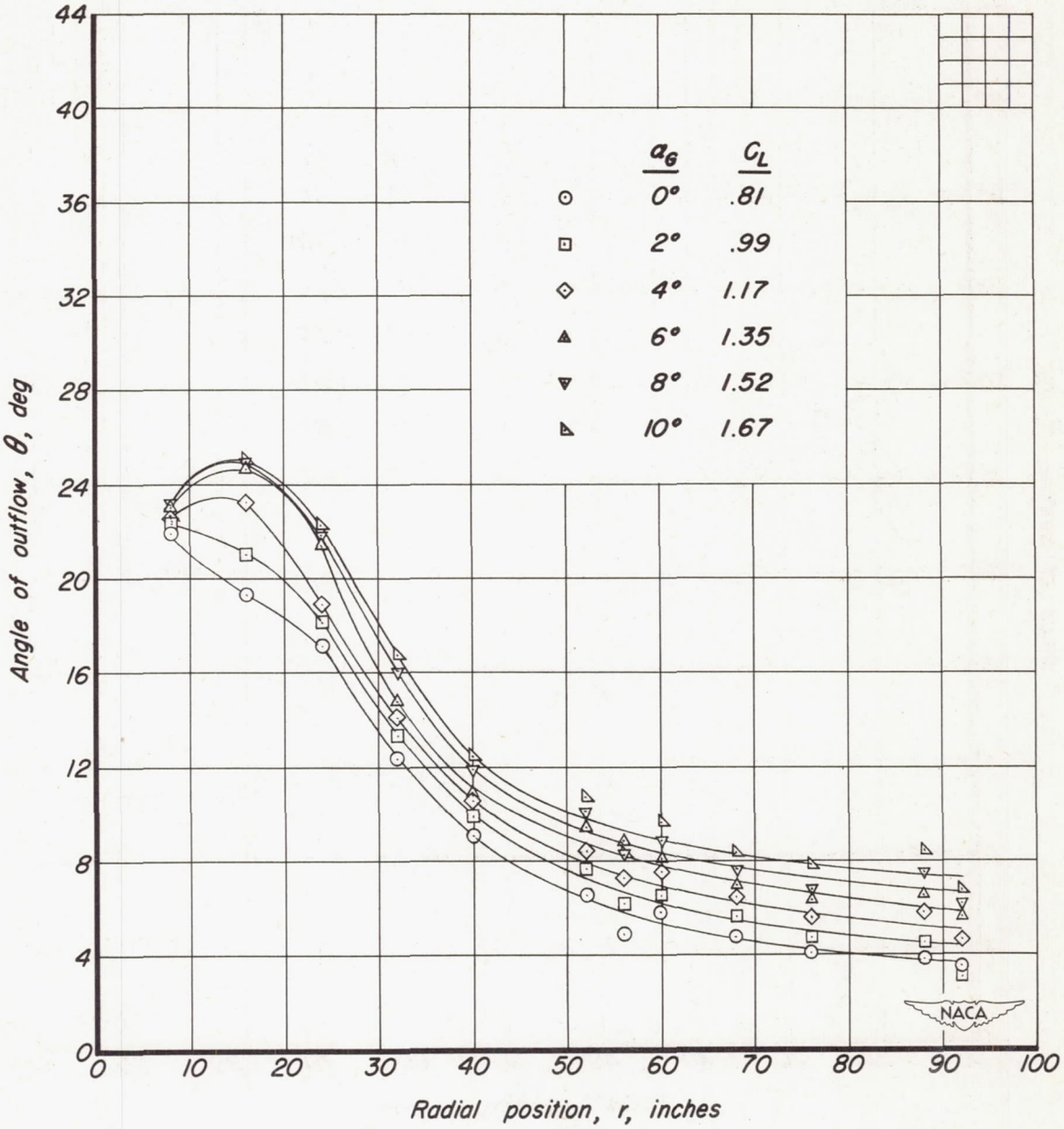
(l) $\Omega = 247.2°$.

Figure 11. - Continued.



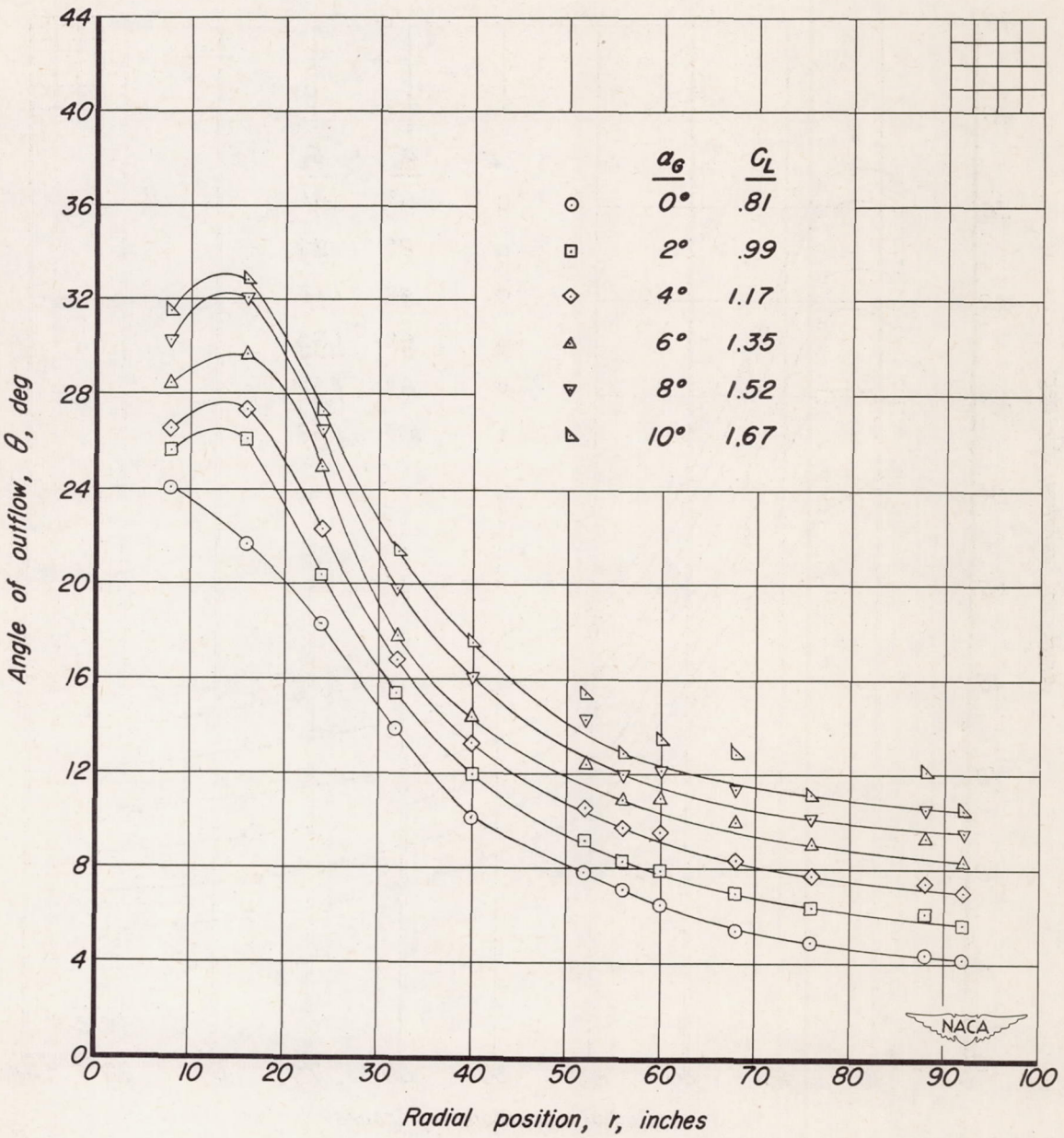
(m) $\Omega = 270.1°$.

Figure 11. - Continued.



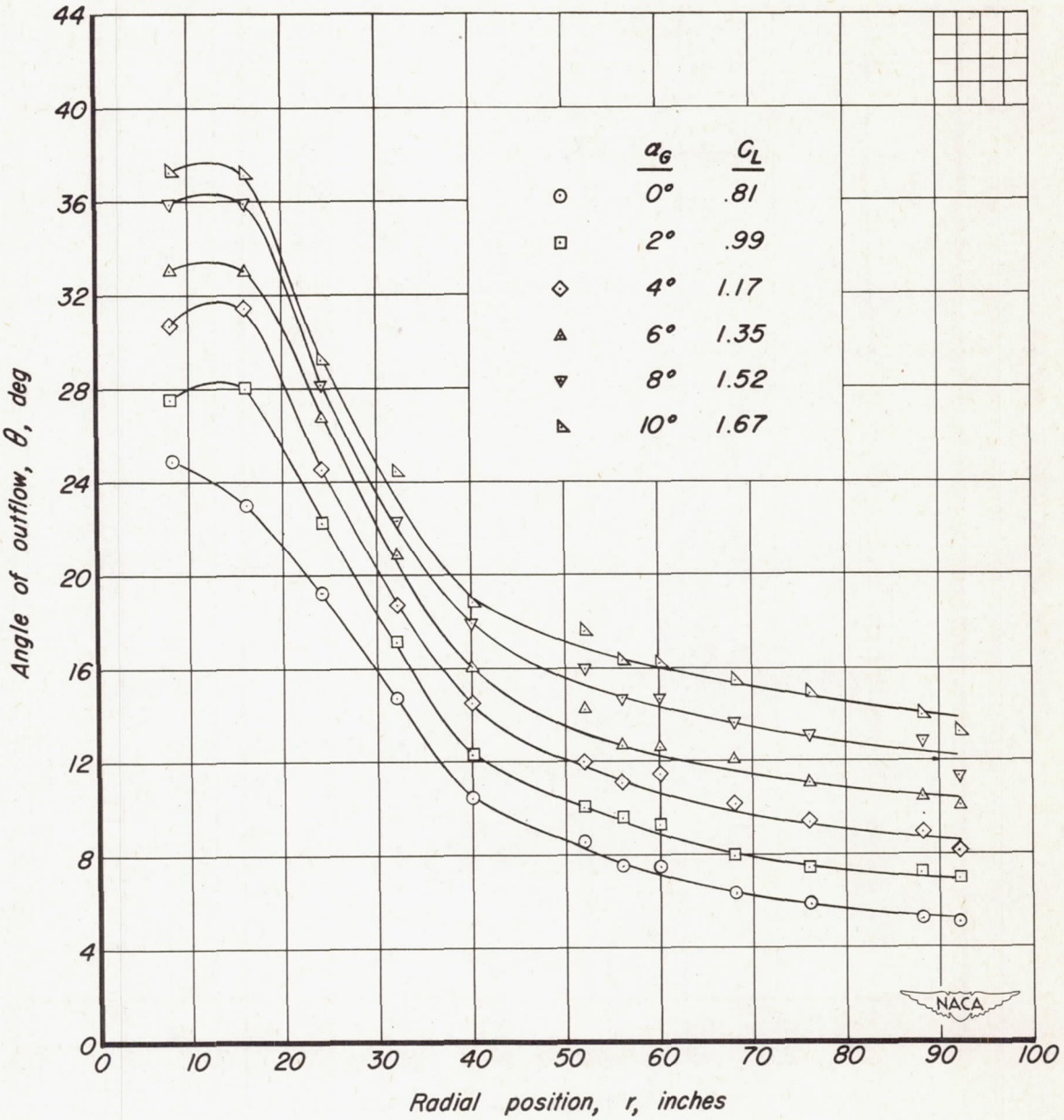
(n) $\Omega = 292.2°$.

Figure 11. - Continued.



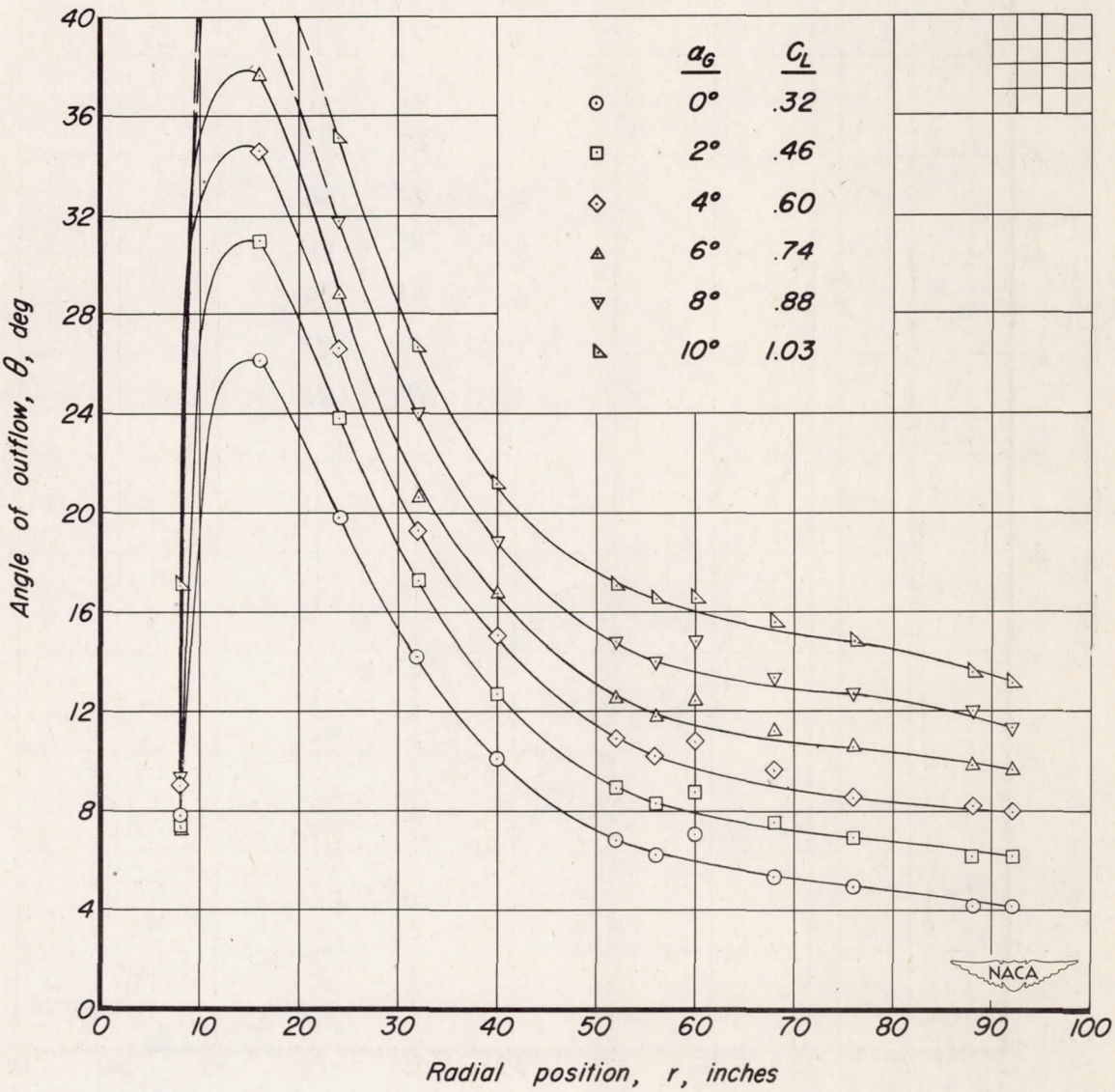
(o) $\Omega = 314.7°$.

Figure 11. - Continued.



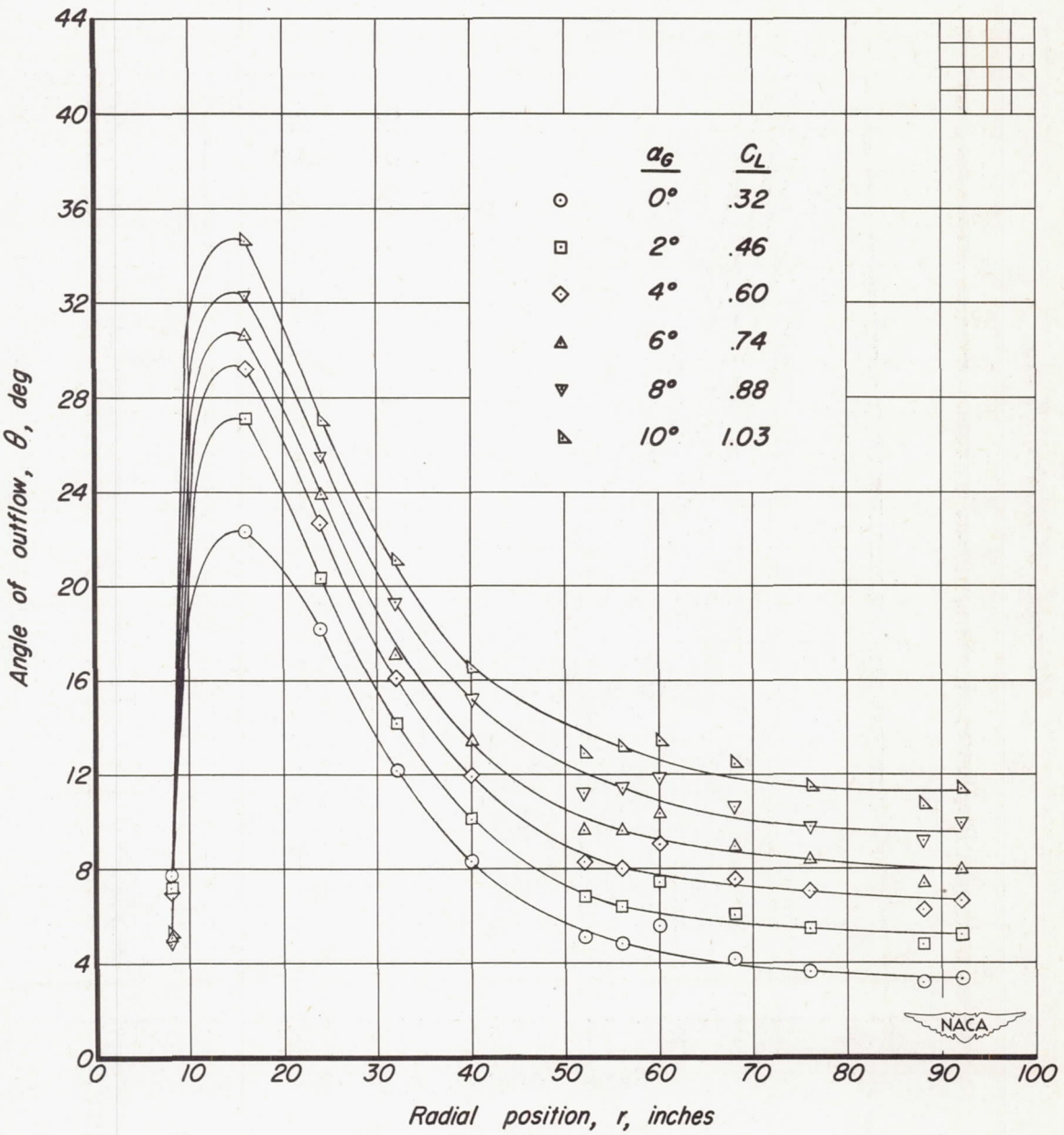
(p) $\Omega = 337.4°$.

Figure 11. - Concluded.



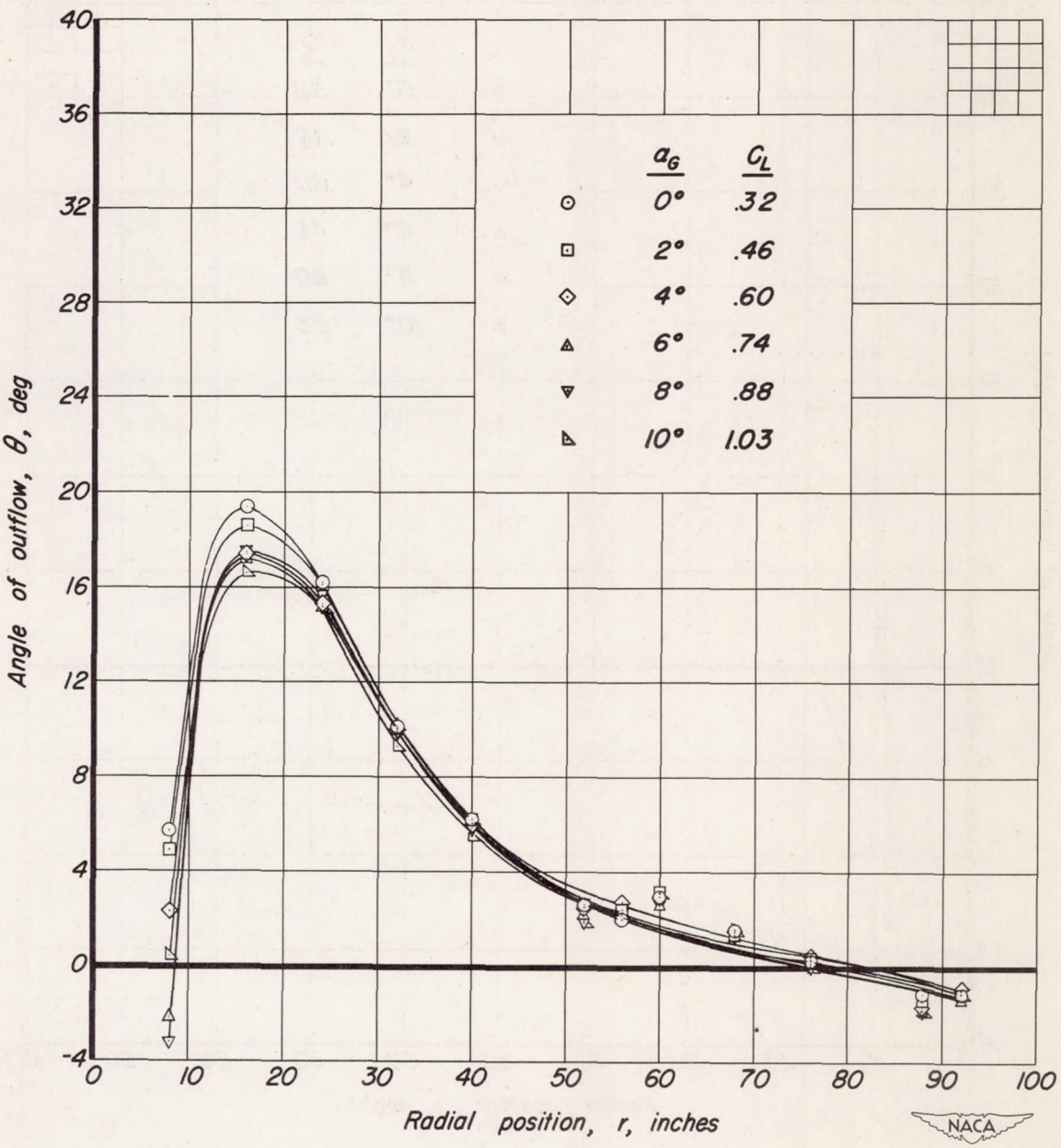
(a) $\Omega = 359.8°$.

Figure 12. - Variation of angle of outflow, θ, with radial position for several angles of attack. m_1/m_0, .14; δ_f, 0°.



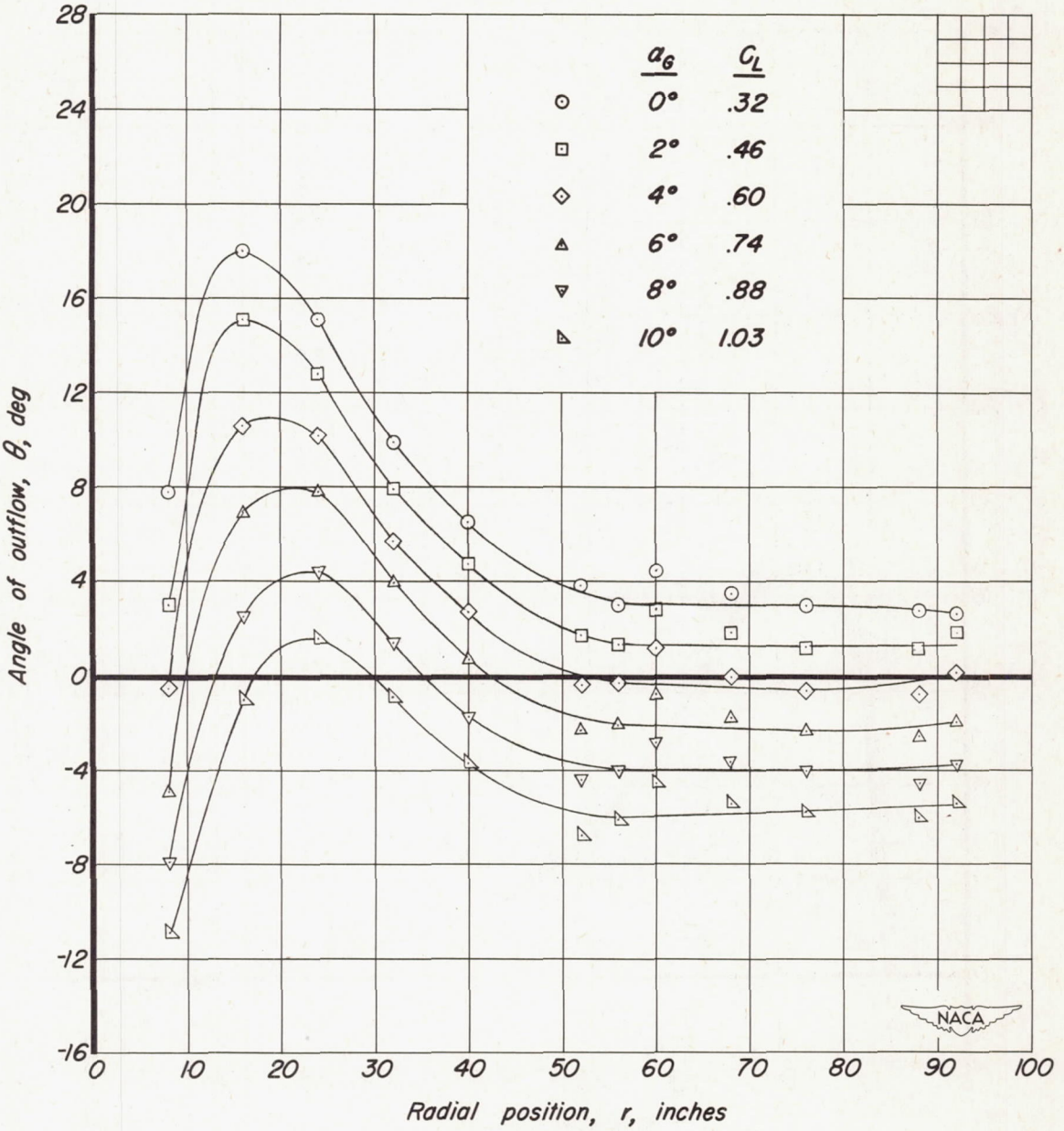
(b) $\Omega = 45.3°$.

Figure 12. - Continued.



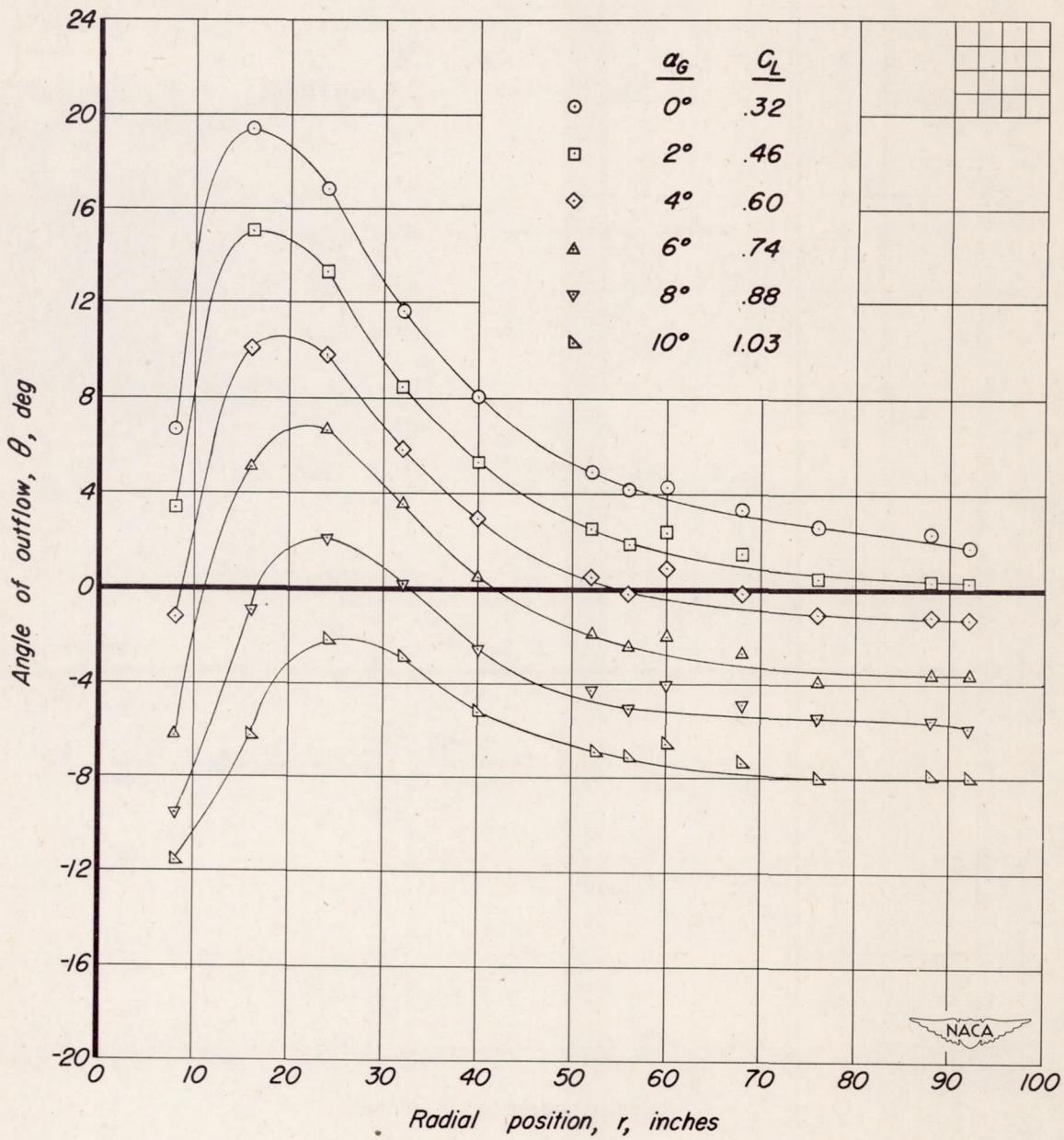
(c) $\Omega = 90.6°$.

Figure 12. - Continued.



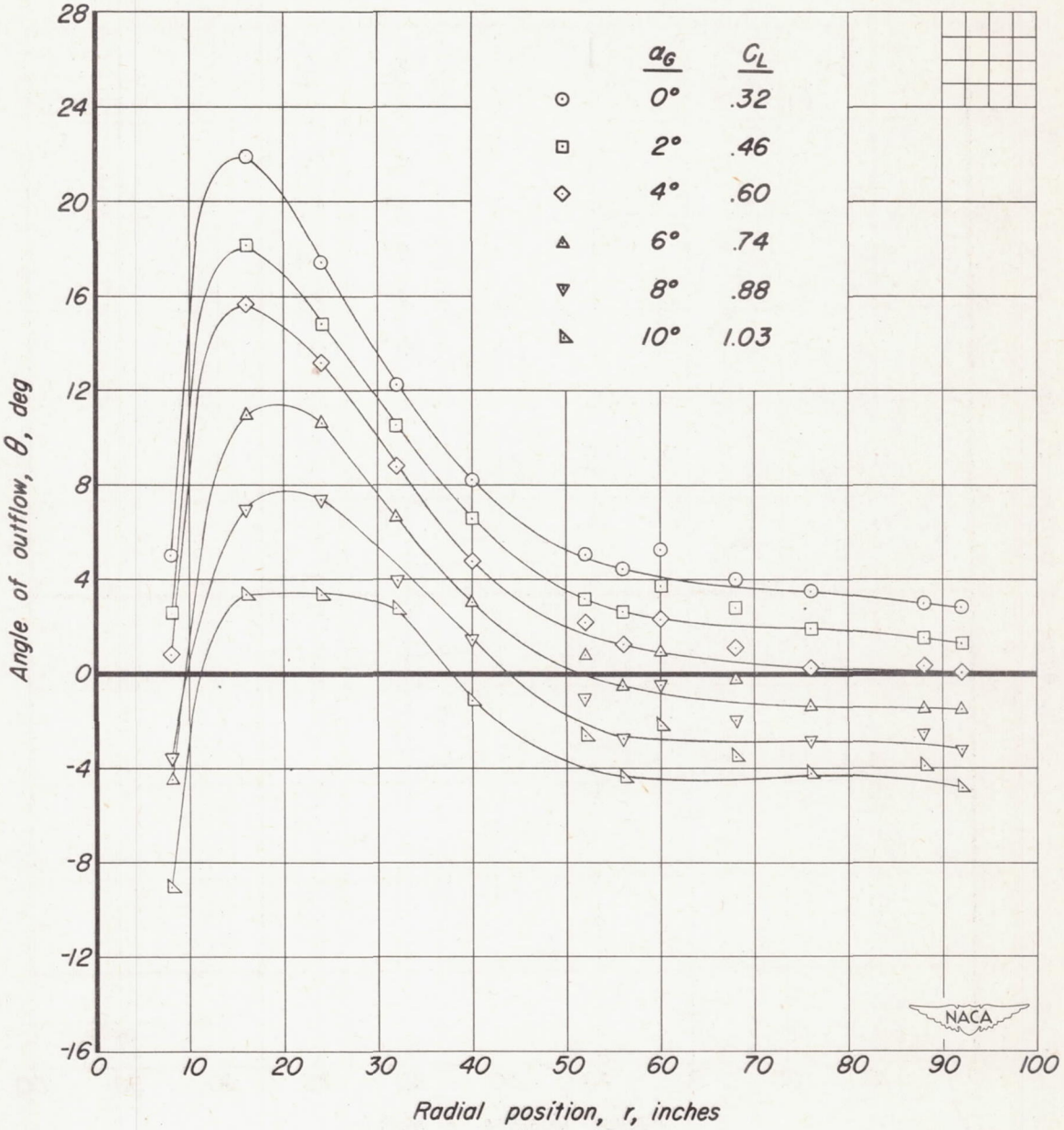
(d) $\Omega = 135.6°$.

Figure 12. - Continued.



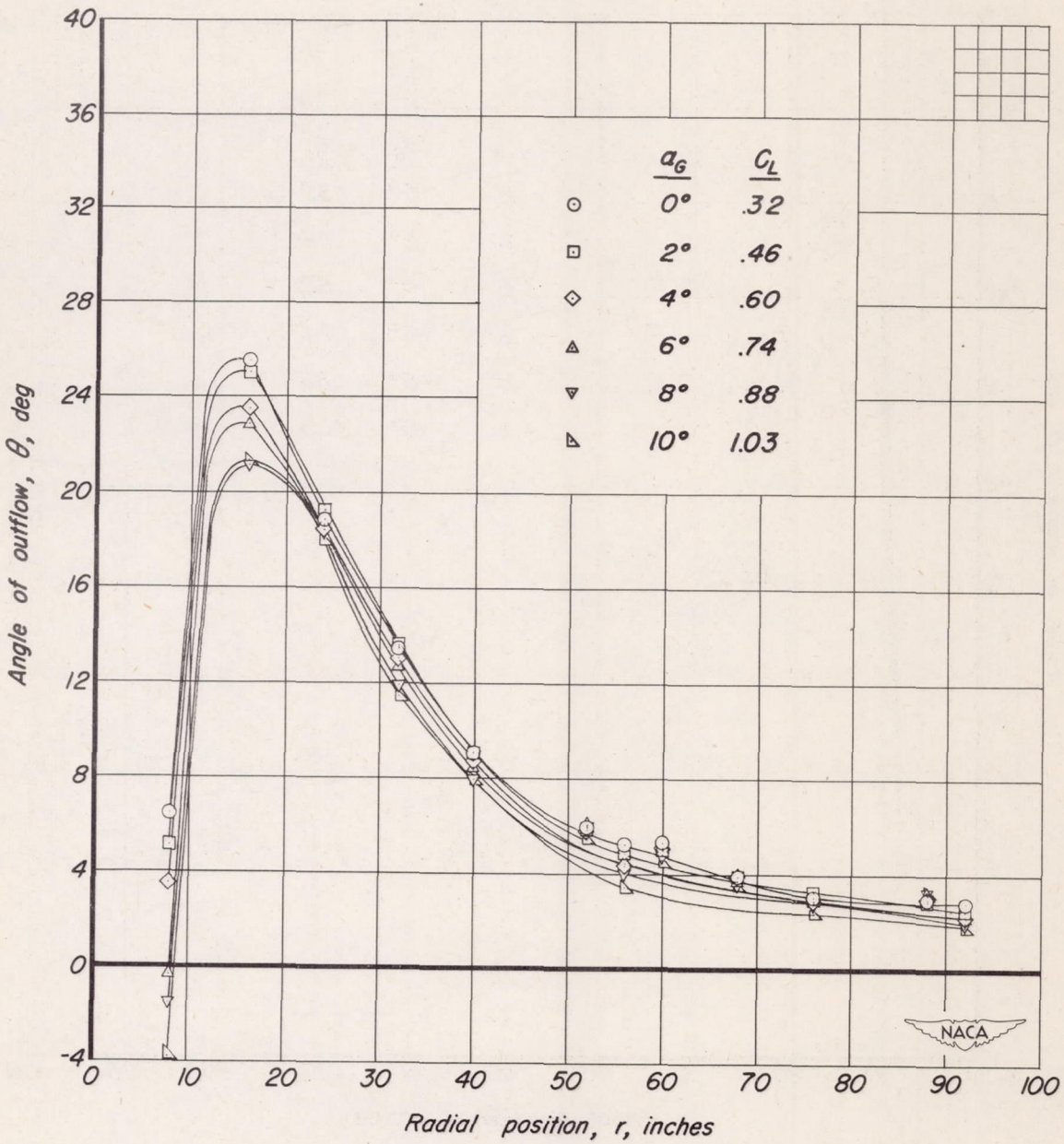
(e) $\Omega = 180.0°$.

Figure 12. - Continued.



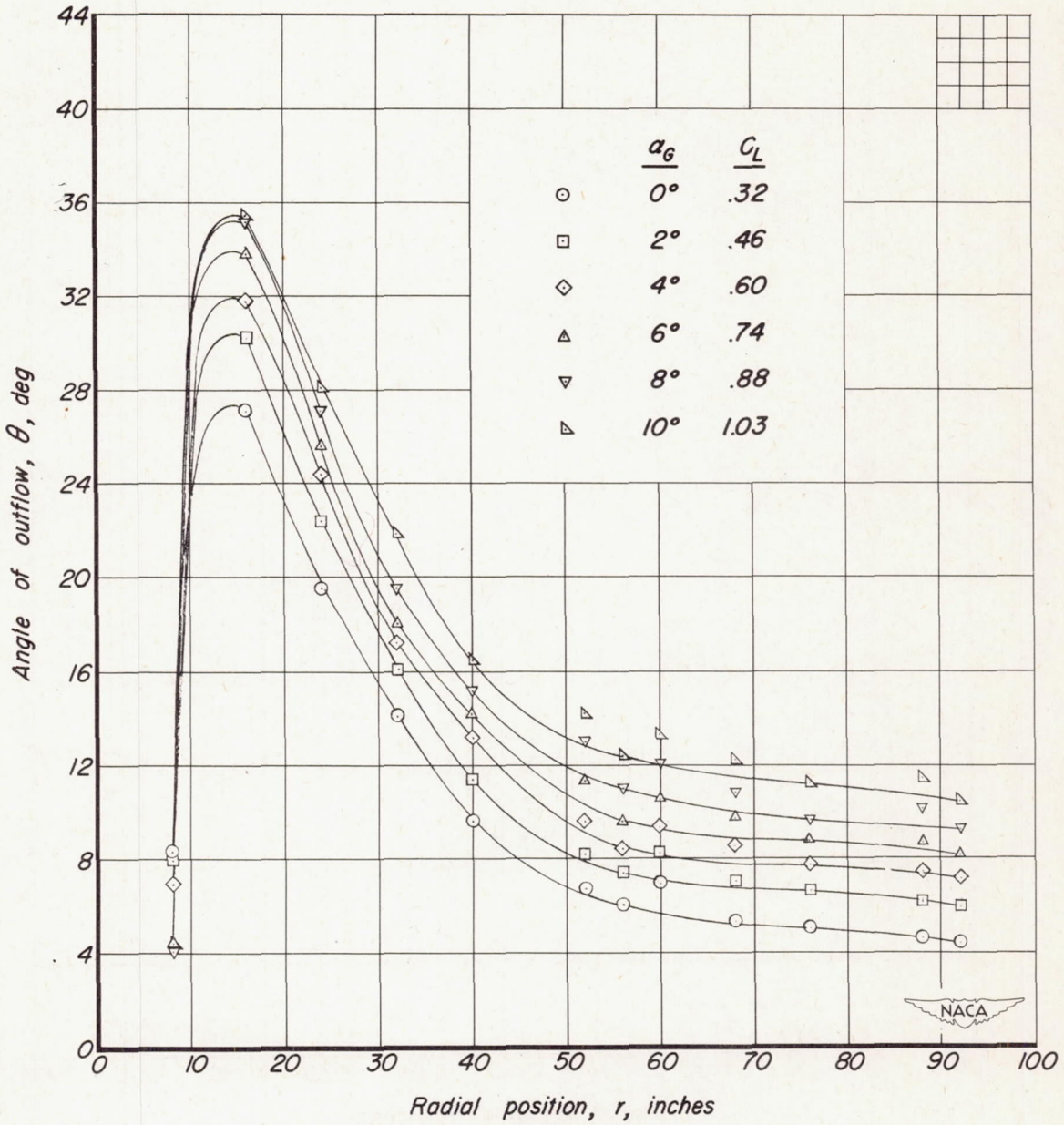
(f) $\Omega = 225.0°$.

Figure 12. - Continued.



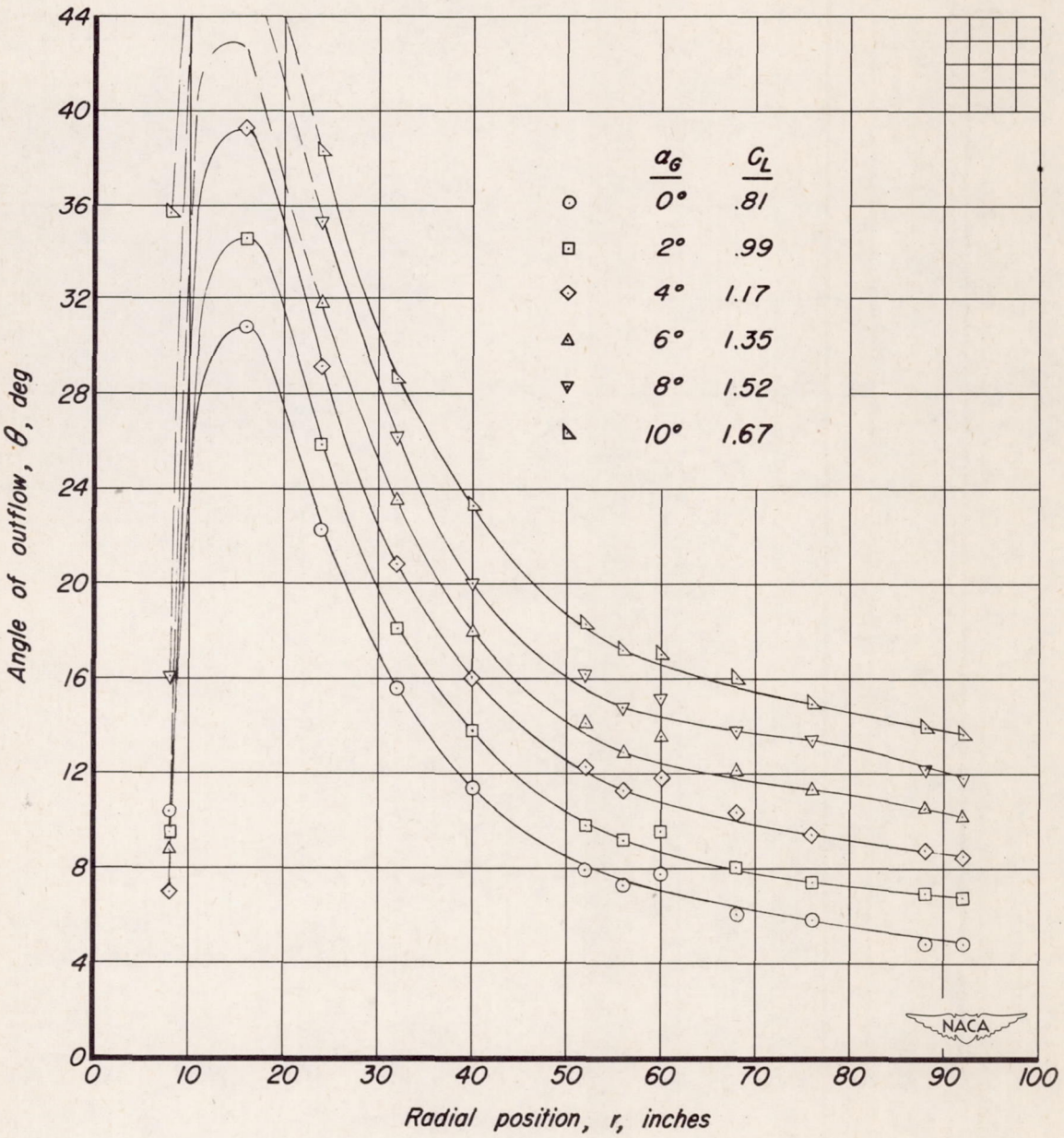
(g) Ω=269.8°.

Figure 12. - Continued.



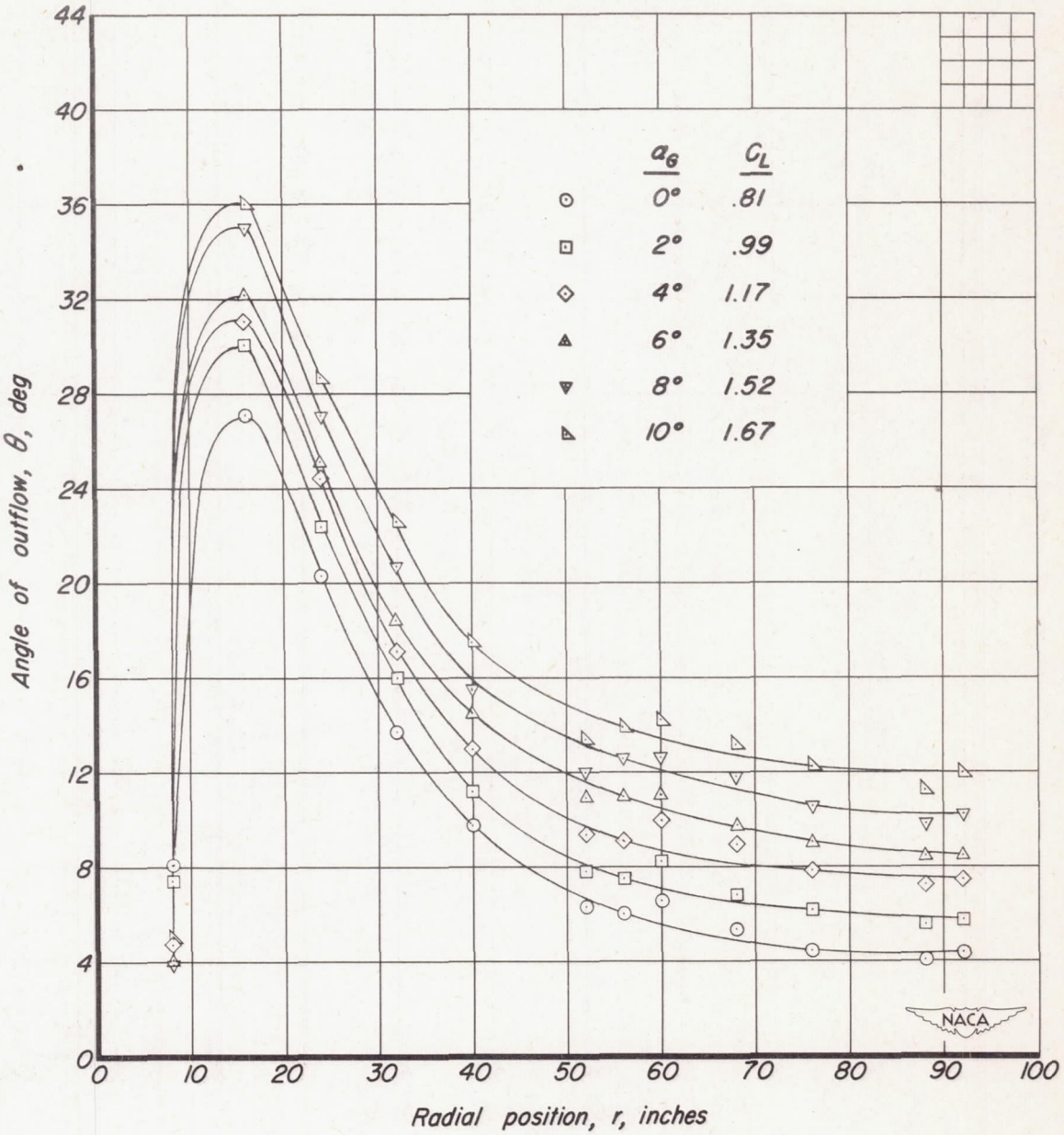
(h) $\Omega = 314.9°$.

Figure 12. - Concluded.



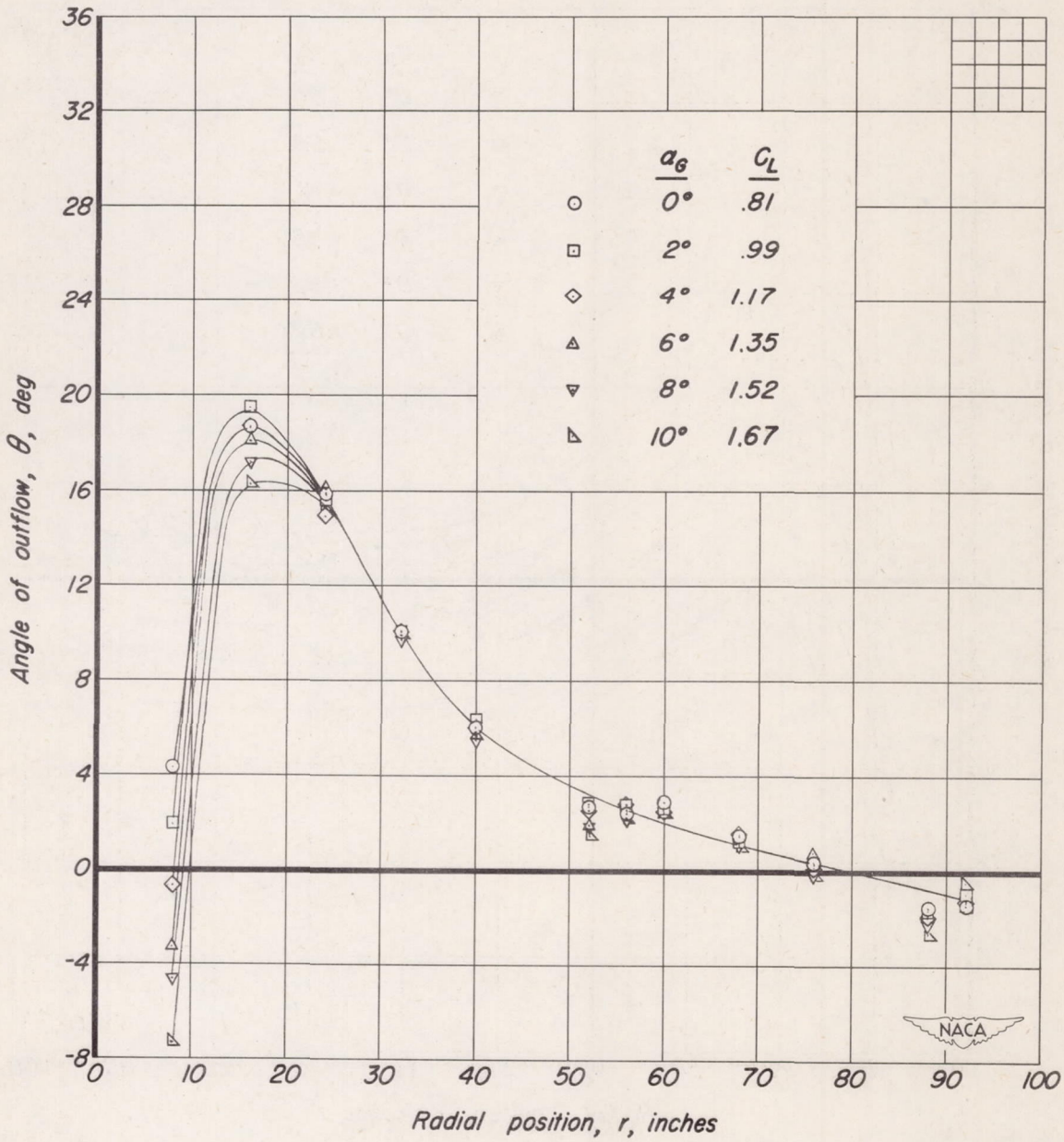
(a) $\Omega = 359.8°$.

Figure 13. - Variation of angle of outflow, θ, with radial position for several angles of attack. m_1/m_0, .14; δ_f, 40°.



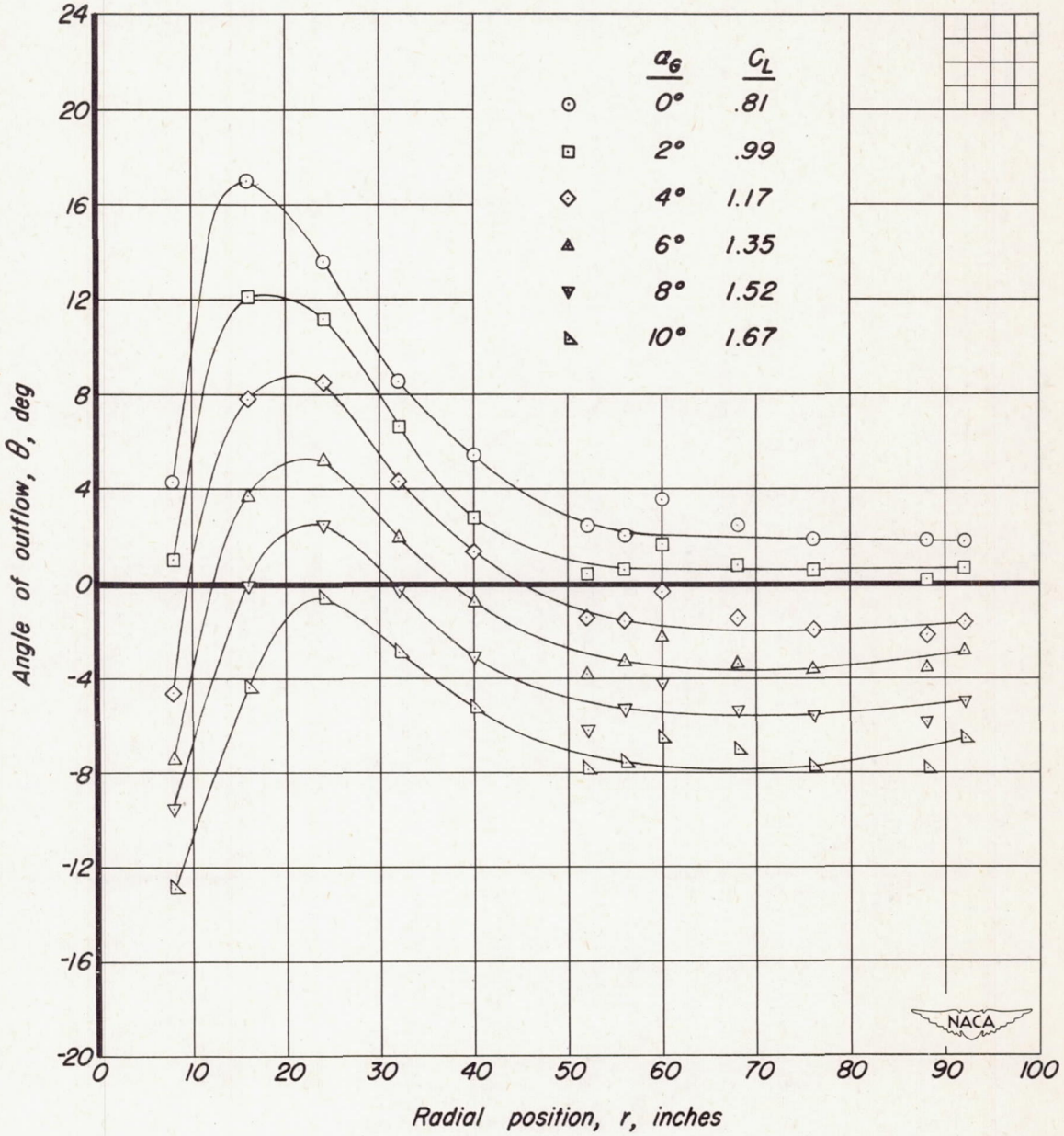
(b) $\Omega = 45.3°$.

Figure 13. - Continued.



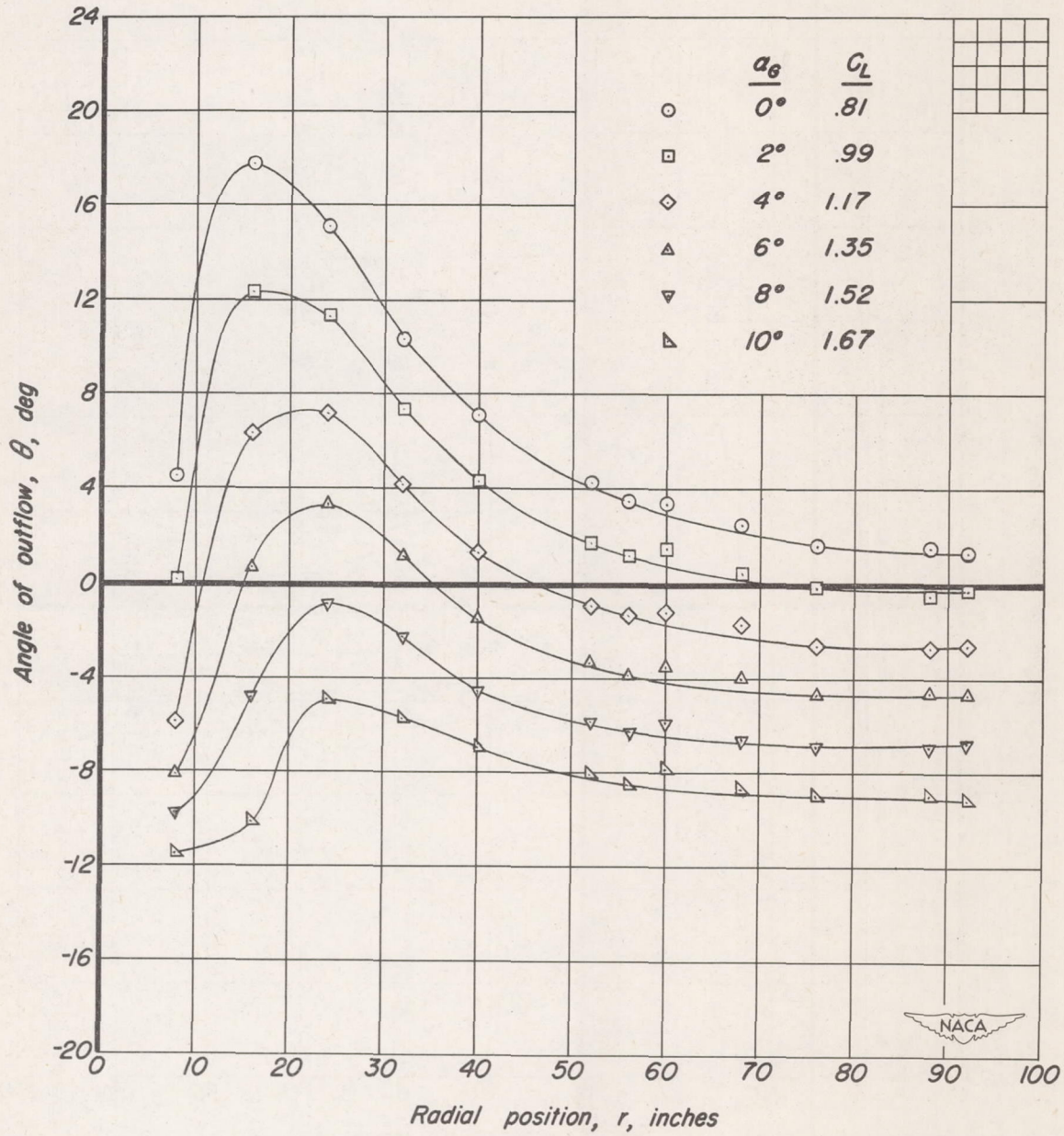
(c) $\Omega = 90.6°$.

Figure 13. - Continued.



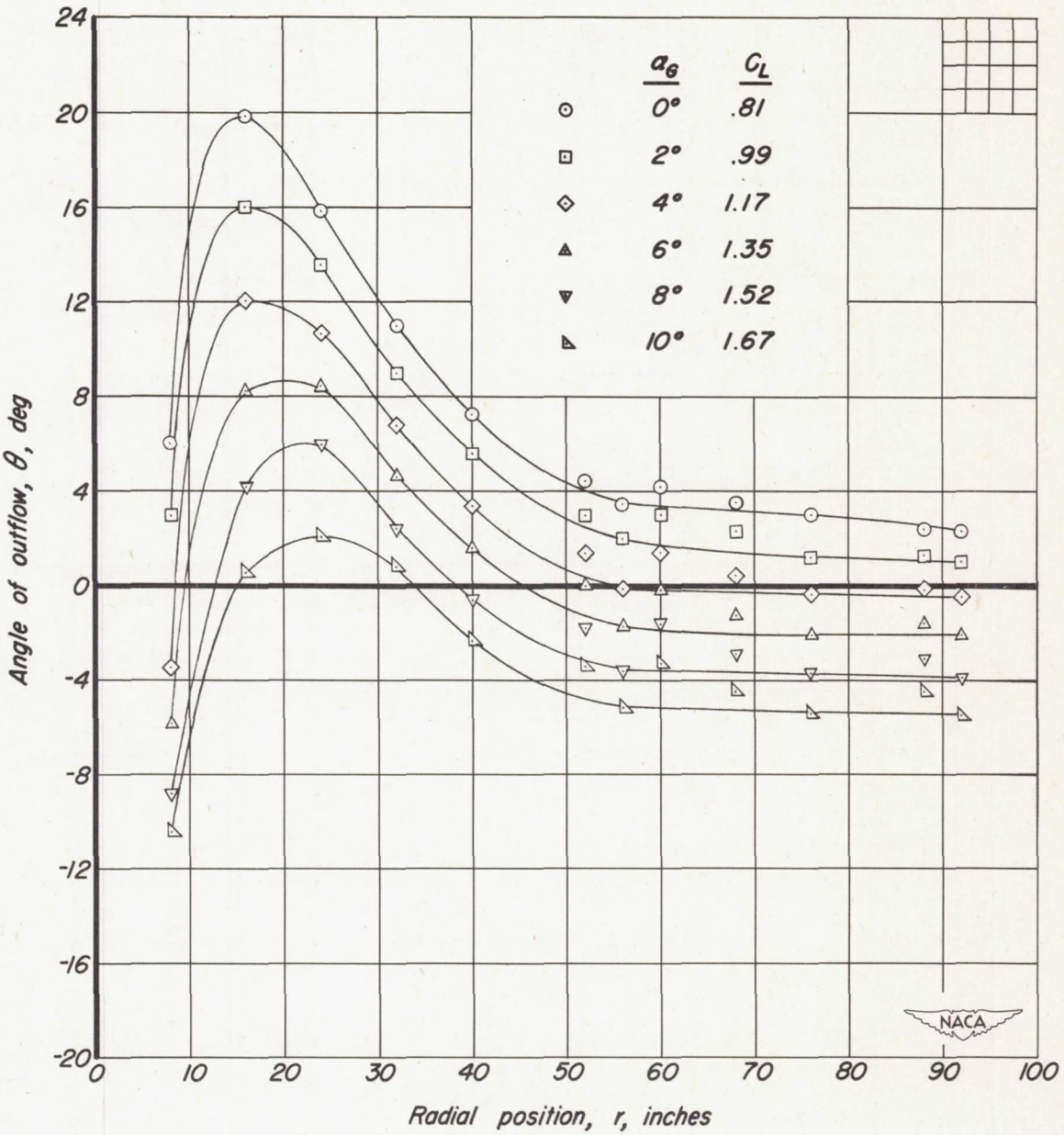
(d) Ω=135.6°.

Figure 13. - Continued.



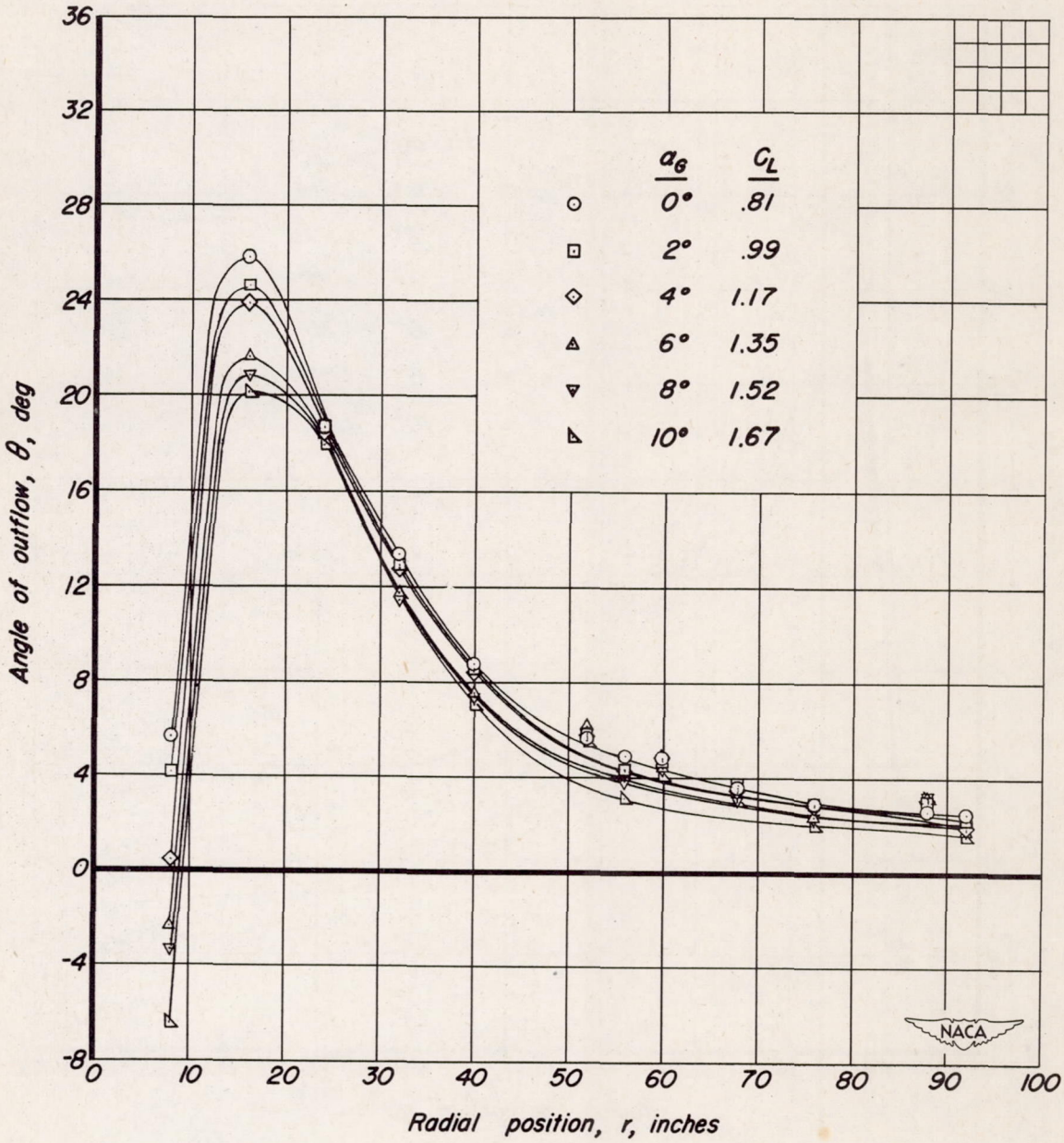
(e) Ω=180.0°.

Figure 13. - Continued.



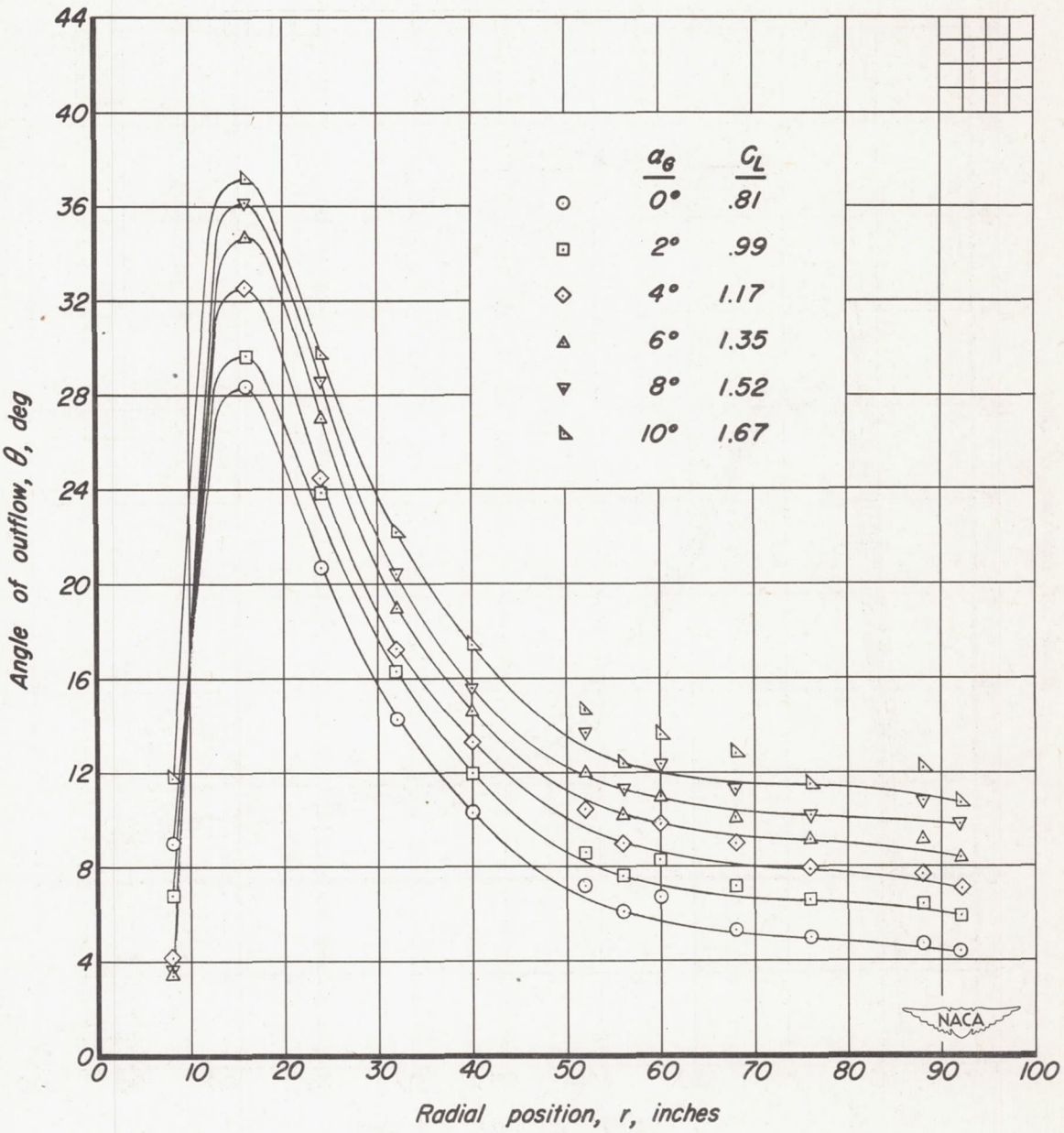
(f) $\Omega = 225.0°$.

Figure 13. - Continued.



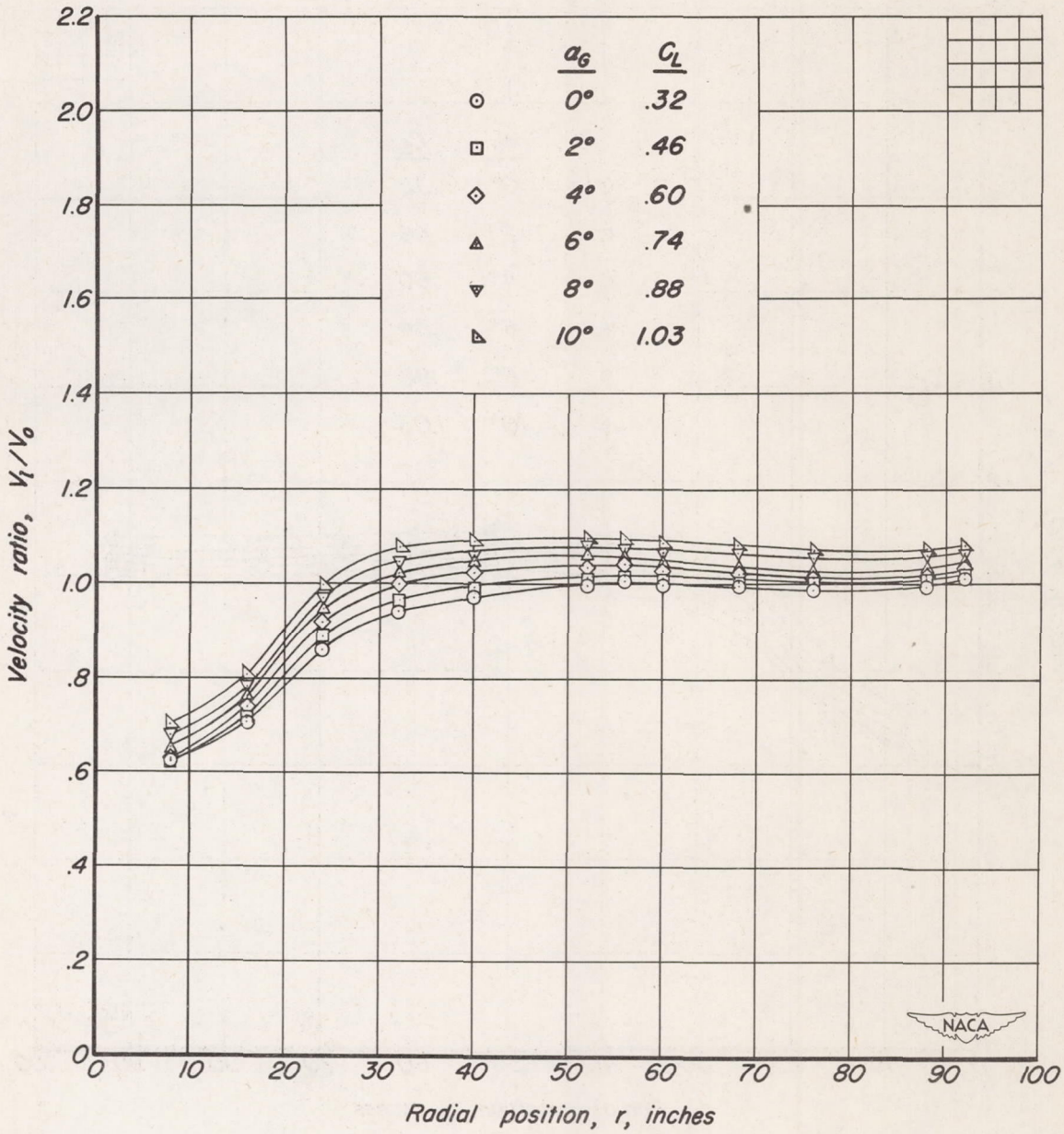
(g) Ω=269.8°.

Figure 13. - Continued.



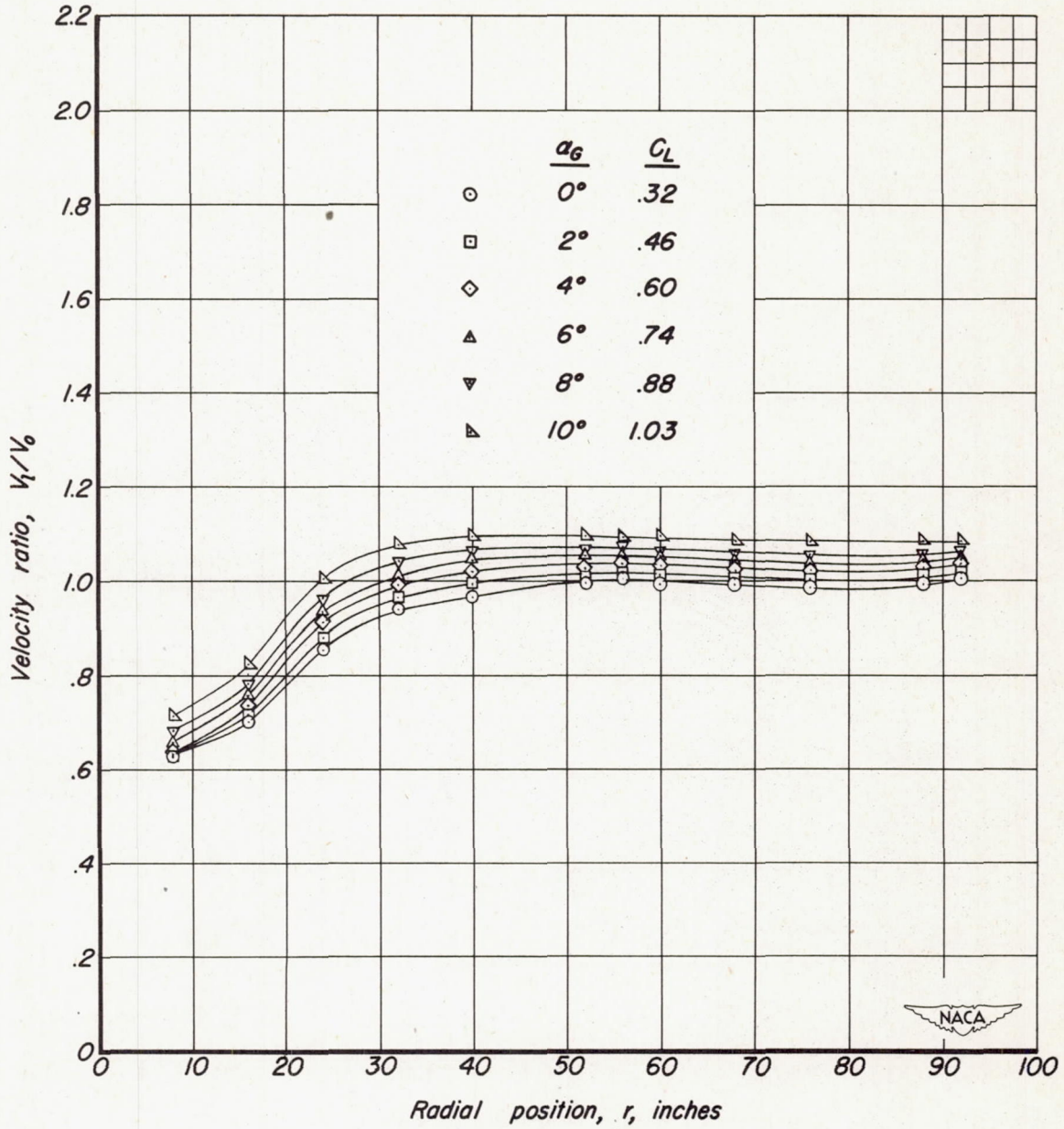
(h) $\Omega = 314.9°$.

Figure 13. - Concluded.



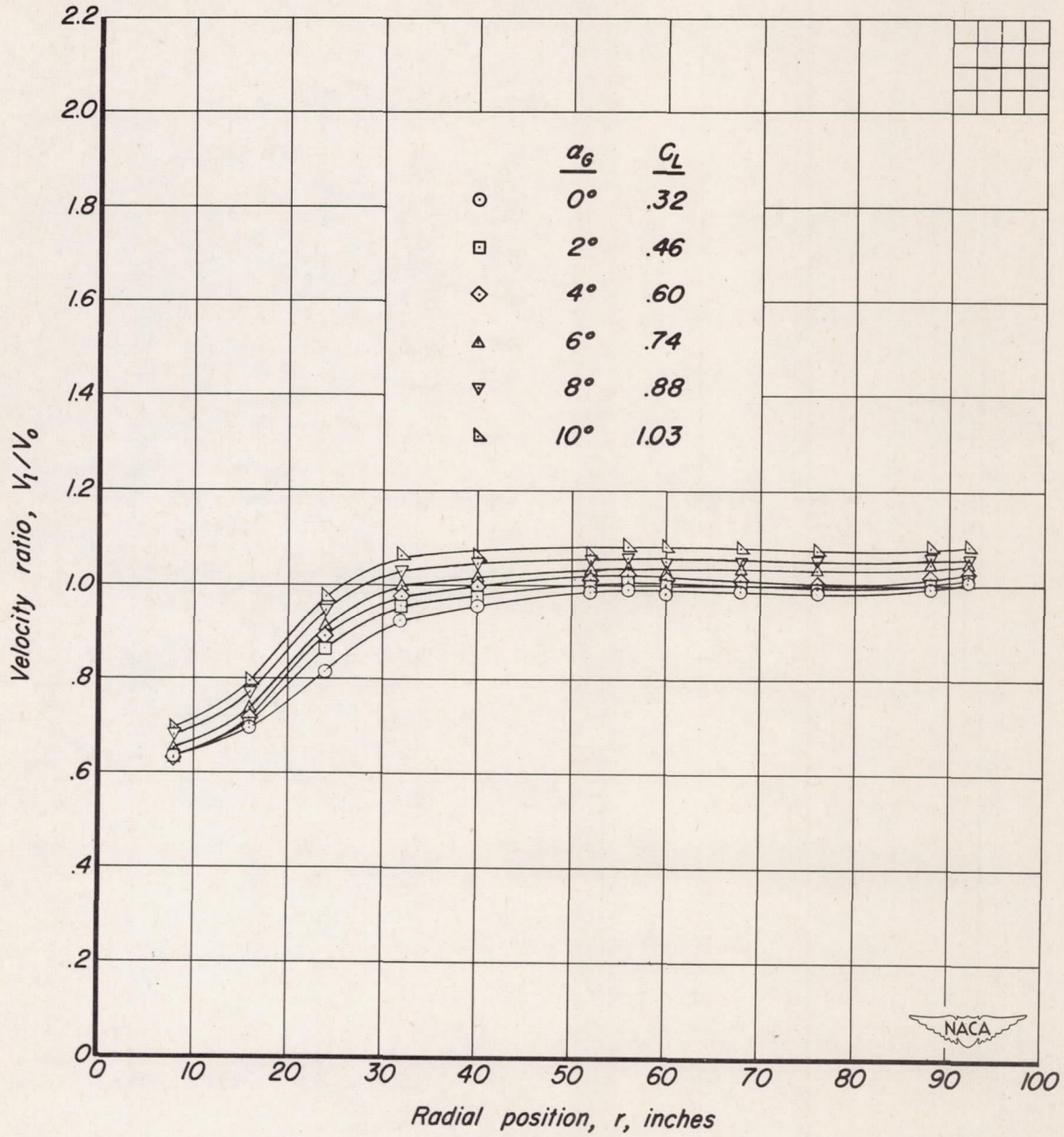
(a) $\Omega = 0.0°$.

Figure 14. – Variation of velocity ratio, V_l/V_o, with radial position for several angles of attack. m_l/m_o, .29; δ_f, 0°.



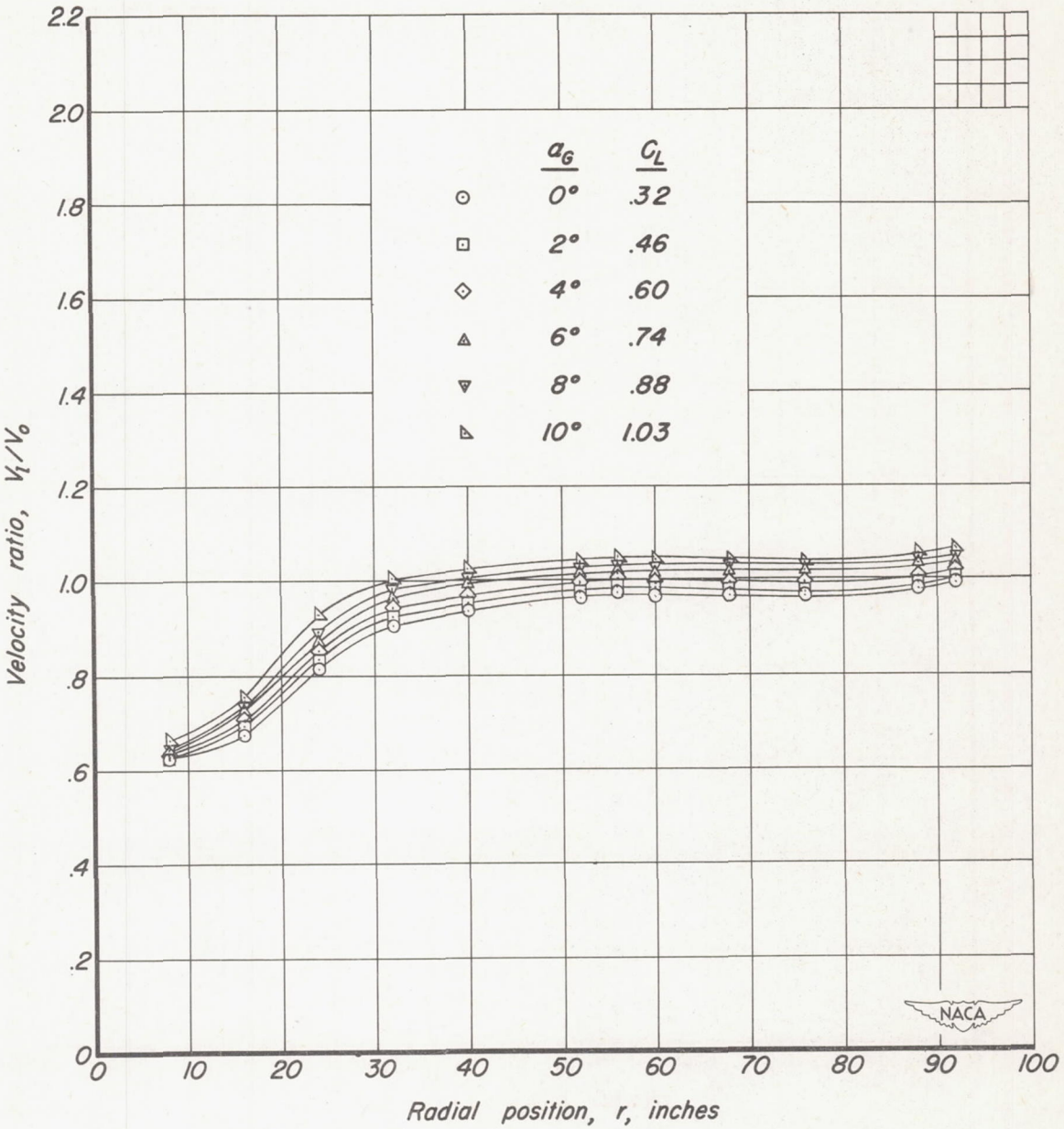
(b) $\Omega = 22.5°$.

Figure 14. – Continued.



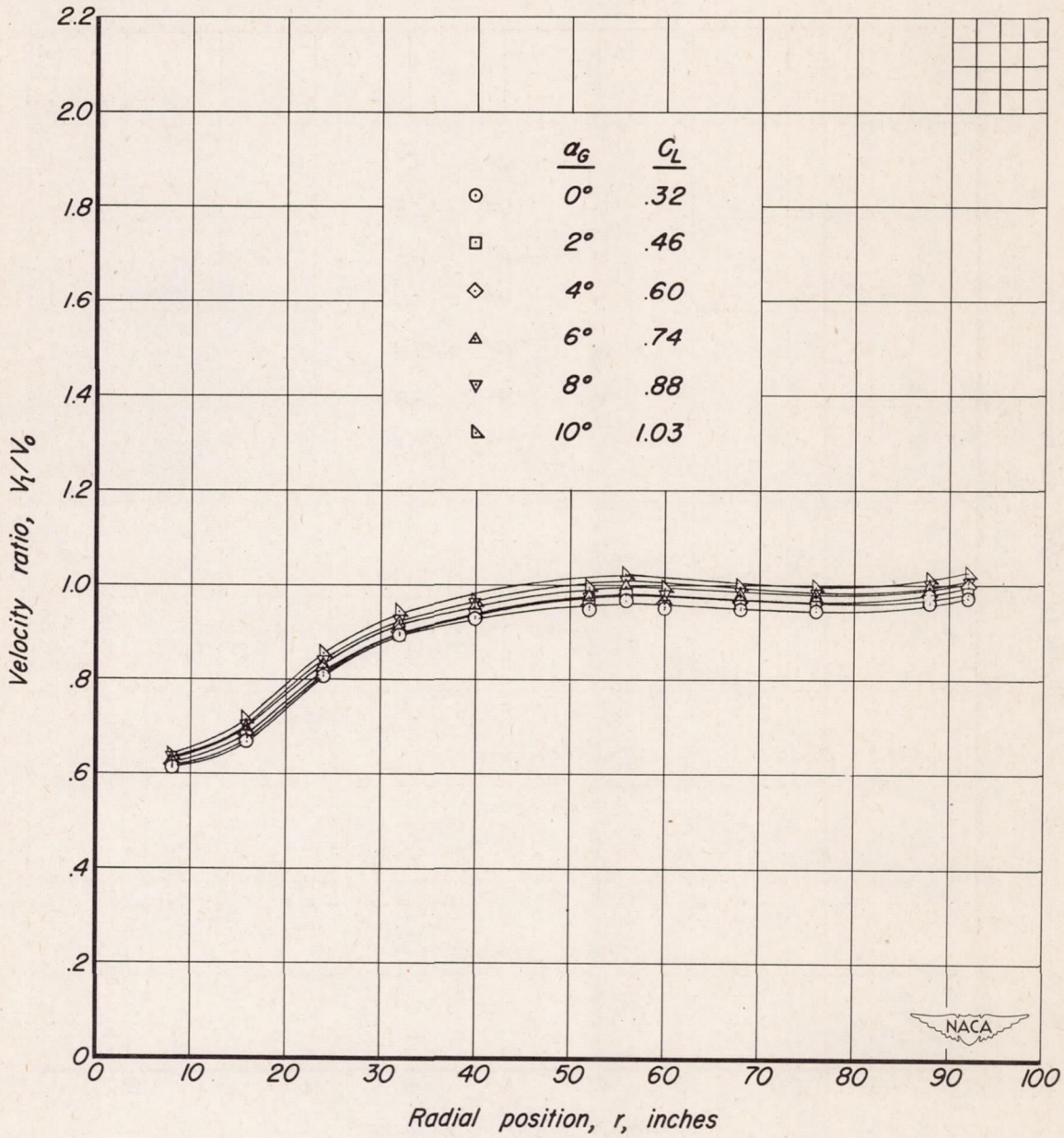
(c) $\Omega = 45.2°$.

Figure 14. – Continued.



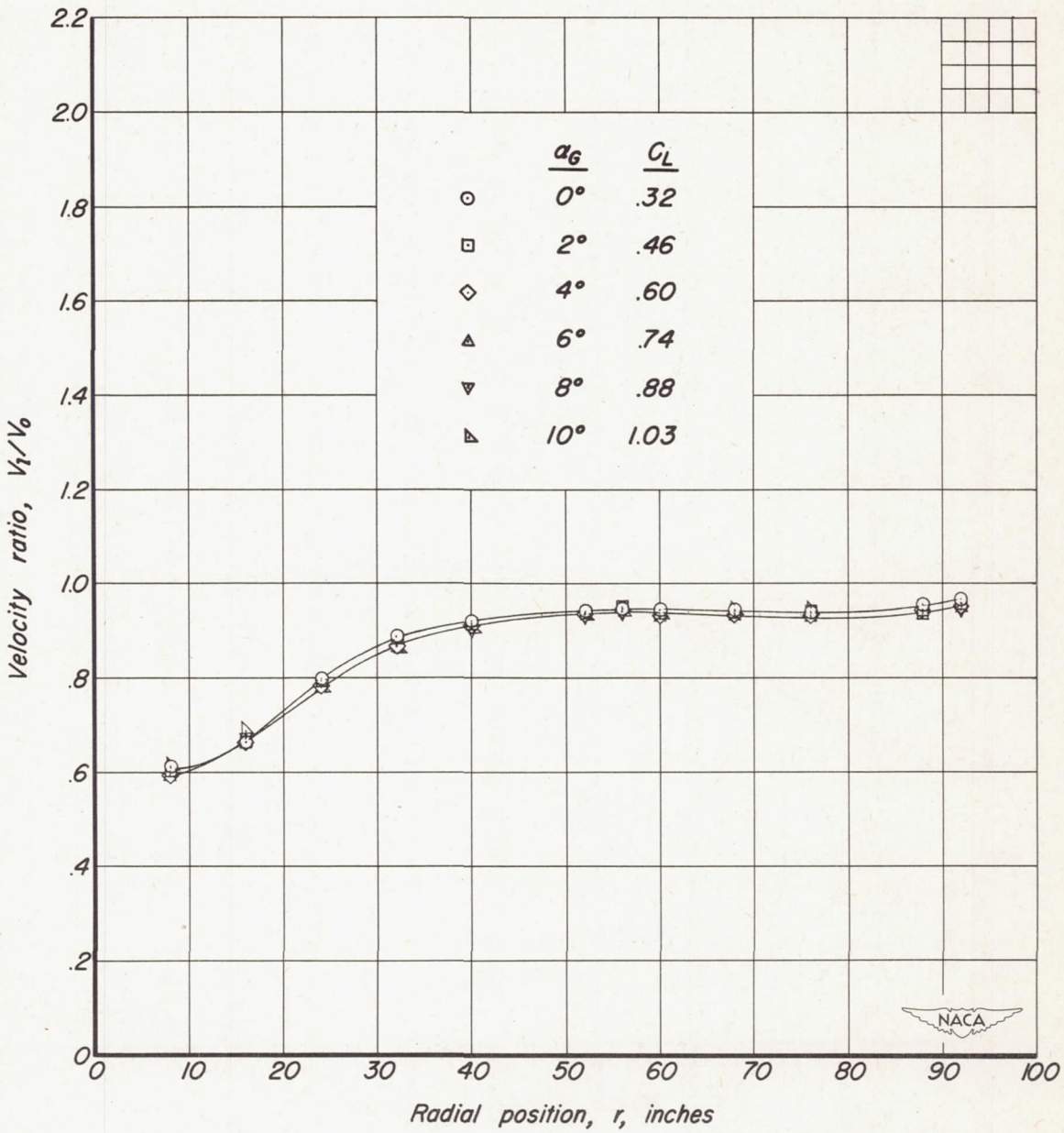
(d) Ω=68.5°.

Figure 14. – Continued.



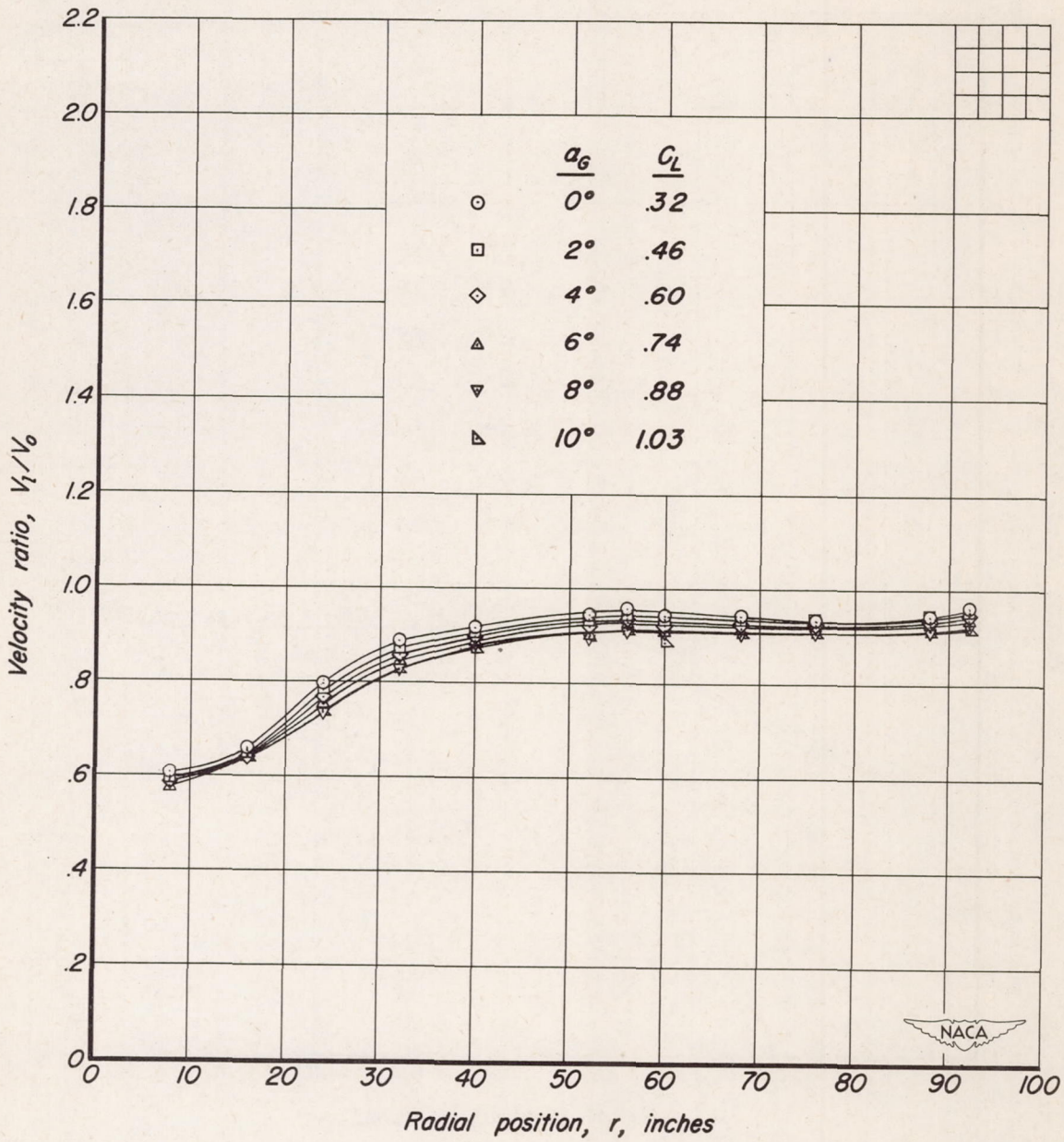
(e) $\Omega = 91.1°$.

Figure 14. – Continued.



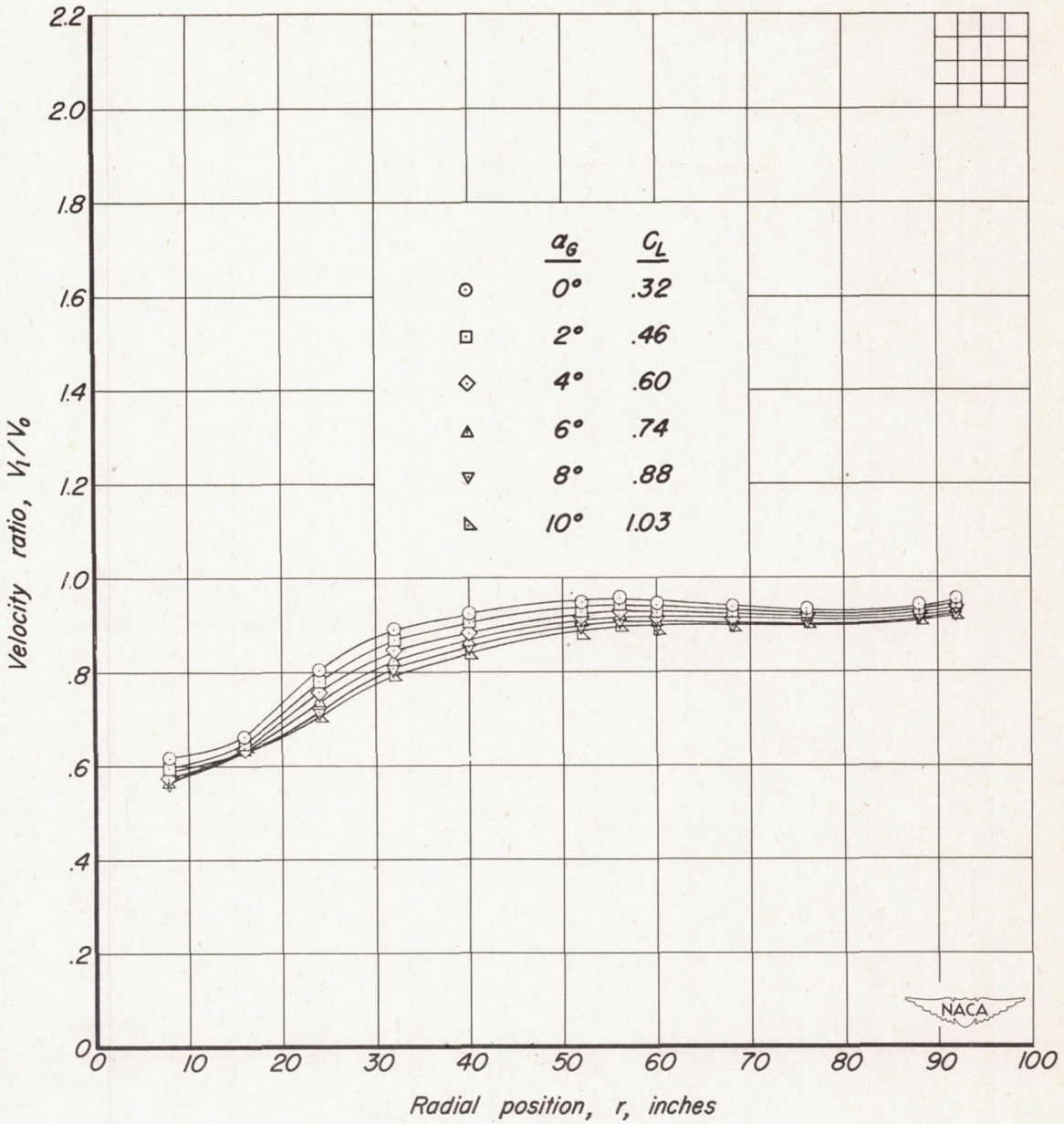
(f) Ω=113.4°.

Figure 14. – Continued.



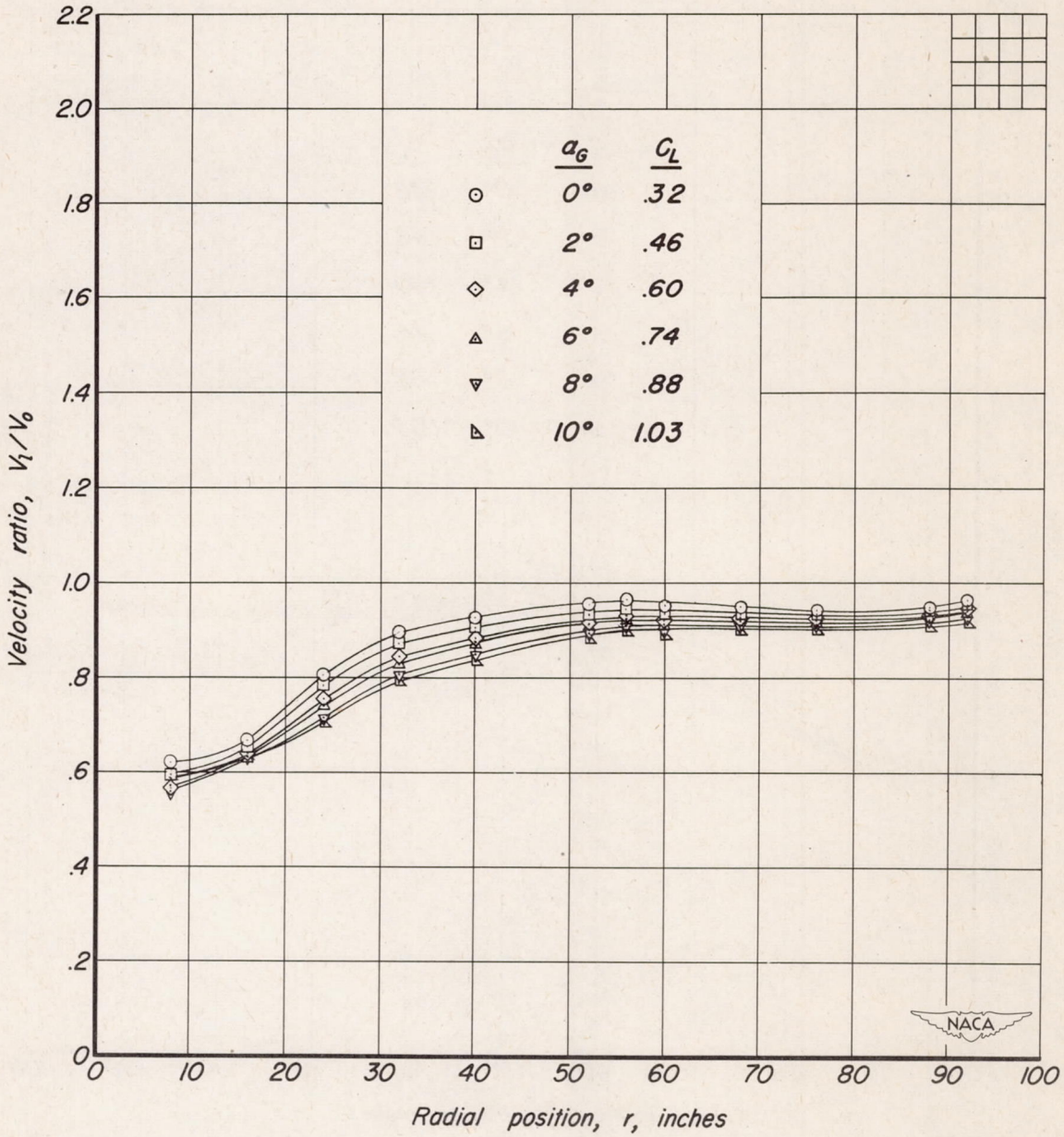
(g) Ω=135.7°.

Figure 14. - Continued.



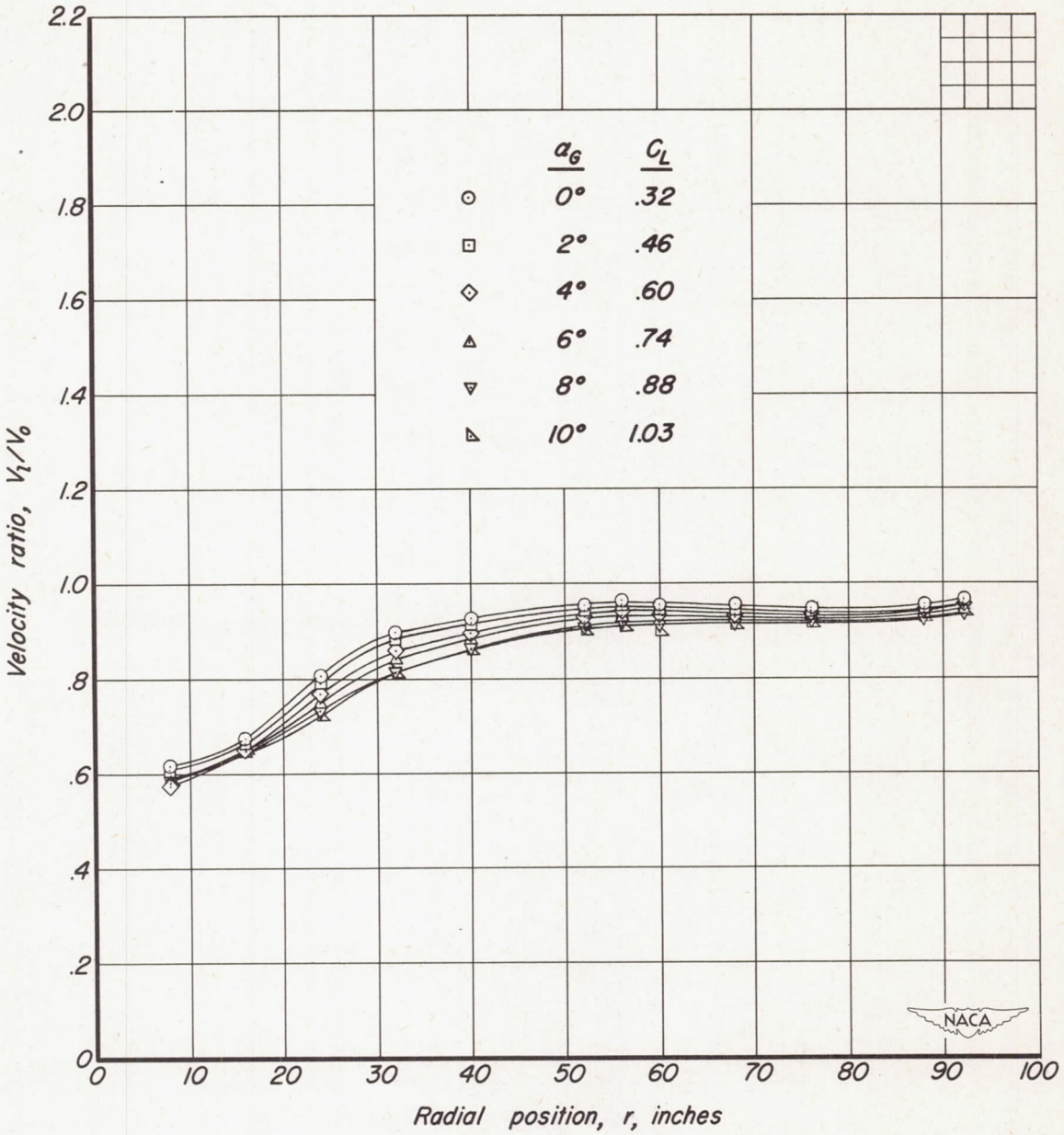
(h) Ω=158.2°.

Figure 14. – Continued.



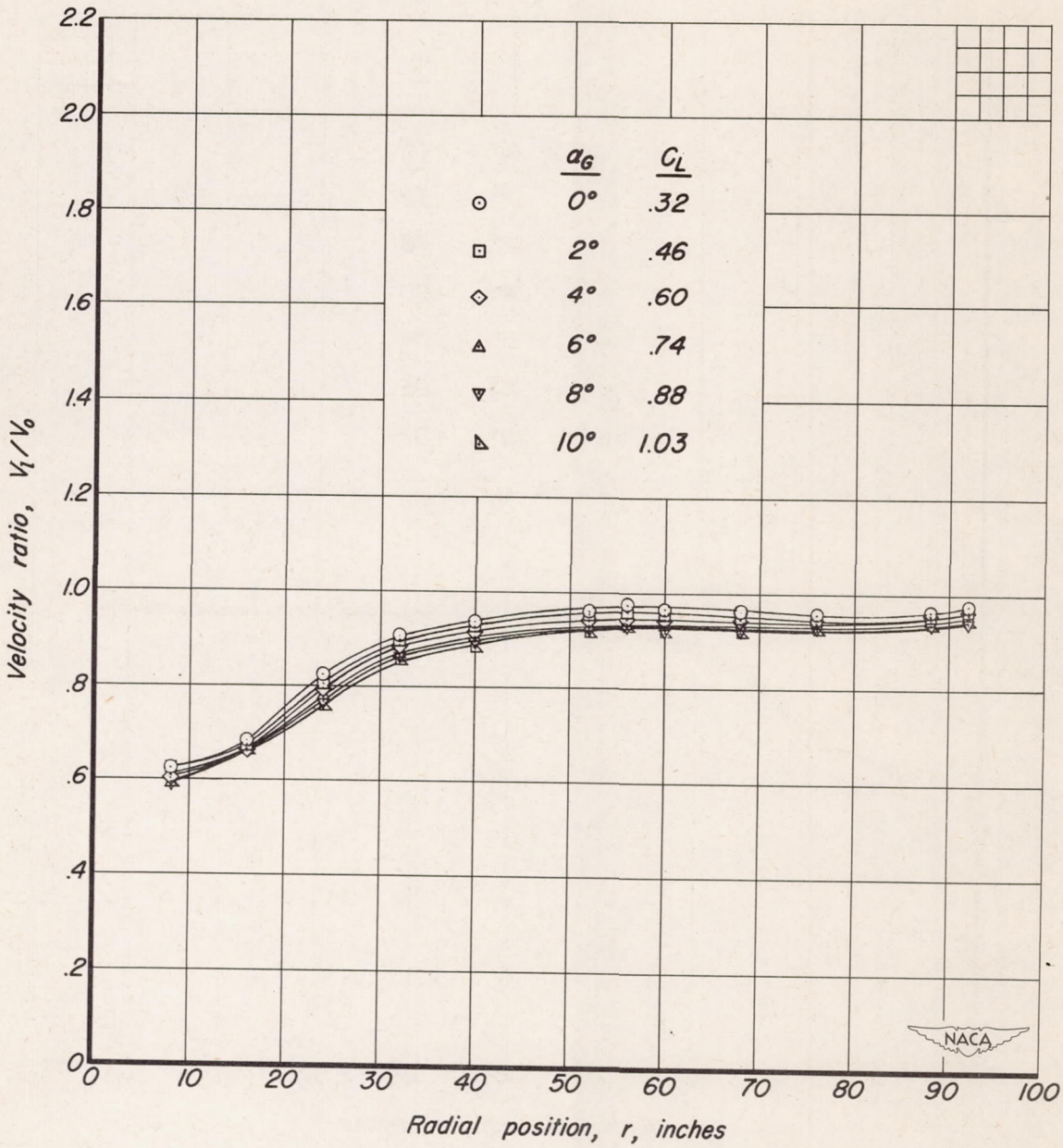
(i) Ω=180.6°.

Figure 14. – Continued.



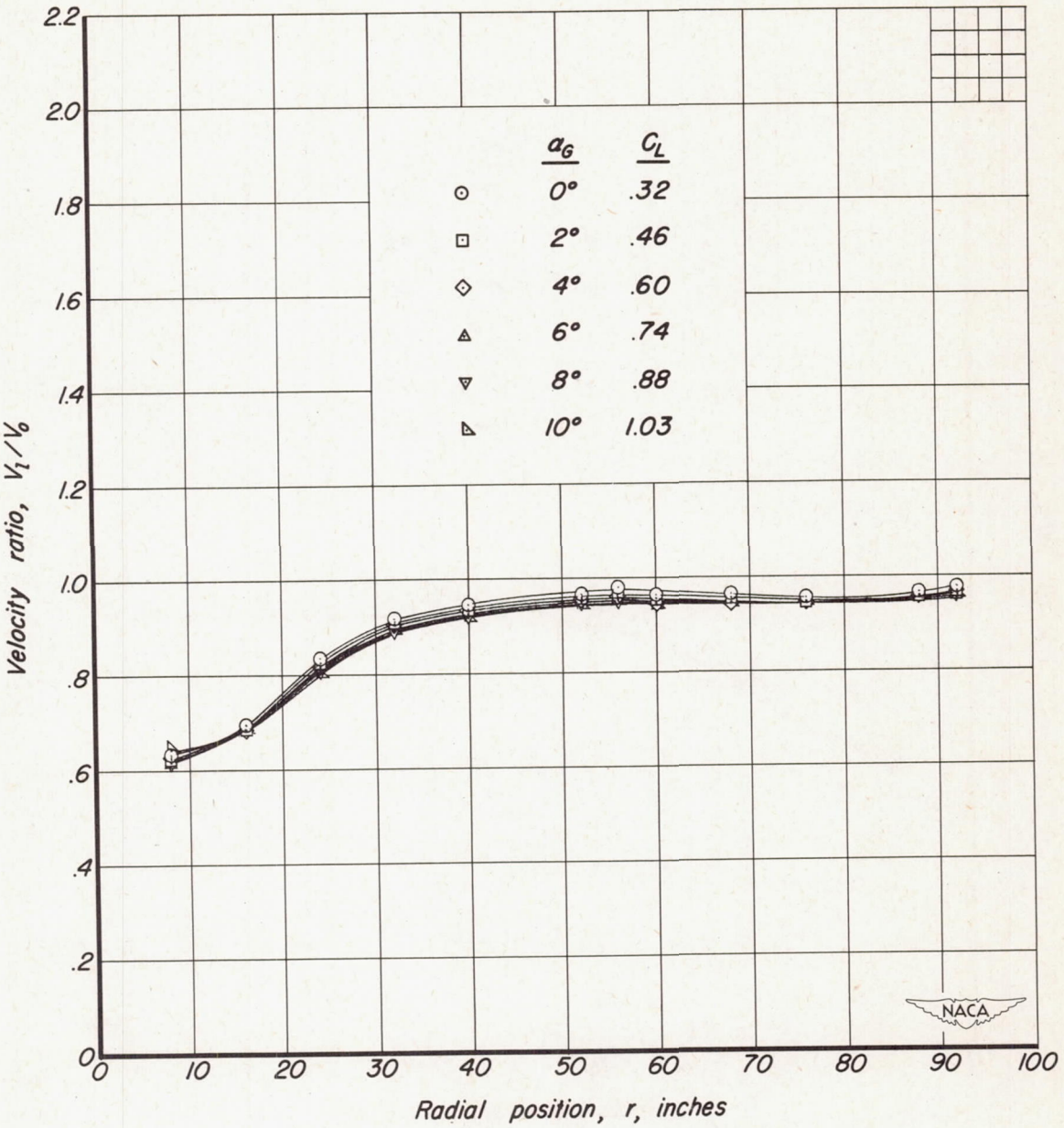
(j) Ω=203.0°.

Figure 14. – Continued.



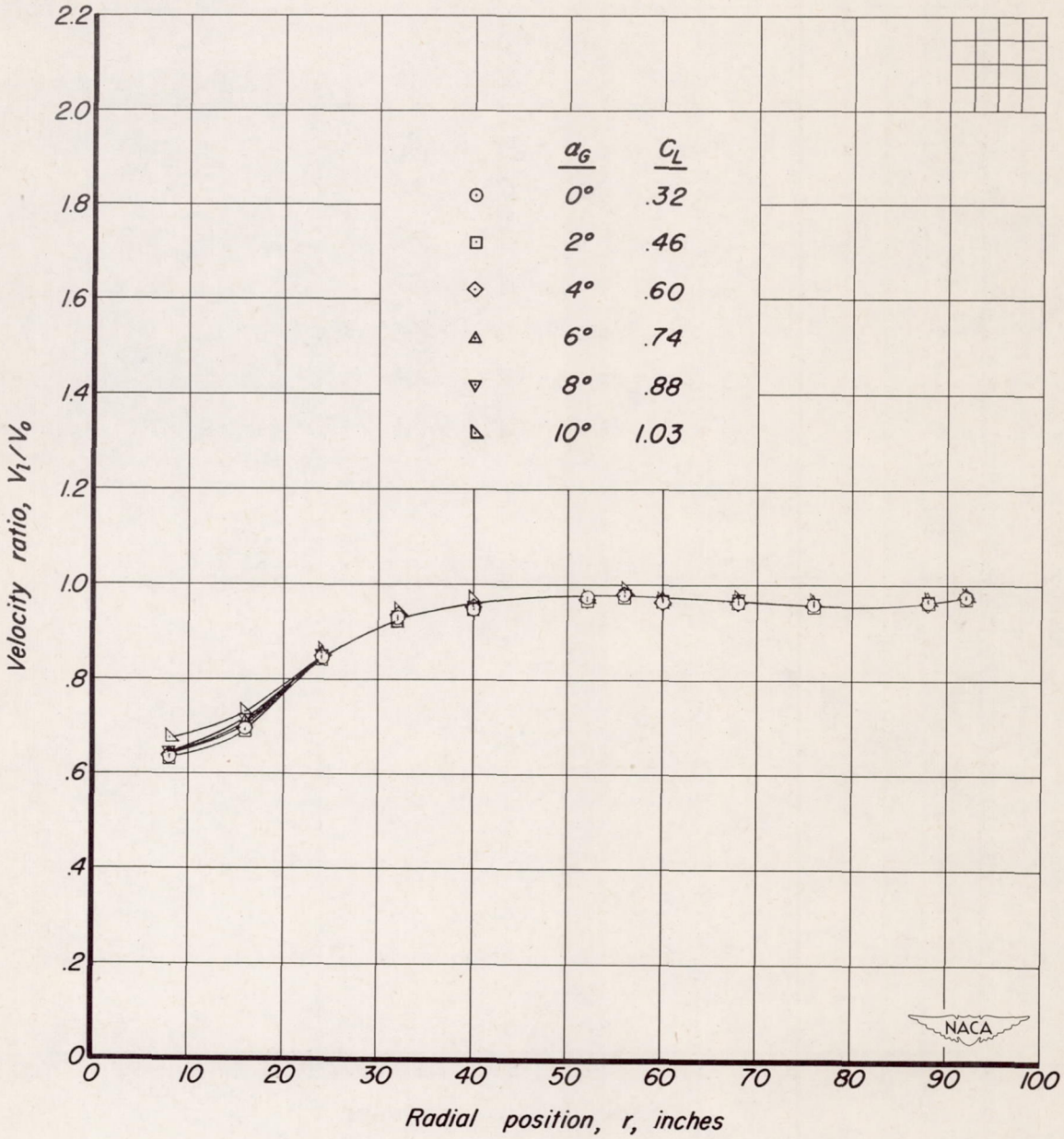
(k) $\Omega = 225.6°$.

Figure 14. – Continued.



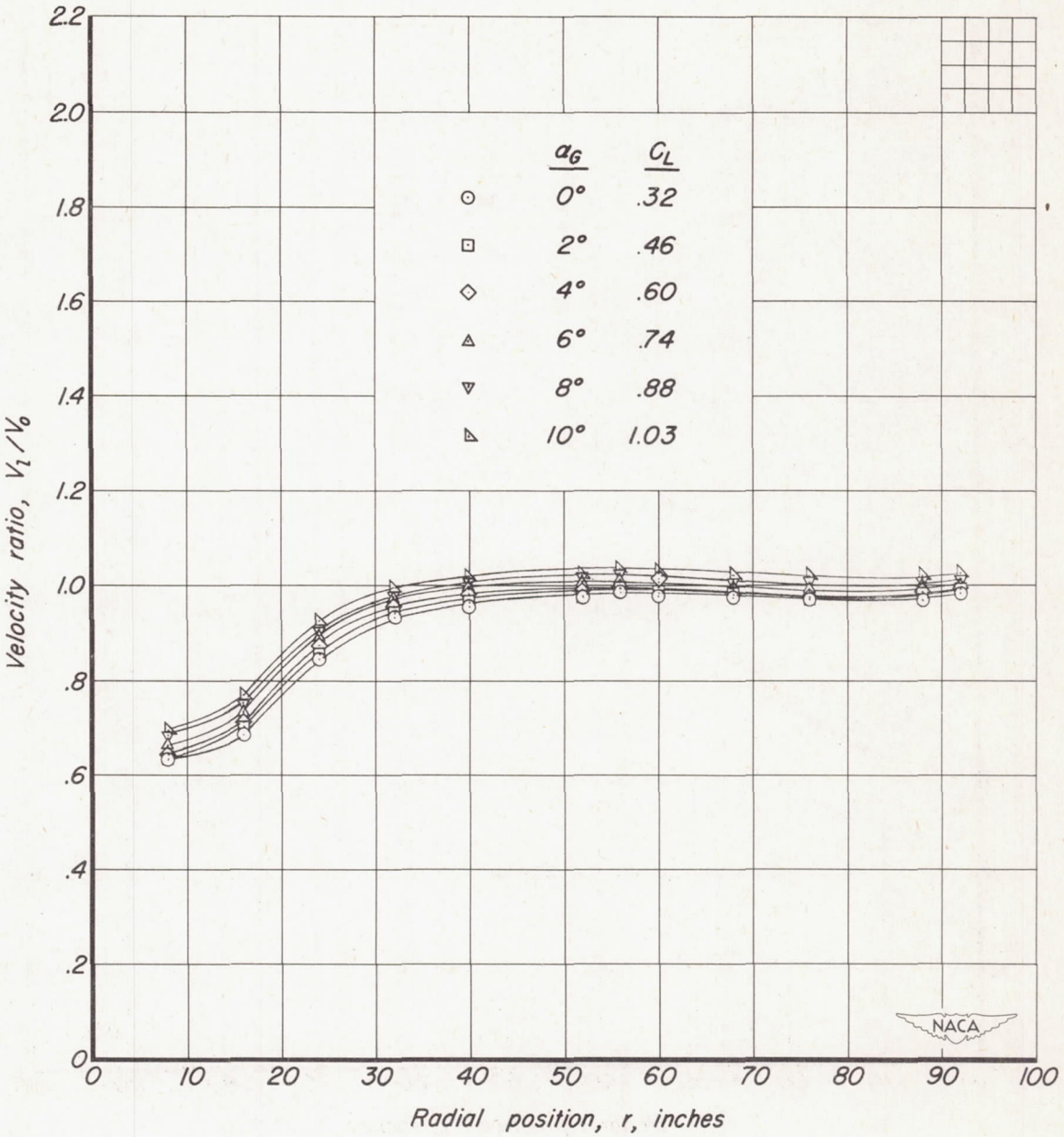
(1) $\Omega = 247.2°$.

Figure 14. – Continued.



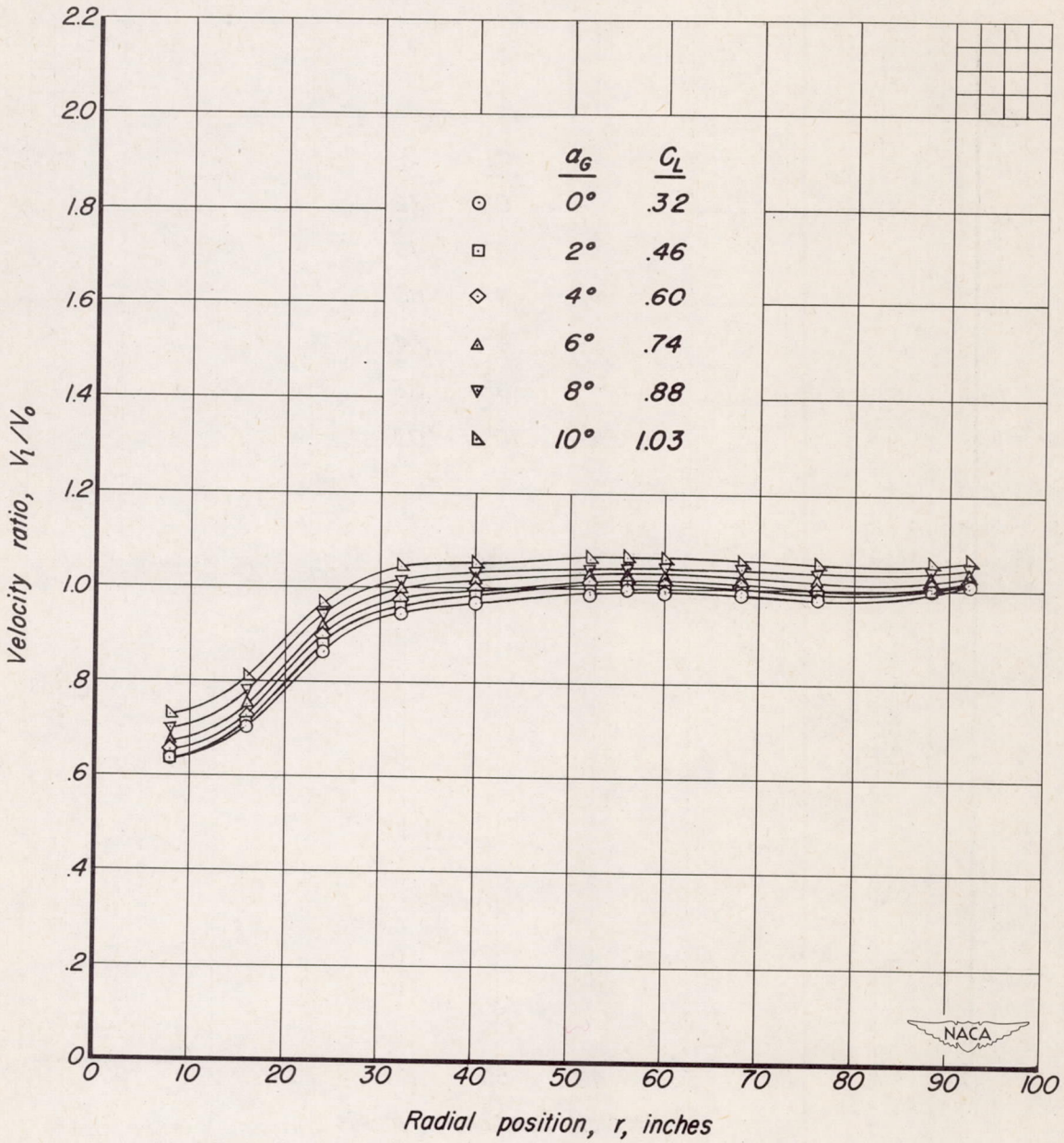
(m) $\Omega = 270.1°$.

Figure 14. – Continued.



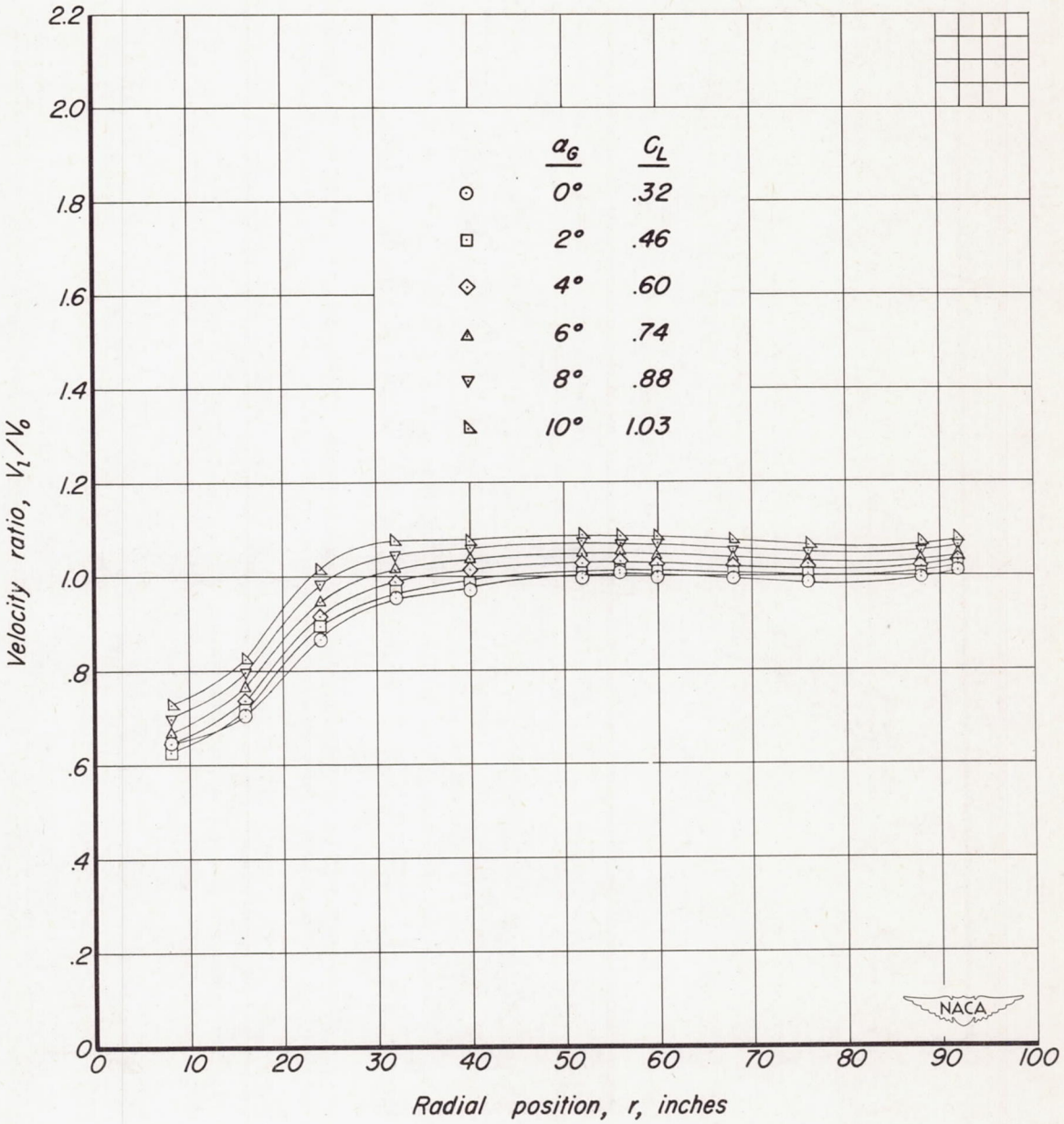
(n) $\Omega = 292.2°$.

Figure 14. – Continued.



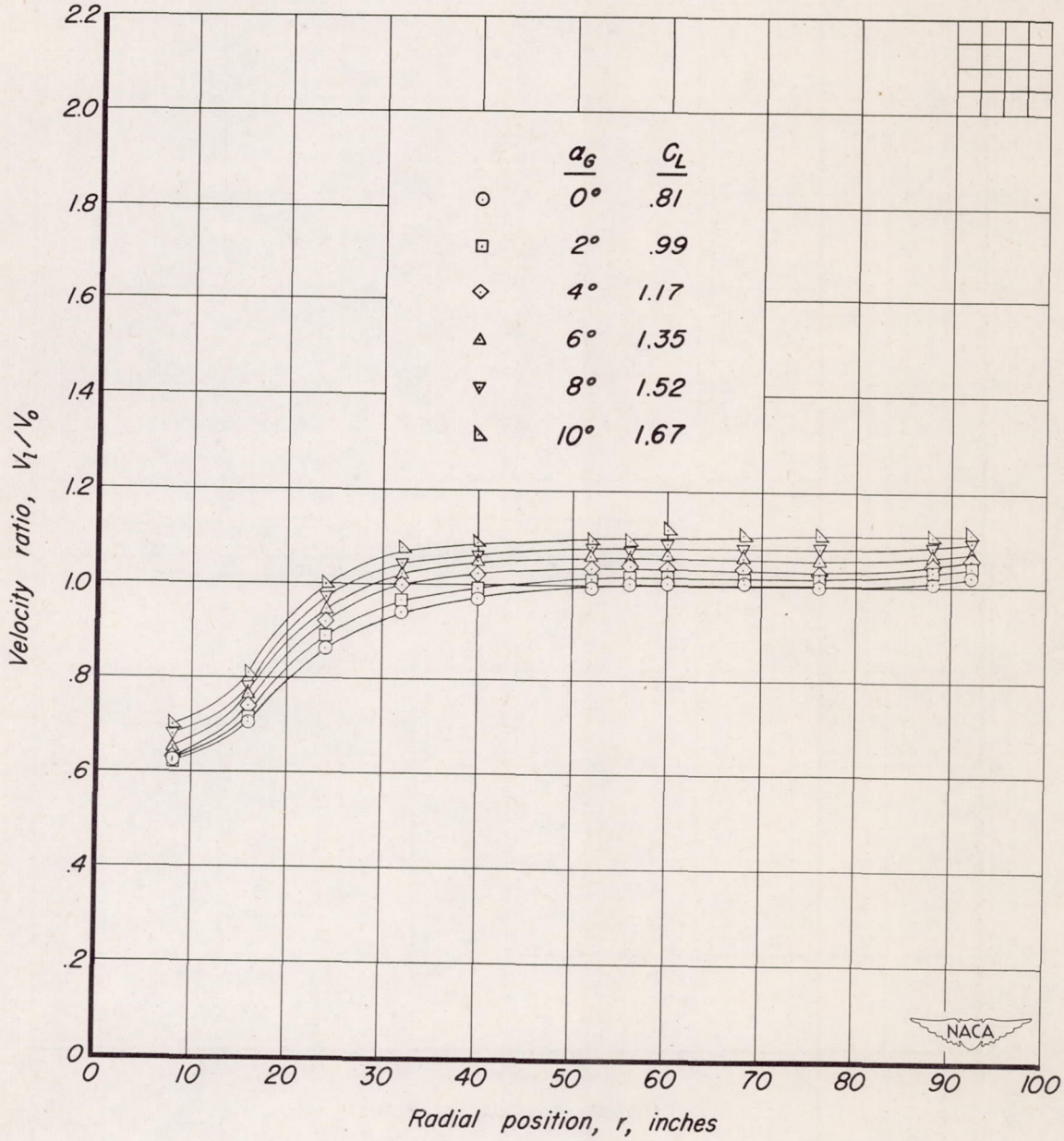
(o) $\Omega = 314.7°$.

Figure 14. – Continued.



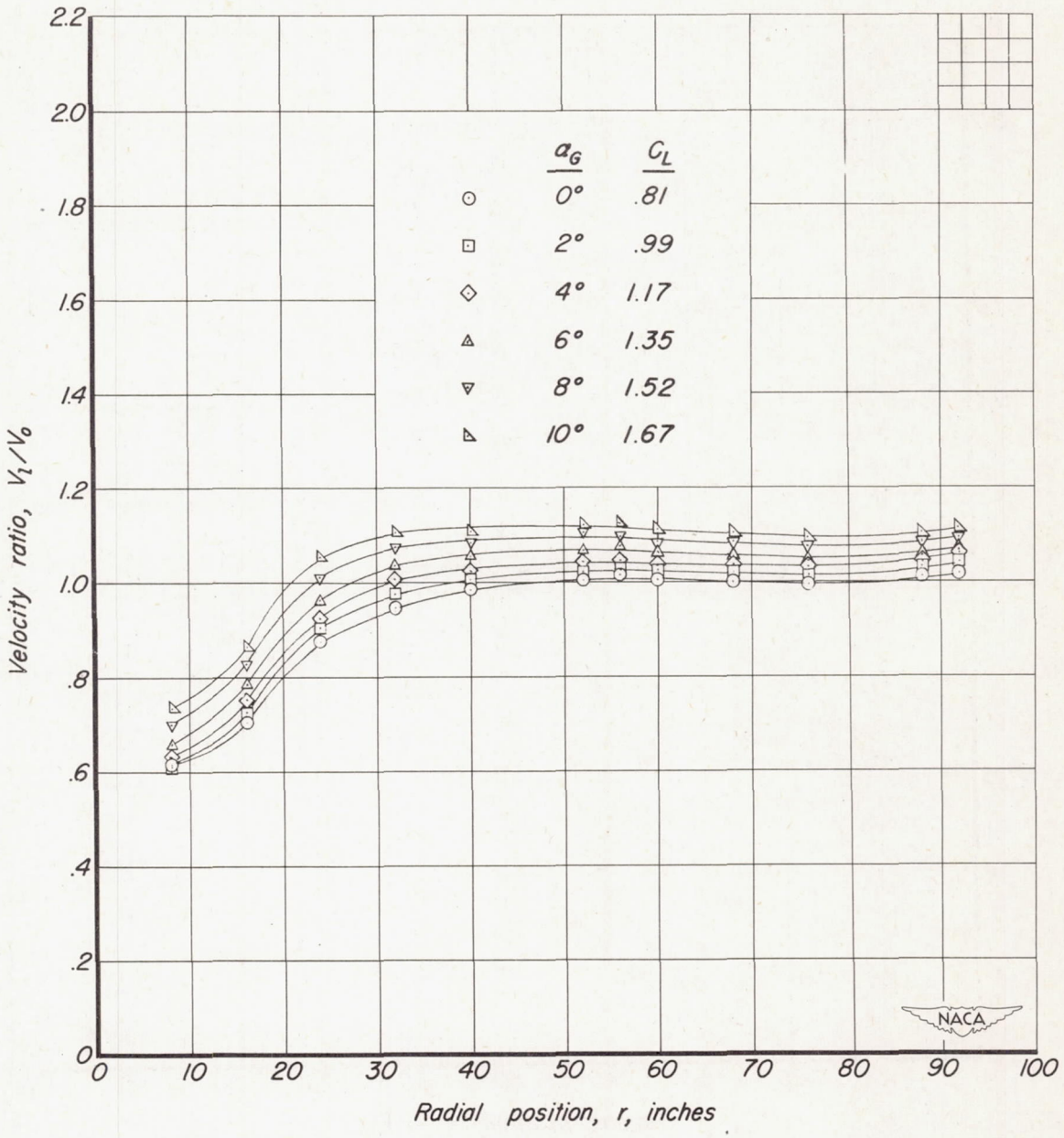
(p) $\Omega = 337.4°$.

Figure 14. – Concluded.



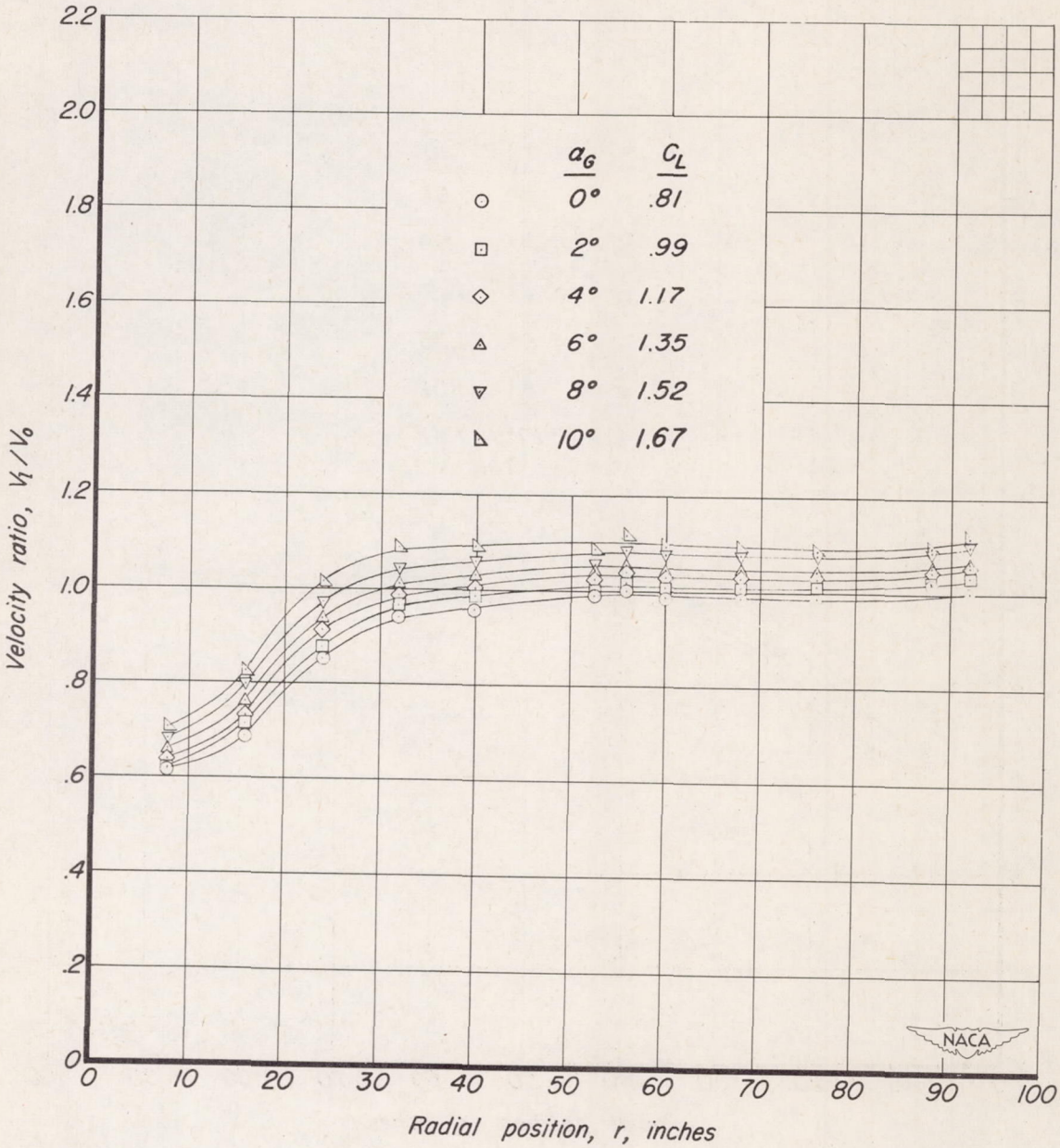
(a) $\Omega = 0.0°$.

Figure 15. – Variation of velocity ratio, V_1/V_0, with radial position for several angles of attack. m_1/m_0, .29; δ_f, 40°.



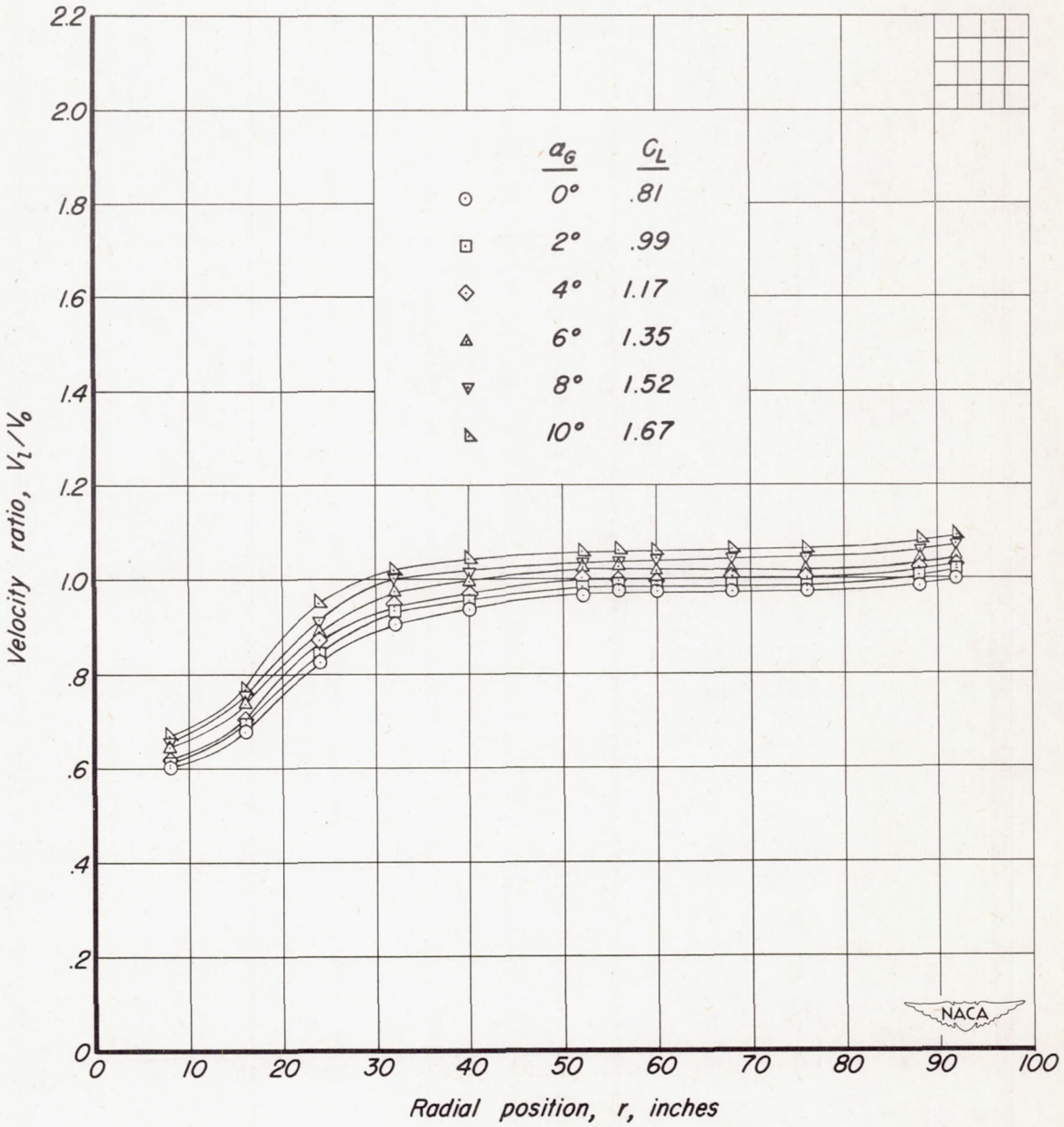
(b) $\Omega = 22.5°$.

Figure 15. – Continued.



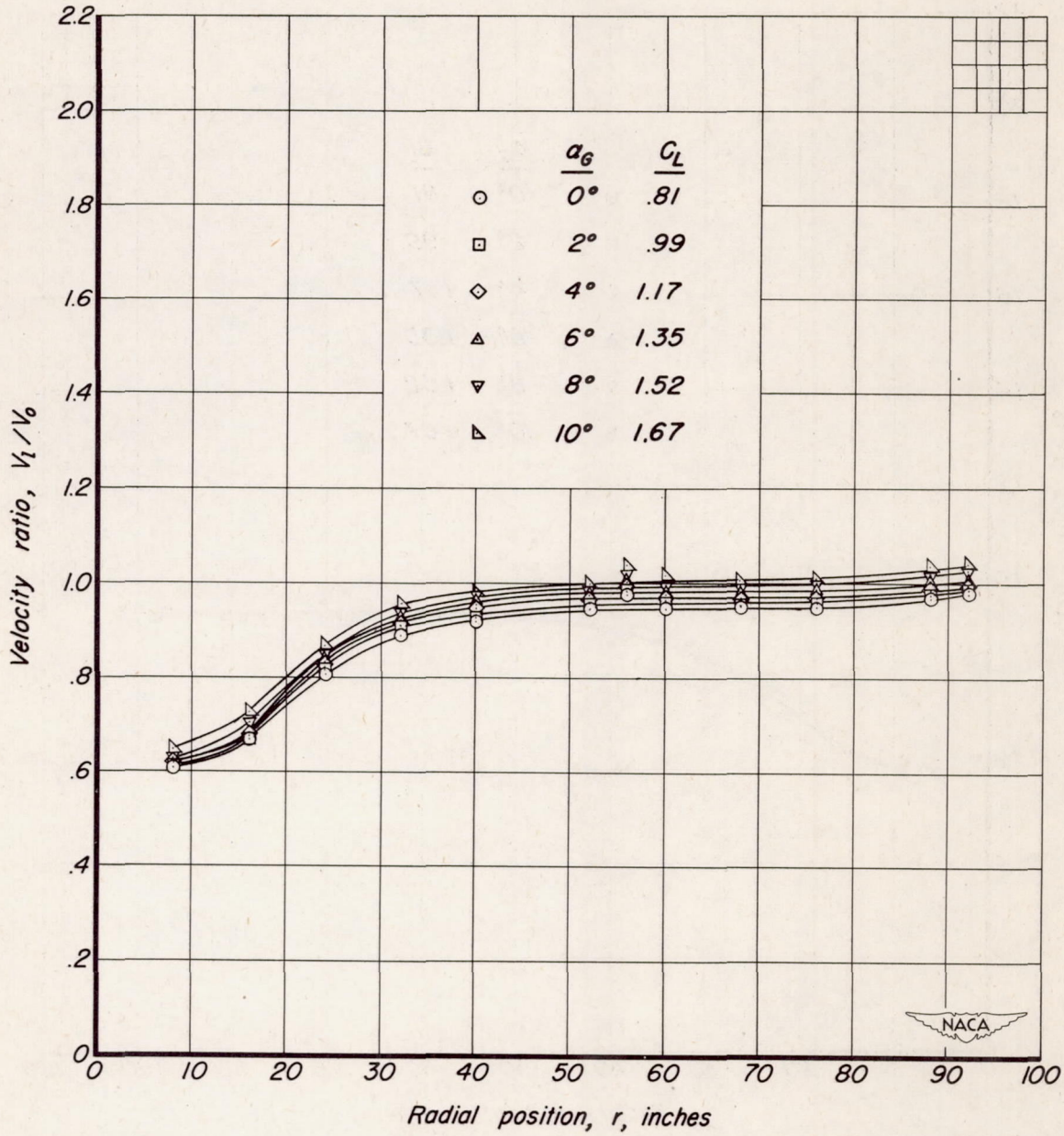
(c) $\Omega = 45.2°$.

Figure 15. – Continued.



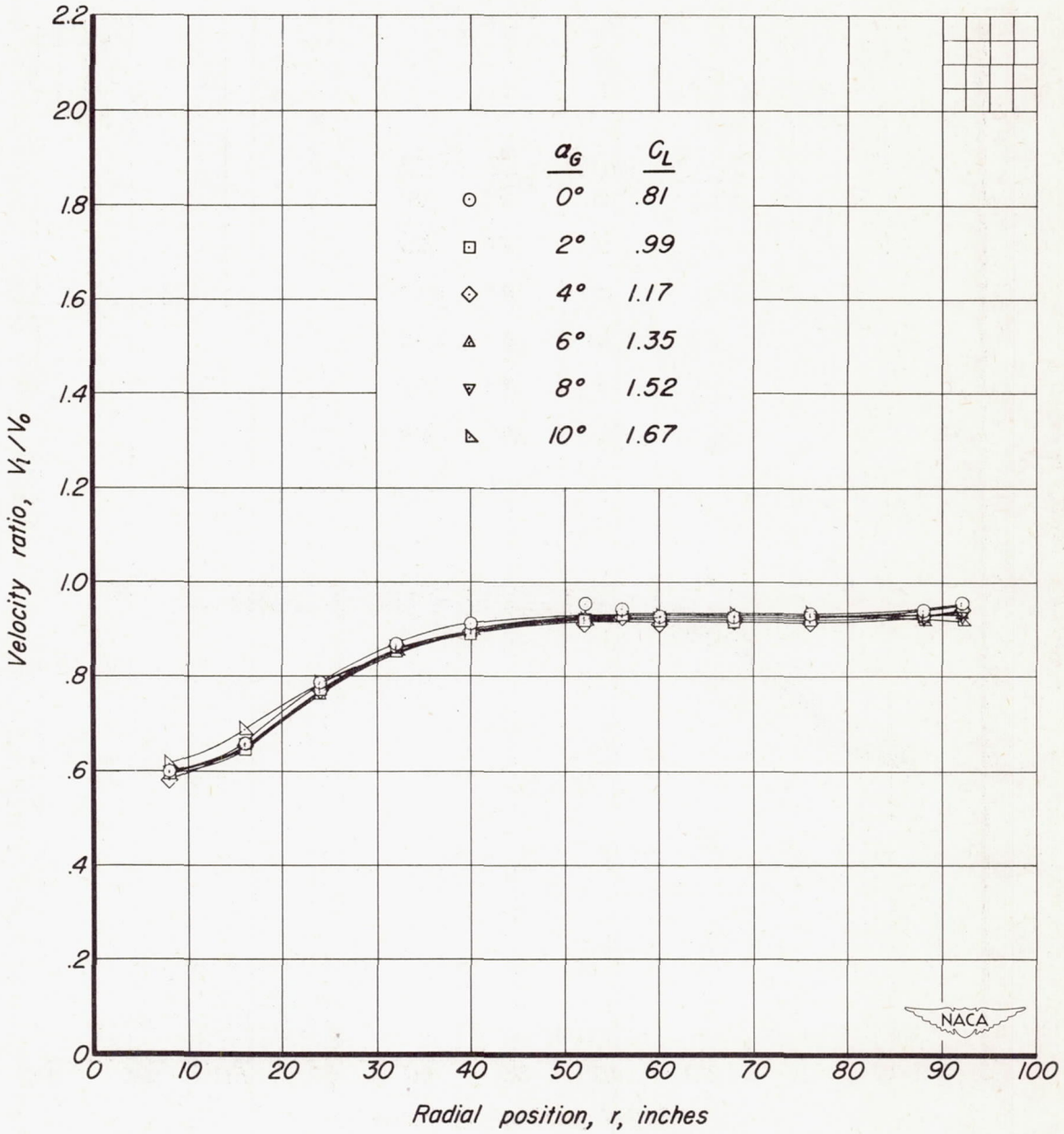
(d) Ω=68.5°.

Figure 15. – Continued.



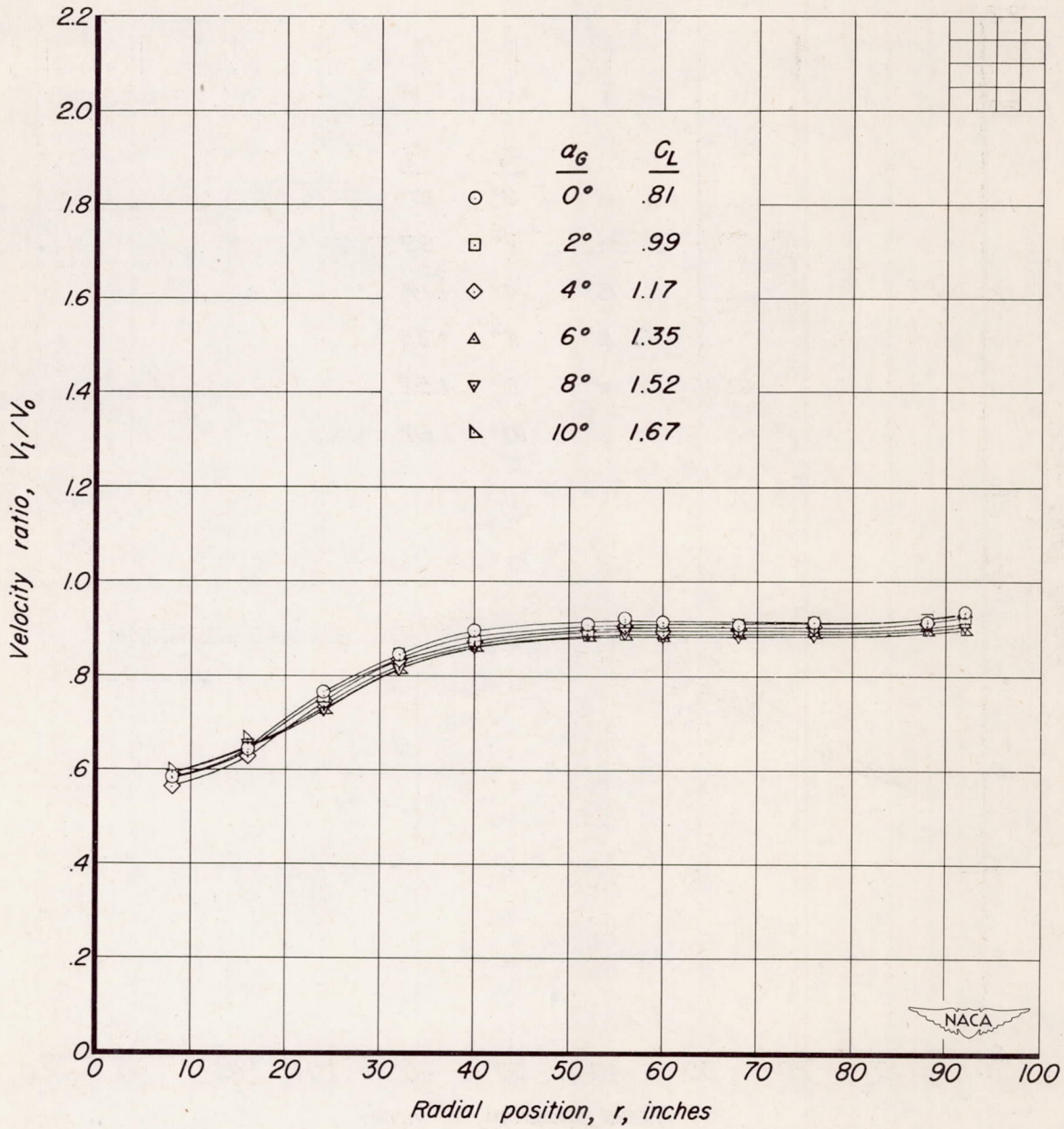
(e) $\Omega = 91.1°$.

Figure 15. – Continued.



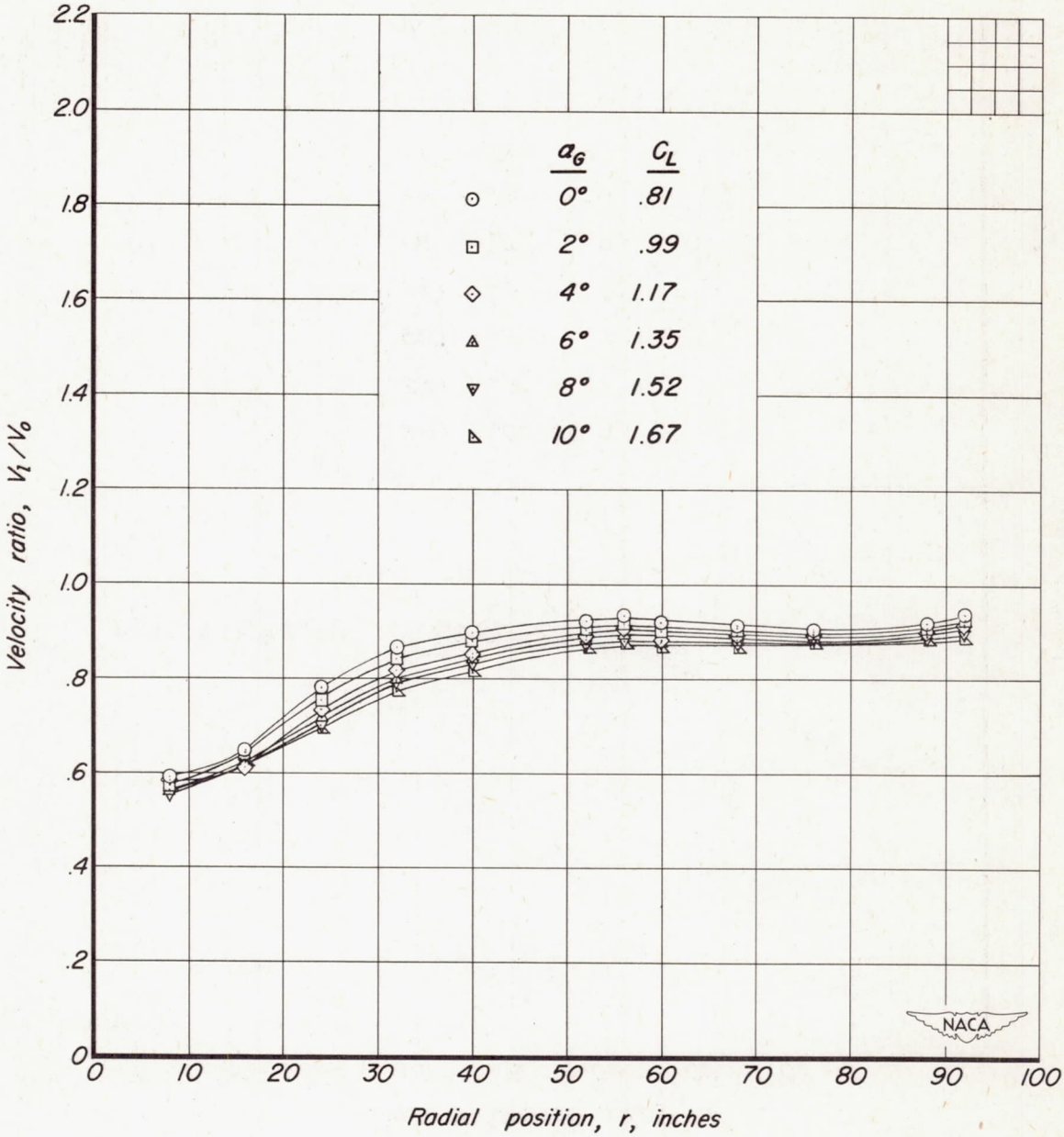
(f) Ω=113.4°.

Figure 15. – Continued.



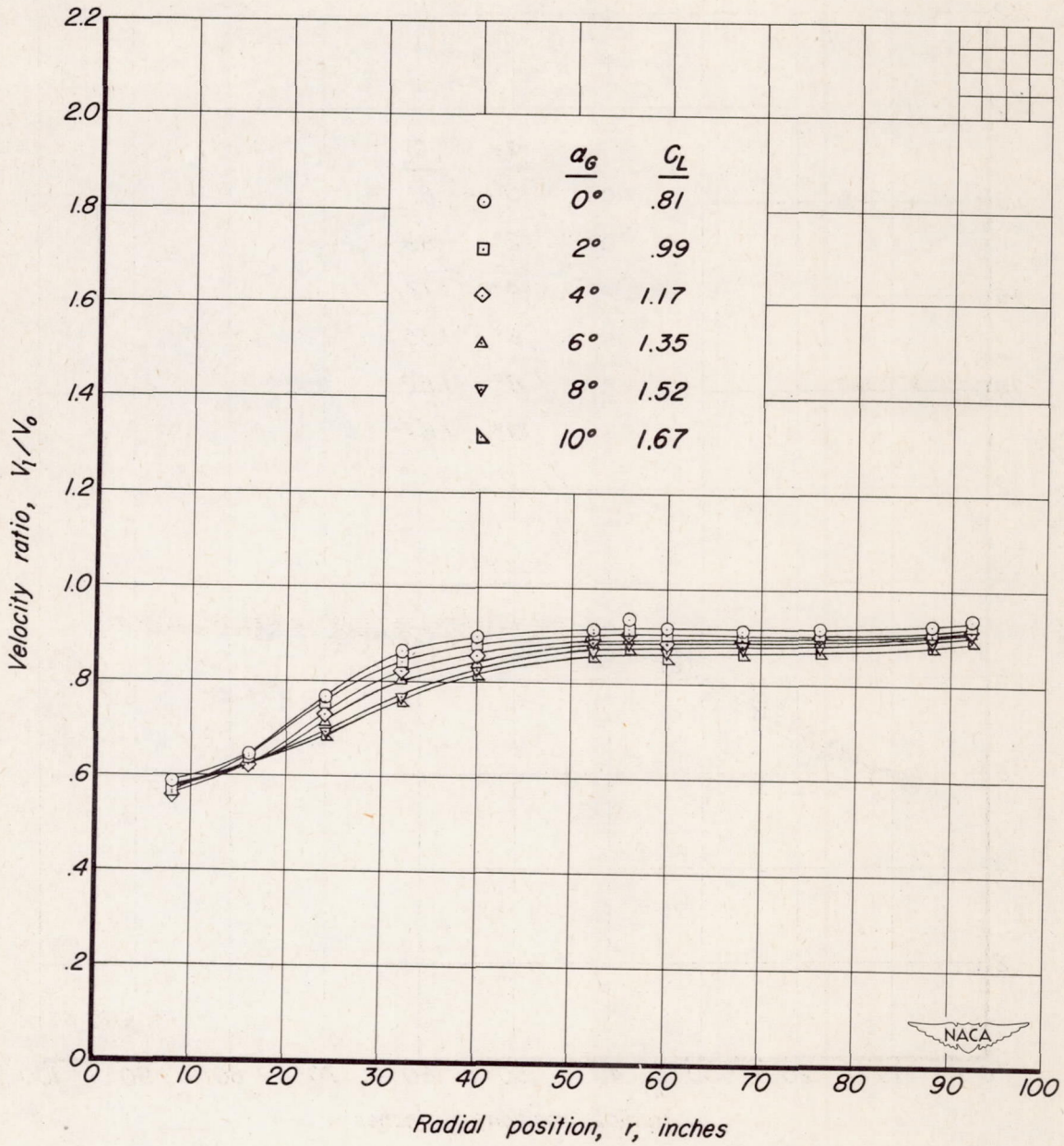
(g) Ω=135.7°.

Figure 15. – Continued.



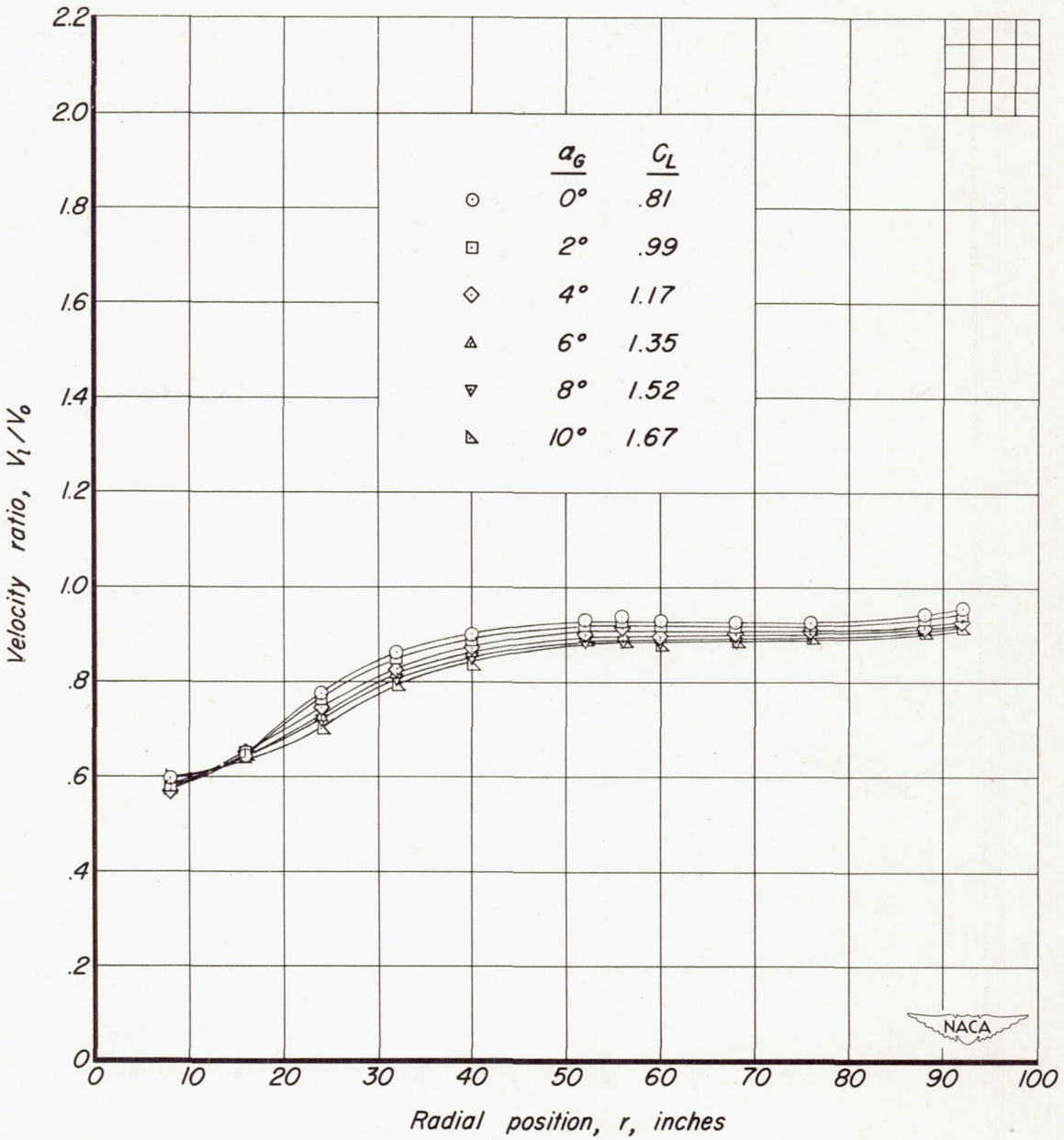
(h) Ω=158.2°.

Figure 15. – Continued.



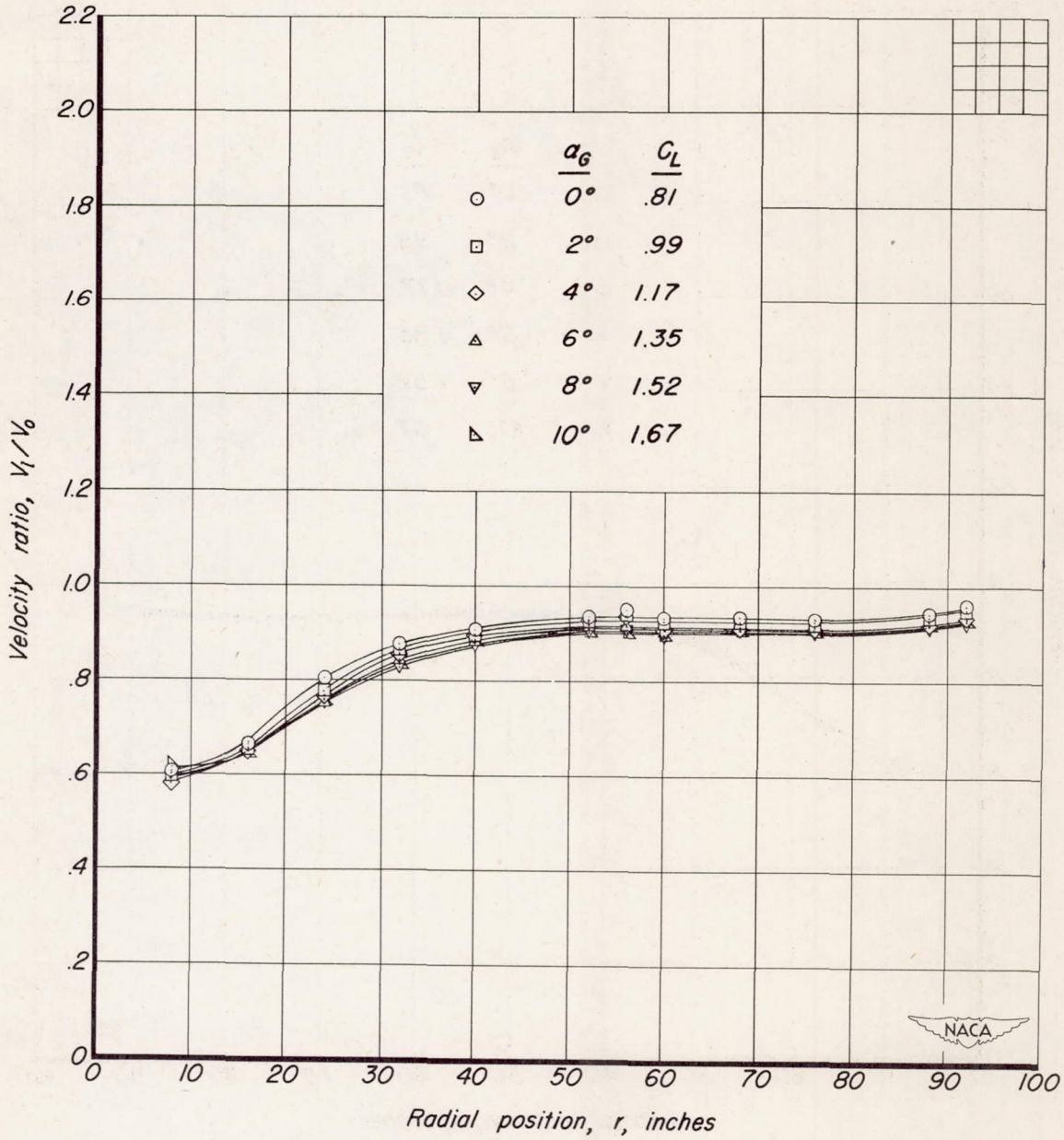
(i) Ω=180.6°.

Figure 15. - Continued.



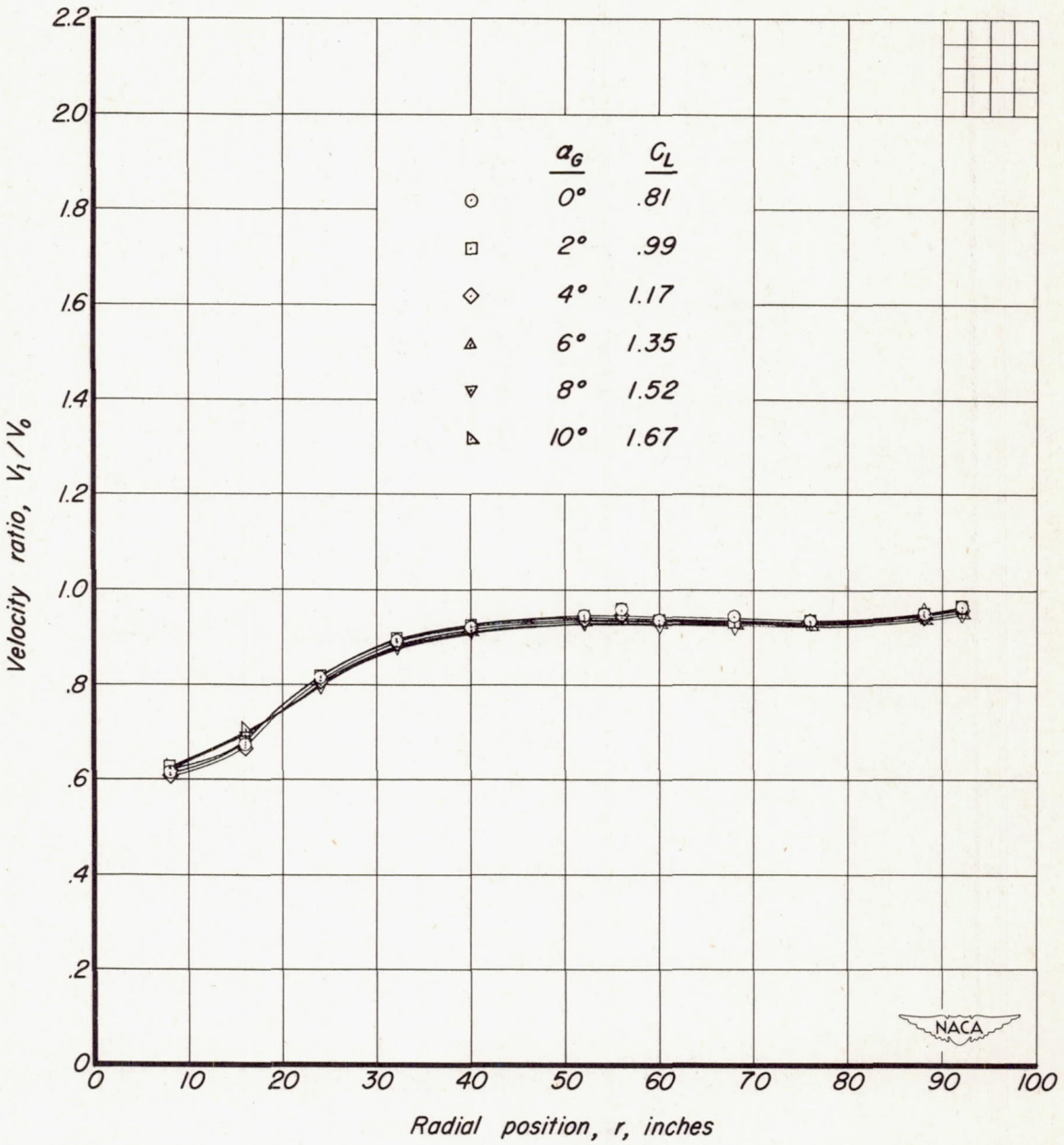
(j) Ω=203.0°.

Figure 15. – Continued.



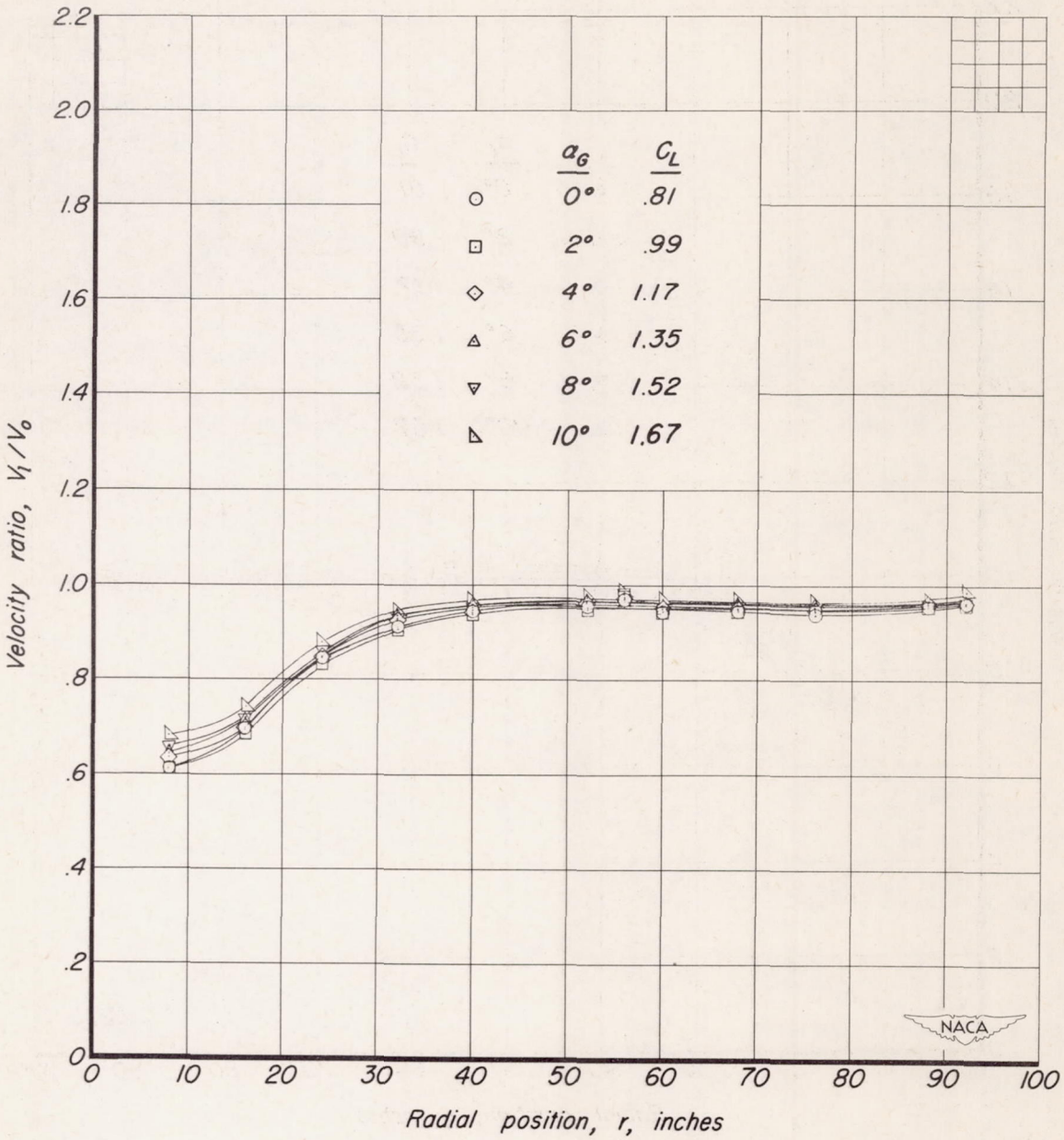
(k) $\Omega = 225.6°$.

Figure 15. – Continued.



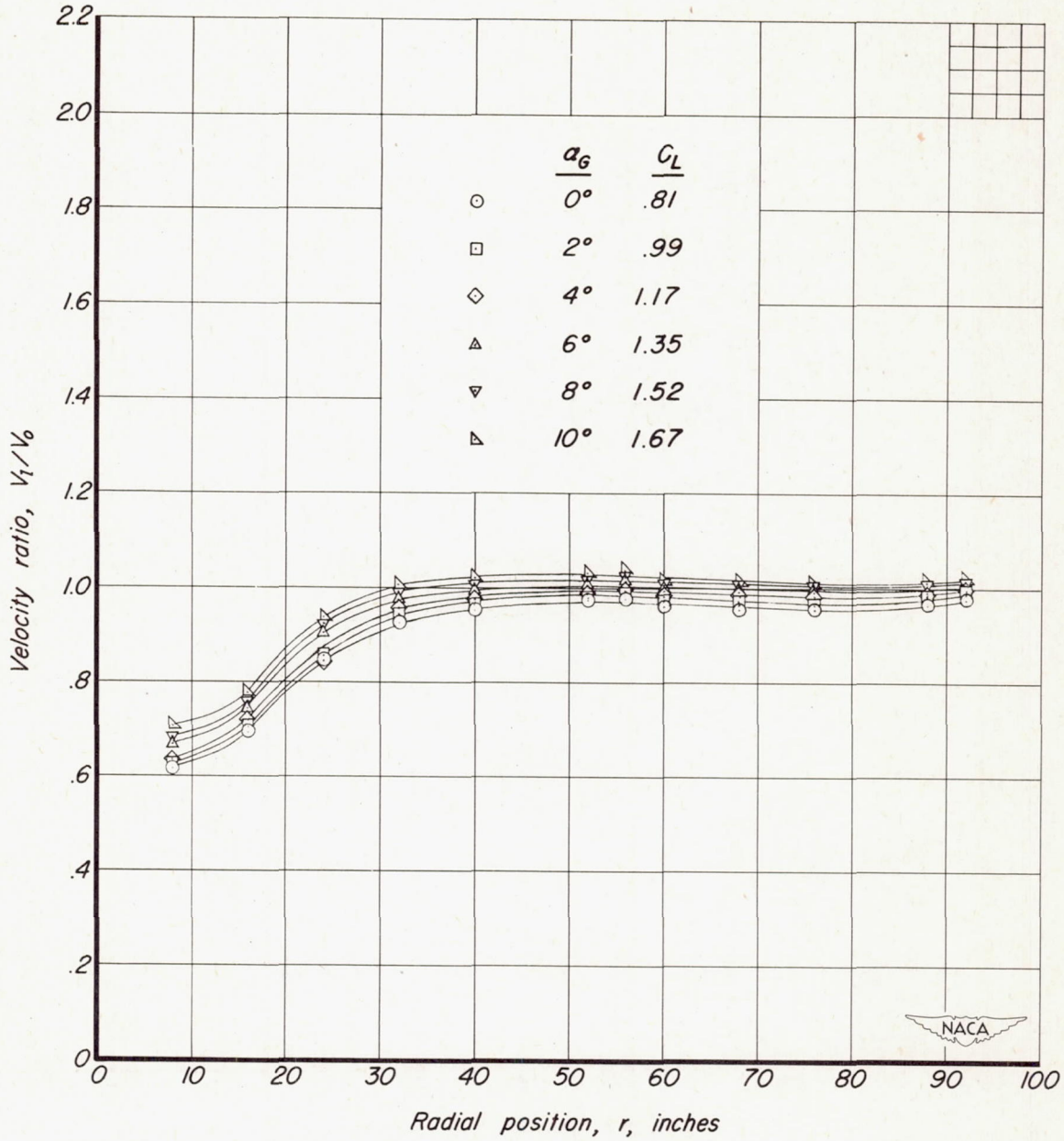
(1) $\Omega = 247.2°$.

Figure 15. – Continued.



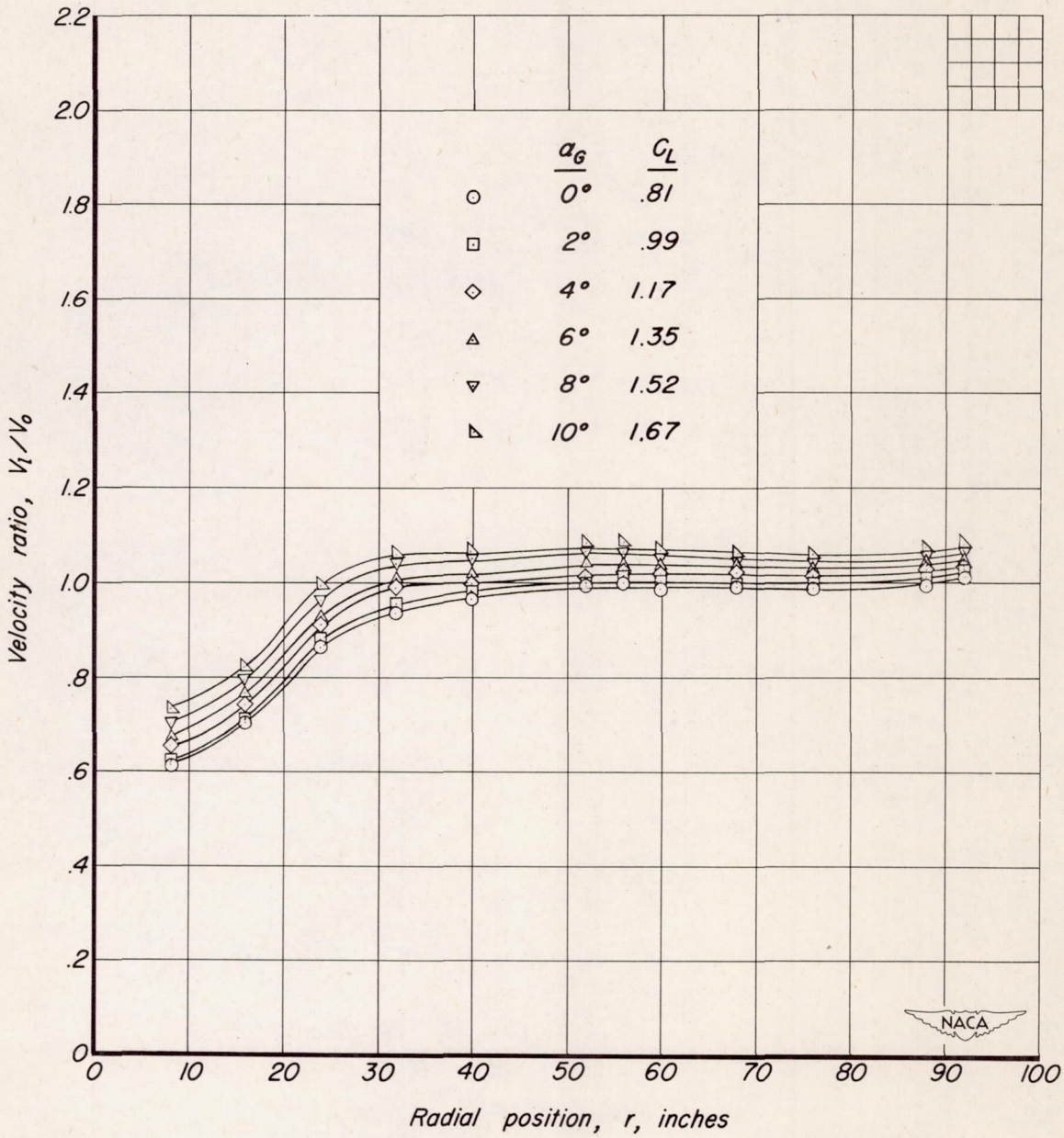
(m) Ω=270.1°.

Figure 15. – Continued.



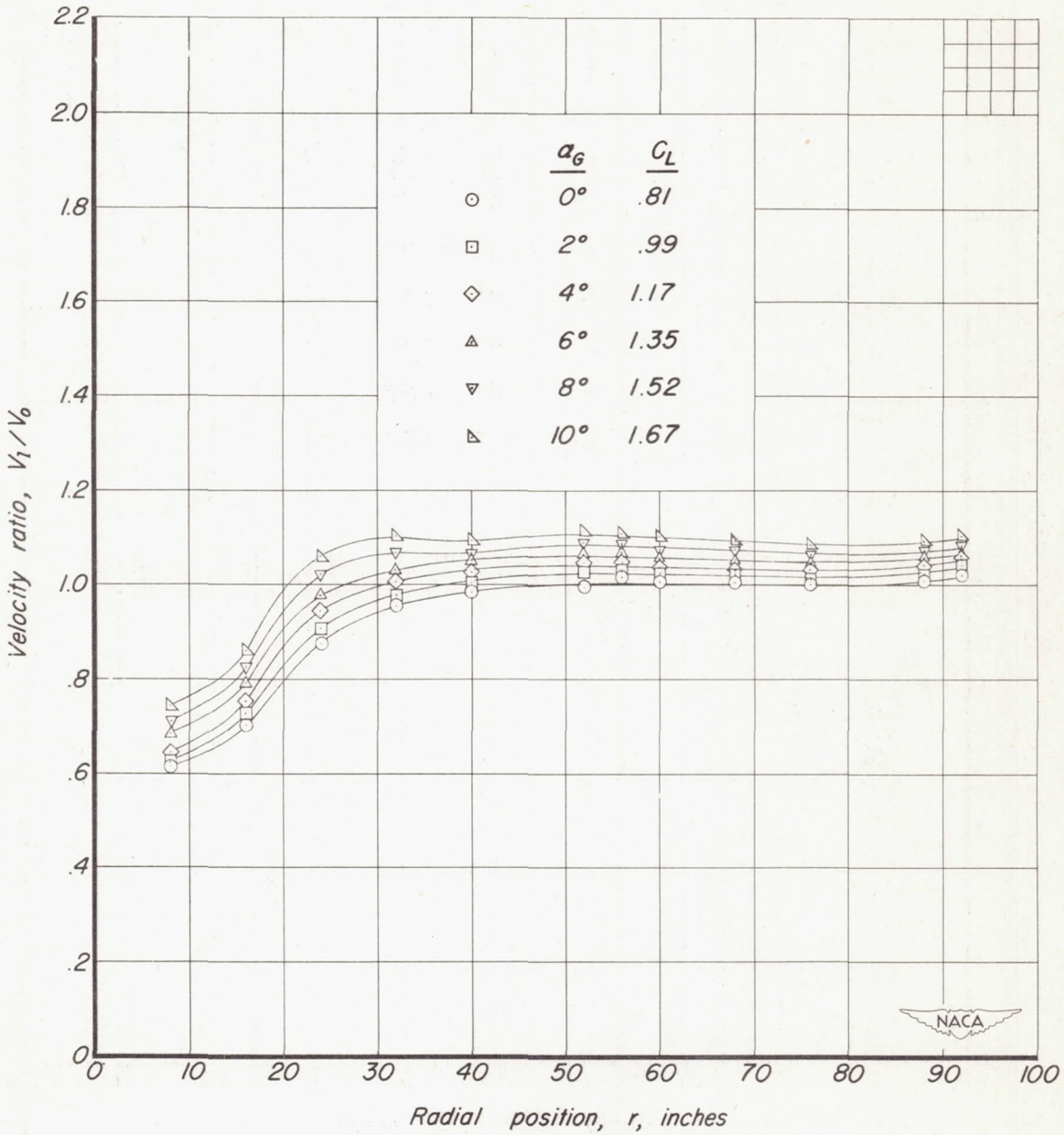
(n) $\Omega = 292.2°$.

Figure 15. – Continued.



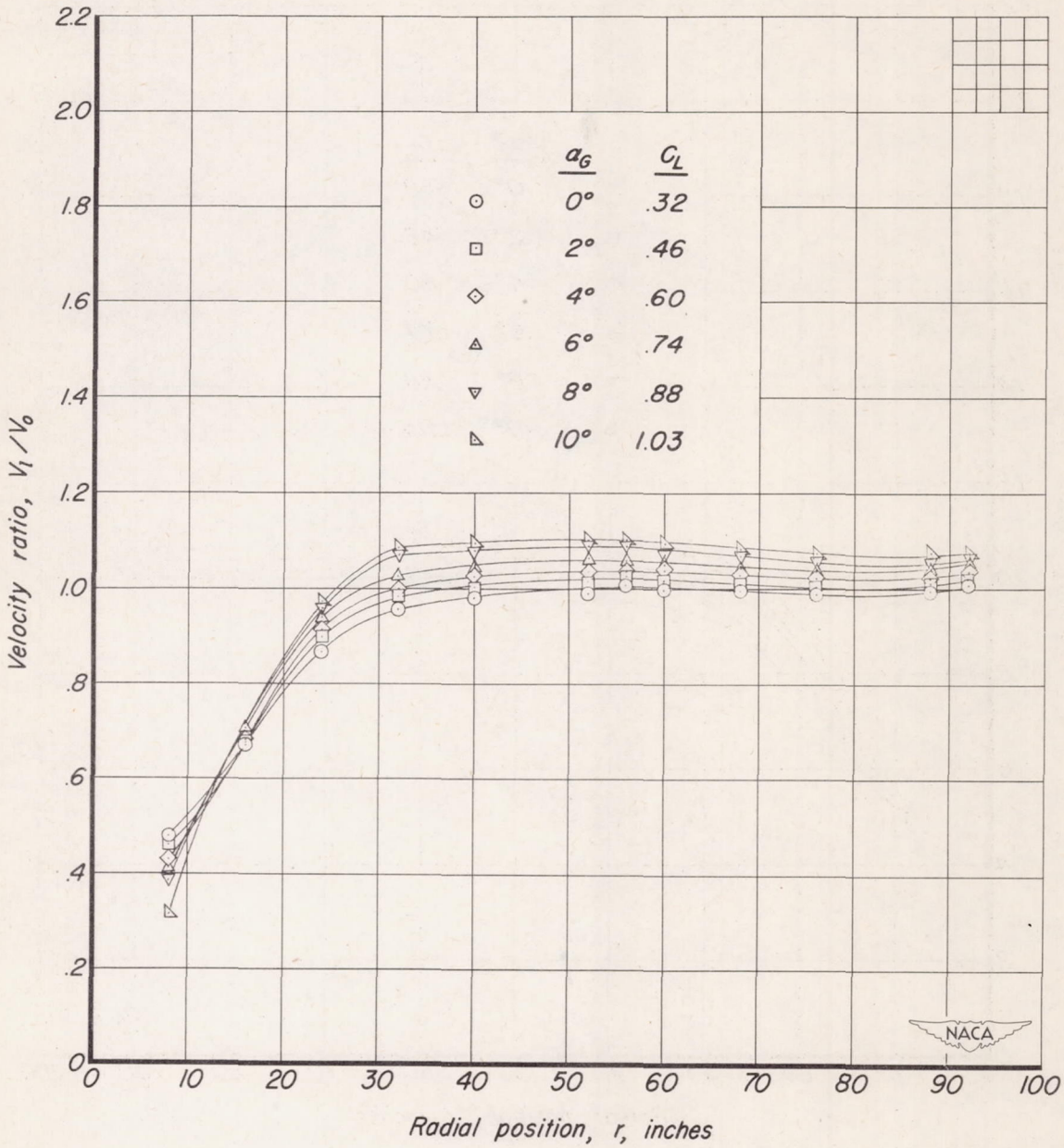
(o) $\Omega = 314.7°$.

Figure 15. – Continued.



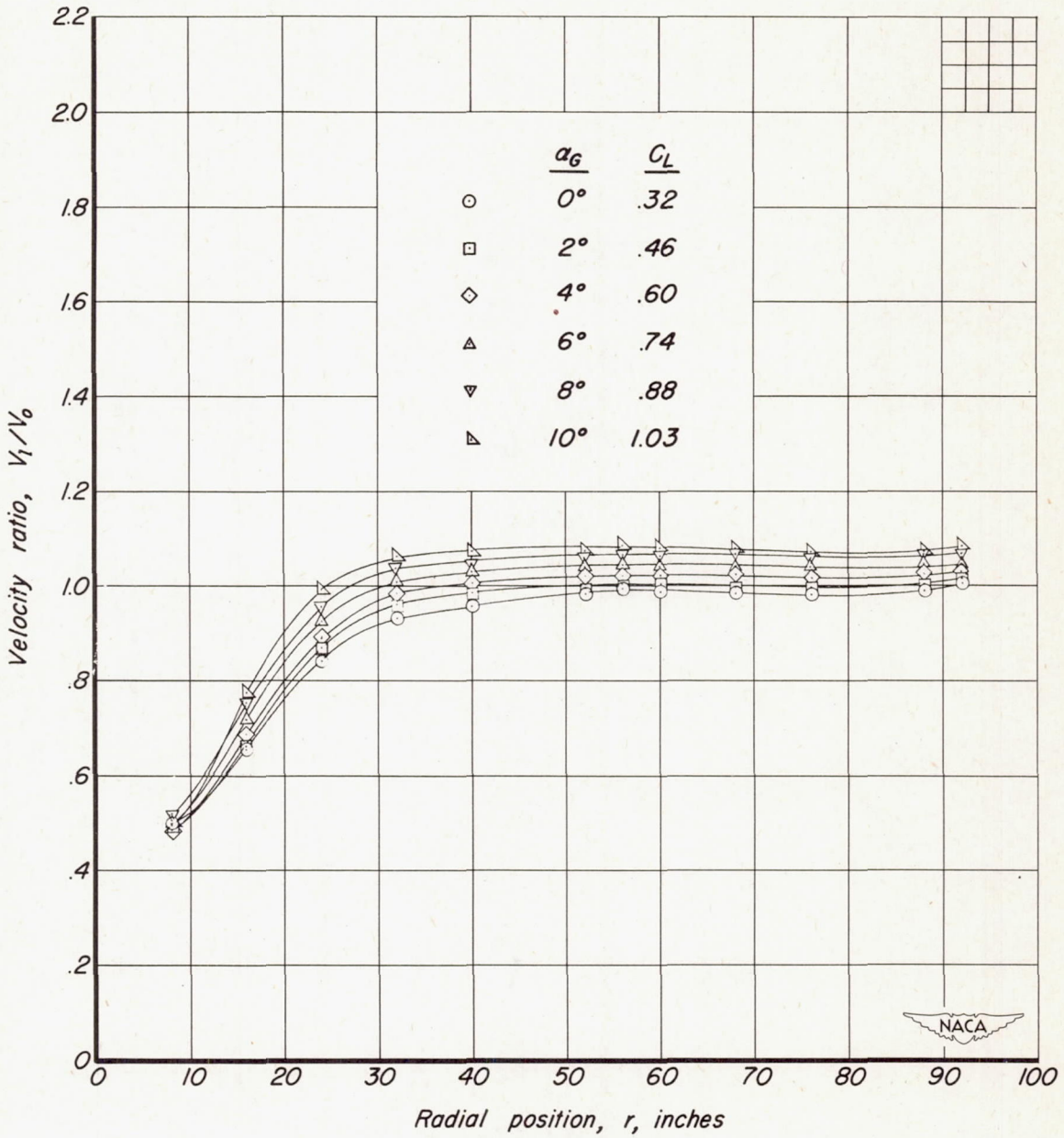
(p) $\Omega = 337.4°$.

Figure 15. – Concluded.



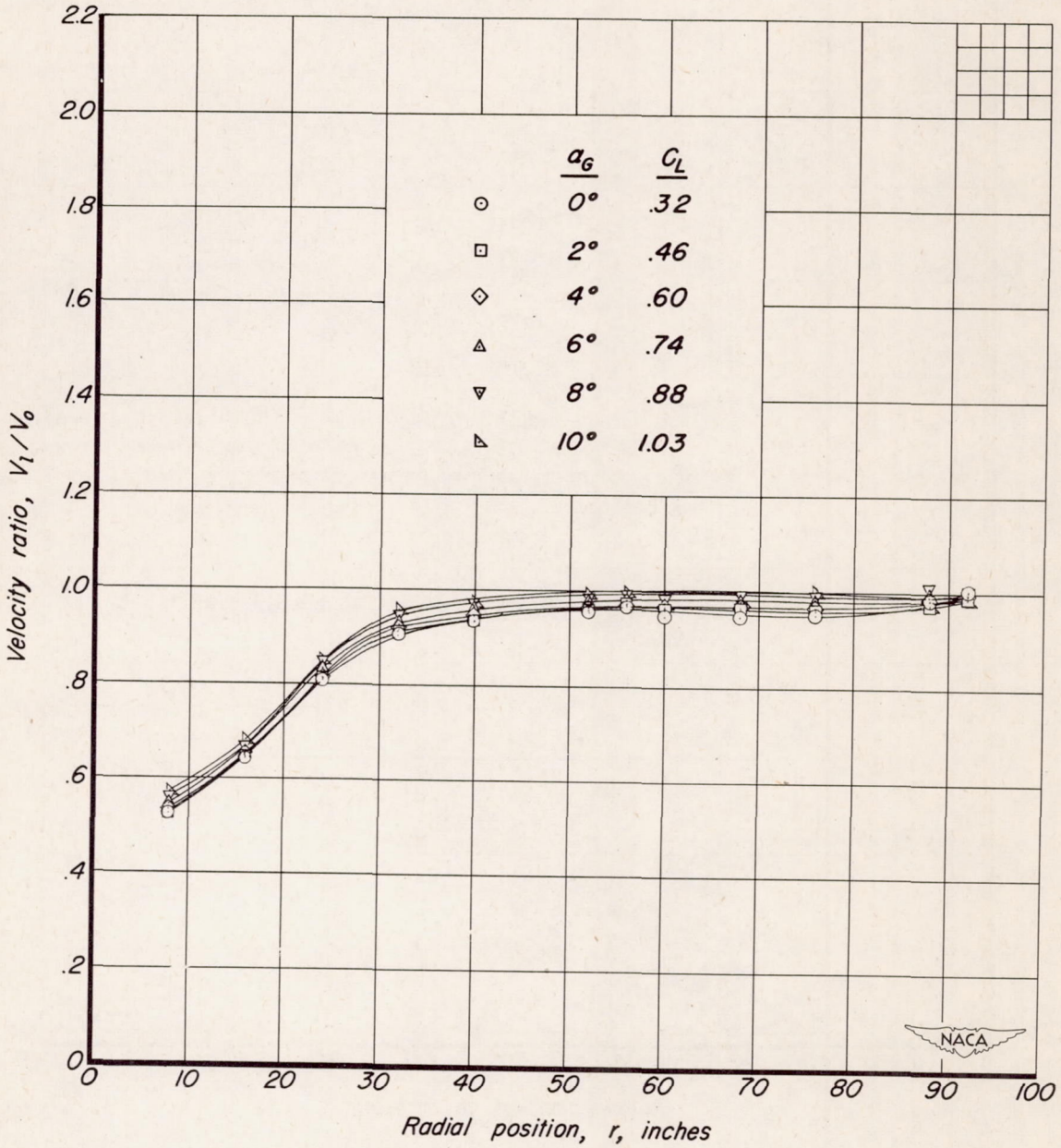
(a) $\Omega = 359.8°$.

Figure 16. – Variation of velocity ratio, V_l / V_o, with radial position for several angles of attack. m_l / m_o, .14; δ_f, 0°.



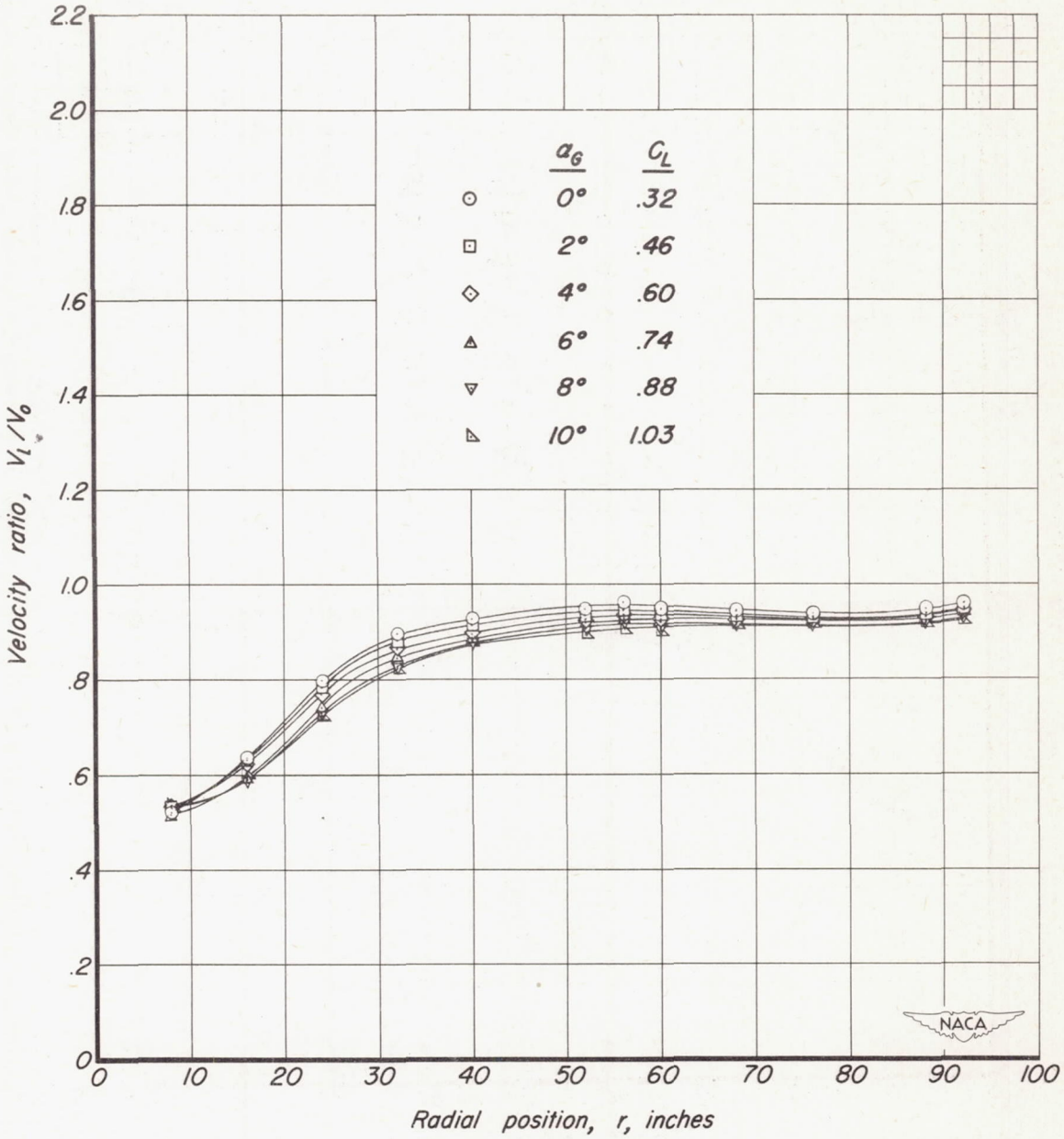
(b) $\Omega = 45.3°$.

Figure 16. - Continued.



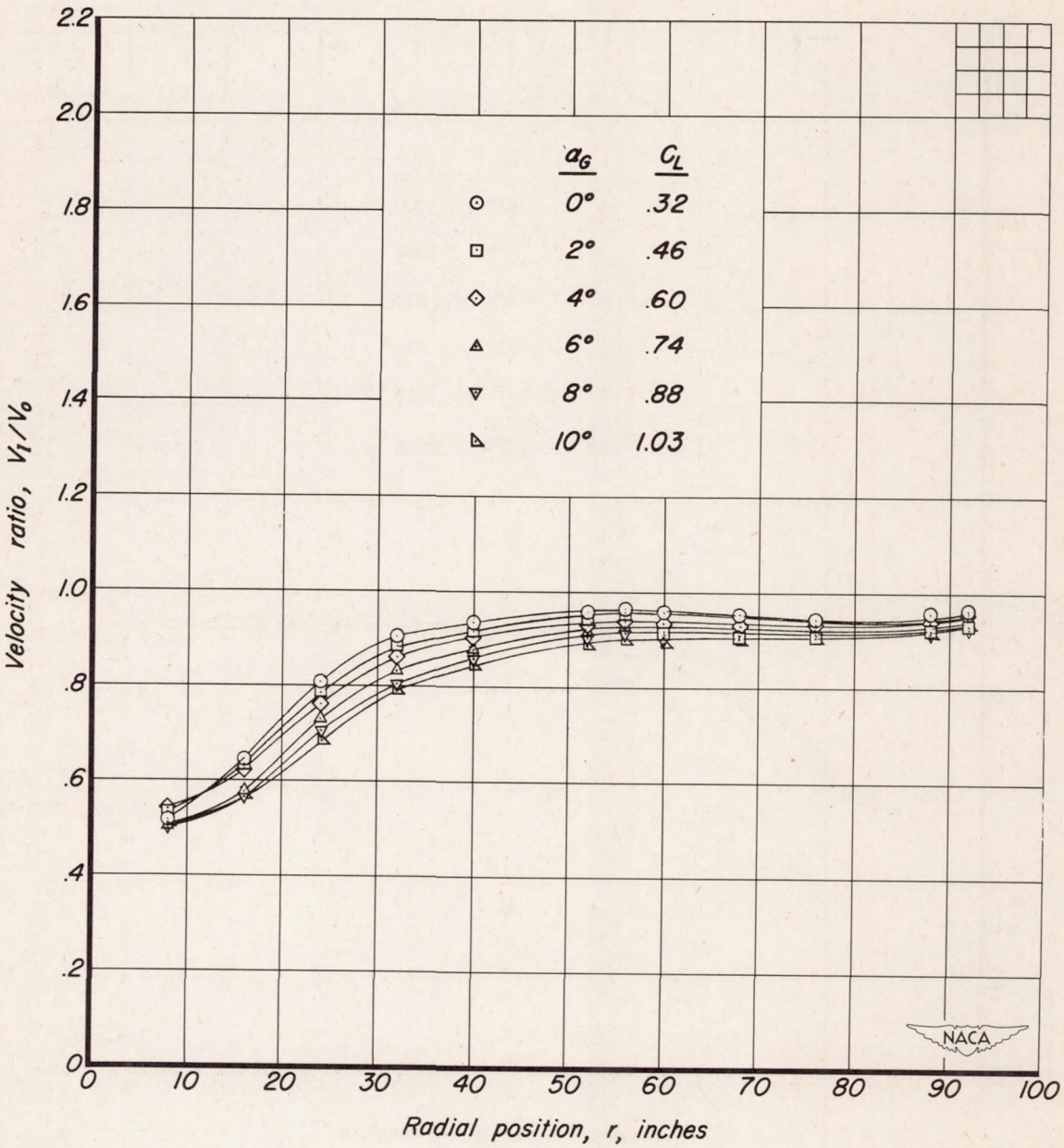
(c) $\Omega = 90.6°$.

Figure 16. - Continued.



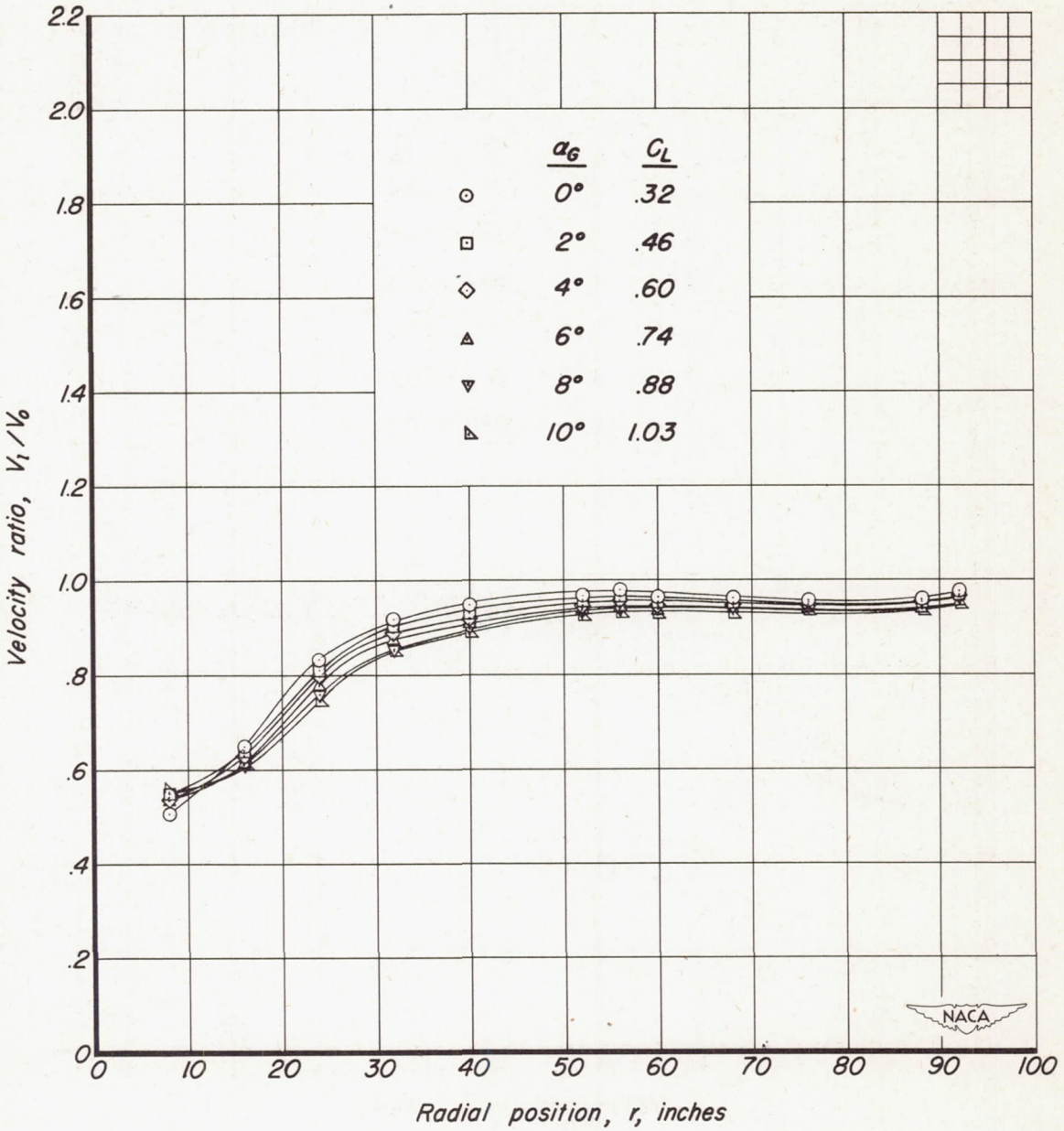
(d) Ω=135.6°.

Figure 16. - Continued.



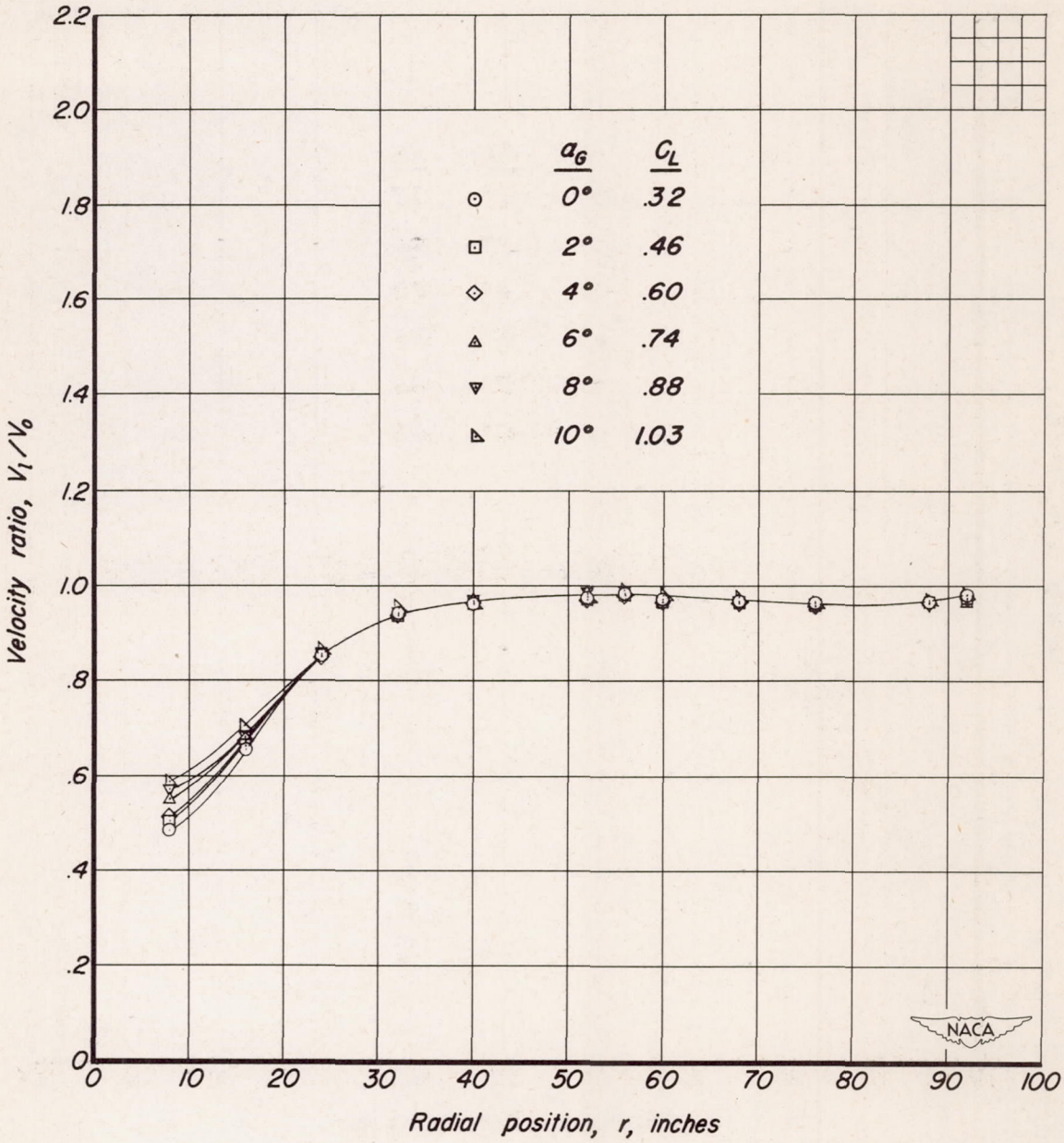
(e) Ω=180.0°.

Figure 16. - Continued.



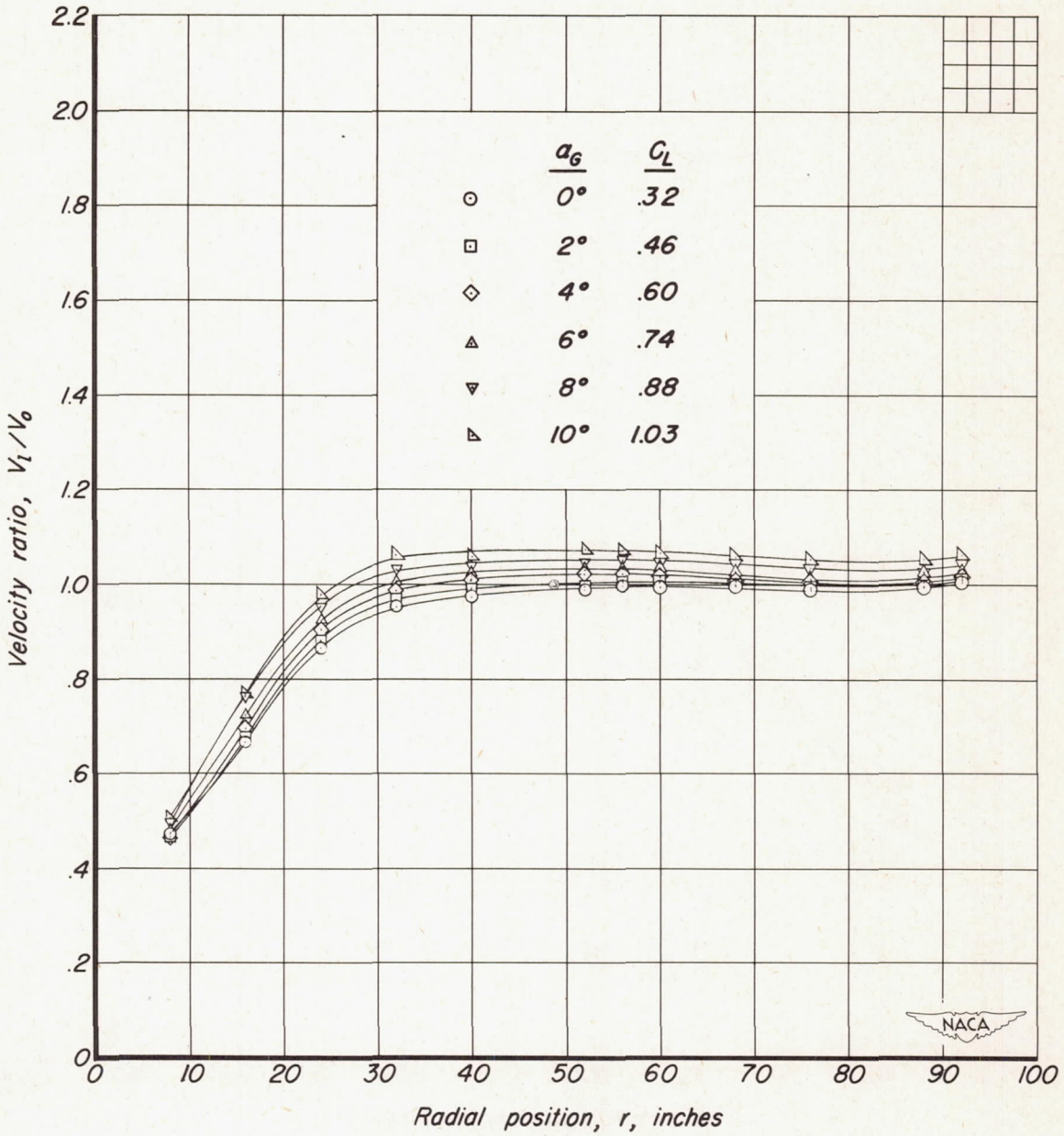
(f) Ω=225.0°.

Figure 16. - Continued.



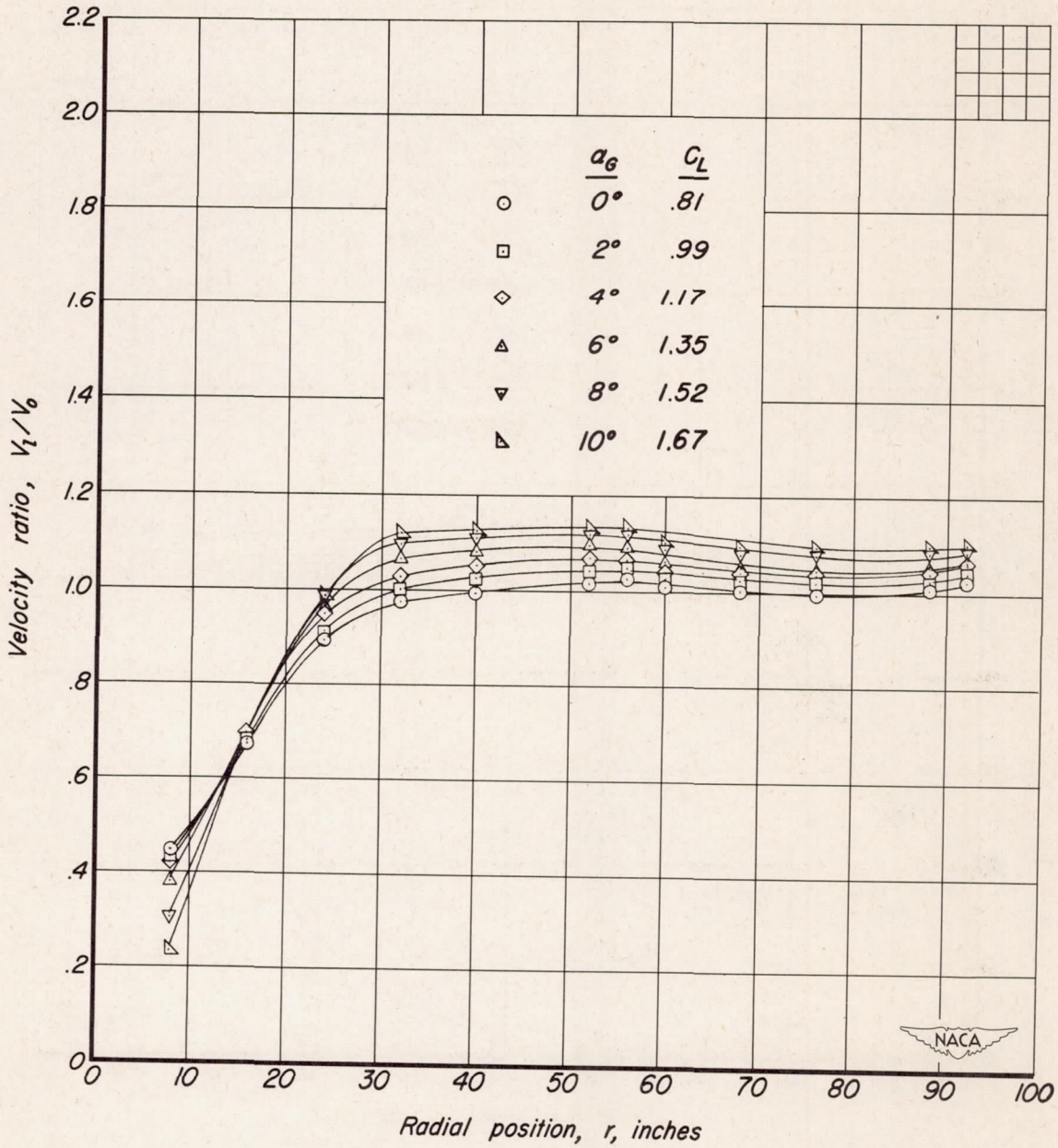
(g) Ω=269.8°.

Figure 16. - Continued.



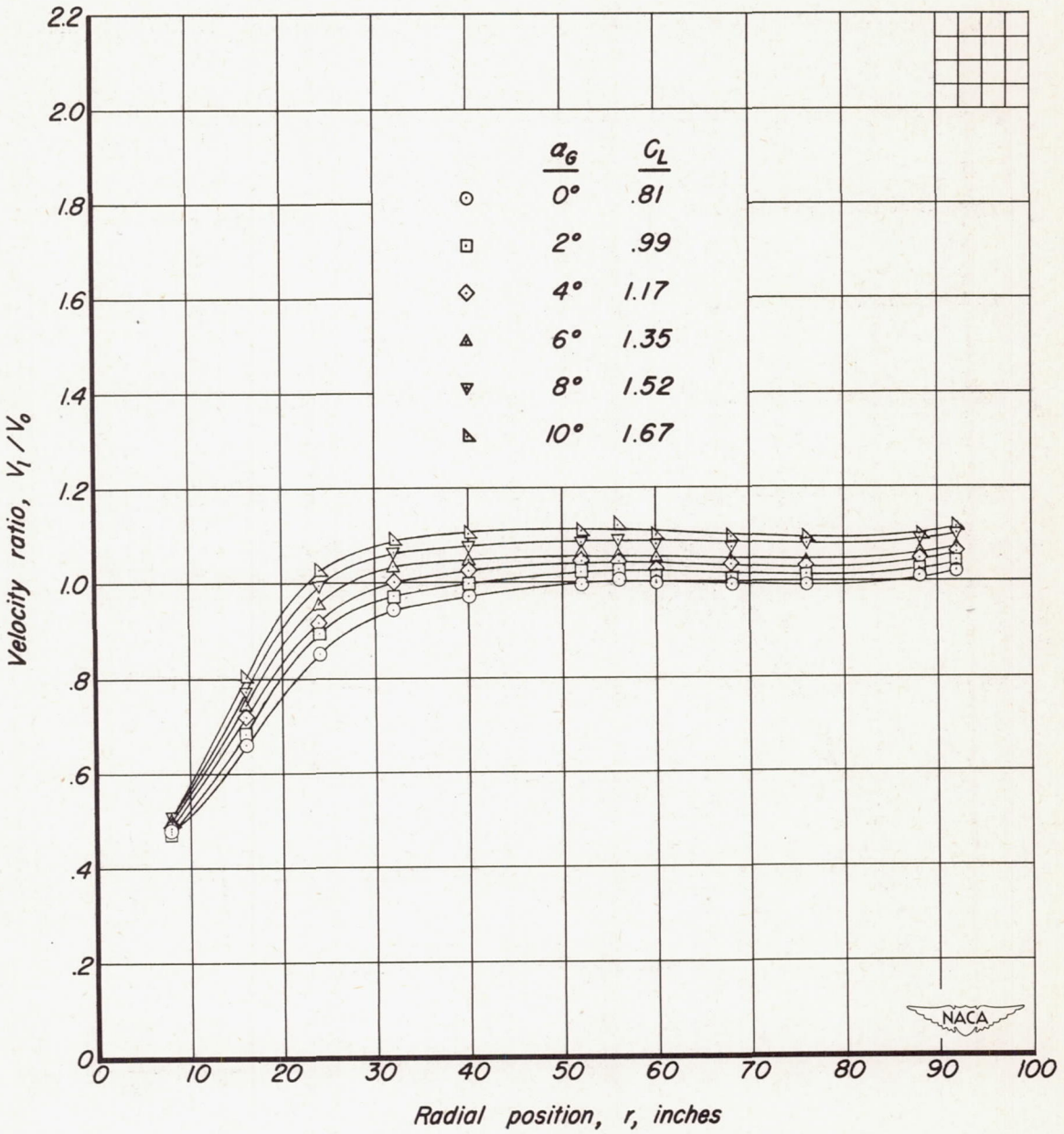
(h) Ω=314.9°.

Figure 16. - Concluded.



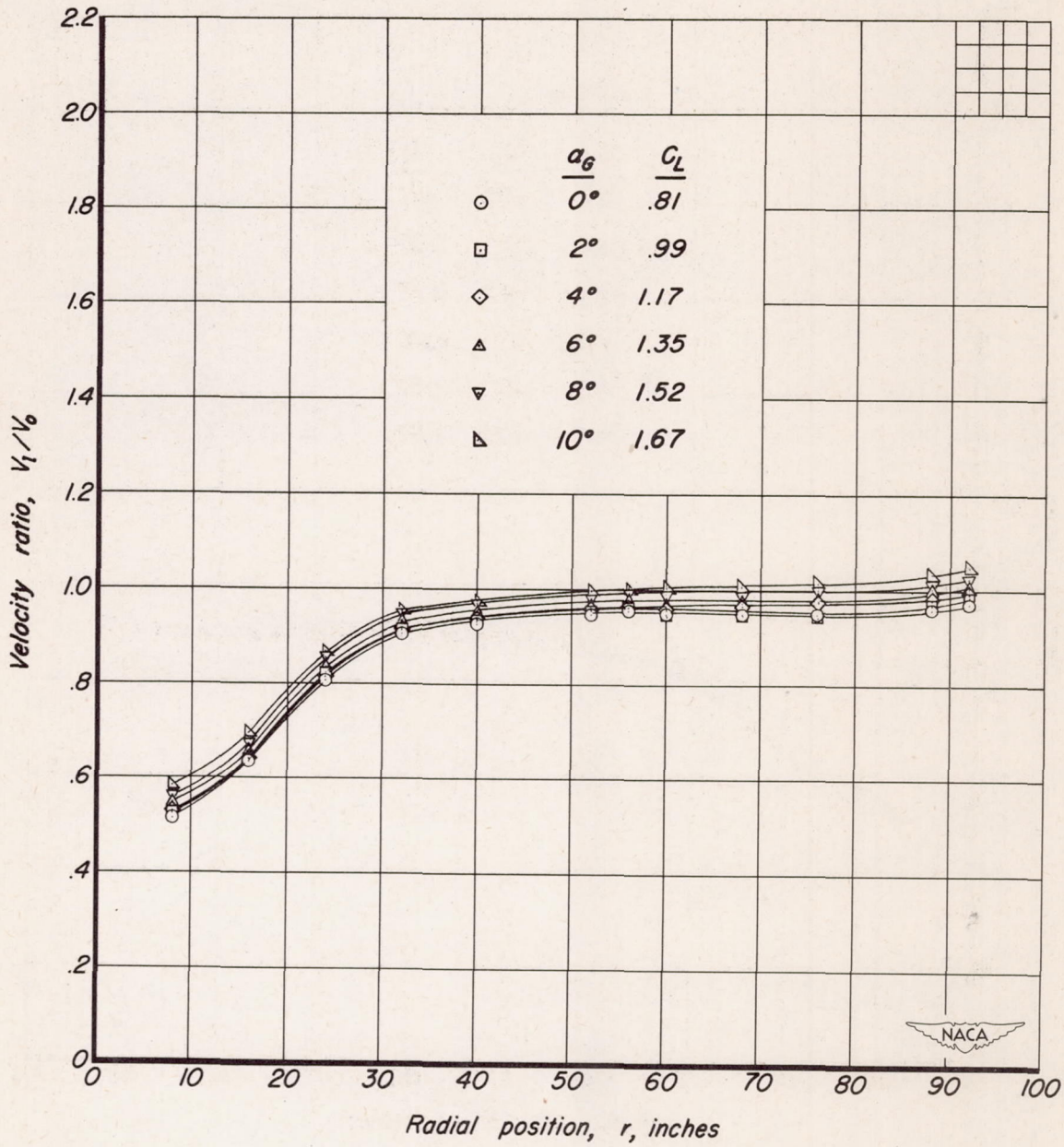
(a) $\Omega = 359.8°$.

Figure 17. – Variation of velocity ratio, V_l / V_o, with radial position for several angles of attack. m_l / m_o, .14; δ_f, 40°.



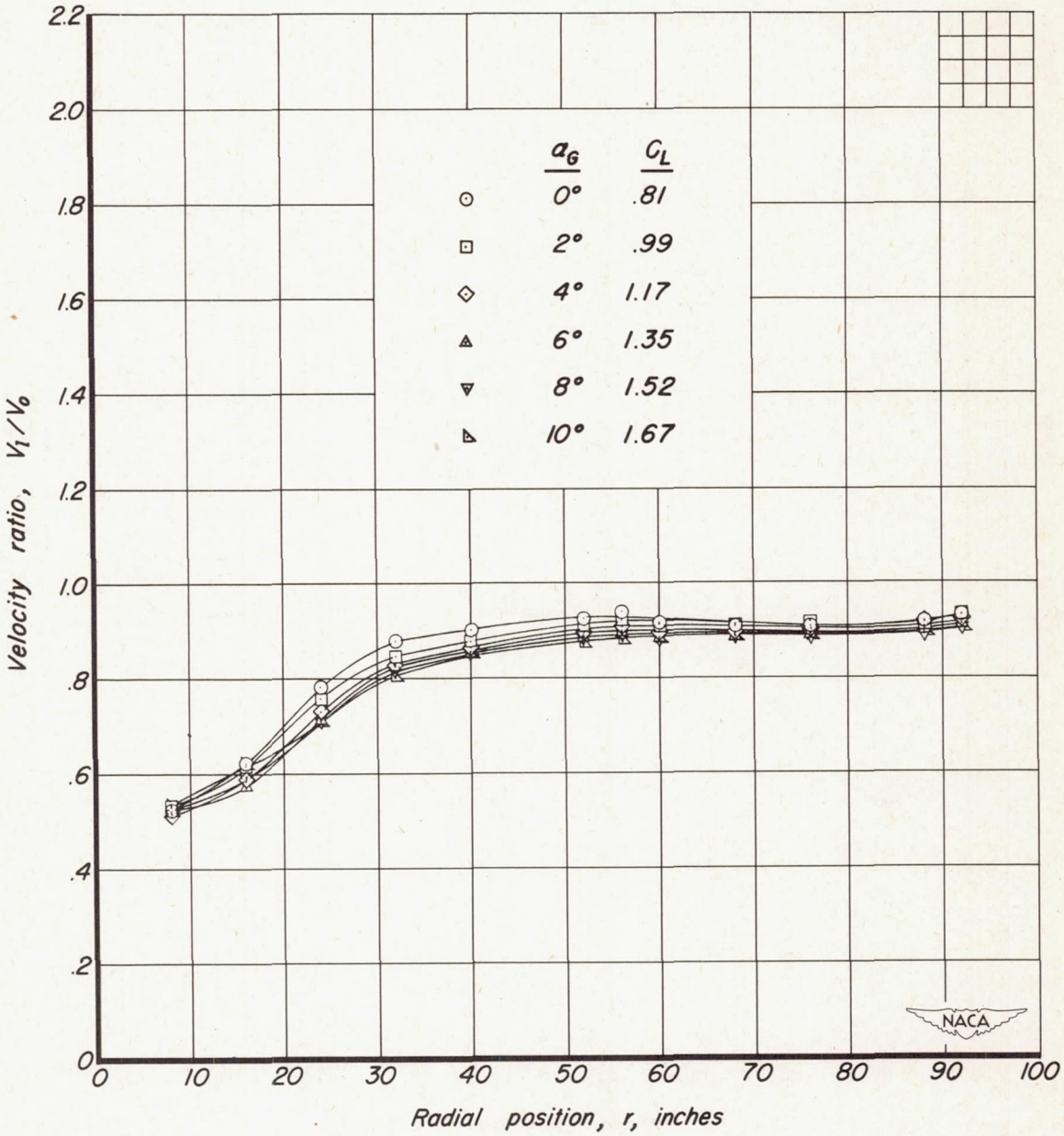
(b) $\Omega = 45.3°$.

Figure 17. - Continued.



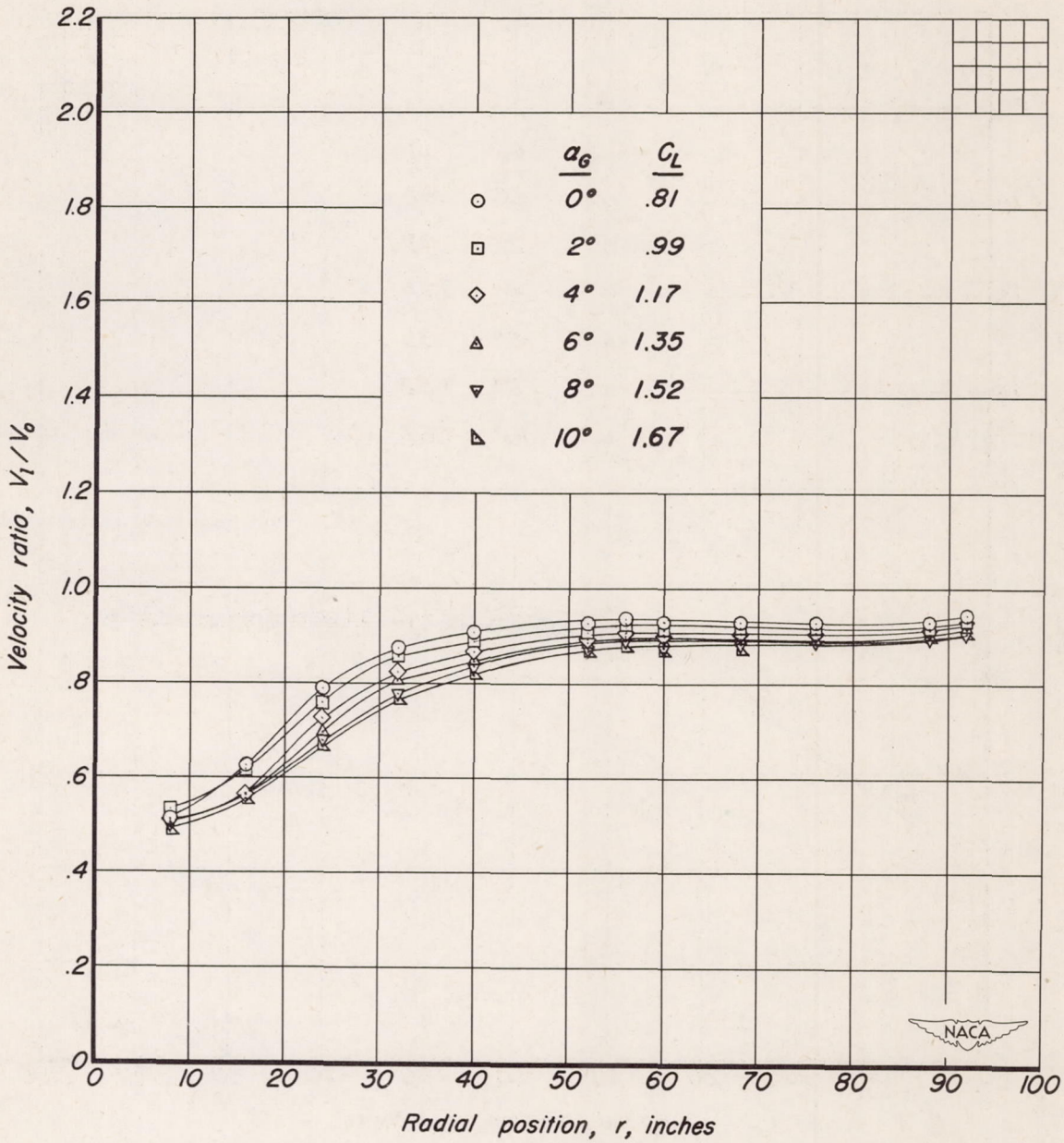
(c) $\Omega = 90.6°$.

Figure 17. - Continued.



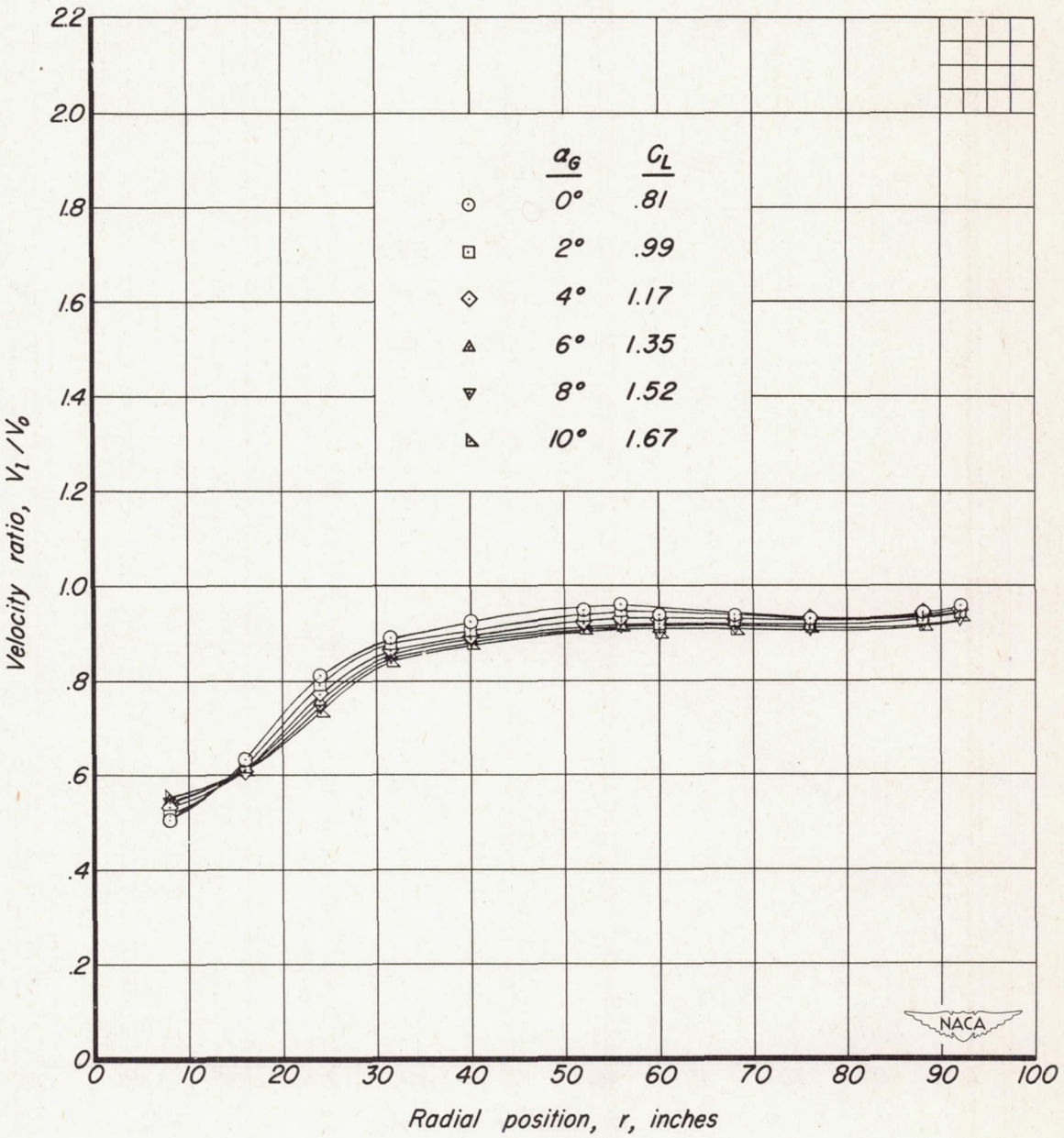
(d) Ω=135.6°.

Figure 17. - Continued.



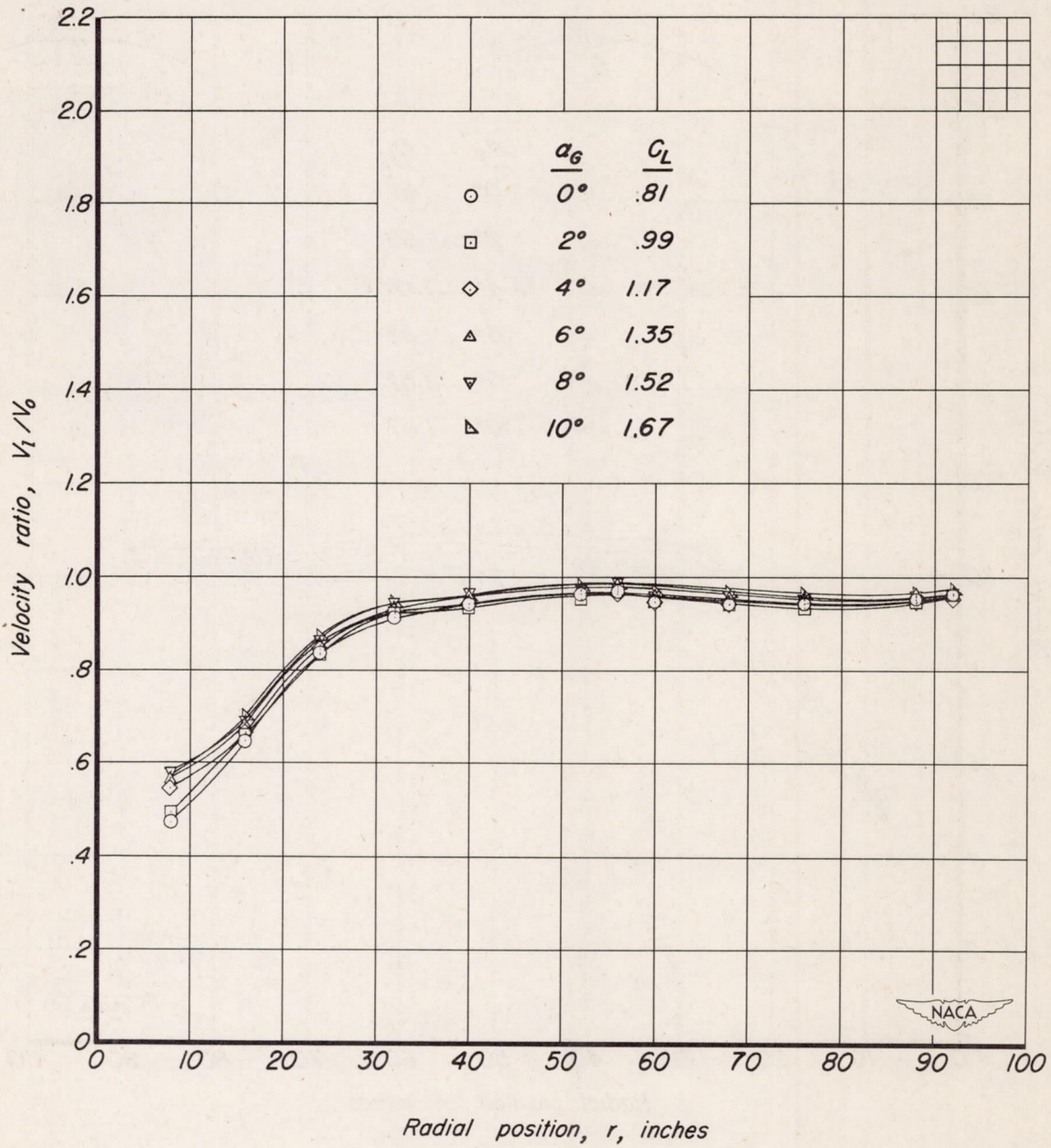
(e) Ω=180.0°.

Figure 17. - Continued.



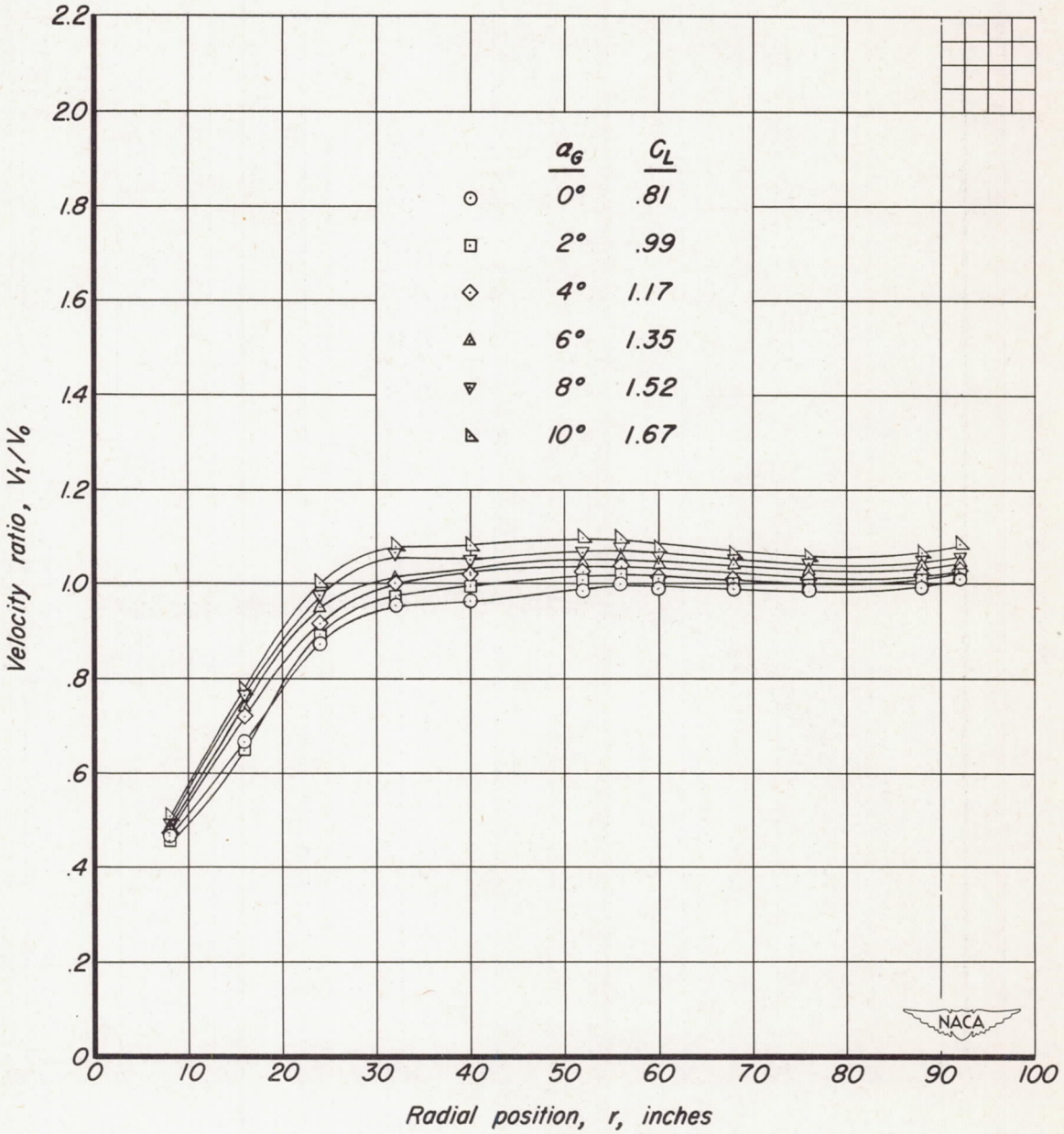
(f) $\Omega = 225.0°$.

Figure 17. - Continued.



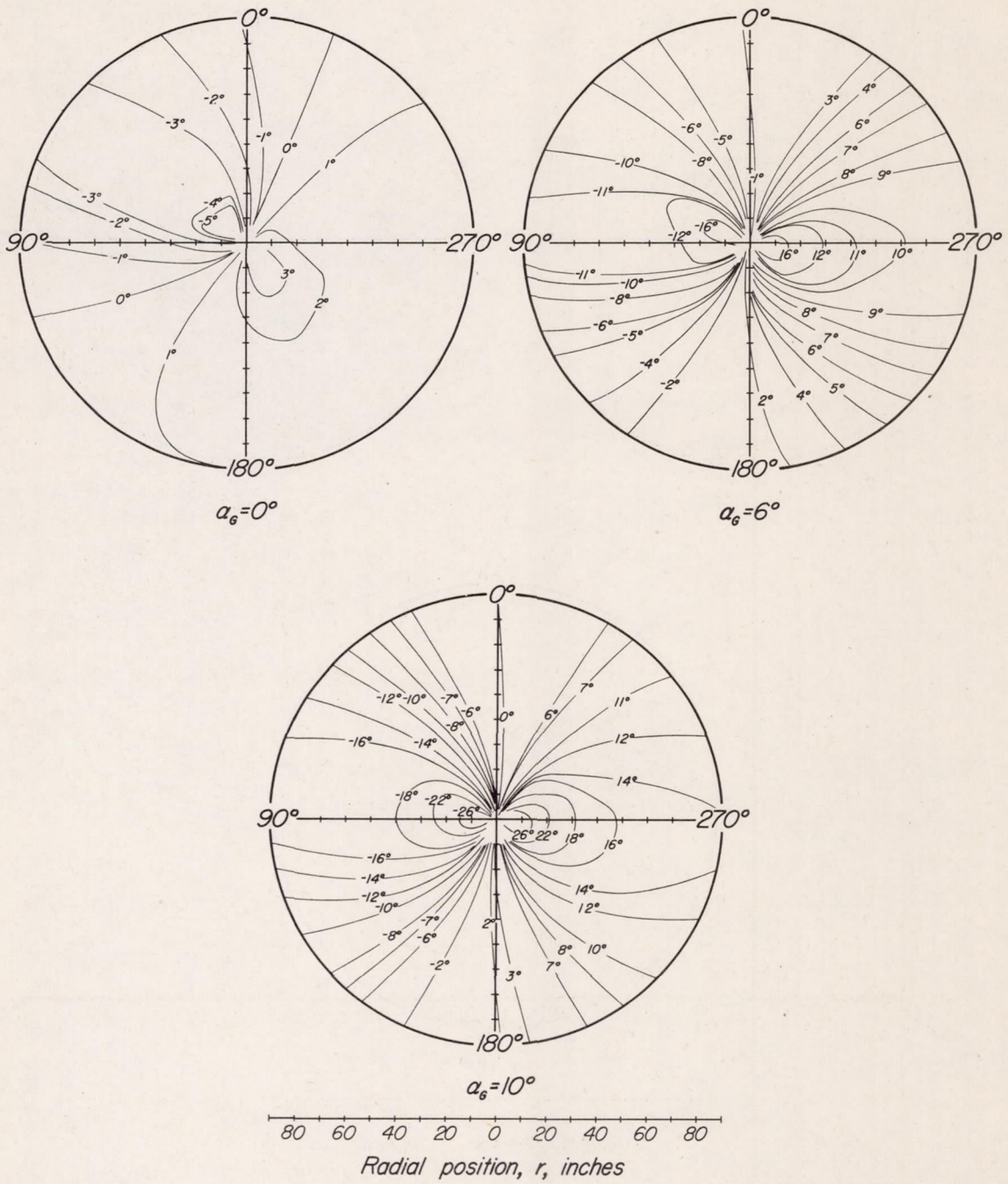
(g) Ω=269.8°.

Figure 17. - Continued.



(h) Ω=314.9°.

Figure 17. - Concluded.



NACA

Figure 18.- Contours of the angle of rotational flow, ψ, at the survey disk for several angles of attack. m_1/m_0, 0.29; δ_f, 0°.

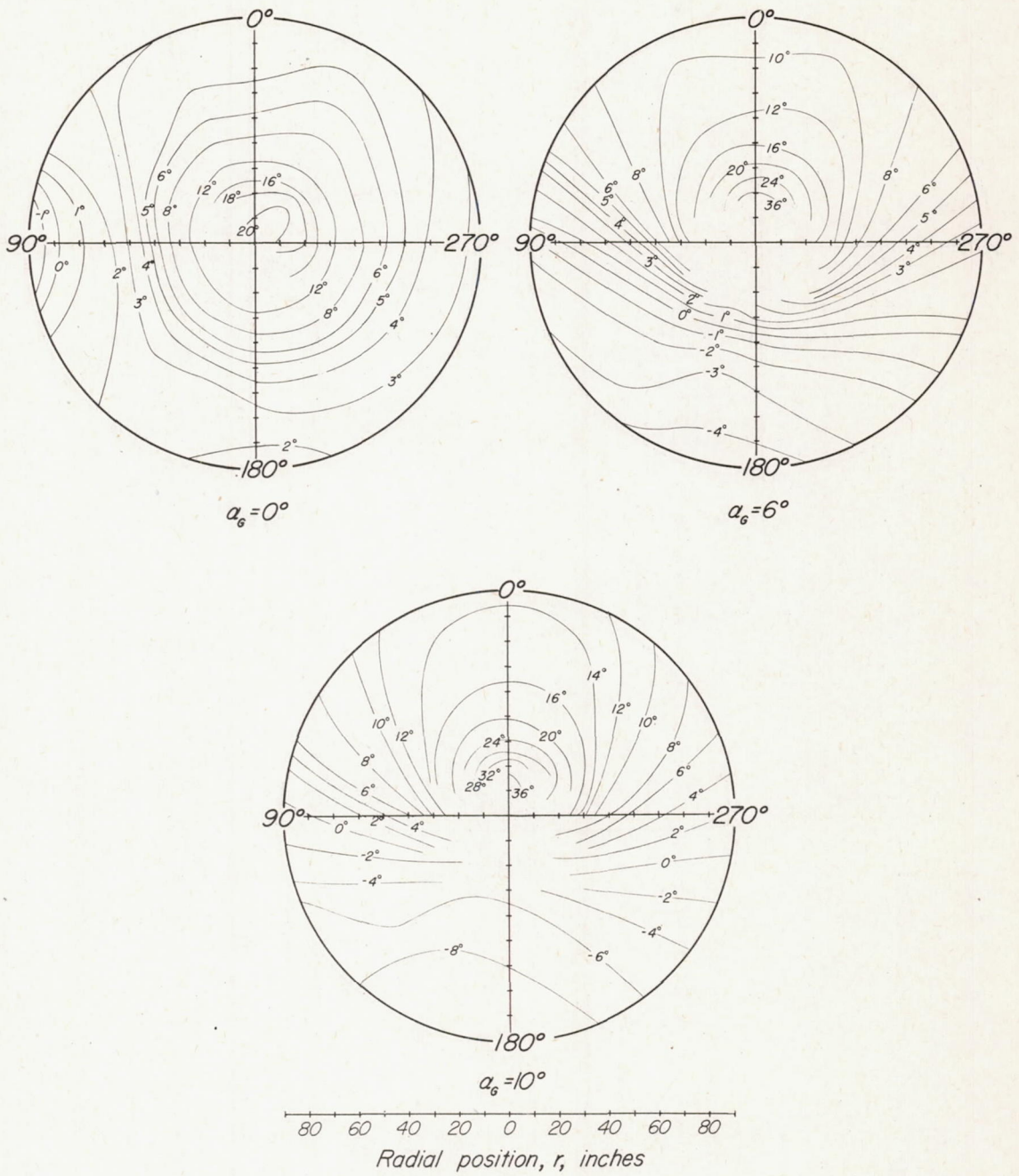


Figure 19.—Contours of the angle of outflow, θ, at the survey disk for several angles of attack. m_1/m_0, 0.29; δ_f, 0°.

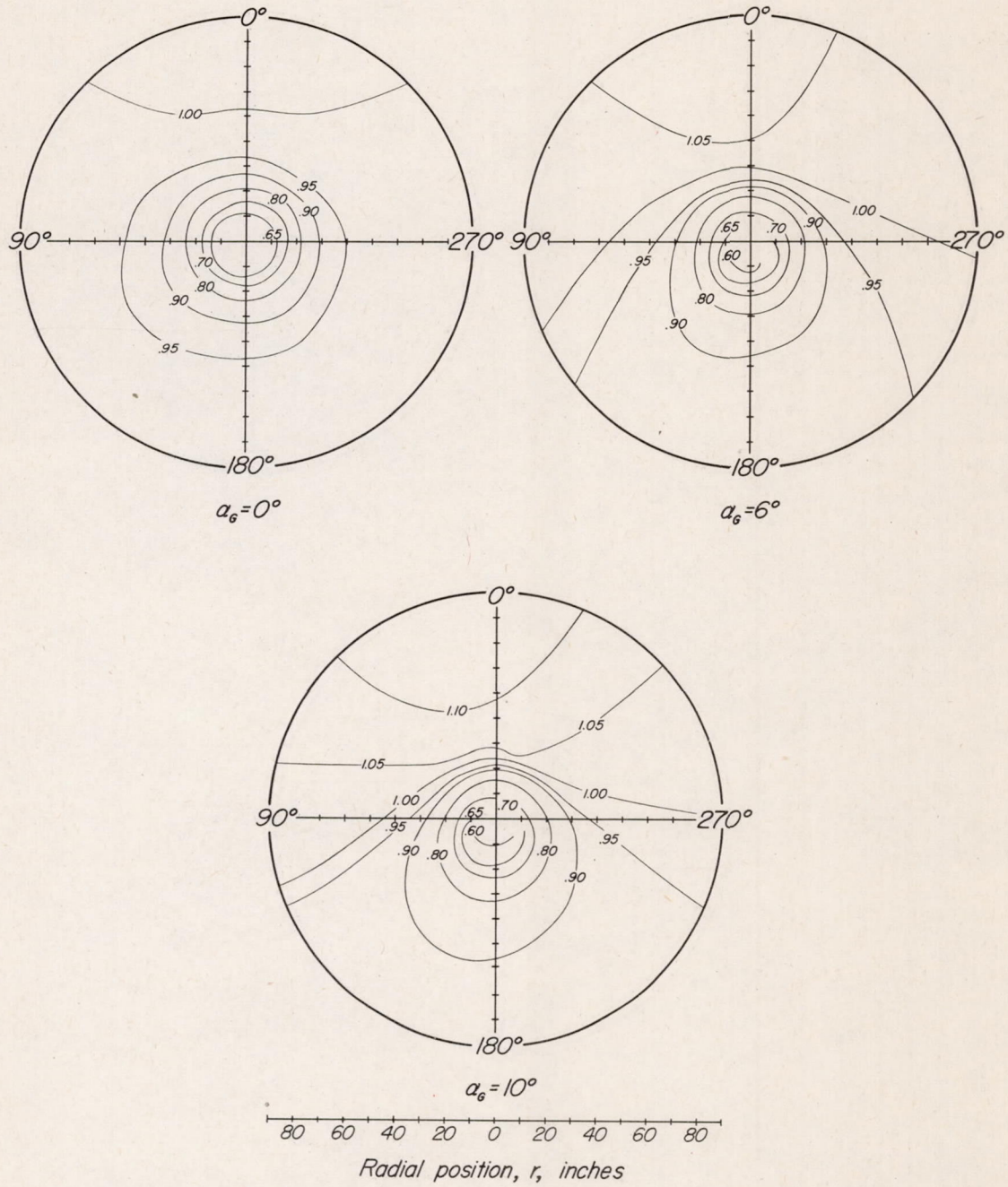


Figure 20.- Contours of the velocity ratio, V_l / V_o, at the survey disk for several angles of attack. m_l / m_o, 0.29; δ_f, 0°.

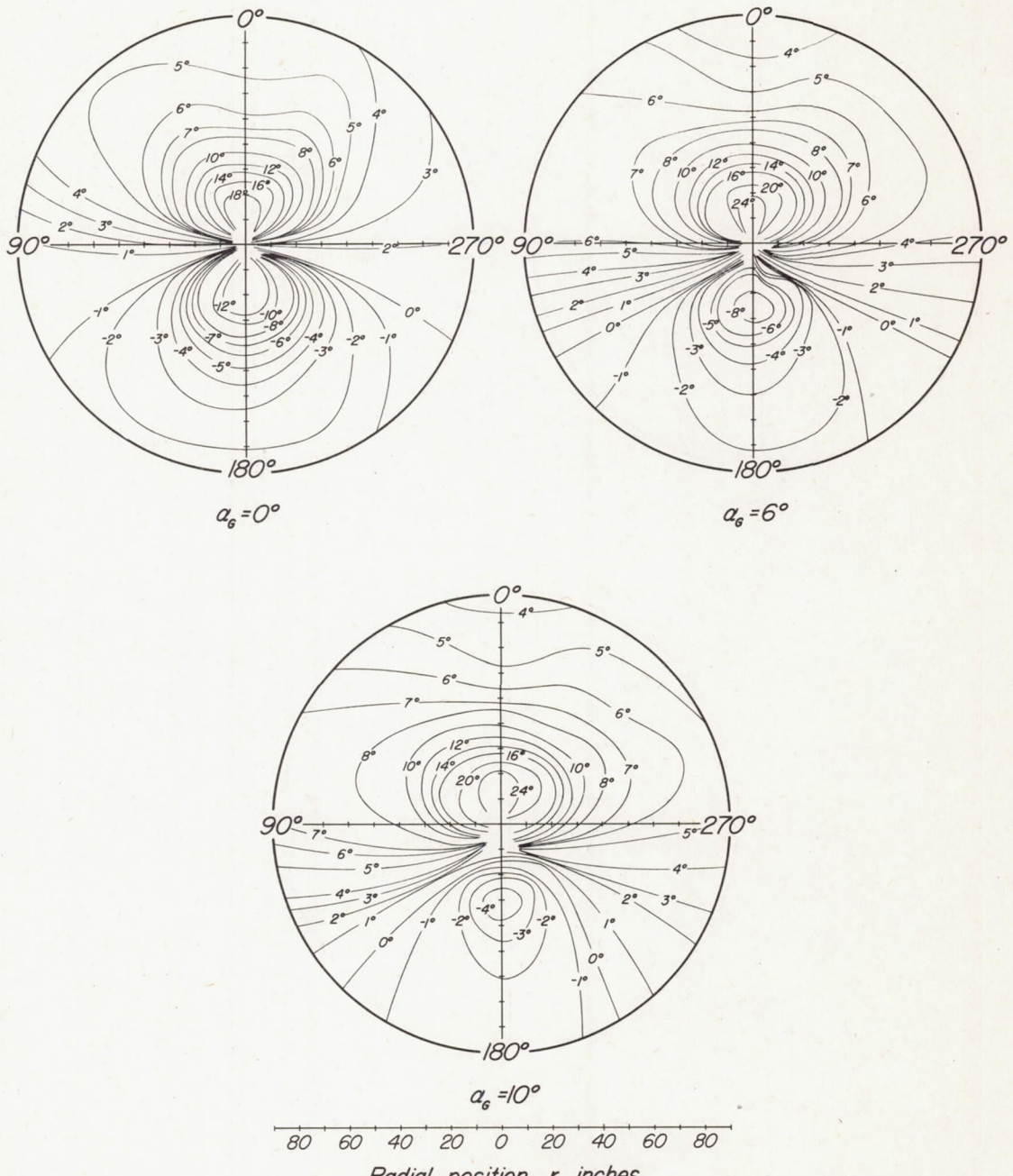


Figure 21.- Contours of the angle of upwash, ϵ, at the survey disk for several angles of attack. m_l/m_o, 0.29; δ_f, 0°.

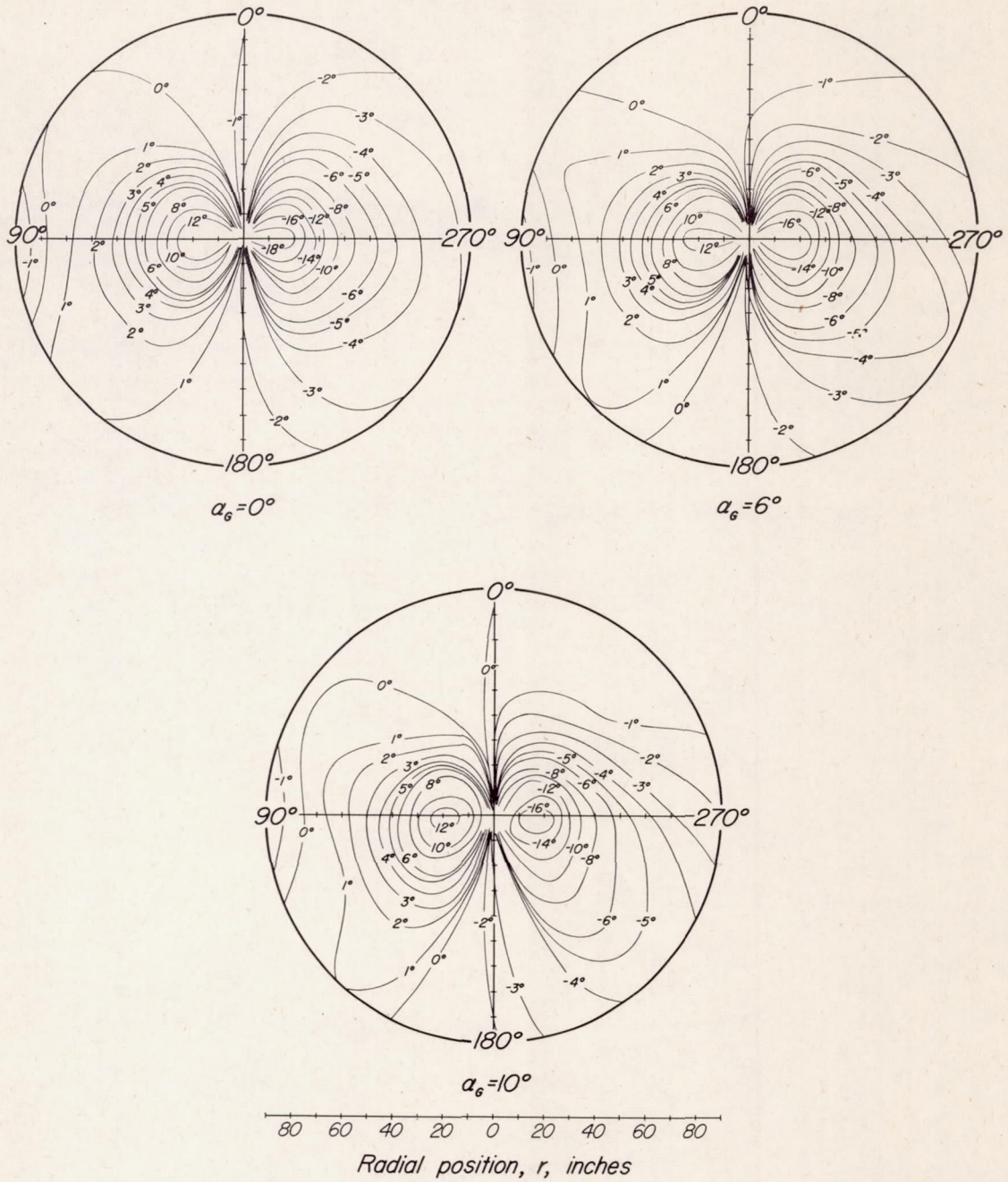
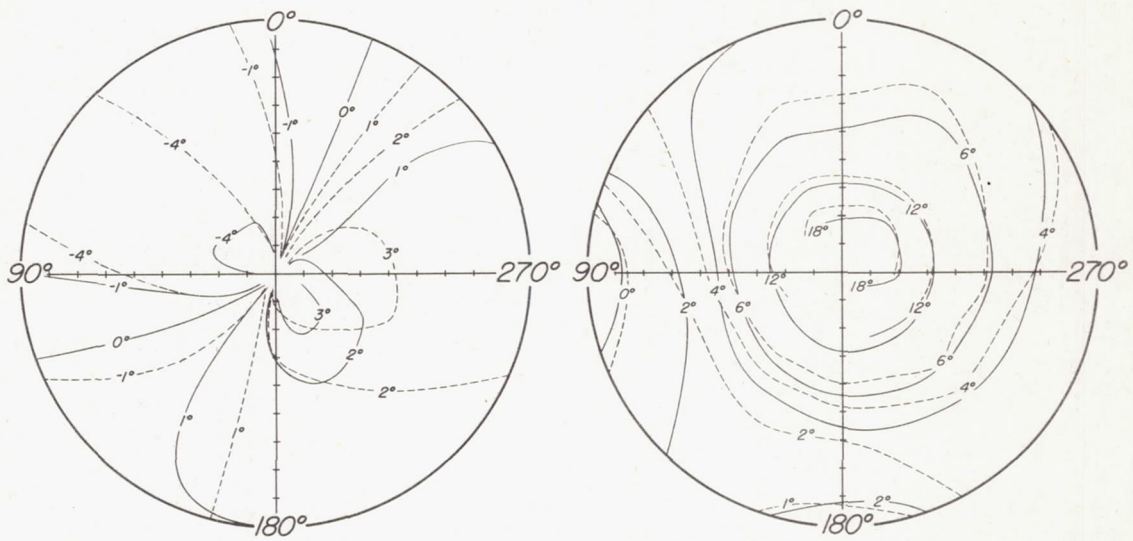
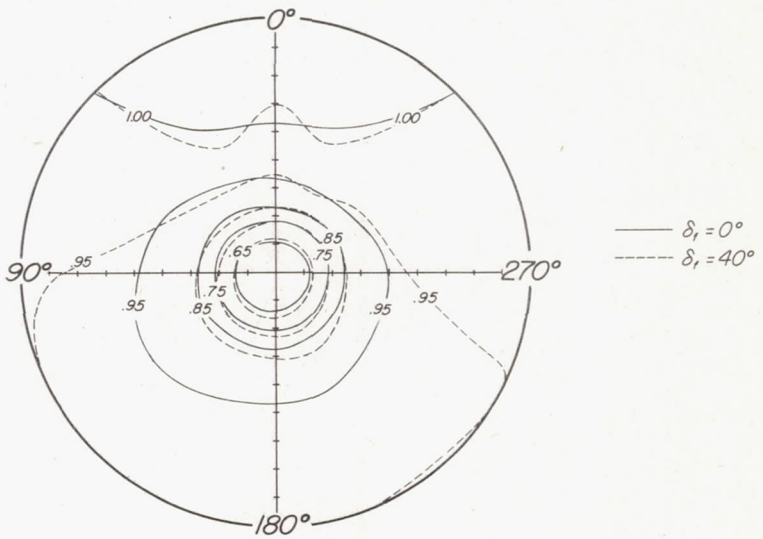


Figure 22.- Contours of the angle of sidewash, σ, at the survey disk for several angles of attack. m_1/m_o, 0.29; δ_f, 0°.



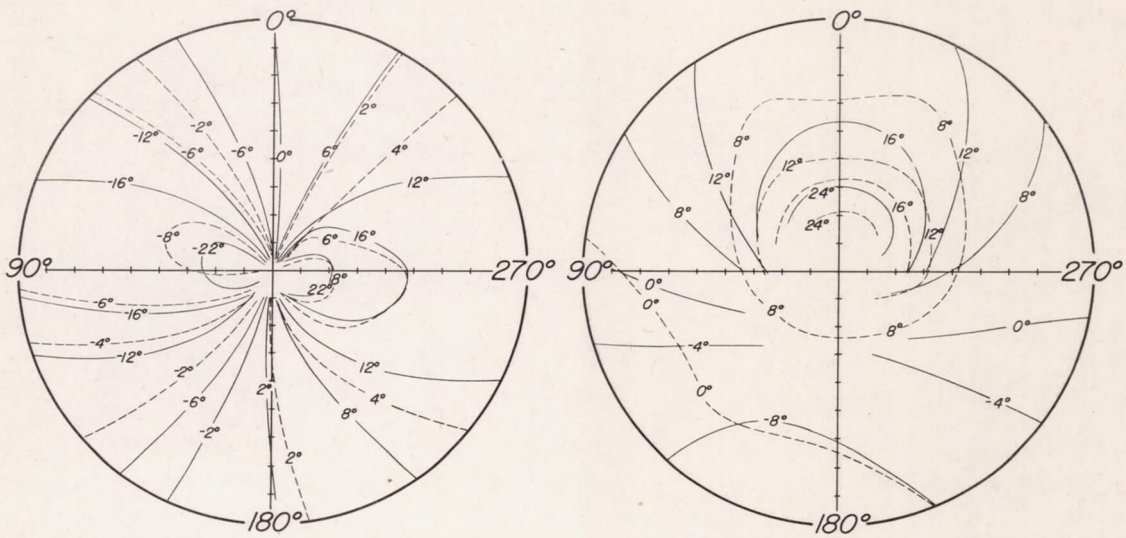
(a) Angle of rotational flow, ψ, deg.

(b) Angle of outflow, θ, deg.



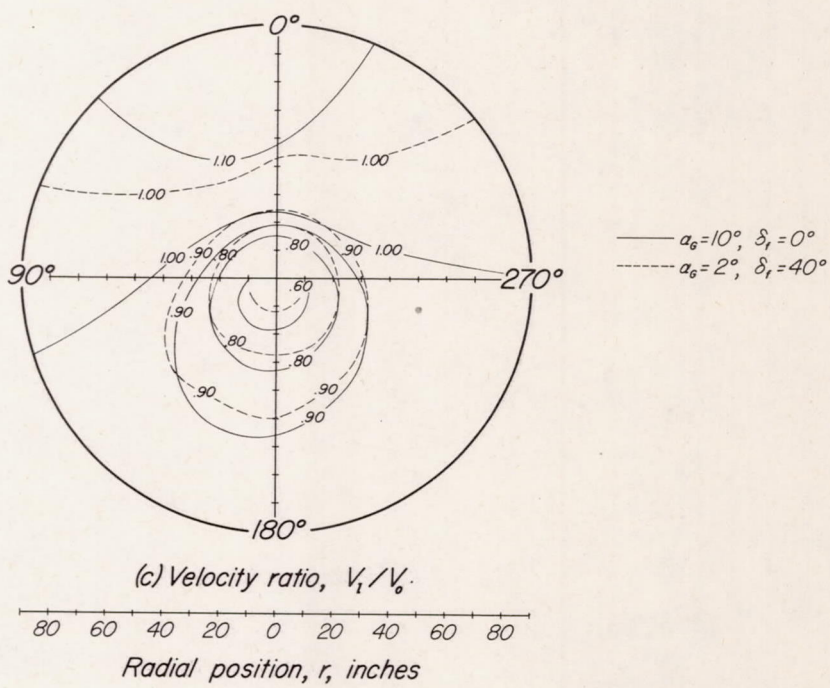
(c) Velocity ratio, V_1/V_o.

Figure 23.- Contours of the flow parameters at the survey disk for two wing-flap deflections. α_G, 0.



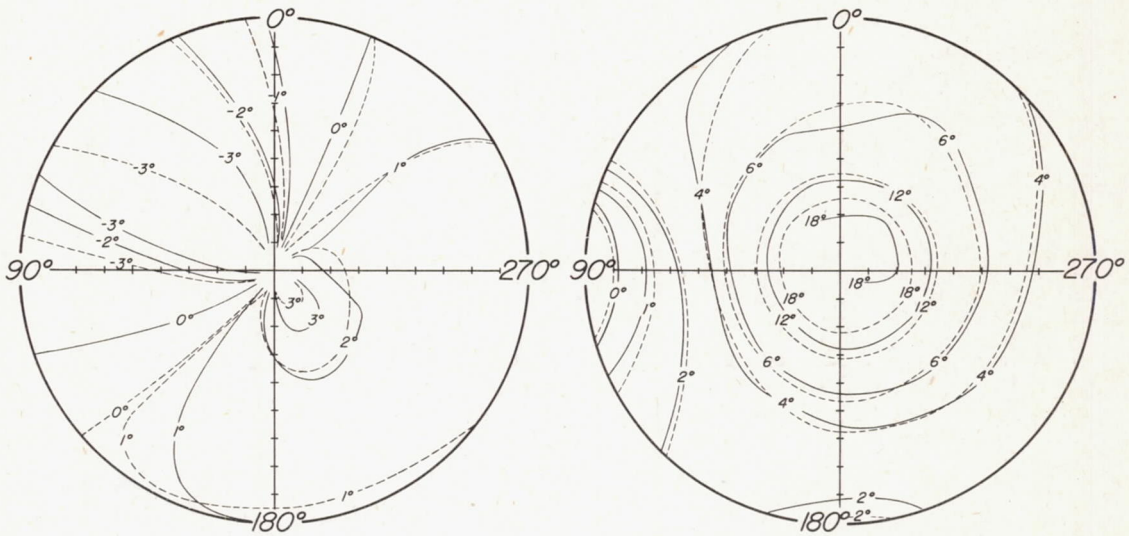
(a) Angle of rotational flow, ψ, deg

(b) Angle of outflow, θ, deg



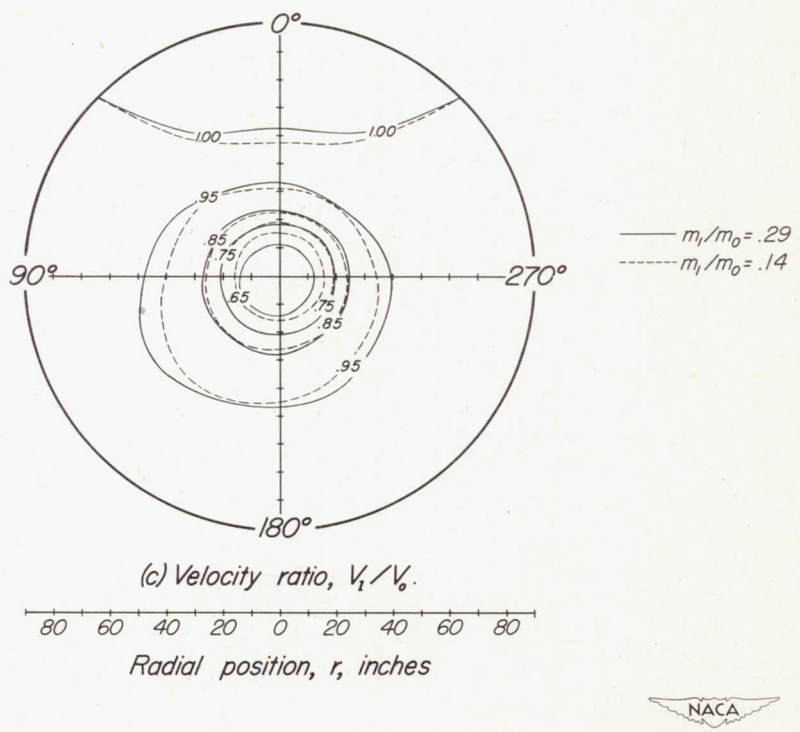
(c) Velocity ratio, V_1/V_o.

Figure 24.- Contours of the flow parameters at the survey disk for two conditions at a constant lift coefficient of approximately 1.0.



(a) Angle of rotational flow, ψ, deg.

(b) Angle of outflow, θ, deg.



(c) Velocity ratio, V_1/V_0.

Figure 25.- Contours of the flow parameters at the survey disk for two nacelle inlet mass-flow ratios. α_G, 0°; δ_f, 0°.

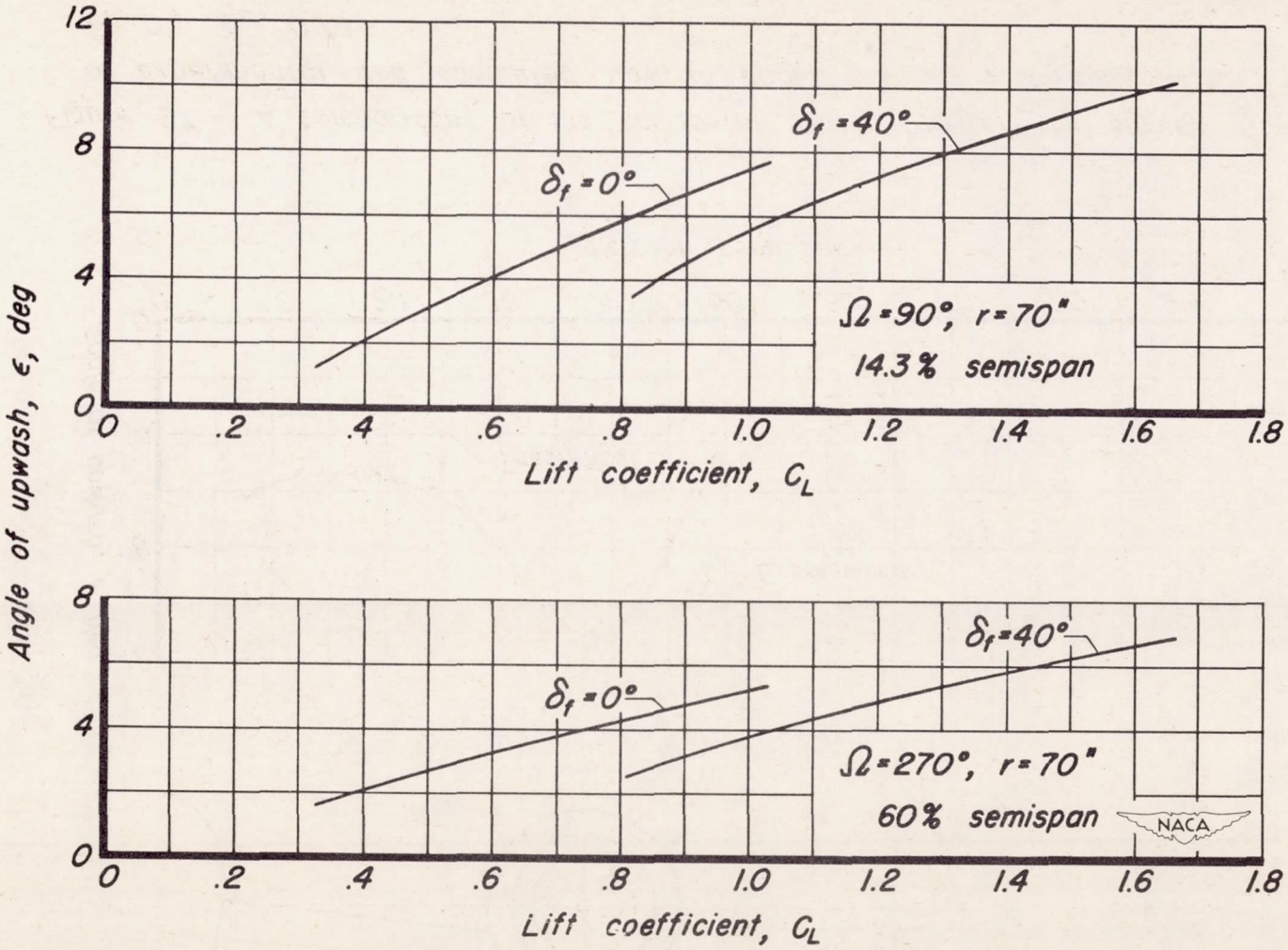


Figure 26.- Variation of angle of upwash with lift coefficient for two wing-flap deflections.

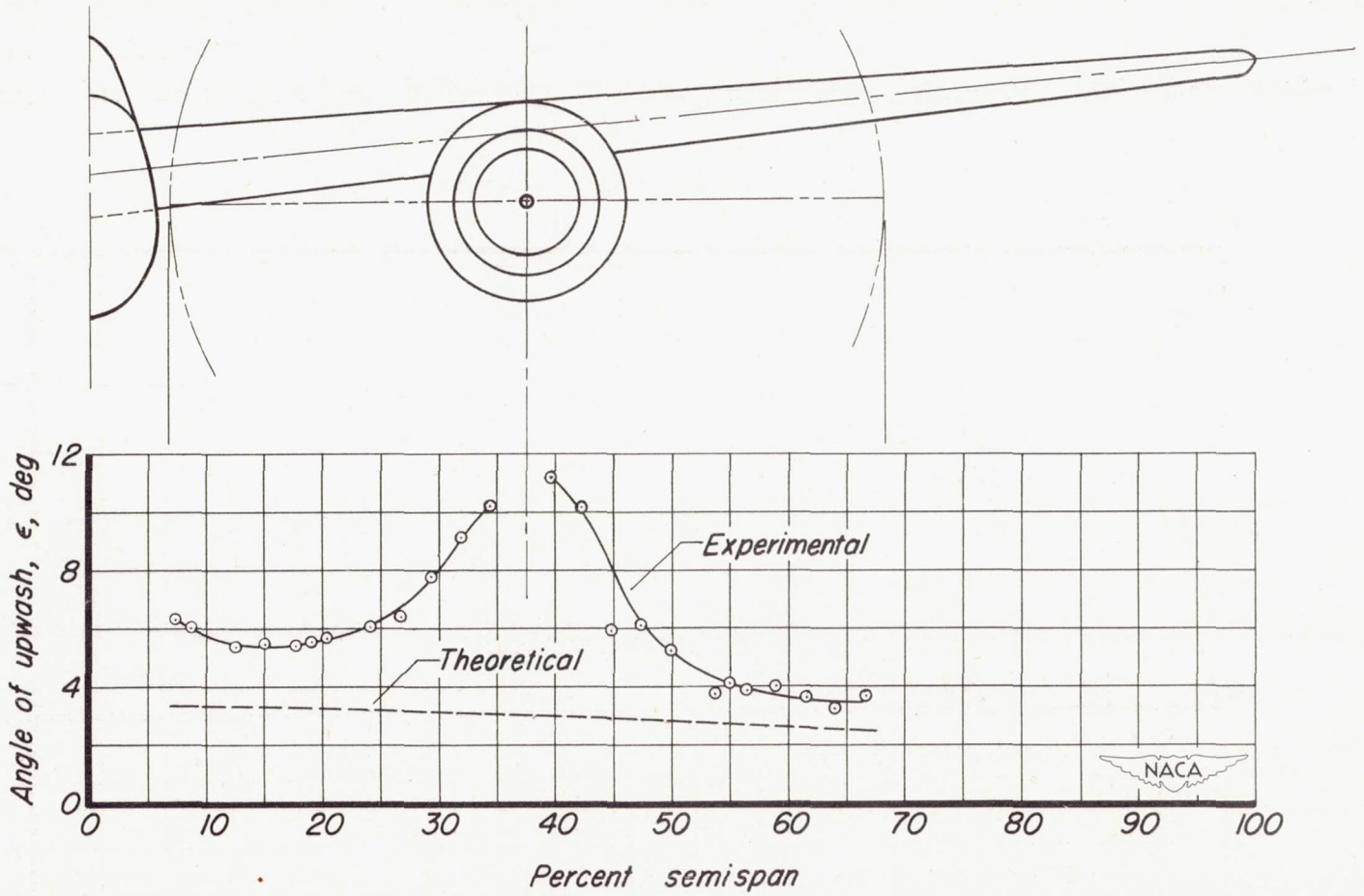


Figure 27. - A comparison, at the horizontal center line of the survey disk, of experimental and computed upwash angles. α_G, 6°; m_l/m_o, 0.29; δ_f, 0°; C_L, 0.74.

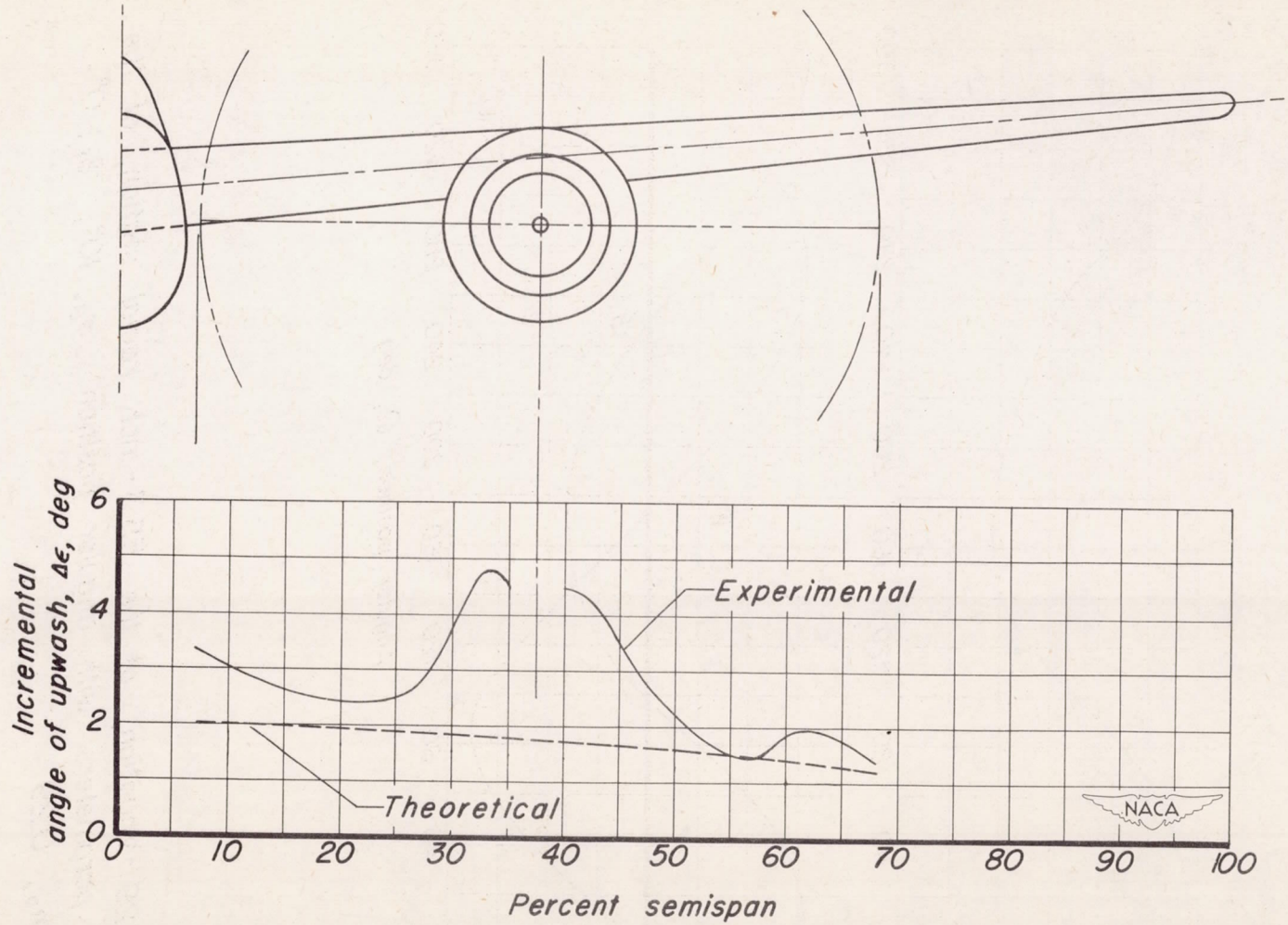


Figure 28. - Upwash angle increment, at the horizontal center line of the survey disk, due to wing-flap deflection of 40°. α_G, 6°.

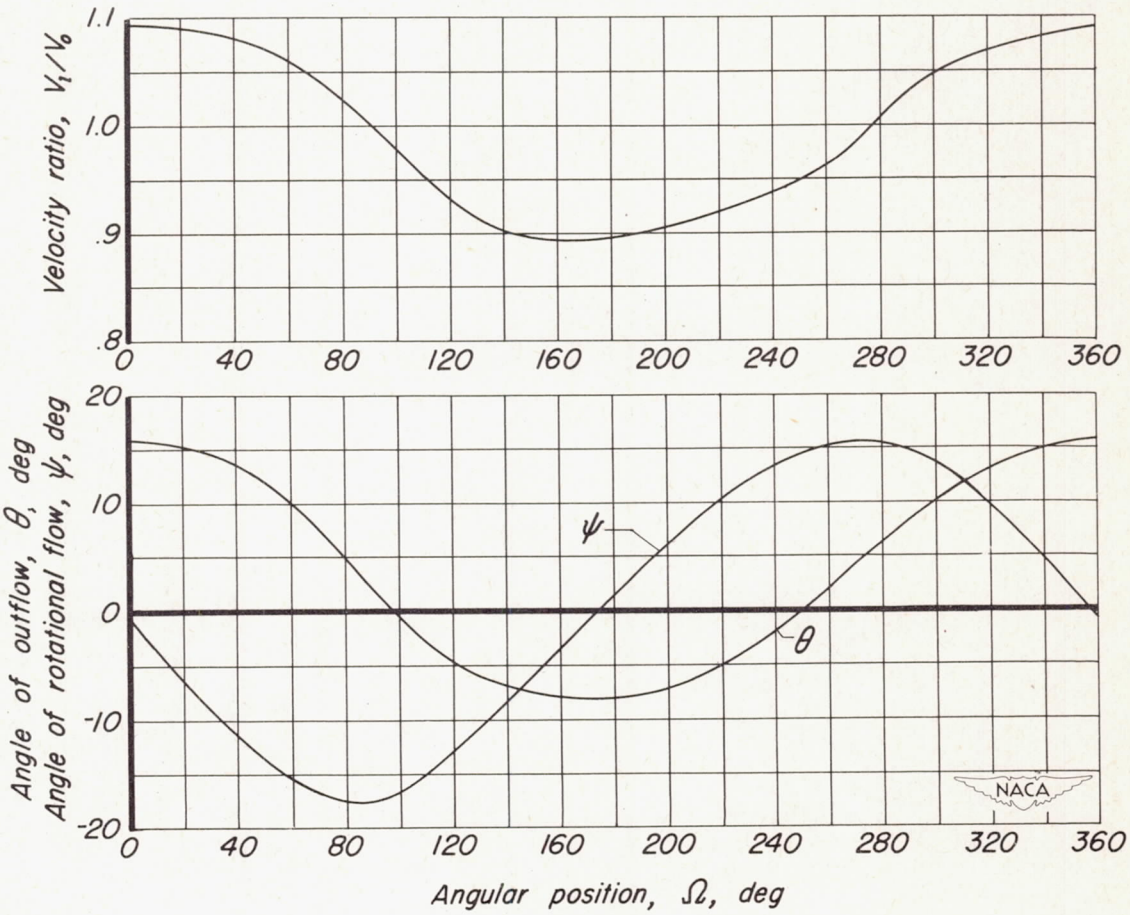


Figure 29.-Variation, at the 55.3-inch radial station, of the flow parameters with angular position. α_G, 10°; δ_f, 0°; m_1/m_0, 0.29.

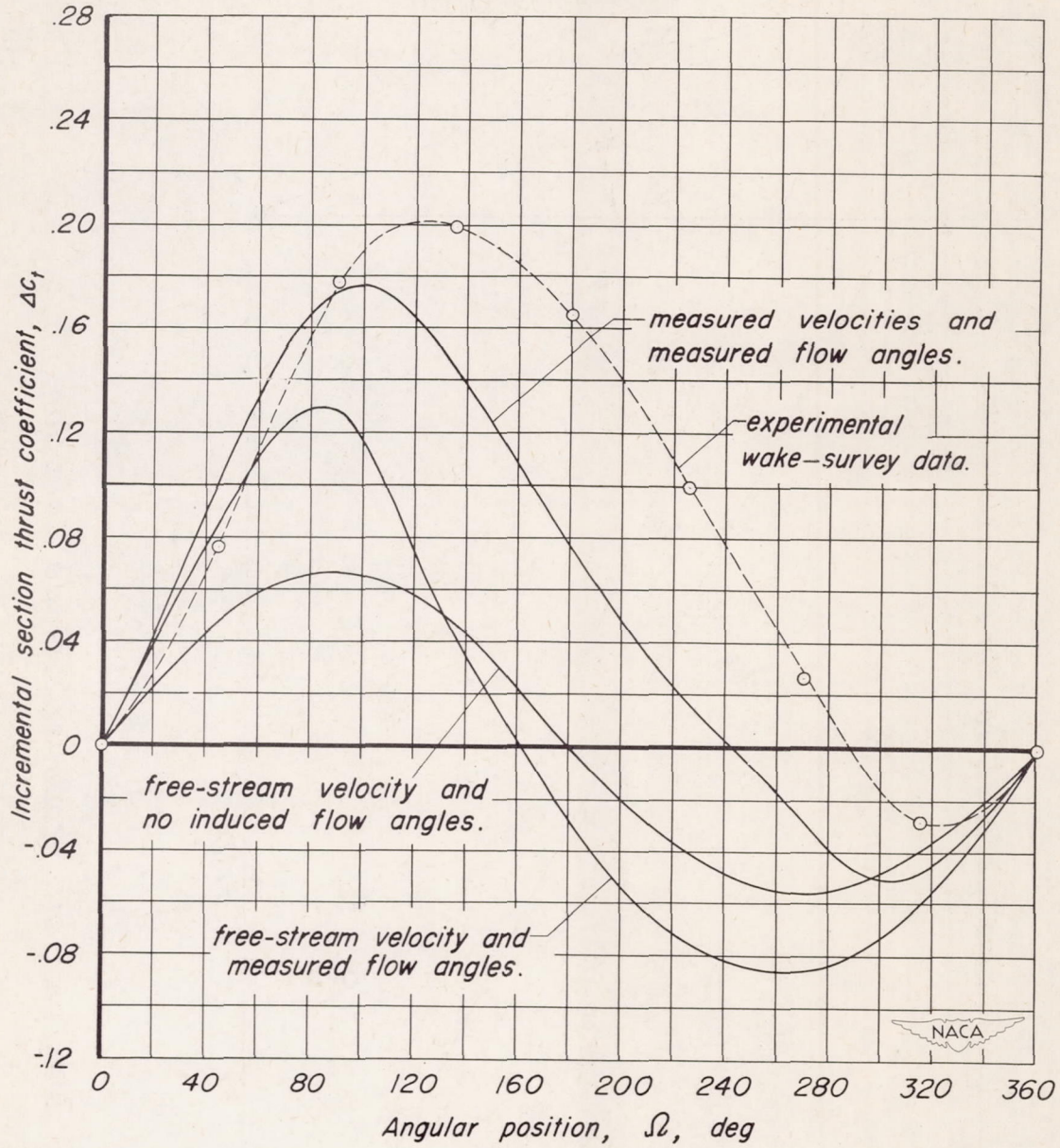


Figure 30.-Variation, at the 55.3-inch radial station, of incremental section thrust coefficient with angular position. a_G, 10°; δ_f, 0°; V_o, 165 mph; β, 21.7°; propeller speed, 1250 rpm.

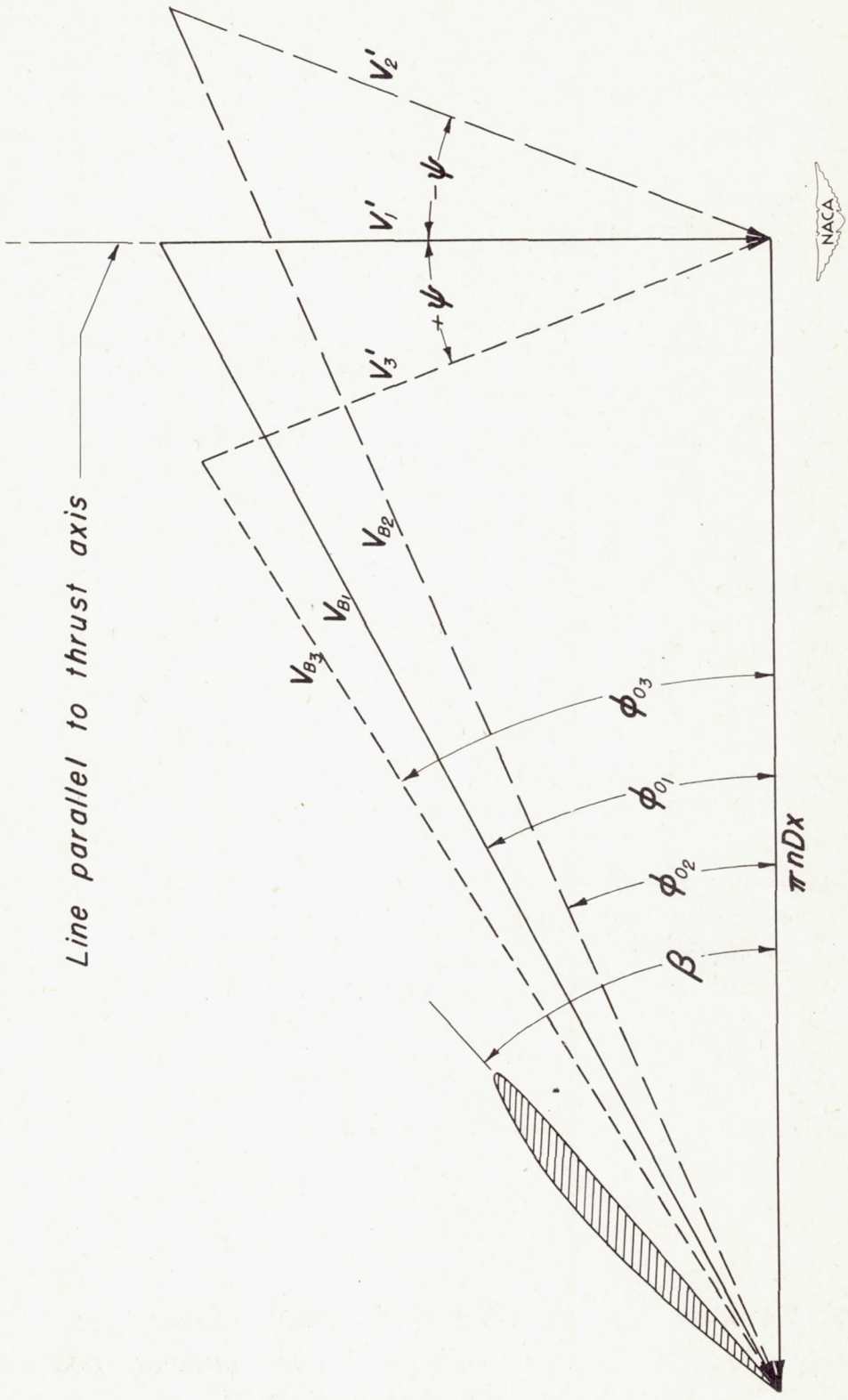


Figure 31.— Velocity diagram of propeller blade section.